Lecture Notes on
Beam Instrumentation and Diagnostics

Peter Forck

Gesellschaft für Schwerionenforschung (GSI)
Darmstadt, Germany

e-mail: p.forck@gsi.de

Joint University Accelerator School
January – March 2020

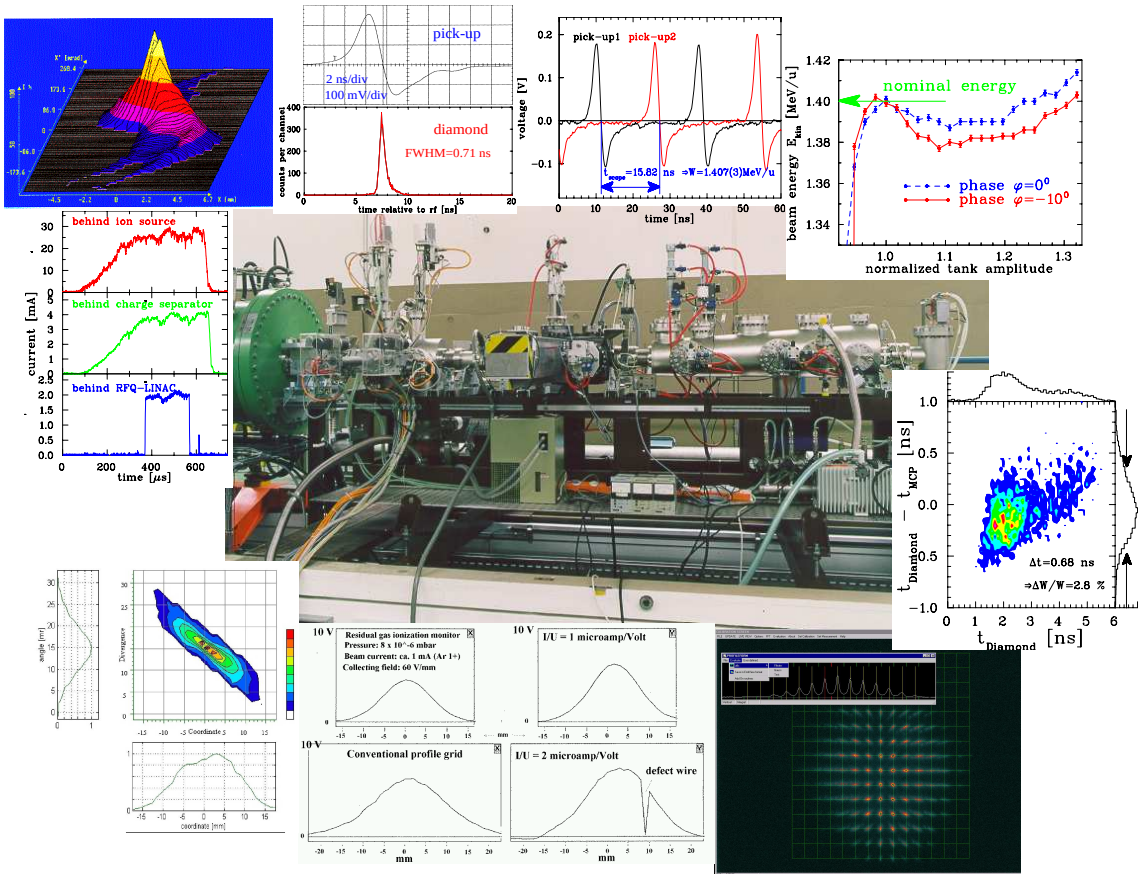

A picture of the mobile test bench including some measurements, as provided for the commissioning of the high current injector at GSI in 1999.

Contents

Chapter 1

Demands for beam diagnostics

Beam diagnostics is an essential constituent of any accelerator. It is the 'organ of sense' showing the properties and the behavior of the beam. It deals with the real beam including all possible imperfections of a real technical installation. Without adequate diagnostics one would 'blindly grope around in the dark' for the accelerator settings, and improvements are hardly achievable. There are three categories of diagnostic demands at any facility:

- Reliable, quick measurements to determine the basic parameters of a machine setting used as a fast check of the general functionality. The readings from the instrumentation give a single number or simple plots. These devices should be non-destructive for the beam, yielding online information. A prominent example is a current measurement by a transformer , as shown in Fig. 2.11 accompanied by the display of the average current in the form of one single number.

- Instrumentation built for a daily check of performance and stability, or for the control of necessary parameter changes in the accelerator setting. It can also be used for solving more straightforward machine problems in case of any malfunction. An example is the transverse profile determination, in most cases performed by a destructive device as discussed in Chapter 3; Fig. 3.4 contains transverse profiles at along the beam path as displayed in the control room at the GSI facility during the regular operating procedure.

- Complex instrumentation for the commissioning of a new accelerator component, for the development of higher performance and for solving more serious problems in case of a malfunction. The devices can be more complex to use and might be destructive for the beam. The importance is the creation of reliable information about the complex beam behavior allowing a clear interpretation. The determination of the beam emittance is an important example for the commissioning of a LINAC, these methods are discussed in Chapter 4. For a synchrotron the measurement of lattice parameters, like tune, chromaticity or β-function are required to achieve higher performance and for the comparison to theoretical calculations; related methods are discussed in Chapter 5.12 and 5.13.

The frontiers between these points are smooth but should give a guideline for the construction and usage of the diagnostics.

An additional application is the active influence of the beam settings after the detection of the beam's properties. This is called feedback of a given parameter to yield an improved beam delivery. An example is the reading of the beam position and the correction of the orbit to its nominal value. Quite different reaction times are typical, from less than μs to s, depending on the application. Such feedback systems involve the beam diagnostics as the input of the correction calculation. These extensive systems for beam control are out of the scope of this lecture and will not be discussed here.

There is a large variety of beam parameters to be measured. For a good alignment of the beam, all relevant parameters should be controllable. Table 1.1 gives an overview of the most essential beam quantities and the commonly used diagnostic devices and methods. The general properties for most of these devices will be discussed in this lecture, without going deeply into details; i.e., the lecture gives a reasonable coverage at the expense of a detailed description. For some parameters, the type of instrumentation differs for LINACs and synchrotrons, due to their different accelerating principles. A prominent example is that in a LINAC or a transfer line, the beam passes only once, while in a

Table 1.1: Beam parameters and the most commonly used beam diagnostics.

Beam quantity		**LINAC, transfer line**	**Synchrotron**
current I	*general*	transformer (dc, pulsed) Faraday cup	transformer (dc)
	special	particle detector (Scint. IC, SEM)	normalized pick-up signal
position $\overline{x}$	*general*	pick-up	pick-up
	special	using profile measurement	cavity excitation (e^-)
profile x_{width}	*general*	SEM-grid, wire scanner viewing screen, OTR-screen	ionization profile monitor synch. radiation (e^-) wire scanner
	special	grid with ampl. (MWPC)	
trans. emittance ϵ_{trans}	*general*	slit grid quadrupole scan	ionization profile monitor wire scanner
	special	pepper-pot	transverse Schottky pick-up wire scanner
momentum p and $\Delta p/p$	*general*	pick-up (TOF) magn. spectrometer	pick-up
	special		Schottky noise pick-up
bunch width $\Delta\varphi$	*general*	pick-up	pick-up wall current monitor
	special	secondary electrons arrival arrival at particle detector electro-optical modulation	streak camera (e^-) electro-optical modulation
long. emittance ϵ_{long}	*general*	magn. spectrometer buncher scan	
	special	TOF application	pick-up + tomography
tune, chromaticity Q, ξ	*general*	—	exciter + pick-up (BTF)
	special	—	transverse Schottky pick-up
beam loss r_{loss}	*general*	particle detector	
polarization P	*general*	particle detector	
	special	Compton scattering with laser	
luminosity $\mathcal{L}$	*general*	particle detector	

synchrotron, the behavior of thousands of passages has to be determined. For a synchrotron, non-destructive methods are preferred to monitor the beam behavior without any modifying influence. Moreover, electron beams have an entirely different behavior as compared to protons or heavy ions. A simple example is the fact that electrons are relativistic just after the first LINAC modules, while for protons, several 100 m long LINACs or even a synchrotron is needed to reach significant relativistic conditions. Another difference is the emission of synchrotron radiation by electrons, while this process occurs for protons only at the highest reachable energies, like in LHC. As seen from Table 1.1, the same beam quantity can be determined with different devices. Which of those are most suited depends on the various beam parameters themselves. On the other hand, several beam quantities can be determined with one type of instrument.

The diagnostics are a vital part of any accelerator. About 3 % to 10 % of the total cost of an accelerator facility (without the civil construction costs) must be dedicated to diagnostic instrumentation. However, due to the complex physics and techniques involved, the personnel involved in the design, operation, and further development of beam diagnostics exceed 10 % of the entire personnel of an accelerator facility in most cases.

As a first look at 'real-life', Fig. 1.1 shows an instrumental assembly installed behind the heavy ion LINAC at GSI during its commissioning phase. With this equipment, all relevant beam parameters had been measured extensively during a several week long period for each LINAC module. The beam quantities were: Current, transverse profile, transverse emittance, energy, bunch position, bunch structure, and longitudinal emittance in dependence of various parameter settings. Now the equipment

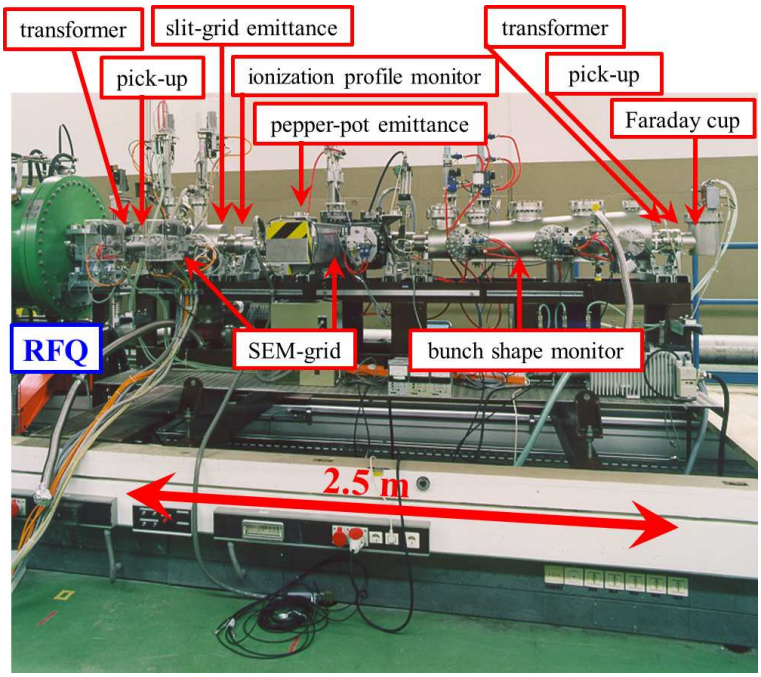

Figure 1.1: Photo of a movable test bench provided for commissioning of the new high current RFQ of GSI (green tank on the left).

is installed behind the last module for permanent use during operation and for further developments.

Most of the diagnostic instrumentation is based on one of the following physical processes:

- The electro-magnetic influence of moving charges on the environment as described by classical electro-dynamics theory as given by the Maxwell equations. The technique is based on a voltage or current measurement on a low or high frequency scale. Examples are beam transformers or pick-ups.

- The emission of photons by accelerated charges. This diagnostic is important for relativistic particles, i.e. electrons or very highly energetic protons. The technique is based on optical methods spanning the visible range up to the x-ray region. Examples are synchrotron radiation monitors for beam profile and time measurements.

- The Coulomb interaction of charged particles penetrating matter, described by atomic or solid state physics. The energy release due to electronic stopping gives the dominant fraction of the detected signal. The technique is based on current measurements or the observation of light by optical methods. Examples are scintillators, viewing screens, secondary electron emission grids, ionization chambers, and ionization profile monitors.

- The nuclear- or elementary particle physics interaction between the accelerated particles and a fixed target or between colliding beams. From the known cross sections, the beam quantity can be deduced. The technique is based on nuclear- or elementary particle physics detectors. Examples are polarimeters, luminosity monitors, or beam loss monitors used for machine protection and alignment.

- The interaction of the particles with a photon beam. The technique is based on lasers, their associated optics, and on detectors used for high energy physics. Examples are laser scanners or Compton polarimeters. Due to the special application, this is not discussed in this lecture.

In this lecture, we can only describe the principles of some commonly used devices, not all can be covered. Excellent introductory descriptions for beam diagnostics exist, as well as several books related to a variety of related topics [1]. Information on particular realizations can be found in the proceedings of dedicated beam diagnostics conferences and as a part of the general accelerator conferences [2]. In the literature, one can find extensive descriptions for the full instrumentation used at an ion synchrotron (RHIC, Brookhaven [3]) and an electron-positron collider (KEKB. Japan [4]).

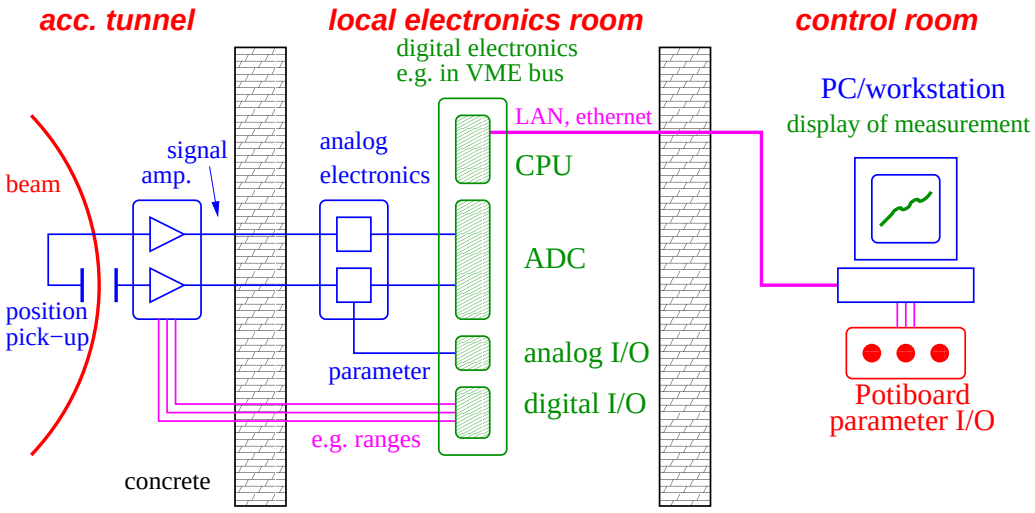

Figure 1.2: Schematics of typical beam diagnostics (here a position pick-up). The beam signal is modified by analog electronics and digitized in a local electronics room. From the control room the parameters of the measurement, as well as for the beam can be influenced.

Normally the yield of information from the diagnostic devices follows three successive steps from the measurement up to the display of the quantity of interest, as shown in Fig. 1.2 for the case of a electromagnetic beam position monitor:

- There is first the interaction of the beam with the detector. This signal has to be amplified and shaped. Low noise processing is essential at this step. In most cases, this is done close to the beam pipe.

- The amplified signal is transferred via cables out of the accelerator area to a local electronics room. The distance between these two locations can be several 100 m. Further shaping can proceed here , and the signal might be combined with other parameters as given by the accelerator settings. This is often realized by analog electronics. The original or modified signal is then digitized and stored. This can be done using an oscilloscope or a digital bus system. Example for bus systems are field buses like CAN- or PROFI-bus, or crate based systems like CAMAC, VME, PXI, μTCA, or CompactPCI. Digital signal processing could be applied to the data, and in a modern realization, it overtakes the role of the previously installed analog electronics. The control of the electronics is to be performed at this location.

- The data, or in most cases a reduced subset of the data, are passed to a PC or a workstation located in the operator's control room. Here the visualization is done, providing only the necessary information. Moreover, the parameters for the accelerator, like magnet currents or rf voltages, are changed from the control room to influence the beam. The resulting effect on the beam is then observed with a new set of measured data.

In this lecture, we focus on the principle of the action of the beam on the detector. For several systems, raw data are shown to visualize the general detector functionality. The preceding analog electronics are only discussed briefly. The technique of digitalization is not treated here, even though it is of great importance and occupies a significant effort. Digital electronics is not a pure diagnostics subject, and the realization is comparable to a great variety of other control applications. From the data analysis on the PC only typical results are presented, the realization of the algorithms is not discussed here. The associated software at the various steps is not described either.

Fig. 1.3 shows a view into the control room at GSI, where the information from the beam diagnostic instruments is displayed in connection with other controls of the accelerator. The various parameters of the accelerator are changed from this control room.

Most of the examples in this lecture are measured at the GSI facility because the author is most familiar with these realizations. This does not mean that GSI has the most advanced systems; at other facilities better installations might exist. The GSI accelerator facility, as shown in Fig. 1.4,

Figure 1.3: One section of the operator control room at GSI.

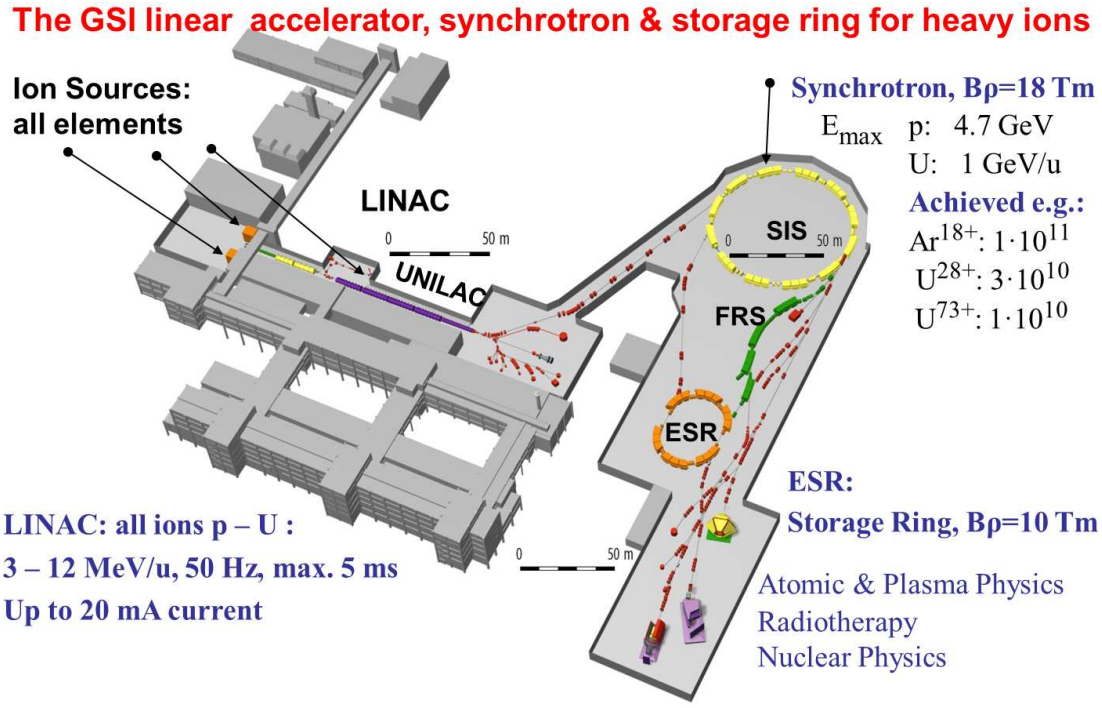

Figure 1.4: The GSI heavy ion accelerator facility.

consist of two pulsed LINACs running on 36 MHz and 108 MHz, respectively to accelerate all ions from different ion sources up to 18 MeV/u, corresponding to a velocity of $\beta = v/c = 0.19$. This energy is well above the so-called Coulomb barrier, where nuclear reactions are possible. Experiments with this beam are performed in the low energy experimental hall. For achieving higher energies up to 2 GeV/u, corresponding to $\beta = 0.95$, a synchrotron with 218 m circumference, the SIS, is used. The beam can be transferred to the storage ring ESR with a single bunch transfer (so-called fast extraction). Alternatively, it can be sent to fixed target experiments in this fast mode, or using slow extraction lasting from 1 to 10 s. The scientific investigations at these targets are related to nuclear, atomic or plasma physics, as well as human cancer therapy.

We restrict the lecture to the instrumentation of accelerators for stable particles, having a moderate current range. Typical applications at these facilities are experiments in atomic, solid state, biological, nuclear, and particle physics, as well as the use as synchrotron radiation sources. We do not treat

the diagnostic needs e.g., for radioactive beams (having a very low current) or the high current beam produced by induction accelerators. Moreover, the special diagnostics for negative H^- beams are not treated. The measurement of polarization and luminosity at colliders uses particle detectors and well-known cross sections for secondary particle production; this will not be discussed here.

At the end of the introduction, we have to state that the beam diagnostics have to help getting a stable operation with the best possible beam quality needed for the physics experiments.

Chapter 2

Measurement of beam current

The total electrical current is one of the most important parameters for the operation of a particle accelerator. In the daily operation, a first check concerns the current in almost all accelerator laboratories; in most cases, it is measured with a beam current transformer. This device works for electron and proton LINACs and synchrotrons, even for short pulses, like the transfer between synchrotrons, as well as for un-bunched beams like in a proton storage ring. These devices are commercially available [5], even though quite different types are used. A general overview of the current measurement device is presented in [6]. They are all non-intercepting. Their principle is the detection of the magnetic field carried by the beam. For currents below about 1 μA, transformers cannot be used due to noise limitations.

From the first days of accelerators, Faraday cups were used. The cup gives a direct measurement of the particle beam's charge because the particles are stopped in the cup. For high current, this destructive method can not be applied, because the total energy carried by the beam can destroy the intercepting material. For higher energetic particles with energies above some 100 MeV/u for ions, the penetration depth reaches more than several cm, and Faraday cups are not useful any more.

For low currents but higher energies above about 100 MeV/u for ions, particle detectors are used. Here the energy loss of the charged particle traveling through matter is detected. Either the particles are counted directly, or the particle flux can be calculated with the help of a calibration. For most parameters, this is an intercepting method. Slow extraction from a synchrotron within a typical duration of some seconds is an example of such beam parameters.

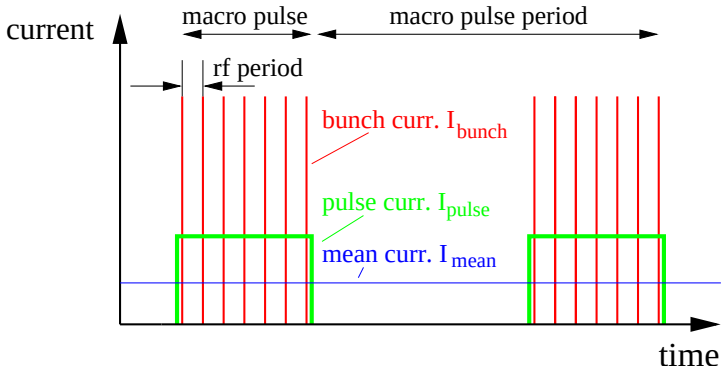

Figure 2.1: The time structure of the different currents at a pulsed LINAC.

Before discussing the devices, we define the time structure of a pulsed LINAC according to Fig. 2.1:

- The average or mean current I_{mean} is the long time average as given in units of A.
- The macro pulse current I_{pulse} is the time average during the beam delivery. In most cases, this is given in units of A.
- The current within a bunch I_{bunch}, sometimes also called the micro pulse current. In most cases, this is given in number of particles or charges per bunch.

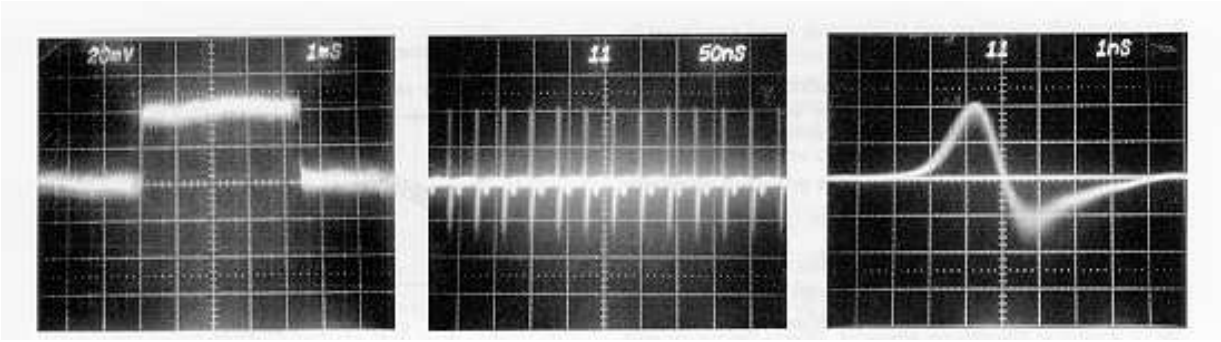

Figure 2.2: Pictures of measured currents. Left: macro pulse current, measured by a beam transformer with 1 ms/div, center: bunch signals within the macro pulse at 50 ns/div, right: differentiated single bunch signal from a capacitive pick-up on an enlarged scale of 1 ns/div.

A typical example of such a structure is given in Fig. 2.2 for a pulse length of 5 ms and an rf period of 27 MHz as recorded at the GSI heavy ion LINAC. Having a long train of bunches, the number of charges within a bunch is not determined with a transformer, as its bandwidth is too low for this purpose. Here capacitive pick-ups, which detect the electrical field, are well suited. Both plots on the right are recorded with these devices, see also Chapter 5.

Pulsed LINACs or pulsed cyclotrons can be used as an injector to a synchrotron, where only a typical pulse length of 100 μs is needed for a multi-turn injection. For a single-turn injection the time is of the order of 10 μs. For other applications, like in atomic or nuclear physics, a cw (continuous wave) accelerator is used. Here the bunches are delivered for an 'infinitely' long time. The macro pulse current I_{pulse} then equals the average current I_{mean}, but the bunch structure remains due to the rf acceleration by a LINAC or a cyclotron. There exist also types of accelerators not producing bunched beams; examples are Van-de-Graaff- and Cockcroft-Walton types based on electrostatic acceleration. Here all three types of current are equal.

2.1 Current transformer for pulsed beams

2.1.1 General considerations and passive transformer

In an accelerator the current is formed by N_{part} particles of charge state q per unit of time t or unit of length l and velocity $\beta = v/c$. The electrical current passing a given location is

$$I_{beam} = \frac{qeN_{part}}{t} = \frac{qeN_{part}}{l} \cdot \beta c \tag{2.1}$$

with e being the elementary charge. The magnetic field B of a current can be calculated according to the Biot-Savart law

$$d\vec{B} = \mu_0 I_{beam} \cdot \frac{d\vec{l} \times \vec{r}}{4\pi r^3} \tag{2.2}$$

with $\mu_0 = 4\pi \cdot 10^{-7}$ Vs/Am is the permeability of the vacuum, $d\vec{l}$ the length in direction of the beam and $\vec{r}$ the distance between the center of the beam and the coordinate the field is determined. Due to the cylindrical symmetry outside of the beam only the azimuthal component has to be considered along the unitary vector $\vec{e}_\varphi$ as shown in Fig. 2.3

$$\vec{B} = \mu_0 \frac{I_{beam}}{2\pi r} \cdot \vec{e}_\varphi. \tag{2.3}$$

For a beam current of 1 μA and a distance of 10 cm the magnetic field has a value of only 2 pT. To put this into perspective, the constant and homogeneous earth magnetic field has a value of about 50 μT.

The beam current can be determined by monitoring the accompanied magnetic field with a current transformer schematically shown in Fig. 2.4. The beam passes through a highly permeable torus as the 'primary winding'. An insulated wire wound around the torus with N turns serves as the 'secondary

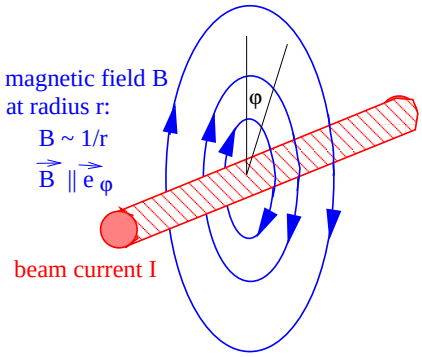

Figure 2.3: The magnetic field of a current.

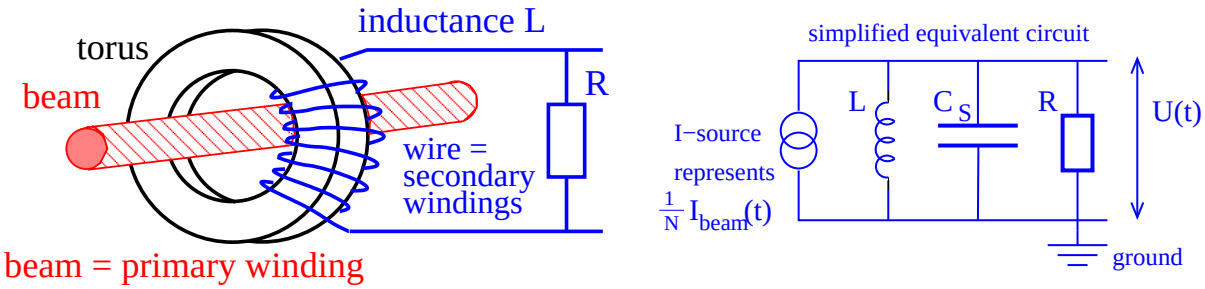

Figure 2.4: Scheme of a current transformer built as a ring-core (torus) around the beam (left) and the simplified equivalent circuit (right).

winding' of the transformer with the inductance L. The inductance L for a torus material of length l in beam direction, inner radius r_i and outer radius r_o having a relative permeability μ_r and N windings is given by

$$L = \frac{\mu_0 \mu_r}{2\pi} \cdot lN^2 \cdot \ln \frac{r_o}{r_i}. \tag{2.4}$$

The value of the induction can be chosen by the core size (as given by r_i and r_o) and the number of windings N. A further reason for the torus is to guide the field-lines, so only the azimuthal component is measured, and the signal strength is nearly independent of the beam position inside the vacuum pipe.

Generally for an ideal current transformer loaded with a low value of ohmic resistance R the ratio between the primary current I_{prim} and secondary current I_{sec} is given by

$$I_{sec} = \frac{N_{prim}}{N_{sec}} \cdot I_{prim} \quad \Longrightarrow \quad I_{sec} = \frac{1}{N} \cdot I_{prim} \quad \text{due to} \quad N_{prim} = 1 \tag{2.5}$$

with N_i the winding number on the primary side, which is one due to the single pass of the beam through the torus. N_{sec} is the winding number on the secondary side and for simplicity it is called N further-on.

For most practical cases a measurement of a voltage U is preferred, therefore the resistance R is introduced leading to

$$U = R \cdot I_{sec} = \frac{R}{N} \cdot I_{beam} \quad . \tag{2.6}$$

The ratio between the usable signal voltage U and the beam current I_{beam} is called sensitivity S (or transfer impedance, for a more stringent discussion see Chapter 5.1)

$$U = S \cdot I_{beam} \quad . \tag{2.7}$$

To understand the design criteria for the various applications, one has to consider the electrical properties of the transformer in more detail. With different external electrical elements, the response to a given time structure of the beam can widely be influenced. We first consider the characteristics of a so-called passive transformer or **F**ast **C**urrent **T**ransformer **FCT**, where the voltage at a 50 Ω

resistor is recorded. The equivalent circuit of the secondary transformer side is depicted in Fig. 2.4 on the right side. The beam current is modeled by a current source with a reduction given by the number of windings N according to Eq. 2.5. One has to take also some stray capacitance C_S into account, which are caused by the capacitance between the windings, the windings and the torus and along the shielded cable to the resistor R. To determine the voltage $U(t)$ the impedance of the parallel shunt of the three elements in dependence of the excitation frequency f or the angular frequency $\omega = 2\pi f$ is

$$\frac{1}{Z} = \frac{1}{i\omega L} + \frac{1}{R} + i\omega C_S \quad . \tag{2.8}$$

Using some algebra, this is equivalent to

$$Z = \frac{i\omega L}{1 + i\omega L/R - \omega L/R \cdot \omega R C_S} \quad . \tag{2.9}$$

This equation can be analyzed for three different frequency ranges:

- **Low frequency range assuming $\omega \ll \frac{\mathbf{R}}{\mathbf{L}}$:**
  In this case, the second and third term in the denominator of Eq. 2.9 can be neglected. The resulting impedance is then
  $$Z \to i\omega L \quad . \tag{2.10}$$
  The meaning of this equation is that the usable signal at the resistor R decreases proportionally to the excitation frequency because the inductance acts as a short circuit for the considered low frequencies. In particular, at $\omega = 0$ no signal can be recorded. This reflects the well-known fact that a transformer can not handle dc-currents.

- **High frequency range assuming $\omega \gg \frac{\mathbf{1}}{\mathbf{RC_S}}$:**
  In this case, the first and second term in the denominator of Eq. 2.9 can be neglected. The impedance is then
  $$Z \to \frac{1}{i\omega C_S} \quad . \tag{2.11}$$
  This reflects the fact that for high frequencies the current is mainly flowing through the capacitor and therefore the voltage drop at the resistor R is low.

- **Working region $\frac{\mathbf{R}}{\mathbf{L}} \ll \omega \ll \frac{\mathbf{1}}{\mathbf{RC_S}}$:**
  For this case the second term in the denominator of Eq. 2.9 dominates, and term one and three can be neglected. The impedance is then
  $$Z \simeq R \quad . \tag{2.12}$$
  This is the usable working region, where the voltage drop at the resistor is significant. The working region can be chosen on a wide range as given by the values of the electronic elements L and C. Generally, for a parallel RLC-circuit like shown in Fig 2.4 oscillations are inhibited if the condition $R < 1/2 \cdot \sqrt{L/C_s}$ is fulfilled. In particular, the low value of the resistor $R = 50\ \Omega$ to ground allows for a current flow, resulting in an over-damping of possible oscillations.

The above-mentioned frequencies restrict the working region with a correct response of the measured signal with respect to the beam current. At the lower frequency boundary the signal decreases; the frequency f_{low} for which the signal is decreased by a factor of $e^{-1} = 0.37$ is called the low cut-off frequency f_{low} and is given by $\omega_{low} = 2\pi f_{low} = R/L$. At the upper boundary the corresponding value $\omega_{high} = 1/RC_S$ is called upper cut-off frequency.

For the following discussion, we are more interested in the time response of the measurement device to a given beam pulse. Therefore, one uses frequently the rise time constant τ_{rise} and the droop time constant τ_{droop} as depicted in Fig. 2.5: If the excitation is given by a step-function, the signal amplitude A increases as $A \propto (1 - e^{-t/\tau_{rise}})$ and τ_{rise} corresponds to the time for an increase by $e^{-1} = 37\ \%$. It is linked to the upper cut-off frequency by

$$\tau_{rise} = \frac{1}{\omega_{high}} = \frac{1}{2\pi f_{high}} \quad . \tag{2.13}$$

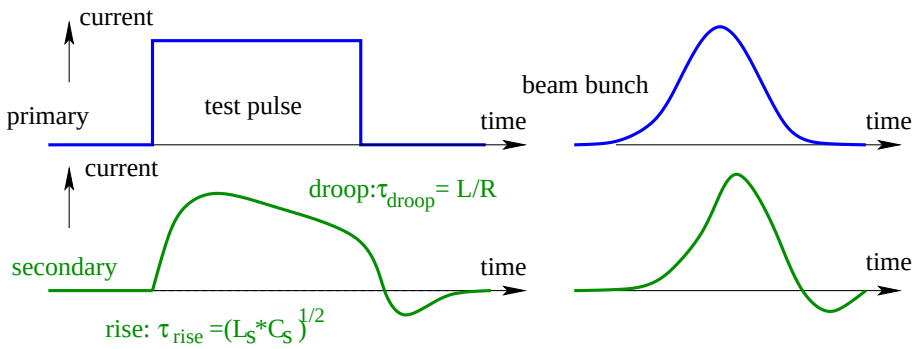

Figure 2.5: The response of an ac-transformer to a rectangular pulse and a more realistic beam pulse.

Correspondingly, the droop time constant is linked to the lower cut-off frequency as

$$\tau_{droop} = \frac{1}{2\pi f_{low}} \quad . \tag{2.14}$$

Both equations have a general meaning and will be used to transfer quantities like bandwidth, as given in the frequency domain, into the corresponding description in the time domain [1].

For the passive current transformer as described by the equivalent circuit of Fig. 2.4 the rise and droop time constant are given by

$$\tau_{rise} = RC_S \quad \text{and} \quad \tau_{droop} = \frac{L}{R} \quad . \tag{2.17}$$

A more realistic schematic diagram of the passive transformer is shown in Fig. 2.6. The main difference is the additional loss resistivity in the cables, which is represented by a serial resistor R_L. Additionally, there is a stray inductance between the windings, which is best modeled by a serial insertion of an inductance L_S. For the higher frequencies response, one has to consider the frequency dependence of the permeability μ_r of the torus made of CoFe-based amorphous alloy (so-called Vitrovac©) with $\mu_r \sim 10^5$ for low frequencies. But the permeability decreases above $f \sim 100$ kHz with a scaling $\mu_r \propto 1/f$ and therefore also the inductance of the torus decreases. For frequencies above ~ 100 MHz the stray inductance is the dominant contribution. With these two modifications the rise and droop times are modified to yield

$$\tau_{rise} = \sqrt{L_S C_S} \qquad \text{and} \quad \tau_{droop} = \frac{L}{R + R_L} \quad . \tag{2.18}$$

Passive transformers are mainly used when short beam pulses have to be measured. An example is the observation of the bunch structure during acceleration inside a synchrotron as shown in Fig. 2.7 for the acceleration of an ion beam injected at a non-relativistic velocity of $\beta = 15$ % of velocity of light and accelerated to $\beta = 69$ %. A second example is shown in Fig. 2.8 for one bunch extracted from a synchrotron within one revolution, the so-called fast extraction. For the latter case, the passive transformer is installed in the beam pipe outside the synchrotron. The beam pulse length is typically between 1 ns and 10 μs. Moreover, with the passive transformer, the bunch structure in time domain can be observed and a bandwidth typically 1 GHz, corresponding to a rise time constant of $\tau_{rise} = 160$ ps, can be achieved [5, 8]. The specifications of the GSI device are listed in Table 2.1. Careful matching is necessary between the torus and the 50 Ω resistor R, where the voltage drop is measured.

To get the right choice of the parameters of a passive transformer we have some requirements:

[1] In time domain one uses either the rise time constant τ_{rise} or more frequently the rise time t_{rise}, as defined from an amplitude increase from 10 % to 90 %. It can be written as

$$t_{rise} = \frac{\ln 0.9 - \ln 0.1}{\omega_{high}} = \frac{\ln 9}{2\pi f_{high}} \simeq \frac{1}{3 f_{high}} \simeq 2.2 \cdot \tau_{rise} \quad . \tag{2.15}$$

Both quantities are therefore connected by $t_{rise} = \ln 9 \cdot \tau_{rise} \simeq 2.2 \cdot \tau_{rise}$.
The same relations hold for the droop time

$$t_{droop} \simeq \frac{1}{3 f_{low}} \simeq 2.2 \cdot \tau_{droop} \tag{2.16}$$

.

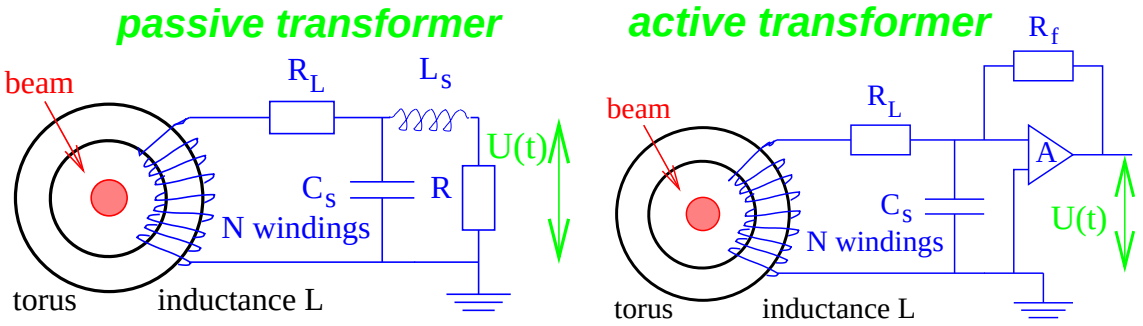

Figure 2.6: Equivalent circuits of a passive beam transformer (left) and an active transformer (right).

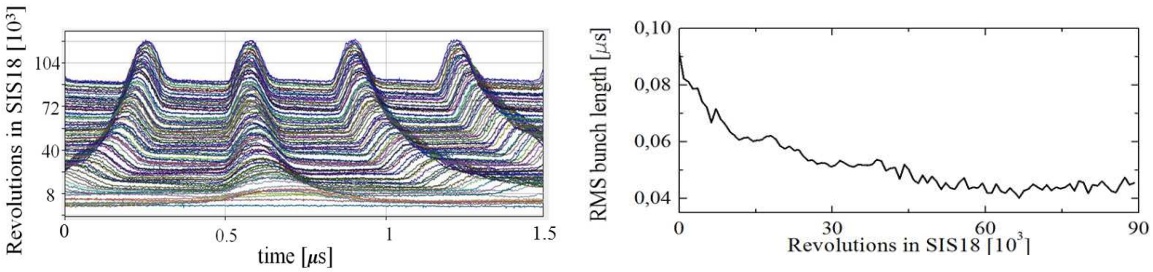

Figure 2.7: Left: Signals from a passive transformer installed in GSI synchrotron during the acceleration of a U^{73+} beam. The beam is injected at 11 MeV/u, corresponding to a velocity of $\beta = 15$ % then four bunches are build and accelerated to 350 MeV/u, corresponding to $\beta = 69$ % with an accelerating frequency swing from 0.85 MHz to 3.80 MHz within 0.3 s. Each 0.15 ms a trace of the circulating bunches are shown. Right: The width (one standard deviation) of the bunches during acceleration is shown.

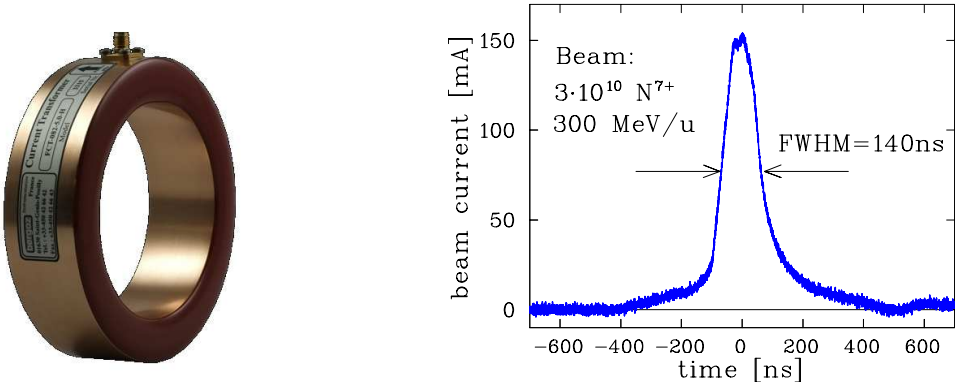

Figure 2.8: Left: Photo of a commercially available passive transformer [5]. Right: The signal from a passive transformer for a single beam bunch extracted from the GSI synchrotron at 300 MeV/u.

Table 2.1: Basic specification of the GSI passive transformer [8].

Parameter	Value
Torus radii	$r_i = 70$ mm, $r_o = 90$ mm
Torus thickness l	16 mm
Torus material	Vitrovac 6025: $(CoFe)_{70\%}(MoSiB)_{30\%}$
Torus permeability μ_r	$\mu_r \simeq 10^5$ for $f < 100$ kHz, $\mu_r \propto 1/f$ above
Number of windings N	10
Sensitivity S	4 V/A at $R = 50\ \Omega$ (10^4 V/A with amplifier)
Current resolution I_{min} for $S/N = 1$	40 μA_{rms} for full bandwidth
Droop time constant $\tau_{droop} = L/R$	0.2 ms, corresponding to 5% per 10 μs pulse length
Rise time constant $\tau_{rise} = \sqrt{L_S C_S}$	1 ns
Bandwidth	$f_{low} = 0.75$ kHz to $f_{high} = 660$ MHz

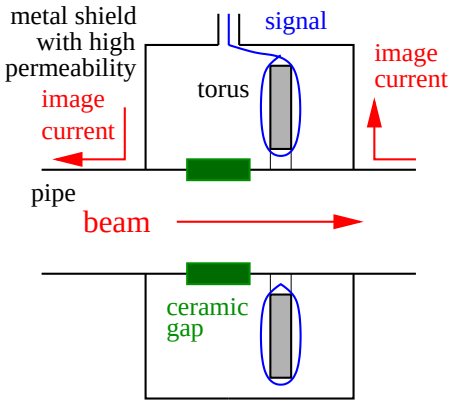

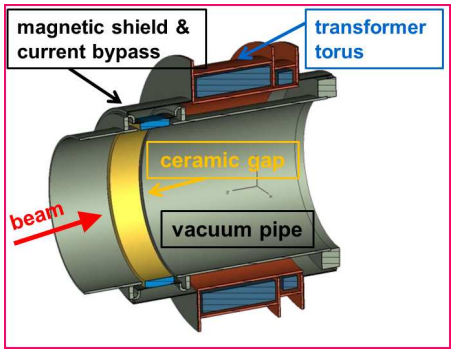

Figure 2.9: Left: The general scheme beam pipe intersected by a ceramic gap and a transformer housing as used as an image current pass and a shielding against external magnetic fields is shown. Right: The technical drawing for a transformer arrangement surrounding a beam pipe including the gap and magnetic shield is shown.

1. For a high sensitivity i.e., a large voltage U a low number of windings is preferred, according to $U(t) \propto 1/N$ in Eq. 2.6.

2. For a long droop time constant, i.e., the possibility of measuring long beam pulses, a large inductance has to be used. The scaling is $L \propto N^2$ and $L \propto \mu_r$ as given in Eq. 2.4. Therefore materials with high permeability are used e.g., CoFe-based amorphous alloy (so-called Vitrovac©) with $\mu_r \sim 10^5$. For higher frequencies, μ_r decreases and, therefore, also the torus inductance L. A typical cut-off frequency is 100 kHz with a scaling for higher frequencies $\mu_r \propto 1/f$.

3. To achieve a fast rise time and therefore a fast response, the stray capacity C_s should be low due to $\tau_{rise} \propto \sqrt{L_s C_s}$

An additional general point is, that close to the transformer the electrical conductivity of the beam pipe has to be interrupted as schematically shown in Fig. 2.9. This is done with an insulator, either a ceramic gap or a plastic vacuum seal. The reason is to prevent a flow of image current inside of the transformer torus. This image current has the opposite sign, and without the gap, the fields of the image current and beam current add up to zero. The image current has to be bypassed outside of the transformer torus by some metallic housing. It is surrounded by high permeability μ-metal, also used for the shielding of the transformer against external magnetic fields. A general review on transformers is presented in [6, 7].

2.1.2 Active ac-transformer

For the observation of beam pulses longer than several μs, the droop of a passive transformer leads to significant deformation of the measured signal, as schematically shown in Fig. 2.5. The droop time constant can be made much longer by using an operational amplifier (op-amp), with a feedback resistor R_f and an open-loop gain A, instead of a constant resistor to measure the voltage. The equivalent circuit is shown in Fig. 2.6, right side. The effect is the reduction of the operational-amplifier input resistance by a factor of R_f/A. This is the setup of a so-called trans-impedance amplifier or current-to-voltage converter. The remaining resistance is in most cases only given by the cable resistivity R_L due to $R_f/A \ll R_L$. The droop is now

$$\tau_{droop} = \frac{L}{R_f/A + R_L} \simeq \frac{L}{R_L}. \tag{2.19}$$

Droop time constants up to 1 second are possible. (Typical values of the cable resistance is $R_L \sim 1\ \Omega$.) An additional winding (not shown in Fig. 2.6 right) has to be used to compensate for the 'natural', known droop. Moreover, the feedback resistor R_f of the operational amplifier can be used for range switching. This principle is called the active transformer or **A**lternating **C**urrent **C**urrent **T**ransformer **ACCT**.

Table 2.2: Some basic specification of the GSI LINAC active transformer. Due to the usage of an operational-amplifier, the sensitivity is significantly higher than for the passive transformer of Table 2.1.

Parameter	Value
Torus radii	$r_i = 30$ mm, $r_o = 45$ mm
Torus thickness l	25 mm
Torus material	Vitrovac 6025: $(CoFe)_{70\%}(MoSiB)_{30\%}$
Torus permeability μ_r	$\simeq 10^5$
Number of windings N	2×10 with opposite orientation
Maximal sensitivity S	10^6 V/A (with operational-amplifier)
Ranges of the beam current	1 μA to 100 mA
Current resolution I_{min} for $S/N = 1$	0.2 μA_{rms} for full bandwidth
Droop	< 0.5 % for 5 ms pulse length
Upper cut-off frequency f_{high}	1 MHz (as given by the op-amp property)
Rise time constant τ_{rise}	160 ns

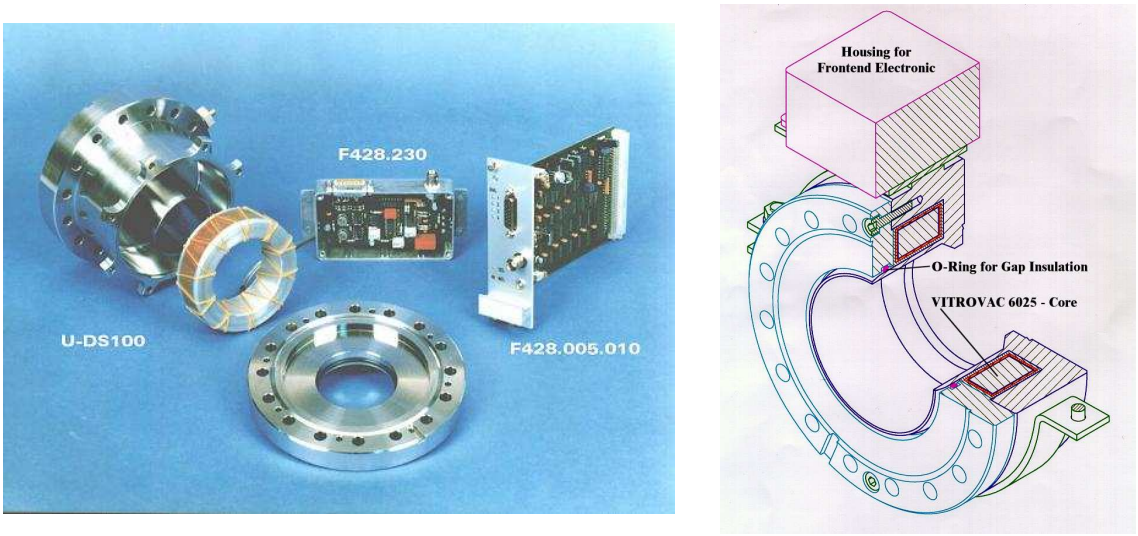

Figure 2.10: Left: Photo of an ac-current transformer used at the pulsed heavy ion LINAC at GSI. The torus with the differential winding is shown together with the electronic modules. Right: Technical drawing of the same transformer.

The rise time τ_{rise} for this active type is much larger than for the passive type. This is mainly due to the choice of a low bandwidth (low value of the upper cut-off frequency) of the operational amplifier to obtain a significant reduction of the amplifier's high frequency noise. This results in the high sensitivity of an active transformer.

We discuss a typical device [8] used at the heavy ion LINAC at GSI with a pulse length of 100 μs (used for the filling of a synchrotron) and 5 ms (used directly by the experiments). The values of the macro pulse current ranges from the low detection threshold of $\sim$ 200 nA up to 100 mA. The large dynamic range depends on the operational needs and on the maximum current the ion source can deliver. In Fig. 2.10 the hardware is shown. A specification is given in Table 2.2, for the parameters for the commercially available type see [5].

The device has a rise time of 1 μs and a maximum droop of only 0.5% for 5 ms long pulses. The torus material is made of amorphous alloy $(CoFe)_{70\%}(MoSiB)_{30\%}$ (Vitrovac©), to enable a large sensitivity. Besides the high permeability of $\mu_r \simeq 10^5$ it has a high electrical resistance resulting in fast decay of eddy currents. The torus is made of flat strips of 25 μm thickness with a thin insulation and is wound to get the final thickness of $r_o - r_i = 15$ mm. Another important material constant is the change of the inductance as a function of external stress, the so-called magnetostriction. A low value prevents the micro-phonic pick-up of vibrations produced e.g., by vacuum pumps.

A measurement done with these types of transformers is shown in Fig. 2.11 left, where one macro-

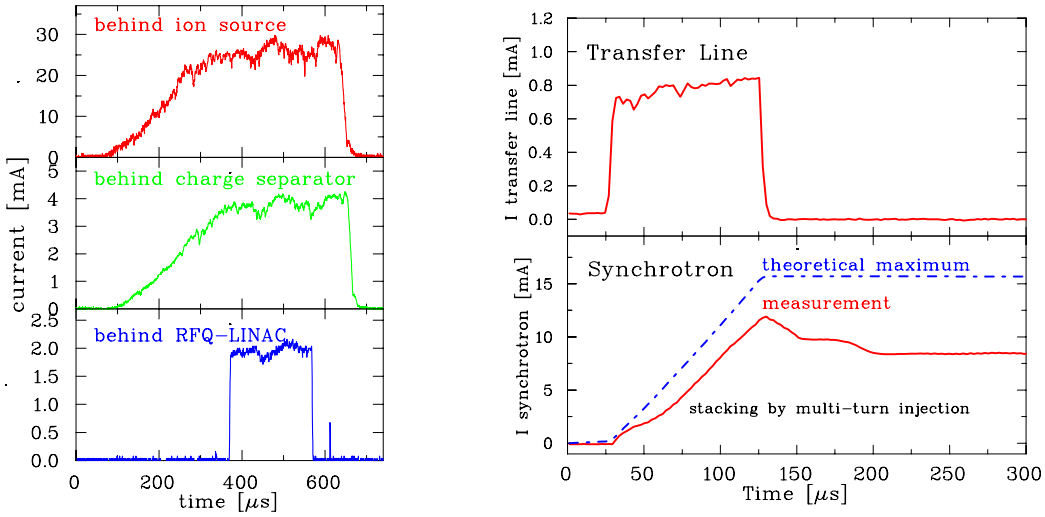

Figure 2.11: Left: Transmission determination by ac-transformers at three different locations at the GSI LINAC using a Ni^{2+} beam from a high current source. The upper curve shows the current after the ion source where all charge states are present. The second curve behind a magnetic bend to filter the Ni^{2+} ionic state. The third curve is the current after the first LINAC module.
Right: The multi-turn injection at GSI measured with two ac-transformers. The upper curve is the current delivered by the LINAC and the lower curve is the stored current in the synchrotron. In this case 20 turns are used, and 70 % efficiency is reached for this Ni^{26+} beam.

pulse is recorded at three locations starting at the ion source until the exit of the first LINAC tank. A high current ion beam is generated in the source with ~ 0.5 ms length. The slow rise of the beam current before the LINAC is due to the build-up of the space charge compensation of the un-bunched beam. A chopper in front of the LINAC is used to generate the needed pulse length. Transformers are essential to determine and maximize the transmission through the accelerator, in particular, if the ion source conditions are not very stable. A non-destructive method is needed to follow the beam pulse for its pass through the full accelerator. During the operation of the accelerator, these transformers are the most frequently used diagnostics.

To control the filling of a synchrotron by a pulse from a LINAC, transformers of the described type are used. One of them is mounted in the external beamline, measuring the delivered current, and the other one is installed inside the synchrotron to determine the stored current. The used multi-turn injection is done with some bumper magnets to fill the large horizontal acceptance of the synchrotron by the LINAC pulse, which is much longer than the revolution period. Such a measurement at the GSI facility is shown in Fig. 2.11 right: the injection takes place over 20 turns, and accumulation by a factor ~ 15 is achieved. For each beam setting, optimization of the injection process is an important task to achieve a maximal matching.

2.2 The dc-transformer

An important task for beam diagnostics is the measurement of coasting (or so-called direct current dc) beam current. The application is either a LINAC producing beam permanently (so-called continuous wave cw-mode) or a synchrotron with storage times from seconds to many hours. The transformers discussed in the previous sections only work for a pulsed beam, even though the droop time constant can be made to be of the order of a second.

The principle of a dc transformer, the so-called **D**irect **C**urrent **C**urrent **T**ransformer **DCCT** [5, 8, 9] is shown schematically in Fig. 2.12. It consists of two tori with three types of windings each. The first windings of each torus with opposite orientation are used as a modulator. The modulation frequency is typically 1-10 kHz. The amplitude of the modulation current is high enough to force the torus into magnetic saturation of $B_{sat} \simeq 0.6$ T, for positive and negative azimuthal orientation each period. The secondary windings with equal orientation act as a detector for the modulated signal, see Fig. 2.13. Assuming perfectly identical magnetic characteristics of both tori, the detector signal,

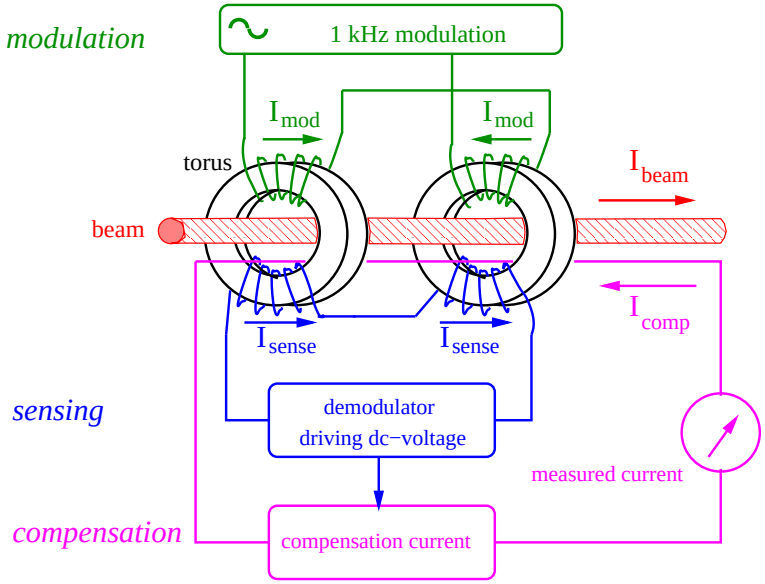

Figure 2.12: Schematics of a dc-transformer, see text.

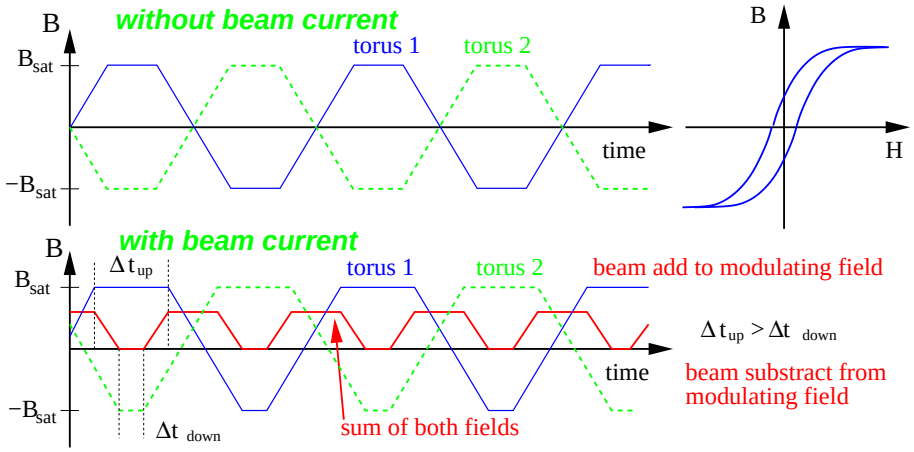

Figure 2.13: The fluxes in the two tori of a dc-transformer without and with a beam. The magnetic field of the beam adds to the modulated field for one modulation phase and 180^o degree later, it is subtracted. The sum of the maximum magnetization gives the measured signal. The scheme is drawn for a triangular-modulation, for a realistic sine-modulation the edges are smoother.

Table 2.3: The specification of the dc-transformer installed at the GSI synchrotron.

Parameter	Value
Torus radii	$r_i = 135$ mm, $r_o = 145$mm
Torus thickness l	10 mm
Torus material	Vitrovac 6025: $(CoFe)_{70\%}(MoSiB)_{30\%}$
Torus permeability	$\mu_r \simeq 10^5$
Isolating gap	Al_2O_3
Number of windings N	16 for modulation and sensing
	12 for feedback
Ranges for beam current	300 μA to 1 A
Current resolution I_{min} for $S/N = 1$	2 μA
Bandwidth	dc to 20 kHz
Rise time constant τ_{rise}	20 μs
Offset compensation	$\pm$2.5 μA in auto mode
	< 15 μA/day in free run
offset current temperature coefficient	1.5 μA/^{o}C

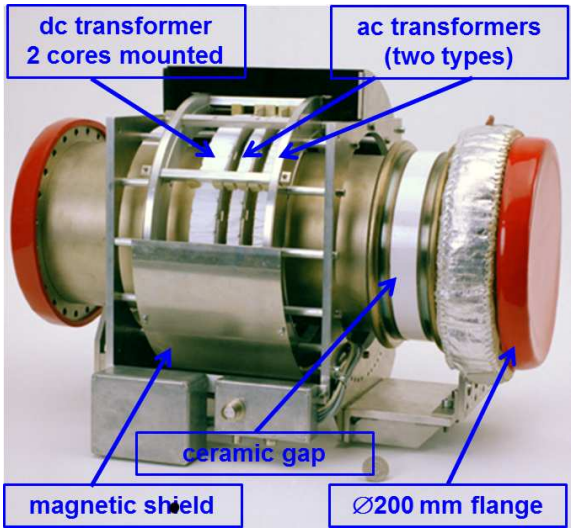

Figure 2.14: The dc-transformer installed at the GSI synchrotron. The left torus is the dc-transformer (two tori mounted closely together), the middle is the ac-transformer used for the feedback of the dc-type and the right one is the ac-transformer for the control of the injection.

as shown in the scheme, should be exactly zero if there is no beam current flowing through the tori. However, an asymmetric shifting of the hysteresis curve results if a dc-beam is fed through the toroids, because of the additional magnetic field from the beam. The sum signal U_S is different from zero with a modulation twice the modulation frequency. In the demodulator stage this signal is rectified. The dc-current is measured by means of the current generated in the feedback compensation circuit, which forces the output signal back to zero flowing through the third winding of both tori. The detector can even be used at even harmonics of the modulation frequency, which results in higher sensitivity and an improvement of the signal-to-noise ratio. Due to the extremely specific requirements concerning the matching of the magnetic characteristics for a pair of tori, the design of a magnetic modulator with high resolution and dc-stability is rather complex and depends very much on the selection and treatment of the core-material as discussed in more detail in [9]. The applied feedback circuit for the zero flux compensation makes the device very sensitive and linear. To get a fast response, the signal from an ac-transformer is added into the feedback circuit. With this enhancement, the time resolution of the full device is in the range of 20 μs.

The specification of a typical dc-transformer developed for the heavy ion synchrotron at GSI is given in Table 2.3 and a photo in Fig. 2.14. The resolution is about 1 μA. The offset drift, mainly caused by the magnetic properties of the tori, is of the order of 20 μA per day. An automatic zero compensation can improve the offset at times; the synchrotron does not contain any beam, e.g., after the ramp down phase of the magnets. For the parameters of a commercially available type, see [5].

An example of a dc-transformer measurement is shown in Fig. 2.15. The electrical current and the number of stored particles are shown. A $^{238}U^{73+}$ beam is injected in the synchrotron, and the acceleration starts shortly after the injection. A loss of particles is seen during the rf bunching process due to some misalignment. During the acceleration the slope of the magnetic field $dB/dt = 1.3$ T/s is constant, resulting in a constant rise of the particle momentum. The current grows linearly only for non-relativistic velocities due to the decrease of the revolution time, inversely proportional to the velocity. For the maximal energy of 750 MeV/u, corresponding to $\beta = 84$ %, the relativistic increase of the mass starts to be significant. After reaching the maximum energy, a ~ 0.5 s flat top is seen for the de-bunching phase. The slow extraction of several seconds is done by changing the tune using a fast quadrupole to get close to a 1/3-resonance to blow up the transverse beam dimension. The resonant beam particles are then separated from the stable circulating beam by an electrostatic septum and are extracted.

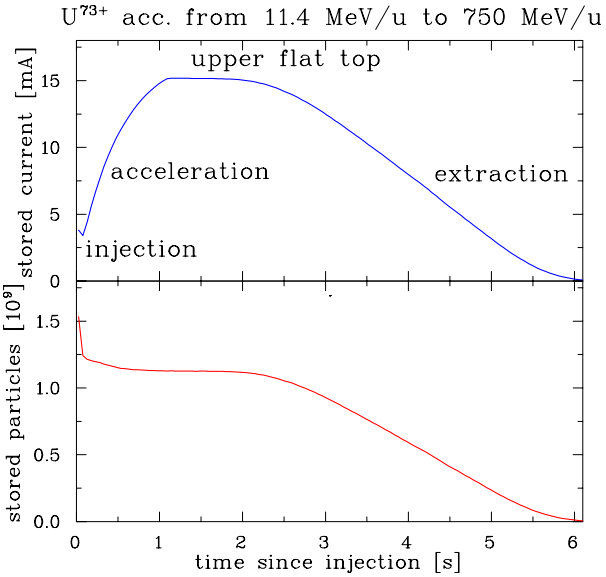

Figure 2.15: The signal of a dc-transformer for a $^{238}U^{73+}$ beam at the GSI synchrotron. The electrical current is shown at the top and the number of stored particles at the bottom. The acceleration needs about 1 s. After a delay of about 0.5 s, the slow extraction of 4 s length follows.

2.3 The low current limit of transformers

The very low magnetic field carried by the beam is detected with a transformer; the detection threshold or the signal-to-noise ratio is discussed briefly:

1. A first general limitation is the thermal noise of the load resistor. The effective thermal noise voltage U_{eff} is given by
$$U_{eff} = \sqrt{4k_B T \cdot R \cdot \Delta f} \tag{2.20}$$
with T is the temperature of the resistor R, k_B the Boltzmann constant and Δf the required bandwidth. A general rule is that the noise is lower for a smaller bandwidth. For a passive transformer $R = 50\ \Omega$ for the load resistor. For an active transformer the amplifier noise dominates.

2. Regarding the magnetization of the core-material on a atomic (or solid state physics) scale, we have the so-called Weiss domains. In a domain, the maximum magnetization is reached, but the magnetization of the different domains do not have the same orientation. By applying an external field the Weiss domains change their orientations in a jerky way. This results in a noisy behavior as schematically demonstrated in Fig 2.16. The effect is called Barkhausen noise. This effect is the limitation of the dc-transformer, because the working principle is the modulation, which drives the tori into saturation. For an ac-transformer the Barkhausen noise is of no importance, because of the low resistive coupling of the secondary winding (50 Ω for the passive type and low impedance input of the op-amp for the active type) prevent magnetization of the torus.

3. A careful choice of the magnetic core-material is essential to have a low temperature influence, as well as a low disturbance of mechanical vibration (low magnetostriction).

4. Even if the local magnetic field is measured precisely, it might not be the field of the beam. In particular, eddy currents in the torus or the surroundings might give rise to a noisy or wrong reading. To reduce eddy currents, a spiral wound flat ribbon ($\sim$ 25 μm thickness) with high resistivity and insulation between layers is used.

5. The transformer has to be well shielded against external magnetic fields. In particular against the fields from the bending and focusing magnets and the fields produced by turbo pumps.

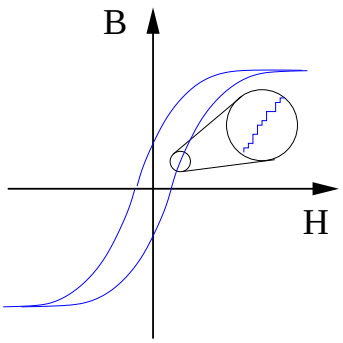

Figure 2.16: Barkhausen noise generated by the change of the orientation of the Weiss domains.

6. One has to prevent the flow of secondary electrons, created by the beam hitting the vacuum pipe through the transformer. This can be a large error contribution to the reading. Shielding within the vacuum pipe is difficult in most cases. Therefore the beam steering has to be controlled carefully.

The actual value of the minimum detected beam current depends on the design of the device. For most cases, it is about 1 μA.

2.4 Energy loss and ranges of particles in matter

2.4.1 Material interaction of protons and ions

For the discussion for all intercepting diagnostics like Faraday cups, ionization chambers, wire scanners etc., the energy loss and the related range of the particles penetrating matter serves as the basic physical mechanism. The energy loss of a proton or an ion is mainly due to the collision of the projectile with the electrons of the stopping target, the so called electronic stopping. Due to the different masses of the ion and the electron, the energy transfer to the electron per collision is in most cases below 100 eV. The electronic stopping power $\frac{dE}{dx}$ can be approximated by the semi-classical Bethe-Bloch formula which is written in its simplest from as [10, 11, 12, 13]

$$-\frac{dE}{dx} = 4\pi N_A r_e^2 m_e c^2 \cdot \frac{Z_t}{A_t}\rho \cdot \frac{Z_p^2}{\beta^2}\left[\ln\frac{2m_e c^2\gamma^2\beta^2}{I} - \beta^2\right] \tag{2.21}$$

with the constants: N_A the Avogadro number, m_e and r_e the mass and classical radius of an electron and c the velocity of light. The target parameters are: ρ density of the target with nuclear mass A_t and nuclear charge Z_t; the quantity $\frac{Z_t}{A_t}\rho$ correspond to the electron density. I is the mean ionization potential for removing one electron from the target atoms; a rough approximation for a target with nuclear charge Z is $I \simeq Z \cdot 10$ eV, more precise values are given e.g. in [14, 13]. The projectile parameters are: Z_p nuclear charge of the ion with velocity β and $\gamma = (1-\beta^2)^{-1/2}$. For more details see [10, 11, 12, 13]. This formula has to be modified due to the fact that ions traveling through matter are not bare nuclei, but have some inner electrons. An effective charge is used instead of Z_p calculated by e.g. semi-empirical methods described for the codes SRIM [14] or LISE++ [15]. The result of such semi-empirical calculation for the energy loss is shown in Fig. 2.17 for different ions into copper. The energy loss is maximal for ions with kinetic energy around 100 keV/u to 7 MeV/u (corresponding to velocities $\beta \sim 1.5$ % to 12 %) depending on the ion species. These are typical energies of a proton/heavy ion LINAC. Below 100 keV/u the energy loss decreases, and nuclear stopping becomes significant. Energies below 10 keV/u are typical for proton/heavy ion sources mounted on a high voltage platform. For relativistic energies above 1 GeV/u the energy loss is nearly constant; these are typical energies of particles extracted from a synchrotron.

For the consideration of a Faraday cup (see section 2.5), the range in a material is important. Copper is often used for cups, due to its high heat conductivity. For a particle accelerated to E_{kin}, the range R is calculated numerically from the stopping power via

$$R = \int_0^{E_{kin}} \left(\frac{dE}{dx}\right)^{-1} dE \tag{2.22}$$

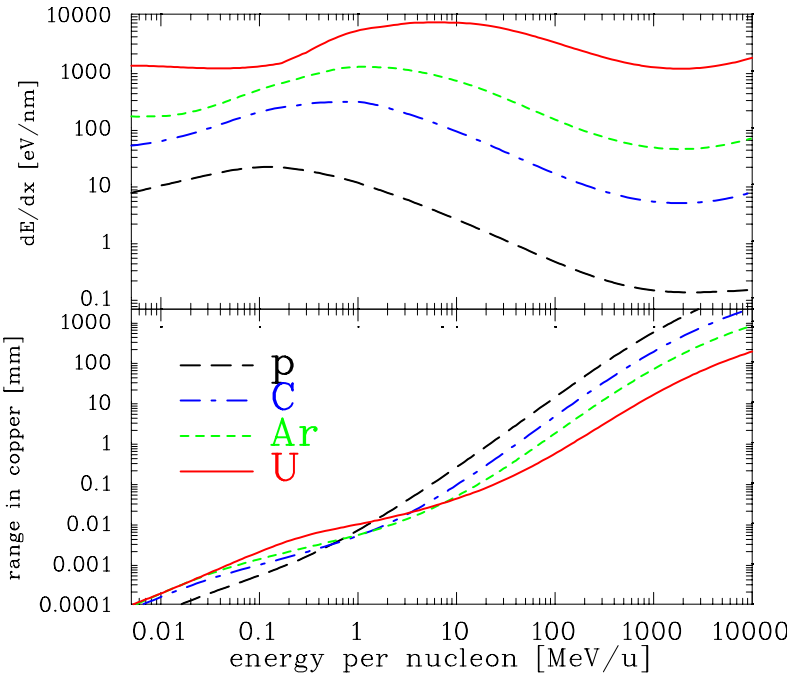

Figure 2.17: The energy loss at the surface and the range in copper as a function of the kinetic energy for several ions. The energy range is plotted from 5 keV/u to 10 GeV/u and the range from 100 nm to 1 m. The calculation of the electronic and nuclear stopping uses the semi-empirical code SRIM [14].

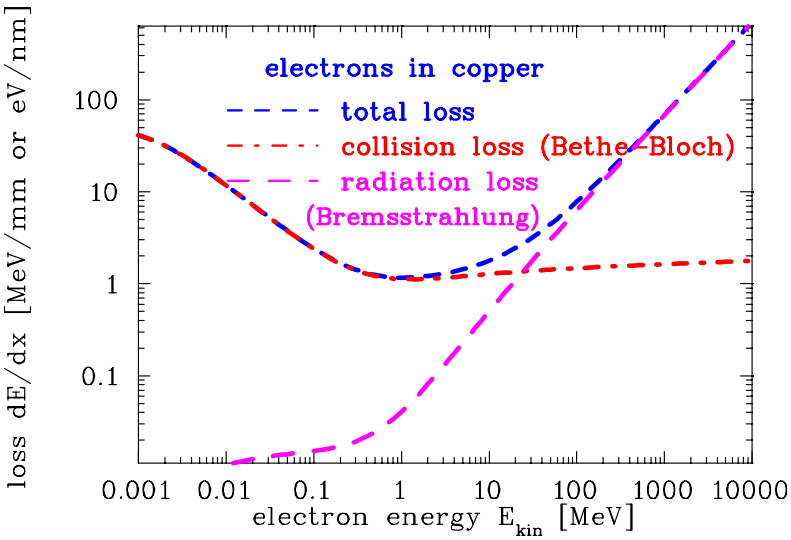

Figure 2.18: The energy loss of electrons in copper for collision loss as given by the Bethe-Bloch equation and radiation losses as dominated by the emission of Bremsstrahlungs-photons, data from [16].

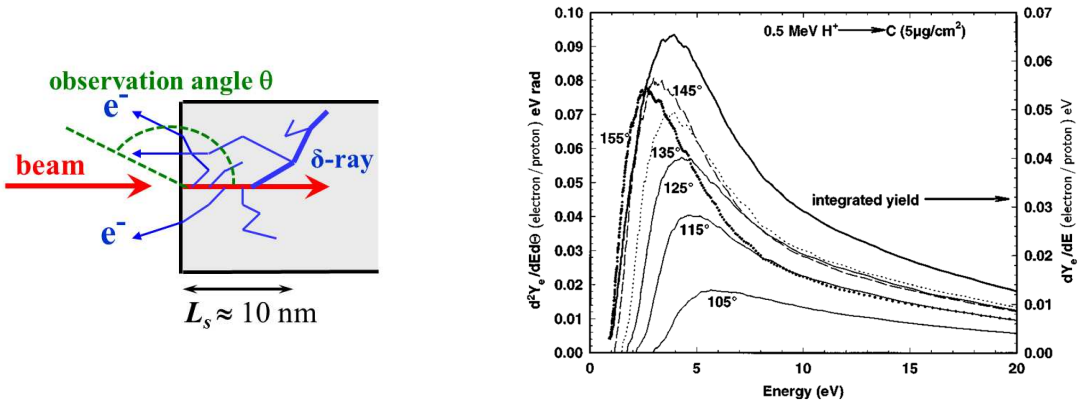

Figure 2.19: Left: Schematic drawing of the secondary electron generation from a surface by charged particle impact; L_s is the scattering length from which electrons can reach the surface. Right: A typical measurement of the electron energy spectrum for different emission angles and the total yield in the backward direction by 0.5 MeV proton impact on a carbon foil, from [18].

and has an approximately scaling for ions above $\simeq$ 10 MeV/u [10]

$$R \propto E_{kin}^{1.75} \ . \tag{2.23}$$

The results are shown in Fig. 2.17. This range should be shorter than the mechanical dimension for a practical Faraday cup design; for energies below 100 MeV/u the range is less than 1 cm. Or, in other words, cups are only useful at LINACs or cyclotrons. For higher energies, the range is too large and other techniques e.g. particle detectors as described in Chapter 2.8 are applied. In addition for particles above the nuclear Coulomb barrier nuclear reactions are possible and charged particles might leave the material resulting in a wrong reading.

2.4.2 Material interaction of electrons

The stopping of electrons in matter differs from protons and ions, see Fig. 2.18 where the sum of the two relevant processes of collisional loss $dE/dx|_{col}$ and radiation loss $dE/dx|_{rad}$ are added. The collisional loss for electrons due to electronic stopping $dE/dx|_{col}$ is also described by a modified Bethe-Bloch formula; the modification is caused by the equal mass of the projectile and the target electrons and their indistinguishably. This regime dominates for energies below below 1 MeV as corresponding to the a velocity of $\beta = v/c = 94$ % and a Lorentz-factor of $\gamma = \left(1-\beta^2\right)^{-1/2} = 2.96$. Even a small electron accelerator reaches higher final energies. For energies above a few 10 MeV, the radiation loss by Bremsstrahlung, i.e. the emission of photons by an acceleration of the electron in the vicinity of the target nucleus, dominant, see e.g. [10]. This radiation loss scales roughly linear to the electron energy and quadratically to the target charge Z_t as $dE/dx|_{rad} \propto E \cdot Z_t^2$. The trajectories of the primary electrons in the target are more curved than for ions, due to the possible high energy- and momentum transfer in a single collision, therefore electrons have much larger lateral straggling than ions. Moreover, the longitudinal straggling is more substantial than for ions resulting in a broader range distribution. Due to this extended range and the production of secondary charged particles, Faraday cups for stopping electrons are seldom used at electron accelerators, see Chapter 2.7.

2.4.3 Secondary electron generation

When a charged particle, either an ion or an electron, travels through matter, it interacts with the target electrons. In a close, primary collision the target electron can be accelerated to high energies much larger than 100 eV, sometimes these electrons are called δ-rays. The energy distribution depends on the impact parameter and the energy of the incoming particle. In a metallic solid state material the fast δ-electrons collide with the surrounding electrons; because both collision partners have equal masses the energy is transferred efficiently and more electrons are liberated, see the schematics in Fig. 2.19. This so-called thermalization of the electrons inside the conduction band is performed in a typical scattering length of some 10 nm, i.e. within the distance of some 100 lattice planes. Due to

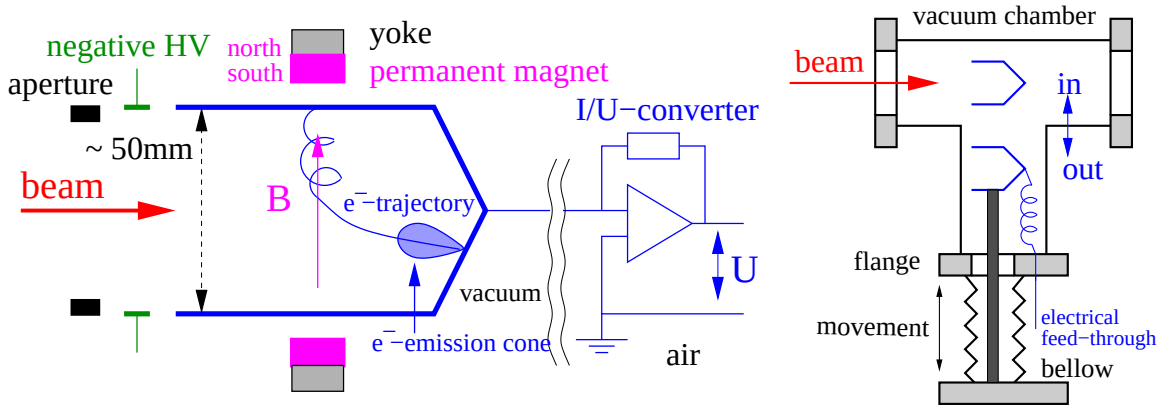

Figure 2.20: Left: Scheme of an uncooled Faraday cup with magnetic and electric secondary electron suppression. Right: Scheme for inside and outside position of destructive diagnostics devices.

this many collisions, there is only a weak correlation between the direction of the incoming particle and the scattered electrons. If these electrons reach the surface and have still an energy higher than the work-function (typically 1 to 5 eV), they have a high probability of escaping from the metal. The current of the secondary electrons is given by the so-called Sternglass formula [17]

$$I_{sec} = Y \cdot \frac{dE}{\rho dx} \cdot I_{beam} \tag{2.24}$$

with I_{beam} being the current of incoming particles and Y being the yield factor describing the amount of secondary emission per unit of energy loss $\frac{dE}{\rho dx}$ at the surface of the metal. The yield Y depends on the metal (via the work-function) and the surface quality e.g., modified by possible adsorbed gas contamination. The mean kinetic energy of the escaping secondary electrons is in the order of 10 eV and has some dependence on the emission angle; an example for the energy spectrum is shown in Fig. 2.19 and discussed in more details in [18]. To first order the angular distribution $P(\theta)$ of the electron emission can be approximated by a $P(\theta) \propto \cos\theta$ law, where θ is the angle of the trajectory with respect to the surface ($\theta = 180^o$ means backscattering).

2.5 Faraday cups for low currents

A Faraday cup is a beam stopper supposed to measure the electrical current of the beam. The basic cup design is shown in Fig. 2.20 and a photo in Fig. 2.21: An isolated metal cup is connected to a current sensitive pre-amplifier. As shown for an active beam transformer, the pre-amplifier consist of a low impedance input and a conversion to a voltage. Range switching is achieved by using different feedback resistors for the operational-amplifier. With a Faraday cup, much lower currents can be measured as compared to a transformer: A measurement of 10 pA for a dc-beam is possible with a low noise current-to-voltage amplifier and careful mechanical design; this is 5 orders of magnitude more sensitive than a dc-transformer. Low current measurement is important, e.g., for the acceleration of radioactive beams.

When an accelerated particle hits a surface, secondary electrons are liberated, see also Chapter 2.4. The flux of these electrons is proportional to $\cos\theta$, where θ is the angle of the electron trajectory with respect to the surface; their average energy is below $\simeq$ 10 eV. If these electrons leave the insulated cup, the reading of the beam current is wrong by this amount. A secondary electron suppression has to be foreseen. It can be realized by:

- Very long cups, where the length in beam direction is much greater than the diameter. The contribution of the lost electrons is low for this geometry; this solution is rarely chosen.
- Using a high voltage suppression close to the entrance of the cup. By applying a voltage well above the mean energy of the secondary electrons, they are pushed back to the cup surface, see Fig. 2.22, left. The disadvantage of this method is related to the fact that the electrical field on the beam axis is lower than on the edges; in the depicted case, the maximum potential is about

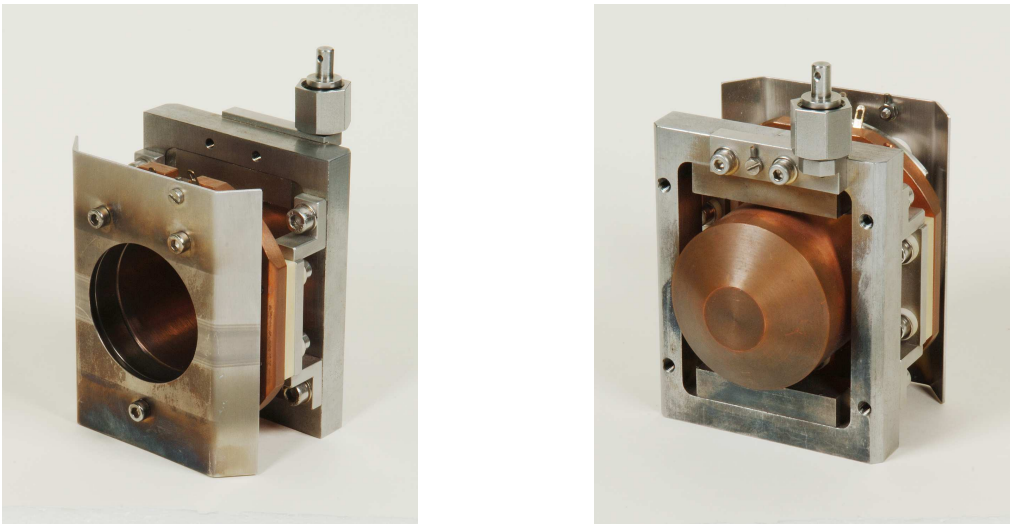

Figure 2.21: Photo of an Ø50 mm uncooled Faraday cup with magnetic and electric secondary electron suppression.

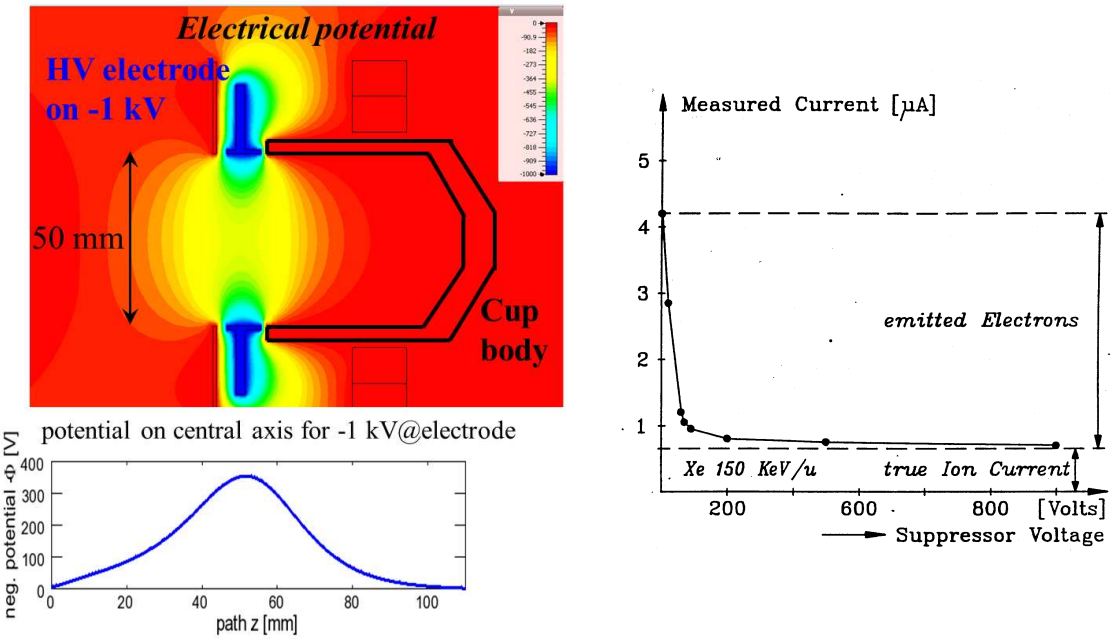

Figure 2.22: Left: The electric potential of the Faraday cup shown in Fig. 2.21 with the high voltage electrode biased by -1 kV is shown at the cylindrical symmetry plane. The beam enters from left. The negative potential along the central axis is depicted at the bottom.
Right: The effect of secondary electrons suppression inside a Faraday cup as determined by the beam current determination a function of the applied voltage.

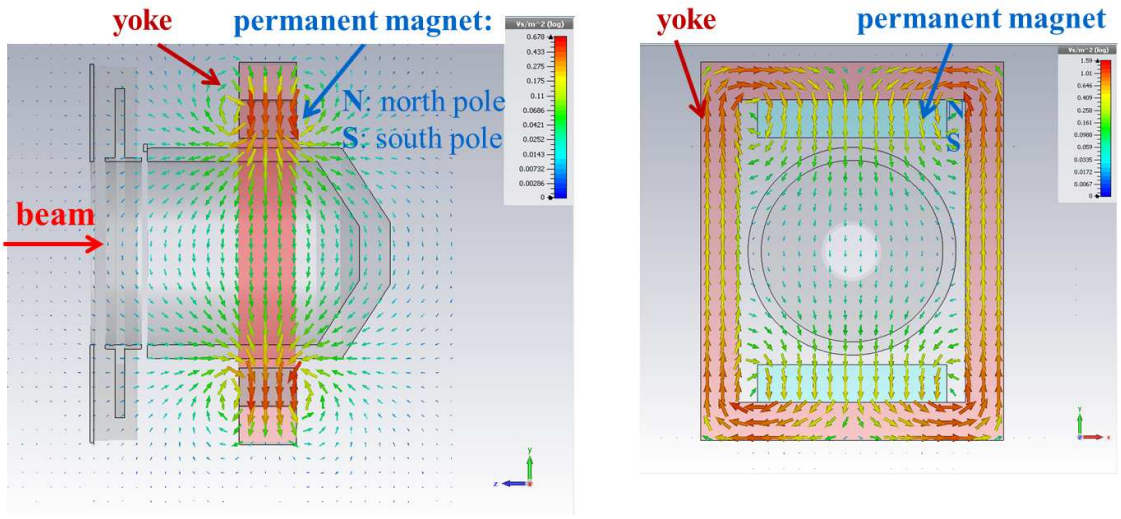

Figure 2.23: Magnetic field lines of the arrangement of Co-Sm permanent magnets within the yoke for the Faraday cup of Fig. 2.21. The homogeneous field strength is $B \sim 60$ mT.

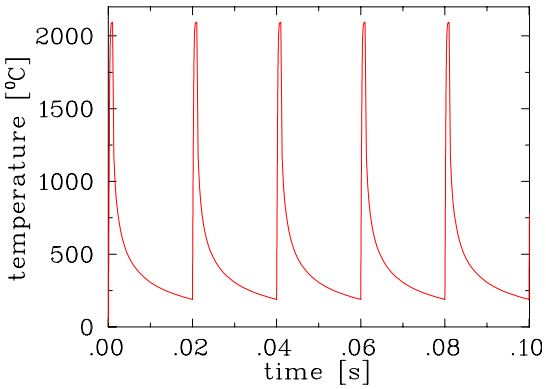

Figure 2.24: Temperature increase for a 1 μm thin tantalum foil (emissivity of $\epsilon = 0.49$) irradiated by a 10 mA Ar^{10+} beam of length 1 ms and repetition time of 20 ms with 11.4 MeV/u. The beam size is 5 mm FWHM in both directions and the absorbed power is ~ 40 kW/mm^2.

35 % of the potential applied to the electrode. The emission of the maximal energetic electrons occurred opposite to the beam direction , and the potential has to be chosen to be higher than the kinetic energy of at least 99 % of the electrons. A measurement with varying suppression voltage is shown in Fig. 2.22, right.

- By using a magnetic field created by permanent magnets. In this field B, the secondary electrons spiral around the magnetic field lines with the cyclotron radius r_c

$$r_c = \frac{\sqrt{2m_e E_{kin}}}{eB} = 3.37 \frac{\sqrt{E_{kin}[\mathrm{eV}]}}{B[\mathrm{mT}]}\ [\mathrm{mm}] \tag{2.25}$$

with m_e the electron mass, e its charge and E_{kin} the kinetic energy component perpendicular to the field lines. For $E_{kin} = 10$ V and a field of 10 mT the radius $r_c \sim 1$ mm. With permanent magnets, field lines perpendicular to the beam axis can be created relatively easily, see Fig. 2.23.

2.6 Faraday cups for high current ion beams

Faraday cups are sometimes used for higher beam currents, where measurements are also possible with ac-transformers because they are simpler to realize. In addition, cups serve as beam dumps. For

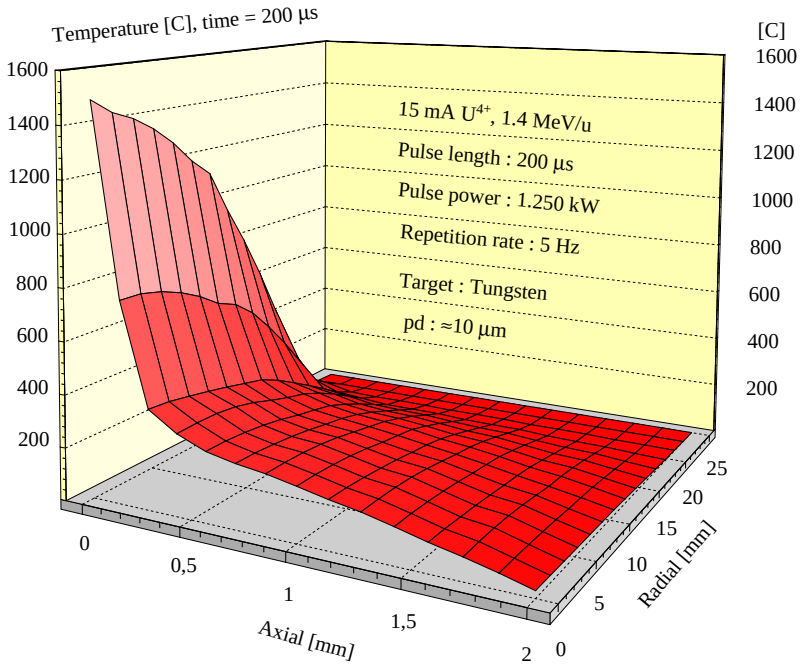

Figure 2.25: A 1.4 MeV/u U^{4+} beam of 15 mA electrical current and 0.2 ms pulse length hitting a cooled cylindrical Faraday cup. The distribution of the temperature is calculated by finite element method.

all intercepting diagnostic devices, the heating by the beam's energy loss has to be considered. An example of the temperature rise is shown in Fig. 2.24, where a pulsed beam (in this case an Ar^{10+} beam with 10 mA electrical current) of pulse length 1 ms and a repetition time of 20 ms hits an uncooled foil. The heat source is the energy loss of the particles, while the heat sink is the radiation power per area P_r as described by the Stefan-Boltzmann law

$$P_r = \epsilon \sigma T^4 \tag{2.26}$$

with T the temperature and $\sigma = 5.67 \cdot 10^{-8}$ W/m^{2}K^4 the Stefan-Boltzmann constant. ϵ is the emissivity of the material with typical values $0.1 < \epsilon < 0.9$. The radiation is a fast cooling process only for high temperatures due to the T^4 dependence. The heat conductivity is a relatively slow process compared to the heating by a short, intense beam pulse. The foil is heated close to its melting temperature during the pulse (here about 2000 ^{o}C). In the intervals between the beam pulses, it cools down to 200 ^{o}C again, and the average temperature is only $\sim 550^o$C. Nevertheless, the material has to survive the high temperature during the beam delivery. The typical beam current needed for a neutron spallation source could easily be higher. A second cooling process is related to the emission of thermal electrons from a hot metallic surface where the electrons' kinetic energy reduces the thermal energy of the solid. The basic formula for the current density of thermal electrons j_{th} is the Richardson law

$$j_{th} = A_R T^2 e^{-\Phi/k_B T} \tag{2.27}$$

where $A_R \simeq 120$ AK^{-2}cm^{-2} is the Richardson constant, k_B the Boltzmann constant and Φ the material-dependent work function, which is for typical metals 2eV $< \Phi <$ 5eV. The cooling by thermal emission contributes significantly if the surface is close to its glowing temperature. Typical cooling properties are discussed in [27].

For a quantitative analysis for a massive material the partial differential equation of heat transfer inside the material has to be calculated numerically

$$\frac{\partial T(\vec{x},t)}{\partial t} = \frac{\lambda}{\rho c} \text{div grad } T + \frac{1}{\rho c}\eta(\vec{x},t) \tag{2.28}$$

for the temperature T as a function of time t at each position $\vec{x}$ inside the material. λ is the heat conductivity, ρ the density and c the specific heat. The source term $\eta(\vec{x},t)$ is the volumetric power

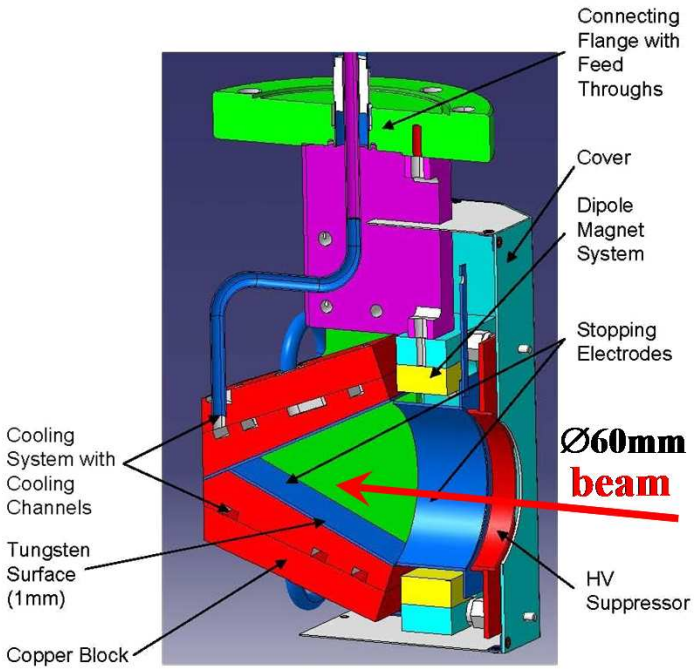

Figure 2.26: A Faraday cup and beam stopper of high intensity beams as installed at the high current LINAC at GSI. The opening of the cup is Ø 60 mm

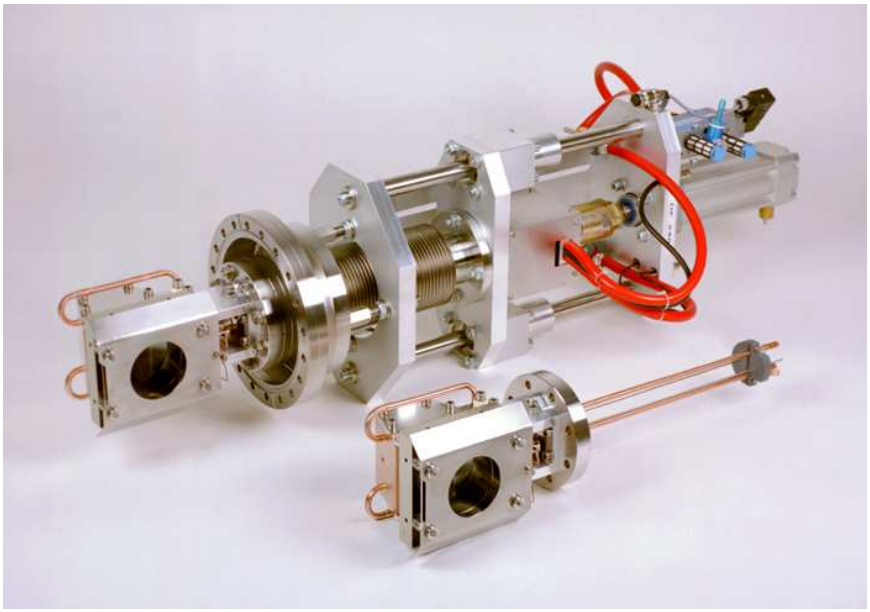

Figure 2.27: Photo of a Faraday cup and beam stopper for high intensity beams as installed at the high current LINAC at GSI. The pneumatic feed-through is mounted on a Ø 150 mm flange.

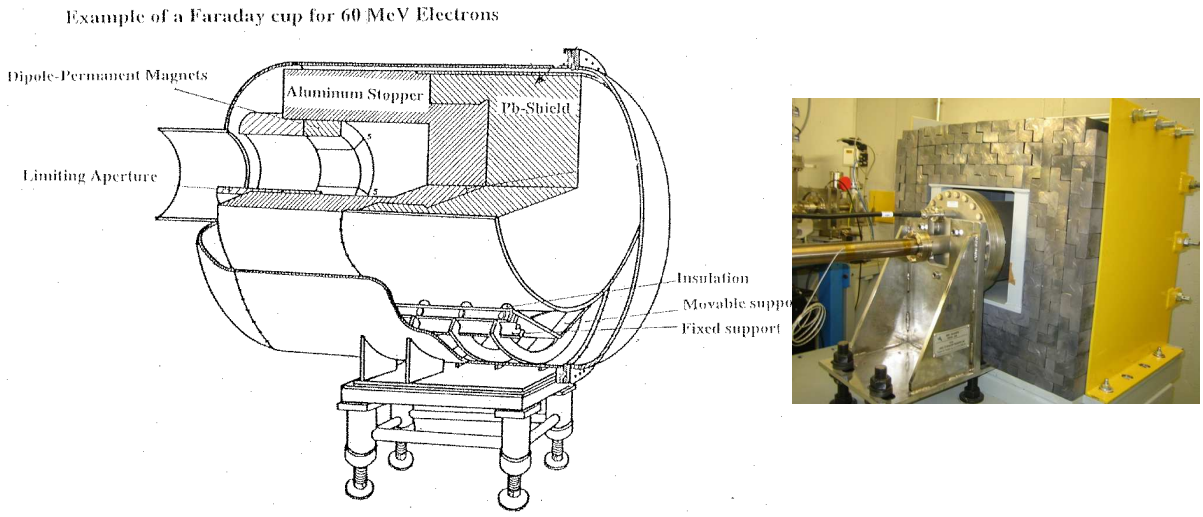

Figure 2.28: Left. A drawing of a cup used for 60 MeV electrons. Right. The installation of a Faraday cup used as a beam dump at ALBA, Barcelona.

deposition by the beam, which depends on position and time. For a more detailed discussion of an optimized material and geometric arrangement, see e.g. [19].

An example of such a calculation is given in Fig. 2.25 for a cylindrical cup for a high power Uranium ion beam at the end of the macro pulse. The value is set to the design power of the high current in the 1 MW LINAC at GSI. One solution to dissipate this large power is to increase the surface area of the irradiated material by a cone-like construction, as shown in Fig. 2.26. The ions at the GSI LINAC have ranges below 1 mm. A 1 mm thin layer of tantalum is used to stop the ions because tungsten has a high melting temperature. Underlying copper is used for its high heat conductivity. The water cooling can only dissipate the average power, and an equilibrium temperature is reached. For pulsed beams, the maximum value at the surface, or more precisely, close to the range of the particles, is much higher than the equilibrium value. This high temperature is what mainly deteriorates the device. A careful design has to be done, and the beam parameters have to be controlled to prevent the destruction of cups and beam dumps for higher power LINACs and cyclotrons.

2.7 Faraday cups for electron beams

Faraday cups for electrons have to be made larger than for ions, see Fig. 2.28. Following the discussion of the energy loss in copper for an electron in Chapter 2.4 the electrons are relatively gently stopped in the low Z material aluminum to limit the production of high energy Bremsstrahlung-photons within the Faraday cup. In addition, one has to prevent the escape of charged particles, e.g., electrons or positrons, created by the Bremstrahlungs-photons. For this reason, a Pb shield is included. Due to the long-range of the electrons in matter, the use of cups is restricted to the first few modules of an electron LINAC.

Generally, at electron accelerators Faraday cups are mainly used behind the electron gun for electrons with typically 100 keV energy. In this case, the construction is comparable to the Faraday cups used for proton beams, see Chapter 2.5. At higher energies, i.e. behind the first few LINAC-modules, the required amount of material to stop the electrons and to absorb secondary charged particles (e.g $e^+ - e^-$ pair production from the Bremsstrahlung-photons) increases significantly due to this long-range. An example of a Faraday cup used for high energies up to some GeV, including the design considerations, can be found in [20]. In most cases, Faraday cups are used as beam dumps at the end of a transport line.

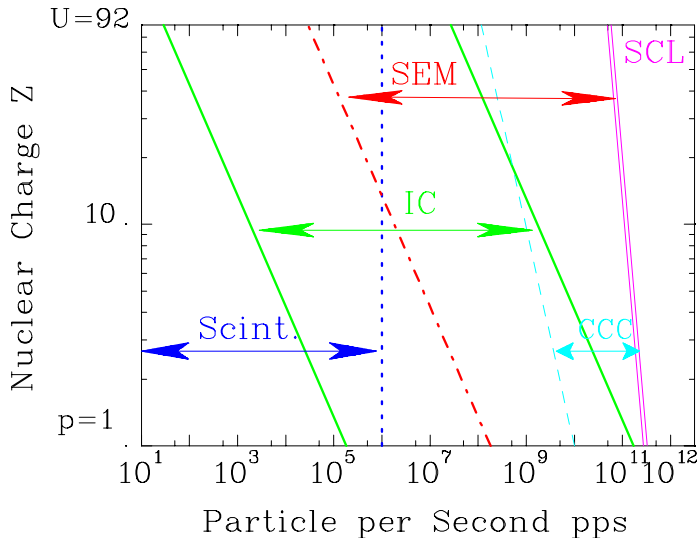

Figure 2.29: Overview of the different detector systems used for slow extraction at the GSI synchrotron. The numbers are given for the different ions with an kinetic energy of 1 GeV/u, extracted within 1 s and a spot size of 1 cm^2. With a scintillator up to 10^6 particles can be counted. The lower limit of the IC and SEM correspond to a secondary current of 1 pA, the upper threshold of the IC is 30 Gray/s. The CCC (cryogenic current comparator) measures the magnetic field. SCL means the incoherent space-charge limit of the synchrotron at injection energy.

2.8 Low current measurement used for slow extraction

Many experiments in particle, atomic or nuclear physics use protons or ions in the energy range as reached in synchrotrons, i.e., higher than some 100 MeV/u. A typical beam current during the acceleration inside the synchrotron, followed by a slow extraction recorded by a dc-transformer was shown in Fig. 2.15. Typical beam currents as slowly extracted from a synchrotron ranges from only 10^3 up to 10^{12} particles per second, which corresponds to an electrical current from 10^{-15} to 10^{-6} A. This is well below the resolution of a dc-transformer. Due to the high energy, the range of the particles is too large for the use of Faraday cups, as shown in Fig. 2.17 for Copper. In addition, a lot of secondary charged particles would be created in the cup material. The techniques of particle detectors are used instead. An overview of the typical dynamic range of detectors is presented in Fig. 2.29:

- For an ion rate below 10^6 s^{-1}, the individual particles can be counted by scintillators.
- For the medium range from about 10^4 to 10^9 s^{-1} the energy loss in gas is measured by an ionization chamber (IC).
- For the higher range from about 10^8 s^{-1} the emission of secondary electrons from a metal surface liberated by the primary ion's energy loss is determined by secondary electron monitors (SEM).

The design of such a system is described in e.g. [21, 22, 23].

2.8.1 Scintillation counter

When a charged particle penetrates a scintillating material, the electronic energy loss by the collision of the beam particles with the target electrons create atomic excitation which might decay via emission of fluorescence photons. These photons can be detected and amplified by a photo-multiplier, converted to a logical pulse by a discriminator, and finally counted by a scaler. Scintillators should have some general properties (for more details see [10, 11]):

- The light output should be linear to the energy loss.
- The fluorescence should decay as fast as possible to get a high count rate.

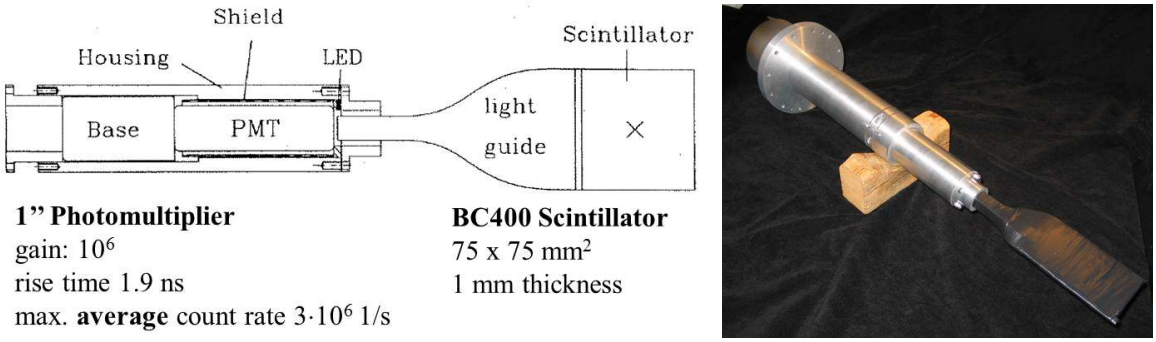

Figure 2.30: Left: The scheme of a plastic scintillation counter connected to the photo-multiplier via a plastic light guide. Right. Photo of scintillator wrapped in black tape and the base in within the metal housing.

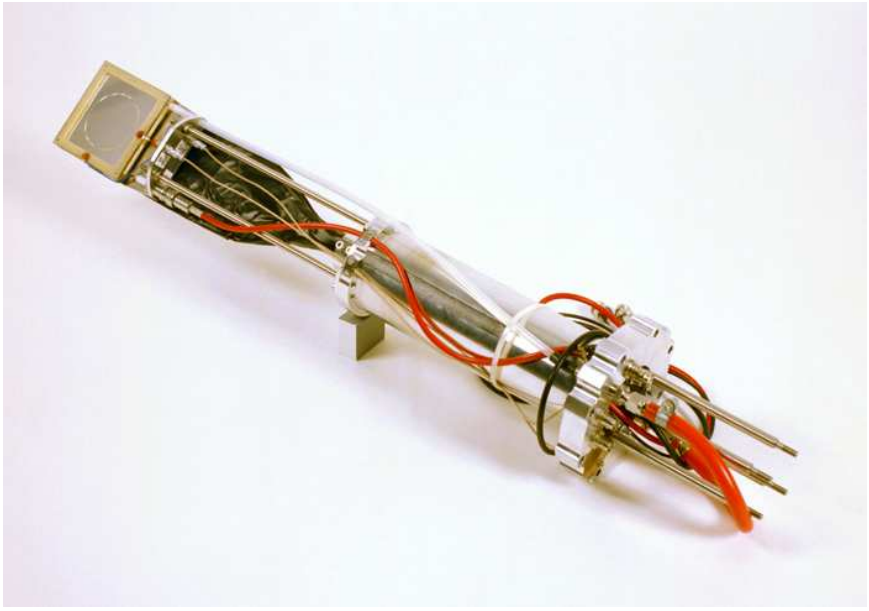

Figure 2.31: The hardware of the scintillators (wrapped in black tape) and the IC installed at GSI.

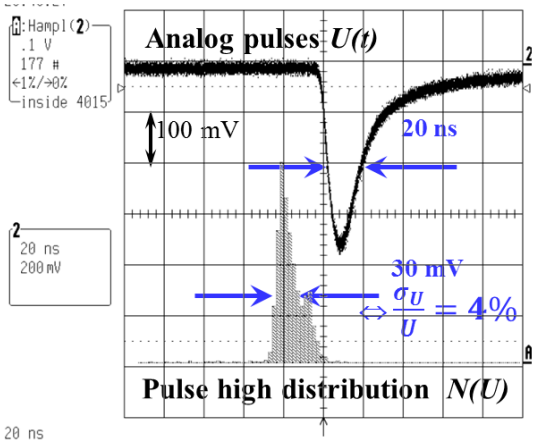

Figure 2.32: Analog pulses from a plastic scintillator recorded with a low current 300 MeV/u Kr beam; the scaling is 20 ns/div and 100 mV/div. The lower curve is the pulse-height distribution.

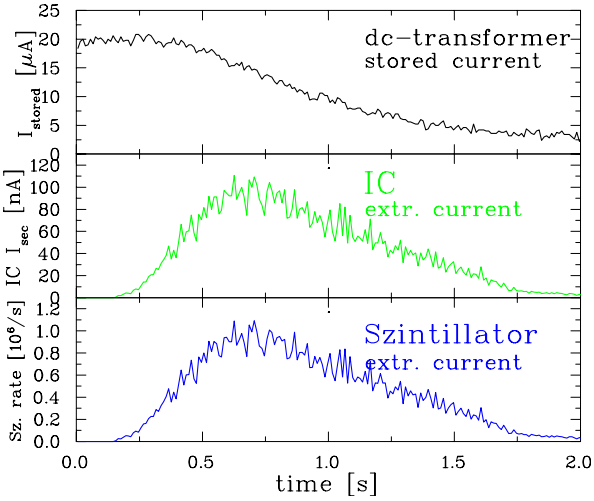

Figure 2.33: The extracted current measured by an IC (middle, given in nA for the secondary current) and a scintillator (bottom, given in particles per second) as compared to the current inside the GSI synchrotron determined by a dc-transformer (top, given in μA) for one extraction of a 250 MeV/u $^{208}Pb^{67+}$ beam with a total amount of 10^6 particles.

- The scintillator material should be transparent for the fluorescence light, and the index of refraction should be around $n = 1.5$ for the use of light guides.
- The material should be easy to form, and it should be possible to get large sizes, about a factor of two larger than the maximum beam size.
- The wavelength of the light should be within the spectral range of the photo-cathode of the photo-multiplier: 350 nm $< \lambda <$ 500 nm is preferred, i.e., near UV to green light. The photo-cathode of the photo-multiplier converts the light into electrons. These electrons are amplified by ~ 10 stages of so-called dynodes, where electro-static fields are applied to accelerate secondary electrons towards the next multiplication stage.
- The scintillator material should be radiation hard, so it will not be destroyed by the incident particles.

In most cases, plastic scintillators are used. They are cheap and easy to produce in nearly every mechanical shape. As an example, the arrangement used at GSI is shown in Fig. 2.30 and a photo together with an ionization chamber in Fig. 2.31. A large size of 75×75 mm^2 has been chosen with a thickness in beam direction of 1 mm. The plastic scintillator (in this case BC 400) has a short decay

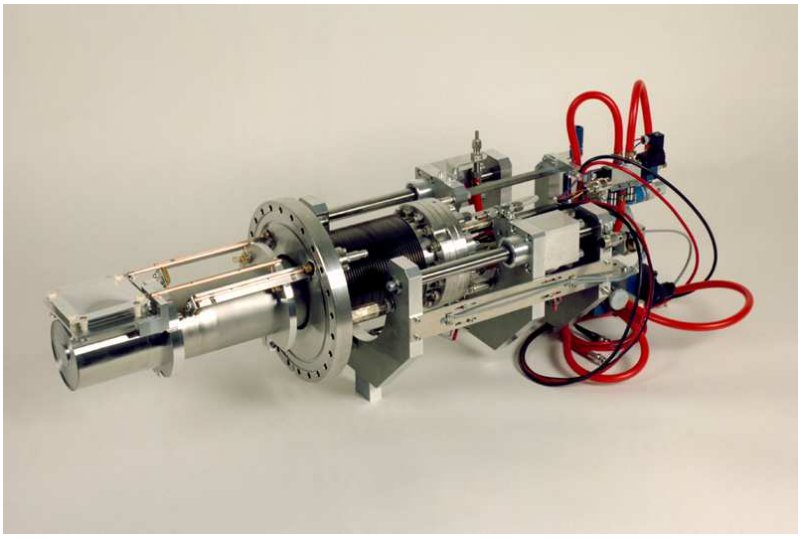

Figure 2.34: The feed-through mounted on a Ø200 mm flange containing the scintillator and IC inside the pocket at atmospheric pressure and the SEM in the vacuum.

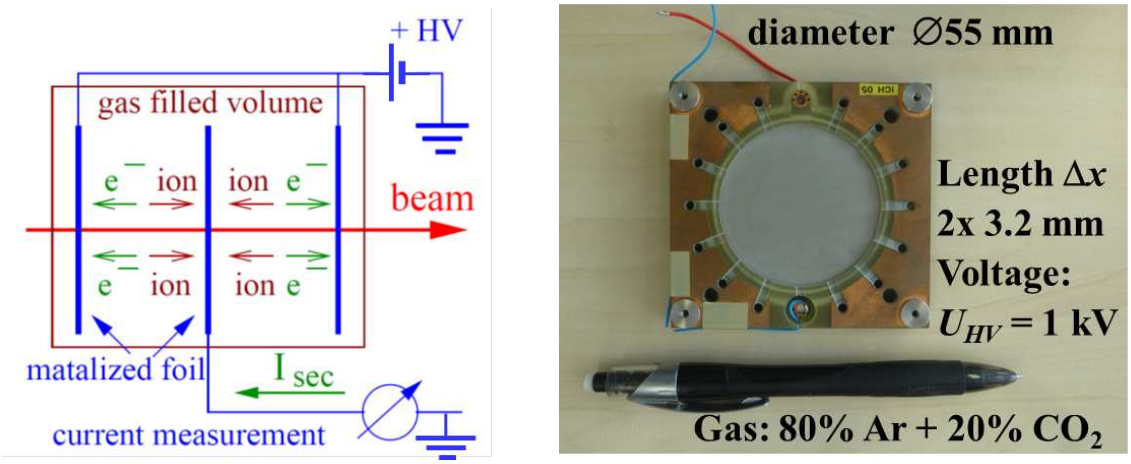

Figure 2.35: The scheme of an IC (left) and its realization with a 2 times 3.2 mm active length in beam direction (right).

time in the range of some ns, see e.g. [11]. Typical pulses are displayed in Fig. 2.32, recorded with a medium energy heavy ion beam. The energy resolution is quite good, which is important because it yields good accuracy of this absolute count rate measurement. Due to the several 100 m long cables between the detector in the beam pipe and the electronic processing, the cable dispersion broadens the peak. Before pile-ups start to play a role, count rates up to several 10^7 s^{-1} can be accepted. A typical measurement of an extracted current is shown in Fig. 2.33, where the particle rate as determined by a scintillator and an ionization chamber are compared. This is corroborated with the signal of the dc-transformer measuring the stored current in the synchrotron.

The disadvantage of the plastic scintillators is the very low radiation hardness, due to their complex organic molecular structure. Inorganic crystals have a much higher radiation hardness. In most case, Ce activated materials are used [11, 24]. However, these inorganic single crystal scintillators are challenging to produce in larger sizes.

2.8.2 Ionization chamber

For the medium particle range, the current is determined by the energy loss of charged particles in a gas inside an **I**onization **C**hamber **IC**. A general description of ICs can be found in [11, 25]. Due to the

Table 2.4: Specifications of the IC at GSI

Parameter	Value
Active surface	Ø55 mm
Active length	2 × 3.2 mm
Electrode material	plastic network
Coating	100 μg/cm^2 silver
Gas (flowing)	80 % Ar + 20 %CO_2
Pressure	1 bar
Voltage	500 ... 2000 V

Table 2.5: Ionization potential and W-values od some gases.

Gas	H_2	He	N_2	O_2	Ar	CH_4	CO_2
Ionization potential [eV]	15.6	24.5	15.5	12.5	15.7	14.5	13.7
W-value [eV]	36.4	42.7	36.4	32.2	26.3	29.1	33.0

large statistics, the average energy for the production of an electron-ion pair is a well-known number, the so-called W-value are given in Table 2.5. The arrangement of an IC is displayed in Fig. 2.35 and a photo in Fig. 2.31. For this realization, the beam passes a 6.4 mm thick active gas volume and creates electron-ion pairs. In most cases, pure Ar is used, sometimes also mixed with about 10% of molecular gases, like CH_4 or CO_2. Metalized plastic foils or networks confine the active gas volume. These metalized electrodes are biased with about 1 kV to separate the charges. The middle electrode measures the amount of secondary charge with a sensitive current amplifier. A secondary current down to the pA region can be measured precisely, see e.g. [26]. The IC, filled with gas at atmospheric pressure, is separated from the vacuum by a metallic foil of typically 100 μm thickness. The foil thickness must be low to prevent significant energy loss in this foil. The specification of the IC at GSI is given in Table 2.4.

With the help of the W-values and the calculated energy loss dE/dx within an active length of Δx, the number of primary ions I_{beam} is determined from the secondary current I_{sec}

$$I_{sec} = \frac{1}{W} \cdot \frac{dE}{dx} \Delta x \cdot I_{beam} \quad . \tag{2.29}$$

The precision of such a measurement depends mainly on the accuracy of the energy loss calculation. For energies above 1 GeV/u the value of dE/dx is only weakly dependent on the energy E, see Fig. 2.17. When the energies of the beam particles are below this, calibrations have to be done to reach an accuracy in the range of 1 %. The IC can be calibrated with respect to a scintillator, where an absolute measurement is performed, like shown in Fig. 2.33. From the number of counted particles and the secondary current of the IC, a calibration factor can be determined. The result for different ions and energies as performed at GSI [23] is summarized in Fig. 2.36. Due to the different ions, three orders of magnitude are covered, from 10^{-16} C/ion up to 10^{-13} C/ion. The linearity is excellent.

The lower limit of an IC is given by the minimum measurable secondary current, which is about 1 pA. Taking this current, the line in Fig. 2.29 is determined. The upper limit is based on the recombination of the electrons with the ions from the gas, as in the case of Ar working gas, the reaction $Ar^+ + e^- \rightarrow Ar$ which is a sink for the generated charges. This is demonstrated in Fig. 2.37: We first discuss the characteristic line of the IC with a moderate primary current: The proportional region is reached after applying a moderate voltage of 500 V, corresponding to 1 kV/cm. The output is then independent of the voltage (or the applied electric field). There is no gas amplification, which starts only above $\sim$ 10 kV/cm. The characteristic line is determined by comparison to the SEM (see below) to get the efficiency. For a higher primary current, the plateau is not reached anymore. A higher voltage cannot be applied without the risk of sparks. This decrease concerning efficiency is due to the recombination of the liberated electrons with the positive gas ions, like $Ar^+ + e^- \rightarrow Ar$. The drift time of the ions toward the electrodes depends on the applied electric field, while the drift time for the electrons is nearly constant for the given parameters [11]. The collision frequency of electrons

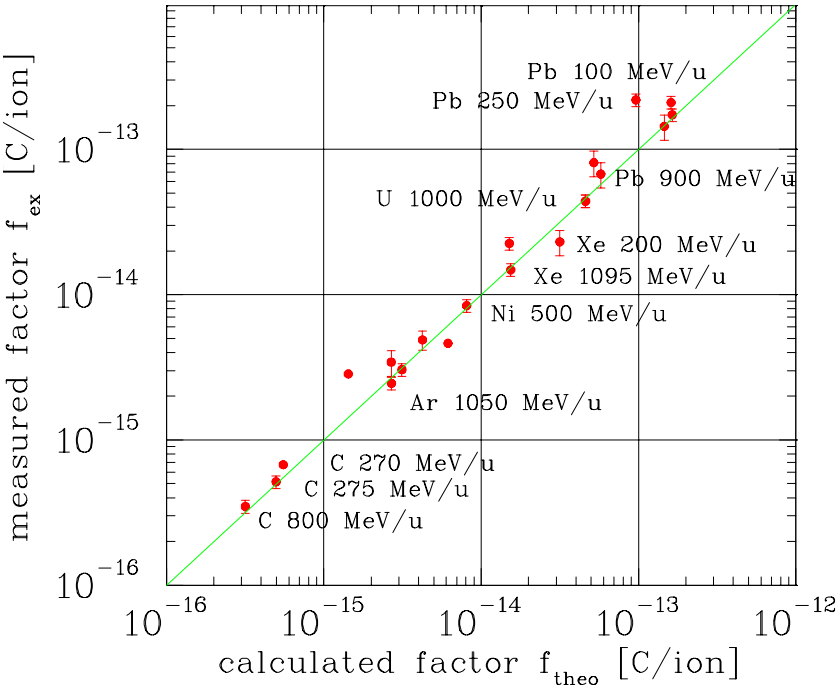

Figure 2.36: The measured calibration factor of an IC and calculated value using energy loss for various slowly extracted ion from the GSI synchrotron [23].

and ions is proportional to their concentration n_e and n_i. The recombination rate is

$$\frac{dn_e}{dt} = \frac{dn_i}{dt} = \alpha \cdot n_e n_i \propto I_{beam}^2 \tag{2.30}$$

with α the rate coefficient. The loss rate is therefore proportional to the square of the primary beam current. Typical values are summarized in Table 2.6. One can conclude that the secondary current for the used IC should be below ~ 1 μA for typical parameters, corresponding to a dose rate of about 30 Gray/s [22]. To get the value of the primary beam current the conversion from the energy loss as given in Eq. 2.29 have to be used.

Table 2.6: Properties of the IC close to the saturation point, see text.

	Ions	Electrons
drift velocity w^{drift}	0.1 mm/μs	20 mm/μs
drift time t^{drift}	50 μs	0.1 μs
saturation density n^{sat}	$2 \cdot 10^9$ 1/cm^3	$4 \cdot 10^6$ 1/cm^3
secondary current I_{IC}	1 μA	
dose rate D_{IC}	30 Gy/s	
aver. rate coefficient α	10^{-9} cm^3/s	

To get a sizeable upper threshold, the use of gases with high electron affinity, like O_2 and H_2O, has to be avoided [11]. The electron affinity describes the probability of an electron capture like $O_2 + e^- \rightarrow O_2^-$. The presence of negative ions enhances the recombination with positive ions, like $O_2^- + O^+ \rightarrow O_3$, resulting in a smaller amount of measured secondary charge. In particular, an IC should not contain any air.

2.8.3 Secondary electron monitor

To cover the high current range from e.g., slow extraction from a synchrotron, the emission of secondary electrons from a metallic surface can be used. Such a setup is shown in Fig. 2.38, where three 100 μm thick Al-foils are visible, installed on the vacuum side of the feed-through. The outer two foils are

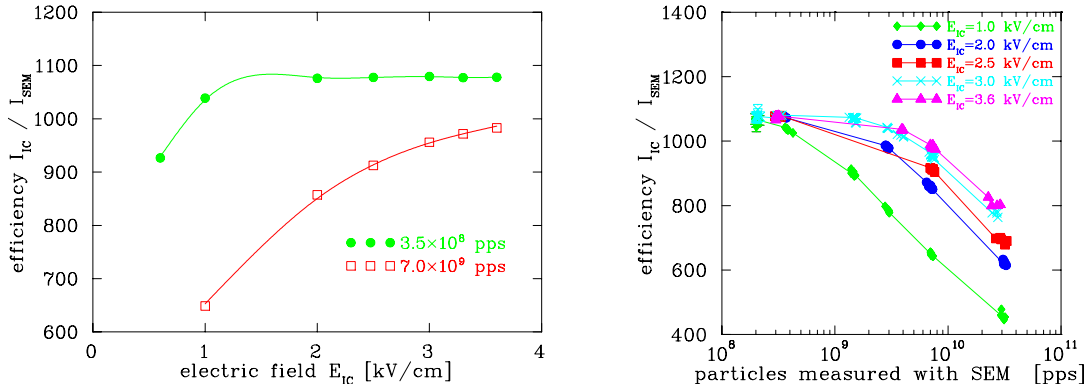

Figure 2.37: Left: The characteristic line for the IC as determined of the 300 MeV/u Ne^{10+} beam. The efficiency, as measured by the ratio of the secondary current of the IC and the SEM as a function of the applied electric field [22]. For a low primary current a plateau is reached, while for a high current the recombination leads to a decrease of the secondary charges. Right: Comparable data shown as a function of transmitted ions per second for different applied electric field.

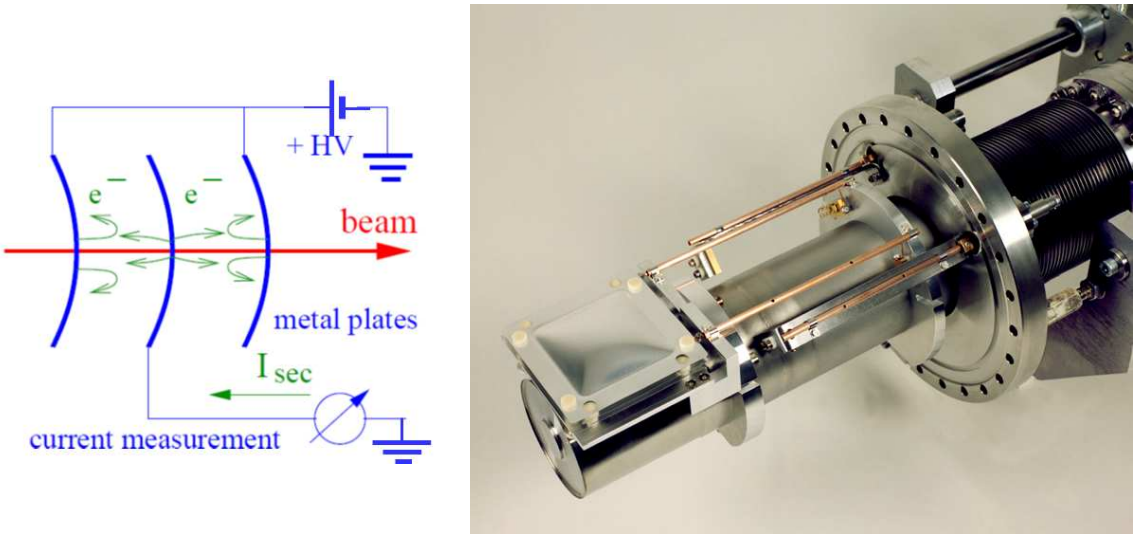

Figure 2.38: Left: Scheme of a SEM made of three metal foils. Right: Photo of the SEM part made of 3 Al foils with a thickness of 100 μm of the feed-through used for slow extraction at GSI.

biased by typically +100 V to sweep out the free electrons. The middle foil is connected to a sensitive current amplifier. The secondary emission current depends on the energy loss at the surface $\frac{dE}{\rho dx}$ and is given by the Sternglass formula [17]

$$I_{sec} = Y \cdot \frac{dE}{\rho dx} \cdot I_{beam} \tag{2.31}$$

with Y being the yield factor describing the amount of secondary emission per unit of energy loss at the surface of the Al foil. A calibration has to be done experimentally to determine the value of Y, yielding a precision of 5 %, see Fig. 2.39. The accuracy is lower than for an IC, because the actual value of the yield is determined by the surface structure of the material, which might vary, depending on the production and cleaning method. Eq. 2.31 reflects the fact that only electrons are knocked out which are excited to the conducting band close to the surface of roughly $\simeq$ 10 nm, see Chapter 2.4 for the discussion of secondary electron emission. The physics of the secondary electron emission is also used for profile measurements, see Chapter 3.2.

The material Al is often used due to its well suited mechanical properties. In particular, it is stiff enough to prevent micro-phonic pick-up by external vibrations caused, e.g., by turbo vacuum pumps. But the emission yield Y might change with irradiation. This is caused by modifications of the surface, which changes the work-function and, therefore, the average yield Y. Measurements have shown a

Table 2.7: Specification of the SEM at GSI.

Parameter	Value
Material	pure Al (≃99.5%)
Thickness	100 μm
Number of electrodes	3
Active surface	80 × 80 mm^2
Distance between electrode	5 mm
Voltage	100 V

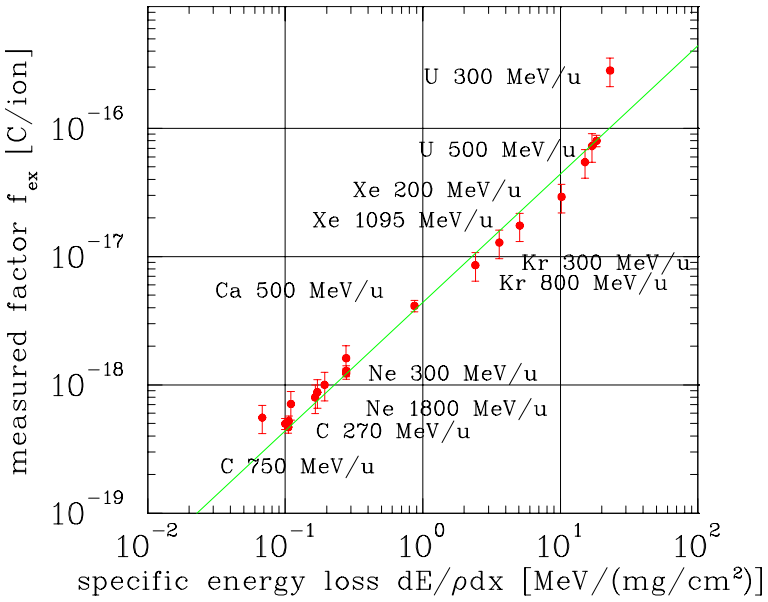

Figure 2.39: The measured calibration factor of a SEM and calculated value using energy loss and a fitted value of $Y = 27.4\ e^-/(\mathrm{MeV/mg/cm^2})$ for various slowly extracted ion from the GSI synchrotron [23].

significant degradation by a factor of two after 10^{18} proton/cm^2 with 450 GeV proton at CERN SPS [28]. Here Ti-foils have a much lower sensitivity to radiation. Radiation hardness is essential, because these devices are often used in front of the target as a permanent current monitor.

A completely different approach for low current measurement in the nA region is related to the determination of the magnetic field. Instead of the transformer principle, the field is measured by a SQUID (super-conducting quantum interference device); we refer to [29] for details.

Chapter 3

Measurement of beam profile

The beam profile can be influenced by quadrupole magnets installed in all accelerating structures and in transfer lines. A measurement is important to control the beam width, as well as the transverse matching between different parts of an accelerating facility. The large number of bending, focusing, and correction magnets demand the need for many profile measurement stations. Depending on the beam particles, current, and energy, a large variety of devices exists. We can only briefly discuss the most popular ones. The beam spot can be directly observed by intercepting it with scintillator screens and viewing the emitted fluorescence with a CCD camera. Secondary electron emission grids SEM-grid are widely used as an electronic alternative to achieve a large dynamic range; a grid of wires with typically 1 mm spacing is inserted. Instead of a fixed grid, one single wire can be scanned through the beam to get high spatial resolution; this is called Wire Scanner. A third approach is a so-called ionization profile monitor IPM or residual gas monitor RGM, where the ionization products of the interaction of the beam with the residual gas atoms or molecules inside the (non-perfect) vacuum of the tube are detected. In these devices, the resulting electrons or ions are accelerated by an external electrical field to a detector having a spatial resolution. A profile can also be obtained by the observation of the light emitted by the residual gas molecules excited by the beam interaction called sometimes beam induced fluorescence BIF monitor. The Ionization profile monitors and beam induced fluorescence monitors are well suited as non-destructive methods for a synchrotron. When charged particles with relativistic velocities pass a metallic foil, radiation is emitted as described by classical electrodynamics; the process is called optical transition radiation OTR. This light is recorded by a camera to receive the beam profile. High energetic electrons emit synchrotron radiation if the trajectory is curved. Monitoring this light by synchrotron radiation monitors SRM yields direct information about the beam spot.

Normally the size of an electron beam is less than 1 mm, while proton or heavy ion beams have large diameters, up to some cm. In particular, in a synchrotron with multi-turn injection, several cm can be reached.

The beam width is mainly given by the settings of the focusing magnets and the beam emittance ϵ. Knowing the lattice, i.e., the β-function $\beta(s)$ and the dispersion $D(s)$ at the monitor location s, the measured beam width $\sigma(s)$ is given by

$$\sigma_x^2(s) = \epsilon_x \beta_x(s) + \left(D(s) \frac{\Delta p}{p} \right)^2 \qquad \text{and} \qquad \sigma_y^2(s) = \epsilon_y \beta_y(s). \tag{3.1}$$

In a synchrotron the lattice functions are well known, or can be measured separately. If also the momentum spread $\Delta p/p$ is known, the emittance can be calculated. (In the vertical direction the dispersion is zero in most cases, because only horizontal bending magnets are used.) Nevertheless, the contribution due to the dispersion has to be taken into account for the interpretation of the beam width. In a LINAC, the lattice functions are not so precisely fixed due to the variable input emittance orientation, leading to a less stringent relation between profile width and emittance.

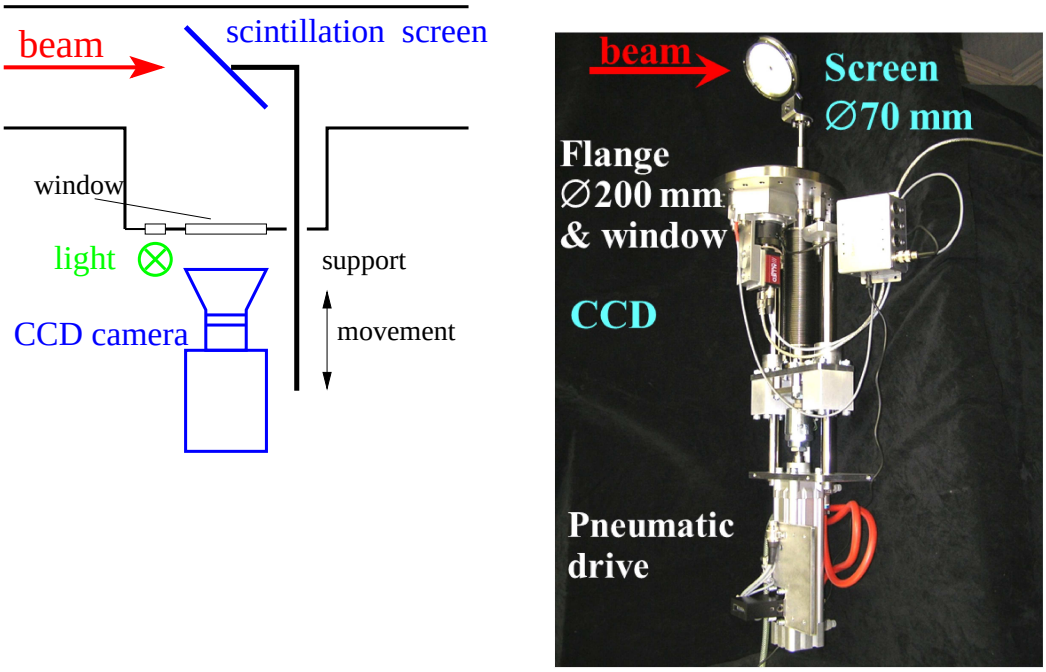

Figure 3.1: Left: The scheme of a intercepting scintillation screen is shown. Right: A photo from a P43 phosphor scintillation screen of Ø70 mm and the CCD camera are mounted on a Ø200 mm flange with pneumatic drive is depicted.

3.1 Scintillation screen

The most direct way of beam observation is recording the light emitted from a scintillation screen intersecting the beam, monitored by a commercial video, CMOS or CCD camera, see e.g. [30, 31] for an overview. These devices are installed in nearly all accelerators from the source up to the target and is schematically shown in Fig. 3.1 together with a realization where the pneumatic drive mounted on a Ø200 mm flange.

When a charged particle penetrates a material, the energy loss can be transformed to fluorescence light, as discussed in the previous Chapter 2.8.1. The important properties of such a scintillator are:

- High light output matched to the optical system of the camera in the optical wavelength range of 400 nm $< \lambda <$ 700 nm.
- High dynamic range, i.e., a good linearity between the incident particle flux and the light output. In particular, a possible saturation of the light gives rise to a deformation of the recorded profile.
- No absorption of the emitted light to prevent artificial broadening by the stray light inside the material.
- Fast decay time, to enable the observation of possible variations of the beam size.
- Good mechanical properties for producing up to Ø100 mm large screens.
- Radiation hardness to prevent permanent damage.

As stated, plastic scintillators have only low radiation hardness, and various kinds of inorganic material are used instead. In Table 3.1 some properties are given [30]; for more details see [11, 24].

The material Chromox is a ceramic, which can be fabricated like pure Al_2O_3, used widely as an insulating material. The scintillation is due to the Cr activators; chemically it is comparable to ruby. The disadvantages are its long decay time of ∼10 ms and the large absorption inside the material. Nevertheless, due to its robustness, it is quite often used. The well-known Ce activated crystal materials like YAG ($Y_3Al_5O_{12}$) have better optical properties and are widely used for particle counting applications [11]. But it is difficult to produce crystalline disks of about 10 cm diameter out of this material. Instead of the expensive single crystal disk, one can use small grains of $\sim$ 10 μm

Table 3.1: Chemical composition and some basic optical properties of inorganic scintillation screens. The matrix Al_2O_3 is used in from of a ceramic, the last four materials are so called phosphor screens, where powder is deposited on glass or metal plates.

Abbreviation	Type	Material	Activator	max. emission	decay time
Quartz	glass	SiO_2	non	470 nm	< 10 ns
Alumina	ceramics	Al_2O_3	non	380 nm	~ 10 ns
Chromox	ceramics	Al_2O_3	Cr	700 nm	~ 10 ms
YAG	crystal	$Y_3Al_5O_{12}$	Ce	550 nm	200 ns
LuAG	crystal	$Lu_3Al_5O_{12}$	Ce	535 nm	70 ns
Cesium-Iodide	crystal	CsI	Tl	550 nm	1 μs
P11	powder	ZnS	Ag	450 nm	3 ms
P43	powder	Gd_2O_2S	Tb	545 nm	1 ms
P46	powder	$Y_3Al_5O_{12}$	Ce	530 nm	300 ns
P47	powder	$Y_2Si_5O_5$	Ce & Tb	400 nm	100 ns

size, deposited on several mm thick glass or metal disks. These phosphor screens are also used very frequently in analog oscilloscopes, electron microscopes and image intensifiers. P46 is an example of a phosphor screen powder offering a much lower production cost compared to the chemically equivalent single-crystal YAG:Ce. The properties of doped materials are strongly dependent on the activator concentration, therefore Table 3.1 gives only approximated values. The sensitivities of the different materials span several orders of magnitude and depend on the particle species as well, see e.g. [31, 32]. Scintillation screens are used in all types of accelerators [31], some examples of investigations are discussed for electron beam [33, 34, 35] and proton or ion accelerator [32, 36, 37] with quite different applications.

The beam image from a YAG:Ce screen is shown in Fig. 3.2 for a low current beam of only $\sim 10^6$ ions at 4 MeV/u, proving the high sensitivity of that material.

For high intensity beams, one has to ensure that the material is not destroyed by the absorbed beam power. In particular, for slow heavy ions with a range comparable to the screen thickness, this restricts the use, see also the discussion in Chapter 2.4. A disadvantage of the screen is related to the interception. The used material is so thick (several mm) that it causes a significant energy loss, so it cannot be used for the diagnostics of a circulating beam inside a synchrotron.

The screen is observed with a CCD or CMOS camera. A modern approach uses a digital link, with a digital data transfer of the camera pixel values enabling fast data rates for long cable length without signal degeneration, see e.g. [38]. A problem is the radiation sensitivity of the CCD sensor and digital equipment. At high levels of radiation, the old fashioned analog VIDICON cameras are used, the analog video output is for this case digitized by a frame grabber.

3.2 Secondary electron emission grid SEM-grid

When particles hit a surface, secondary electrons are knocked-out form the surface, as described in Chapter 2.8.3. For the profile determination, individual wires or ribbons interact with the beam; this is called a **S**econdary **E**lectron E**M**ission grid or a harp as reviewed in [39]. Each of the wires has an individual current-to-voltage amplifier. This is an electronic alternative to a scintillation screen with a much higher dynamic range, i.e., the ratio of minimal to maximal detectable current is orders of magnitude larger. For the metallic wires or flat ribbons, W-Re alloys are often used for their excellent refractory properties. In particular, at low energy LINACs, this is important because no cooling can be applied due to the geometry. A photo of such a device is shown in Fig. 3.3, and the specifications are given in Table 3.2.

For low energies at proton or heavy ion LINACs, the particles are stopped in the material or undergo a significant energy loss. The ratio diameter-to-spacing of the wires determines the attenuation of the beam current (and of cause also the signal strength on the individual wires). Typically only 10 % of the beam area is covered by the wires, in this sense the profile measurement is nearly non-destructive. For energies above 1 GeV/u, the relative energy loss is negligible, and large size ribbons are used. A typical example of the SEM-grid measurement used for beam optimization is shown in

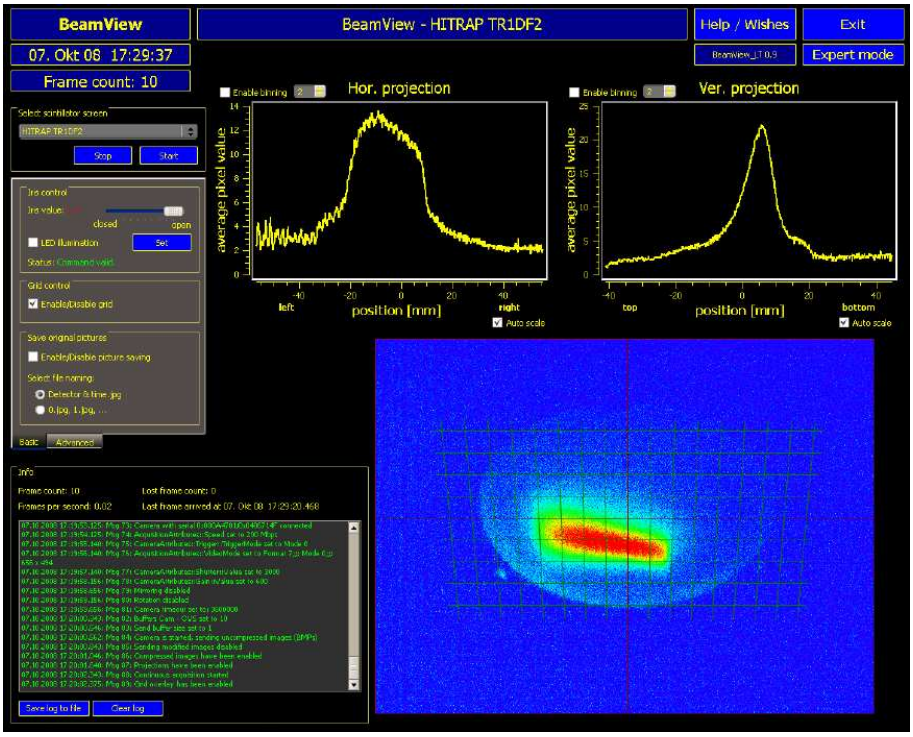

Figure 3.2: Beam spot of a low current 4 MeV/u beam at GSI on a YAG:Ce screen recorded with a digital CCD camera. The original black-white image is converted to false-color for better visibility. The projection on the horizontal and vertical axes are shown in the upper part, from [38].

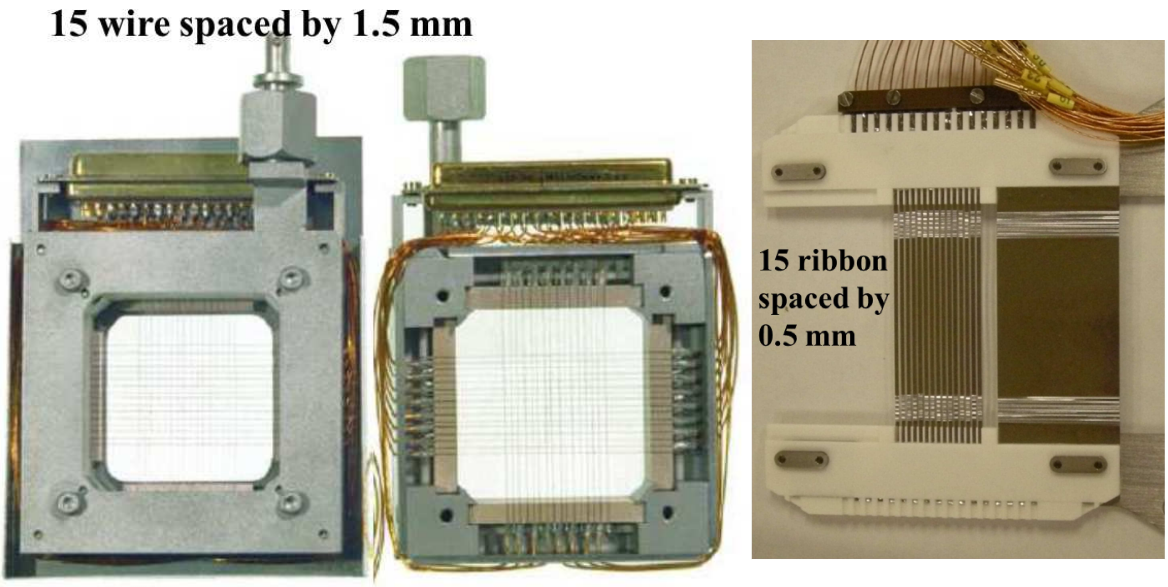

Figure 3.3: Left: SEM-grid for both planes with 15 tungsten wires spaced by 1.5 mm as typically used at a proton LINAC. The individual wires are insulated with glass-ceramics.Middle: The same SEM-grid with removed tin cover. Right: SEM-grid based on ribbon made from 25 μm thick aluminum foil by laser cutting; the spacing is 0.5 mm. This type is used for high energetic protons above typically 1 GeV. The devices are mounted on a pneumatic drive to move it in and out of the beam (not shown).

Table 3.2: Typical specification for an SEM-grid used at proton and heavy ion LINACs.

Parameter	Value
Diameter of the wires	0.05 to 0.5 mm
Spacing	0.5 to 2 mm
Length	50 to 100 mm
Material	W or W-Re alloy
Insulation of the frame	glass or Al_2O_3
number of wires	10 to 100
Max. power rating in vacuum	1 W/mm
Min. sensitivity of I/U-conv.	1 nA/V
Dynamic range of electronics	$1{:}10^6$
Integration time	1 μs to 1 s

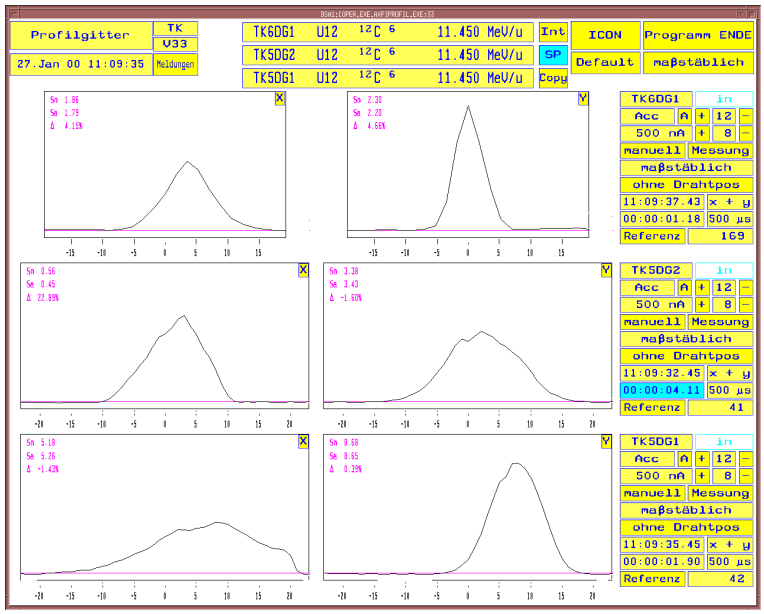

Figure 3.4: The measured profiles of SEM-grids in one transfer line at the GSI heavy ion LINAC, displaying the horizontal profile left and the vertical right in mm.

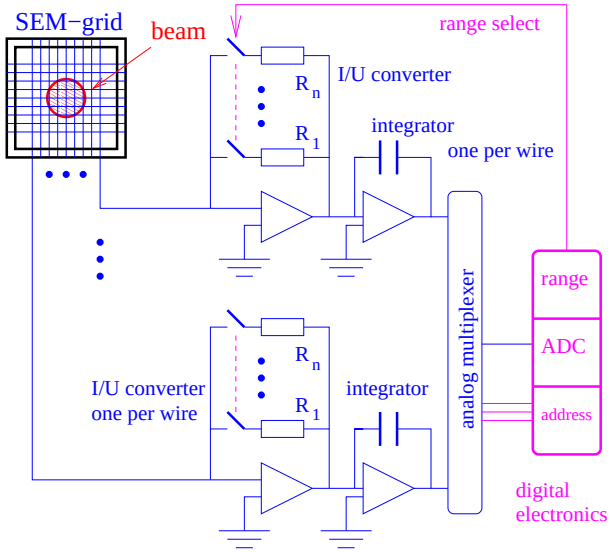

Figure 3.5: Typical analog signal processing for a SEM-grid.

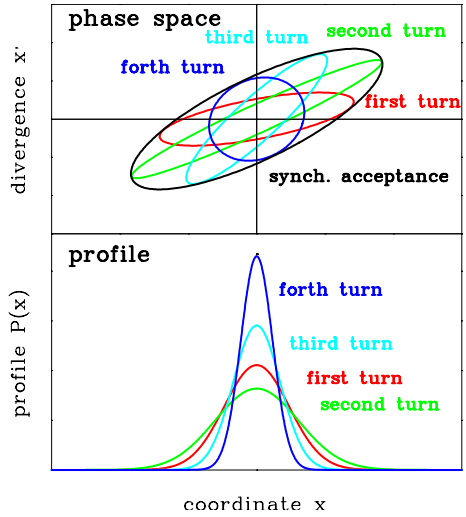

Figure 3.6: Schematics for the betatron mismatched injection into a synchrotron. If the orientation of the injected beam emittance does not fit the acceptance, variations of the beam profile occur.

Fig. 3.4 for a transfer line.

Each wire has an individual pre-amplifier, in most cases an I/U converter, followed by a sample-and-hold circuit, see Fig. 3.5. These electronics have to be installed close to the accelerator hardware. With a multiplexer, the analog values are transported to an ADC located outside of the accelerator tunnel. Readout of a full SEM-grid in less than an ms is typical for the use of pulsed or dc beams.

Application: Betatron mismatch for synchrotron injection

An interesting application for a profile measurement is the control of the injection into a synchrotron. If the orientation of the injected beam emittance is wrong due to a misaligned focusing, beam storage is still possible. But then the emittance ellipse starts to rotate with an angle per revolution as given by the fractional part q of the tune Q of the synchrotron as shown in Fig. 3.6. A rotating ellipse is equivalent to a variation in the beam profile from turn to turn. After several hundred turns, the full synchrotron acceptance is filled due to the de-coherence of the single particle phases, leading to a larger circulating beam and an emittance blow-up. The mismatch can be determined by recording the profile width on a turn-by-turn basis. An example is shown in Fig. 3.7 for a proton injection into the CERN PS synchrotron with 1.4 GeV energy and a bunch length of 80 ns [46, 47]. The revolution period is 2.2 μs. Thin SEM grids are used, and the data are digitized each revolution of the short bunch. The energy loss of the protons in the wires is too low to influence this measurement during only a few turns. The oscillation of the profile width is seen, and the fitted Gaussian width is plotted as a function of the turn number. It results in a blow-up of the stored emittance by ~ 10 %. A better injection is created by changing the setting of the quadrupole magnets in the transfer line.

3.3 Wire scanner

Instead of using several wires with individual, expensive electronics, a single wire can be swept through the beam [39]. The advantage is that the wire spacing does not limit the resolution, and therefore this technique is often used at electron accelerators with beam sizes in the sub-mm range. It can also be applied in proton synchrotrons due to the small amount of intercepting matter.

An arrangement with a straight wire on a fast pendulum mechanics is shown in Fig. 3.8, from [40, 41]. Scanning velocities up to 10 m/s can be achieved with a dedicated pneumatic mechanism. Sometimes this setup is also called flying wire. As the wire material, carbon or SiC is used due to its low weight and low nuclear charge Z, resulting in a low energy deposition in the wire (Bethe-Bloch Eq. 2.21 gives $dE/dx \propto \rho \cdot Z/A$). Besides, these materials can withstand high temperatures without melting. The thickness can be down to 10 μm. However, due to the single scanned wire, the profile is not taken at a single instant, even with high scanning velocity. Therefore only the steady-state distribution can be probed.

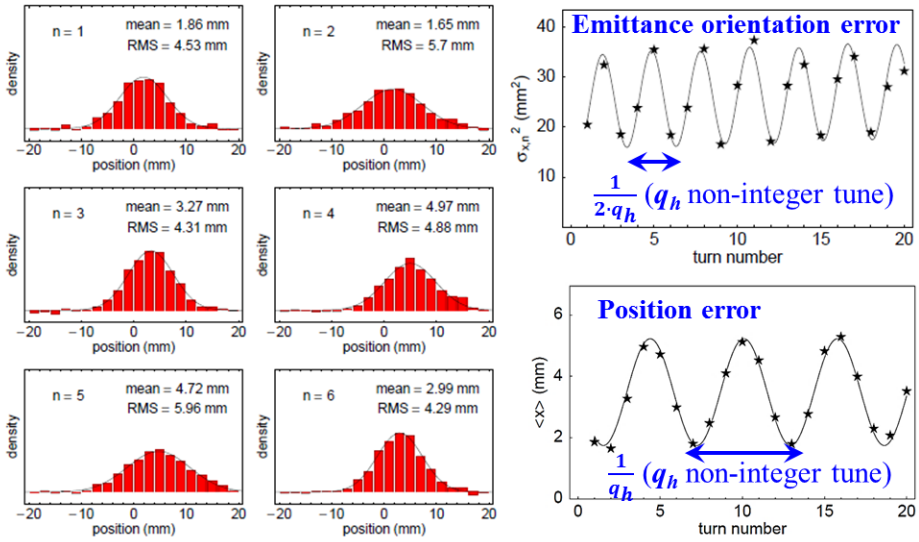

Figure 3.7: Left: Profile measurement for a mismatched injection into the CERN PS synchrotron for the first $n = 1...6$ turns Right: Fitted square of the beam width and center as a function of time, from [46].

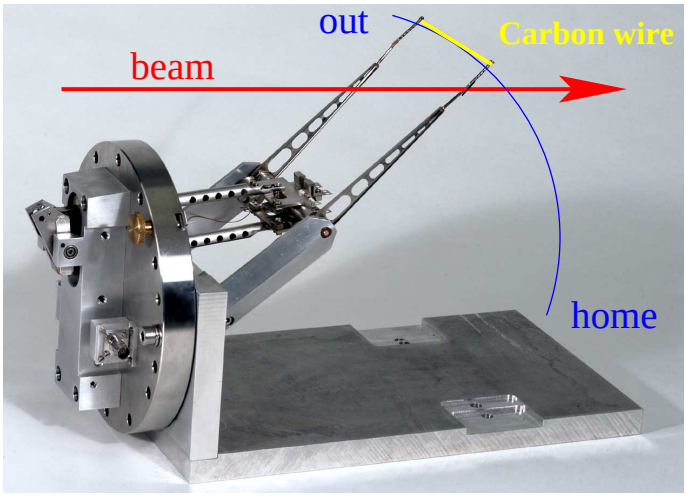

Figure 3.8: Pendulum scanner or 'flying wire' used at CERN synchrotron [40].

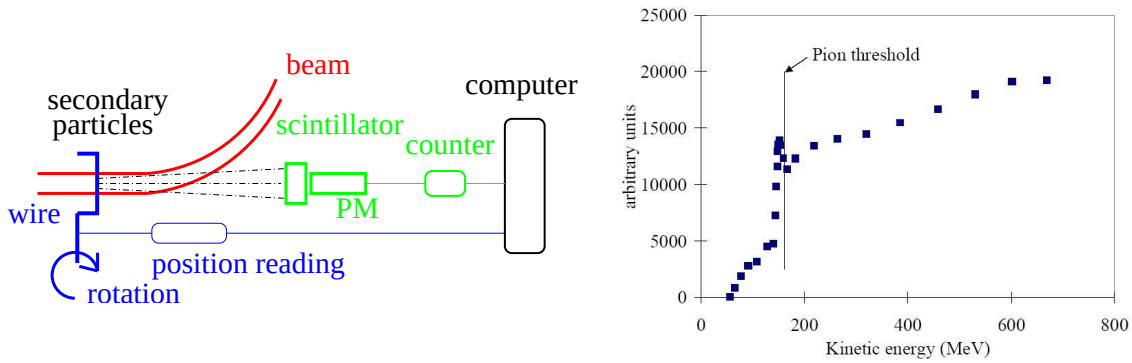

Figure 3.9: Left: Scheme of a wire scanner using the production of secondary particles as the signal source. Right: The total rate from a wire scanner under proton impact at CERN PS-Booster, showing the rate increase above the π-threshold at $\sim$ 150 MeV, from [42].

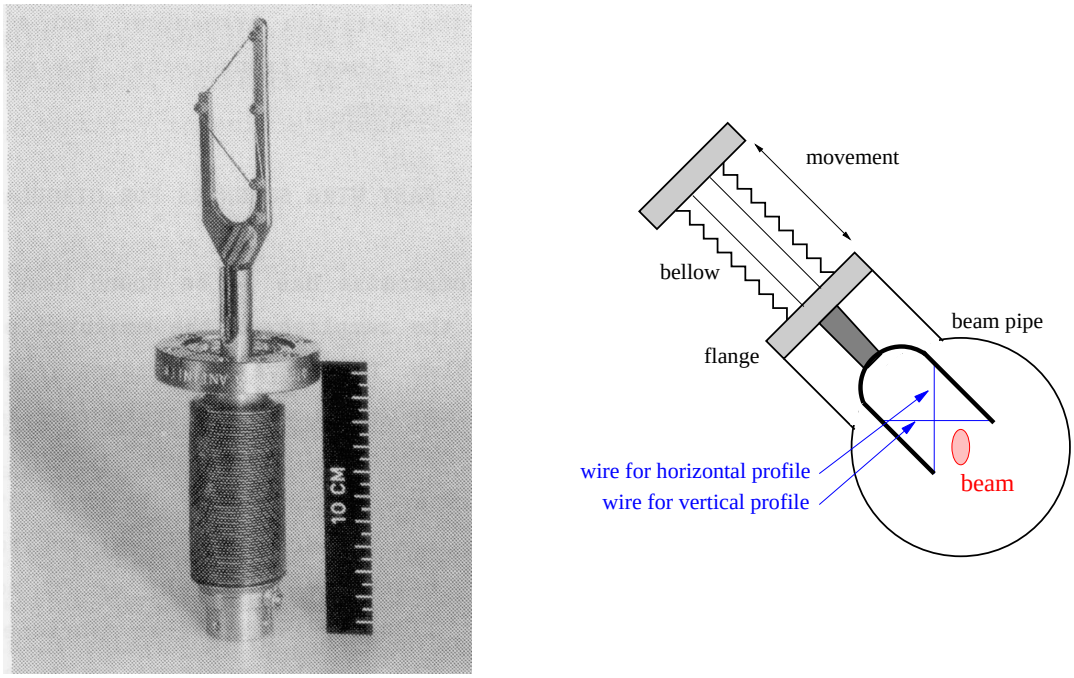

Figure 3.10: Linear scanner used at CERN [43].

For the display of the profile, the position of the wire, determined by the position encoder, is plotted on the horizontal axis. The beam signal for the vertical axis can be deduced from the current given by the emitted secondary electrons, like for an SEM-grid. This is done in particular for low energy protons and heavy ions. In most cases for beam energies larger than 150 MeV/u for ions (the threshold for π-meson production) or 10 MeV for electrons, the signal is deduced by monitoring the secondary particles outside of the beam pipe, see Fig. 3.9. These secondaries might be hadrons created by the nuclear interaction of the proton or ion projectiles and the wire, having enough kinetic energy to leave the vacuum chamber. For the case of electron accelerators, the secondaries are mainly Bremsstrahlung-photons. The detector is just a type of well-suited beam loss monitor, e.g. a scintillator installed several meters away (see also Chapter 8). The count-rate is plotted as a function of the wire position as a precise representation of the beam profile.

For the fast movement, the vibration of the wire restricts the spatial resolution. Much higher precision can be achieved with a much slower movement of, for example, only 0.1 m/s with a linear drive as shown in Fig. 3.10 [43]. With these types, a resolution of 1 μm is reached in electron accelerators [44]. To get this low beam width σ_{beam} assuming a Gaussian beam, a deconvolution of the contribution of the wire (4μm thick carbon wire in this case) from the measured width σ_{meas} has

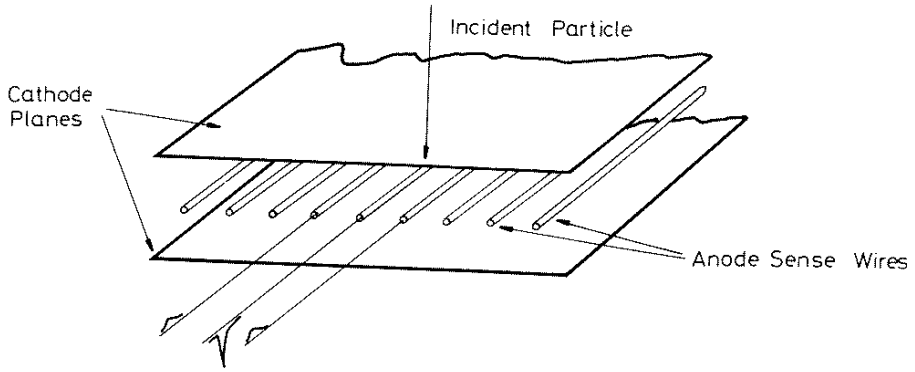

Figure 3.11: The scheme of a MWPC for one plane showing the type of signal generating by a particle interaction.

to be done according to

$$\sigma^2_{beam} = \sigma^2_{meas} - 4 \cdot r^2_{wire} \quad . \tag{3.2}$$

In most cases, the wire is mounted on a fork, which is inserted into the beam pass by a drive mounted on 45^o. Then only one drive is sufficient for measuring both transverse planes by mounting the wires in a crossed orientation, as shown in Fig. 3.10. If the signal generation is performed by reading the secondary emission current then two isolated wires can be mounted compactly. If the signal is generated by beam loss monitors outside the beam pipe, the two wires are separated (as shown in the Fig. 3.10 left), so the wires cross the beam one after the other.

A comparison of the wire scanner and the SEM-grid shows the advantages and disadvantages of both types [39]:

- With an SEM-grid the beam intensity is sampled concurrently, whereas a moving wire samples the parts of the profile at different locations at different times. Therefore variations of the beam intensity in time will be mixed with transverse intensity variations using a scanning device.
- In case of pulsed beams, a synchronization between the readout of the electronics and the beam pulse is required as well as a movement within the beam pause. The synchronization between readout and beam pulse is more easy to achieve for an SEM-grid.
- The resolution of an SEM-grid is fixed by the wire spacing (typically 1 mm), while a wire scanner can have much higher resolution, down to 10 μm, due to its constant movement. (For high resolution mechanical vibration has to be avoided.)
- The electronics for data acquisition is cheaper for a scanning system. An SEM-grid requires one channel per wire.
- For the cost of the mechanics, it is vice versa: The precise vacuum actuator for the scanner is more expensive than the pneumatic drive needed for a SEM-grid.

3.4 Multi-wire proportional chamber MWPC

For slowly extracted beams from a synchrotron, the current is much too low to be measured by an SEM-grid. One can use the amplification of electrons in a gas as done in a **M**ulti-**W**ire **P**roportional **C**hamber **MWPC**; for the principle of operation, see e.g. [11]. As discussed for the ionization chamber for current measurements in Chapter 2.8.2, the primary particles traverse a gas (like 90 % Ar mixed with 10 % CH_4 or CO_2), creating secondary electrons. A MWPC consists of a grid held at a high voltage, typically several kV, and a grounded grid, which is read by a charge-sensitive pre-amplifier, like for SEM-grids. The distance between the anode and the cathode plane is typically 1 cm and the spacing of the wires about 1 mm. The principle is shown in Fig. 3.11. Close to the anode wires, having typically 25 μm diameter, the electrical field increases with $\propto 1/r$, see Fig. 3.12. After

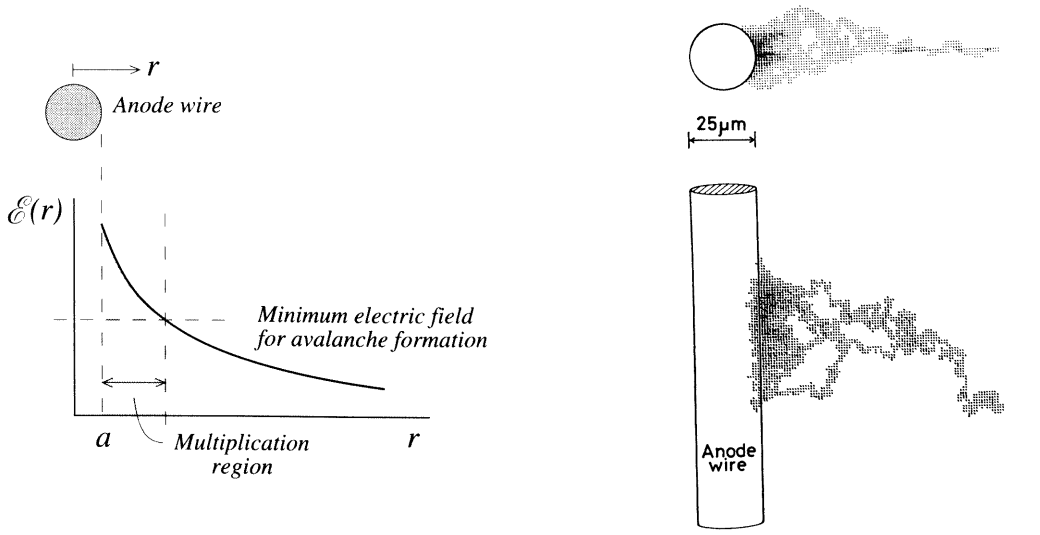

Figure 3.12: Left: The electric field close to the anode wires with the region of amplification indicated. Right: A Monte-Carlo simulation shows the concentration of the electron avalanche by the gray shading, from [45].

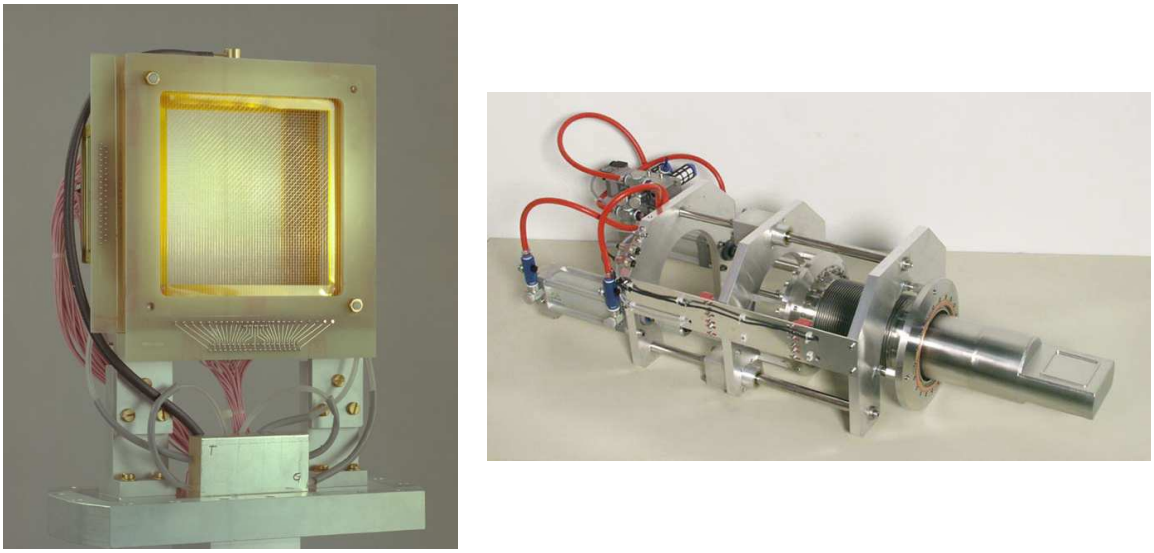

Figure 3.13: Left: The MWPC used for profile measurement of slowly extracted ion beams at the GSI. Right: The pneumatic drive with the MWPC mounted inside the pocket having normal pressure and is separated from the vacuum by a 100 μm thick foil.

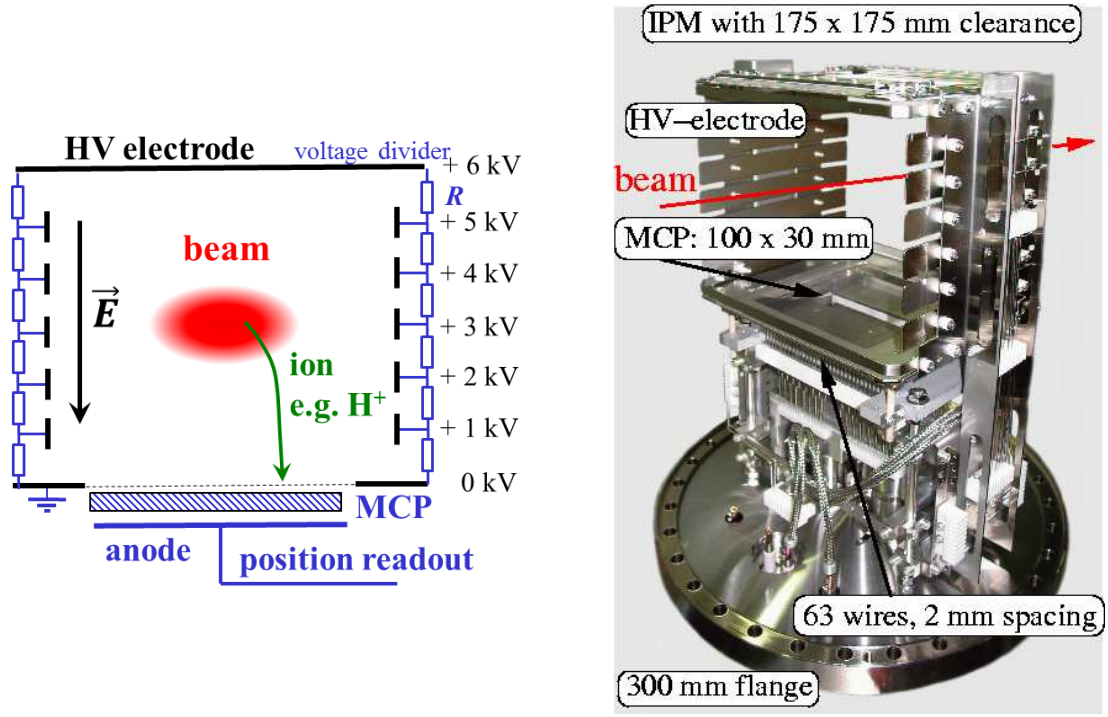

Figure 3.14: Left: Scheme of a ionization profile monitor for the horizontal profile determination. Right: The large aperture ionization profile monitor installed at the GSI synchrotron for the horizontal direction, the clearance is 175×175 mm^2. The monitor is mounted on a Ø 300 mm flange. The read-out behind the MCP (bottom) is done with an array of 63 wires with 2 mm spacing.

reaching a threshold, the energy of the electrons accelerated toward the wires is high enough to knock-out additional electrons from the gas atoms or molecules. This gives rise to an avalanche, which results in a $\sim 10^4$ amplification of the number of electrons. This amplification inside the detector volume is nearly noise-free due to the electrically spoken high source impedance of the free charge carriers. The resulting low noise could not be achieved by an electric amplifier due to its thermal noise. The following electronics (further amplifier and ADC) as well as the display of the profile measurement is comparable to the procedure for SEM-grids.

3.5 Ionization profile monitor IPM

A frequently used non-destructive method for the profile determination is the **I**onization **P**rofile **M**onitor **IPM** sometimes also called **R**esidual **G**as **M**onitor **RGM**. These monitors are installed in nearly every proton/heavy ion synchrotron for the detection of beam sizes between some mm and several cm; a review is given in [48]. For electron synchrotrons, they are seldom used, due to the smaller electron beam dimensions. The principle is based on the detection of the ionized products from a collision of the beam particles with the residual gas atoms or molecules present in the vacuum pipe. A scheme for such a monitor is shown in Fig. 3.14. Typical pressures for LINACs and transfer lines are in the range $10^{-8} - 10^{-6}$ mbar containing mainly N_2 and O_2 as well as for synchrotrons $10^{-11} - 10^{-9}$ mbar containing mainly H_2; the different compositions are due to the different vacuum pumps used. Due to the electronic stopping process, electrons are liberated, and electron-ion pairs are generated. An estimation of the signal strength can be obtained by Bethe-Bloch formula. However, due to the single collision behavior, W-values (see Chapter 2.8.2) are only a first order approximation for the conversion of the energy loss to the numbers of secondaries; the process is better approximated by considering some 100 eV for the creation of one electron-ion pair. To separate the electron-ion pairs, an external electric field is applied in the order of 1 kV/cm by metallic plates installed in the vacuum pipe, but outside the beam path. To get an electric field of higher homogeneity, guiding strips are installed at the side to get a smooth transition from the HV side to the ground plane. For most applications, the residual gas ions are detected in this setup. A realization from the GSI synchrotron

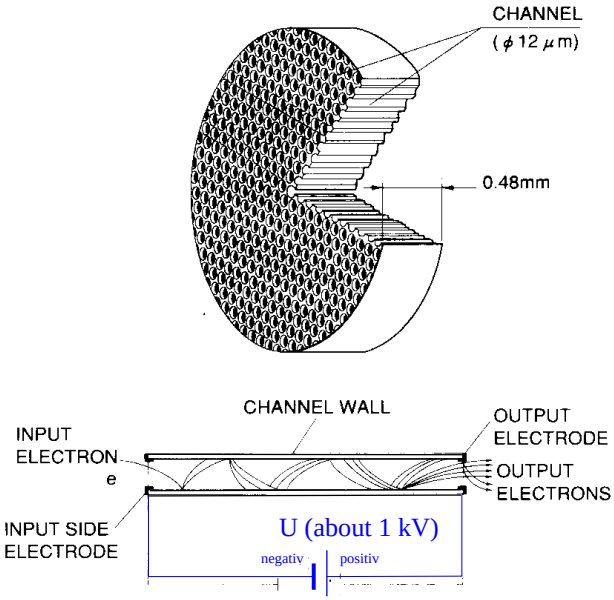

Figure 3.15: Scheme of a single MCP made of a glass plate with small channels, where the amplification of the secondary electrons takes place.

is shown in Fig. 3.14, providing a large opening of 17 cm [49].

For the LINAC case, the vacuum pressure is high, and the energy loss is larger due to the lower beam energy. Enough electron-ion pairs are generated to give a measurable current (down to 0.1 nA per strip) of secondary ions for direct detection by a sensitive SEM-grid like wire array [50]. In a synchrotron, the pressure and the stopping power is lower. A multi-channel plate (MCP) particle detector is used as a 'pre-amp'. A MCP is made of a 1 mm thick glass plate with round channels of ~ 10 μm, see Fig. 3.15. These channels are coated with high resistivity materials, and a voltage of ~ 1 kV is applied across them. When a residual gas ion (or electron) hits the surface, secondary electrons are liberated, i.e., the ions are converted to electrons. These electrons are multiplied like in a photo-multiplier by a factor of typically 10^3 per MCP. Due to the diameter of the channels, the spatial resolution of a single step MCP is in the order of 0.03 mm. For higher amplification, a two-step device (s.c. Chevron geometry) with a gain of $\sim 10^6$ is used, resulting in a resolution of about 0.1 mm.

For the detection of the secondary electrons at the MCP output, three types of anodes can be used:

- An SEM-grid made of wires with ~ 0.5 mm diameter and 1 mm spacing. The advantage is the fast readout is possible by using appropriate electronics [51]. The disadvantage is the limited spatial resolution.

- An anode type using a particle detection schemes, like wedge and strip anodes or resistive anodes, see e.g. [52]. It is based on the detection of single particles, leading to the advantage that the resolution can be improved by collecting data with high statistics up to the spatial resolution limit of the MCP.

- A phosphor screen installed close to the MCP backside. The secondary electrons create a light pulse, which is imaged by a CCD camera. The advantage is the high resolution due to several hundreds of pixels for one plane and the cheap and direct data acquisition system supplied by the commercial CCD camera. However, with this technique, the time resolution and the image repetition rate is limited by the CCD camera frame-rate of about 100 frames per second. For faster readout, the CCD is replaced by a photomultiplier or avalanche diode, e.g. [53].

During the acceleration of a beam inside a synchrotron, the beam width should shrink. This is related to the fact that the emittance is defined in the lab-frame by the angle between the transverse-

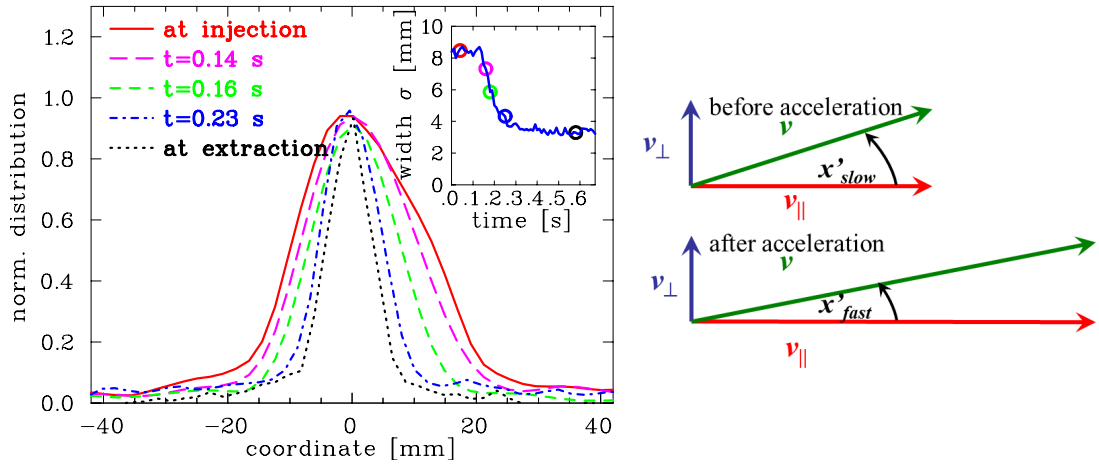

Figure 3.16: Left: The evolution of the horizontal beam profile is shown during the acceleration of C^{6+} from 6.7 MeV/u to 600 MeV/u within 0.4 s at the GSI synchrotron. The insert depicts the evolution of the beam width of one standard deviation during the acceleration started at 0.15 s; the depicted colored circles indicate beam profiles. Right: Schematic visualization of the transverse $v_\perp$ and longitudinal $v_\parallel$ velocity evolution during acceleration leading to a decrease of the angle x'.

and longitudinal velocities. During acceleration, the longitudinal velocity increases (for the non-relativistic case), while the transverse component remains, leading to a decrease of the angle between both vectors as schematically shown in Fig. 3.16. This is called transverse adiabatic damping by the conservation of the normalized emittance, see also the discussion in Chapter 4 and Eq. 4.13. The normalized emittance is defined as $\epsilon_{norm} = \beta\gamma\epsilon$ for a beam of velocity β, Lorentz factor γ and actual emittance ϵ. The beam width x_σ scales as $x_\sigma \propto \sqrt{\epsilon}$ as a function of emittance. In Fig. 3.16 the decrease of the beam width is demonstrated for the acceleration of a C^{6+} ion beam from an kinetic energy of $E_{ini} = 6.7$ MeV/u, corresponding to a velocity of $\beta_{ini} = 12$ % and a Lorentz factor of $\gamma_{ini} = 1.007$, to $E_{final} = 600$ MeV/u, corresponding to $\beta_{final} = 79$ % and $\gamma_{final} = 1.64$. The assumption of normalized emittance preservation would lead to the scaling of the expected beam width as $x_{\sigma,final} = \sqrt{\frac{\beta_{ini}\cdot\gamma_{ini}}{\beta_{final}\cdot\gamma_{final}}} \cdot x_{\sigma,ini} = 0.33 \cdot x_{\sigma,ini}$ for the depicted case of Fig. 3.16. The experimental value $x_{\sigma,final} = 0.37 \cdot x_{\sigma,ini}$ is close to that theoretical value; the larger value for the experimental case is related to a change of the focusing and further imperfections during the acceleration. An ionization profile monitor as a non-intercepting device is well suited for a long-time observation without any influence on the beam.

Application: Transverse cooling

An example of the importance of a profile measurement is shown in Fig. 3.17 at the GSI synchrotron, where beam cooling is applied. Cooling is often performed to get a high brilliance beam by shrinkage of the transverse emittance and momentum distribution. This is important for high-resolution experiments or for the increase of the number of stored particles using so-called stacking methods. This is performed by electron cooling (see e.g. [54]) or stochastic cooling (see e.g. [55]). In Fig. 3.17 the effect of transverse cooling is clearly seen.

Ion detection: Resolution limit by the beam's space charge

The residual gas ions or electrons are accelerated toward the detector by applying an external electrical field of typically 0.3 to 3 kV/cm. But the beam, made of charged particles, also carries an electrical field, the space charge field, which influences the trajectory additionally. The radial electrical field E_{space} of a round beam is given non-relativistically for a Gaussian distribution with standard deviation σ (FWHM=$2.35 \cdot \sigma$) by

$$E_{space}(r) = \frac{1}{2\pi\epsilon_0} \cdot \frac{qeN}{l} \cdot \frac{1}{r} \cdot \left(1 - e^{-\frac{r^2}{2\sigma^2}}\right) \tag{3.3}$$

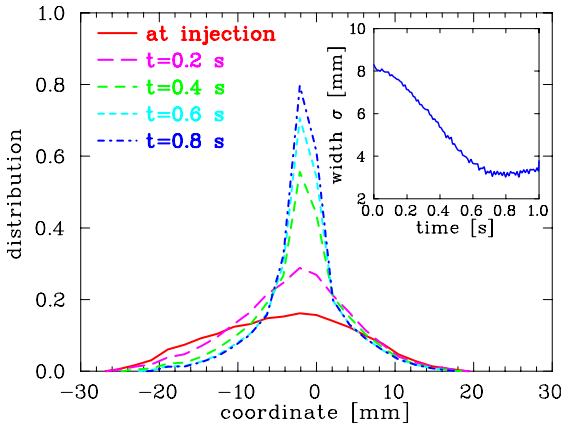

Figure 3.17: The profile during an electron cooling cooling process for an 11 MeV/u Ar^{18+} beam at the GSI synchrotron. Five profiles from the injection (broad peak bottom) to the maximal cooled profile recorded at different times during the cycle. The inlet shows the standard deviation of the profile as a function of time.

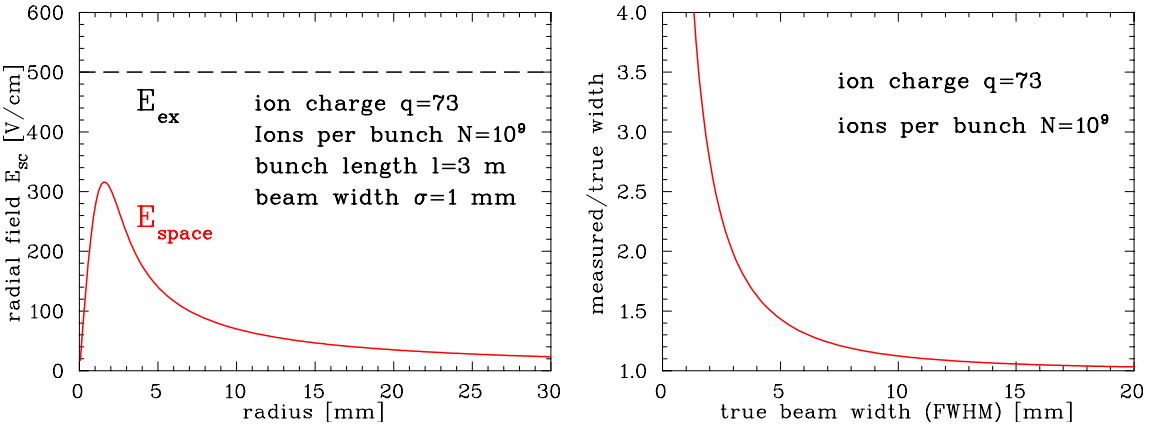

Figure 3.18: Left: The space charge field of $7 \cdot 10^{10}$ charges per 3 m bunch length. Right: The resulting relative broadening using an ionization profile monitor with ion detection is plotted using Eq. 3.5.

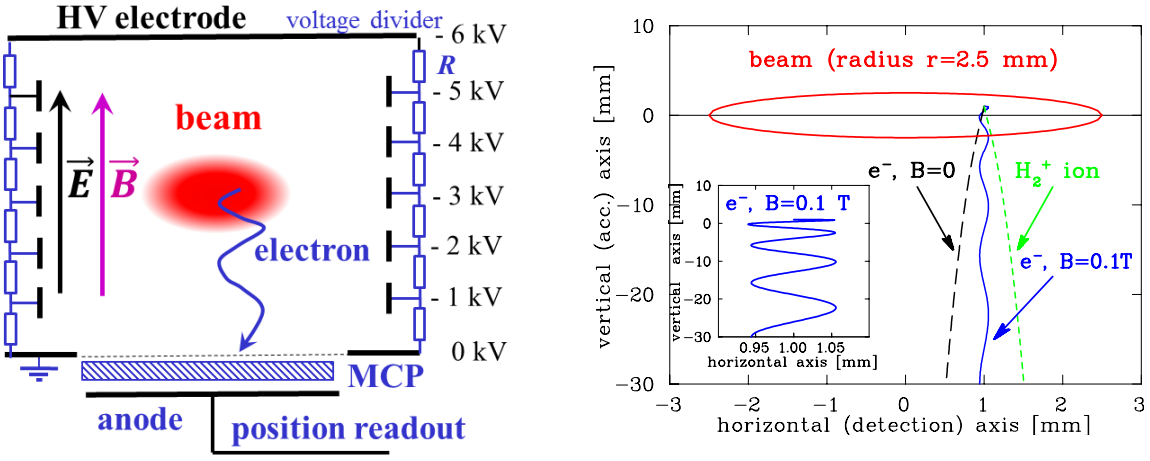

Figure 3.19: Left: Schematic trajectory of an electron in an ionization profile monitor in the presence of a homogeneous electric E and magnetic field B. Right: The comparison of the trajectories of an H_2^+-ion and an electron with and without a magnetic field visualizes the broadening due to the beam space-charge field. By applying a magnetic field, the electron is fixed to the field line, as shown in the insert. The beam parameters are: 10^9 U^{73+} within a 10 m long bunch with a radius of 2.5 mm.

assuming equal beam size in horizontal and vertical direction, which leads to a radial symmetric field. qeN/l is the number of particles in charge state q per unit length. For high current operation this field strength is comparable to the external field, see Fig. 3.18. The residual gas ions or electrons are accelerated by both fields, leading to a broadening of the measured profile, see Fig. 3.19. To get an estimation of the real beam size, the correction can be calculated via

$$\sigma_{beam}^2 = \sigma_{meas}^2 - \sigma_{corr}^2. \tag{3.4}$$

σ_{corr} is given in a first order approximation by the beam space charge and the external field according to

$$\sigma_{corr}^2 = \frac{e^2 \ln 2}{4\pi\epsilon_0\sqrt{m_p c^2}} \cdot d_{gap} \cdot qN \cdot \sqrt{\frac{1}{eU_{ex}}}. \tag{3.5}$$

The correction is proportional to the number of beam particles N. It is inversely proportional to the square root of the external field (created by the static voltage U_{ex}) and therefore an increase of the external field has only a relatively weak influence on the broadening. A large distance d_{gap} between the two high voltage electrodes result in a longer drift time and therefore in a prolonged influence of the space charge field. To calculate this correction for a real case with different horizontal and vertical size and a longitudinal extension within the bunch, numerical simulations are required.

The initial velocity of the residual gas ions right after the ionizing atomic collision between the residual gas molecule and the beam particle (Bethe-Bloch regime) is too small to affect the resolution (in contrast to the electron detection scheme, see below).

Electron detection in the presence of a magnetic field

For the measurement of intense beams, detection of electrons is more suited to overcome the space charge induced broadening, see Fig. 3.19. For this, the HV is reversed, to accelerate now the negative electrons created by the beam interaction toward the detector. If an additional magnetic field B is applied parallel to the external electrical field, the electrons spiral around the magnetic field lines with the cyclotron radius $r_c = \sqrt{2m_e E_{kin,\perp}}/eB$ with $E_{kin,\perp}$ being the kinetic energy fraction perpendicular to the magnetic field. This transverse kinetic energy is determined by the initial transverse velocity given by the kinematics of the atomic collision. The cross-section depends on the beam and residual gas molecule properties [56], resulting in kinetic energies for the emitted electron up to keV for the typical case. The cyclotron radius, and therefore the detector resolution, is mainly determined by this initial energy and is nearly independent of the beam space-charge field. The projection of the trajectory in the plane perpendicular to the field is a circle with less than 0.1 mm radius (corresponding

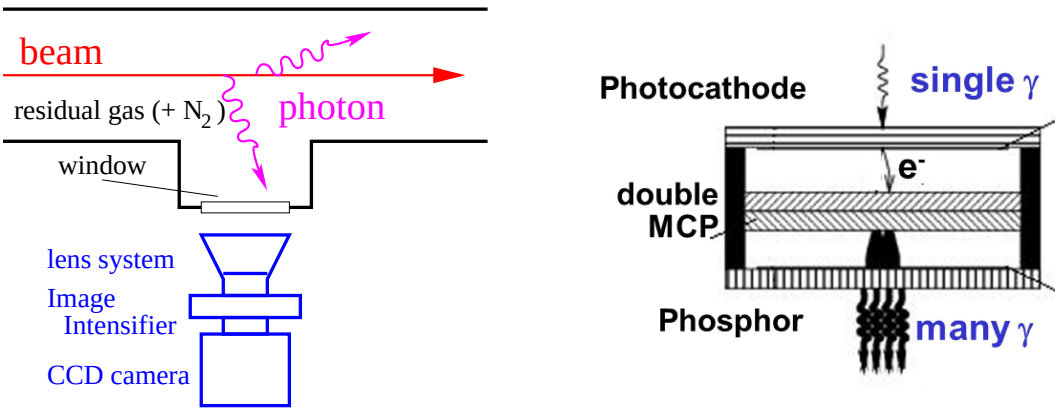

Figure 3.20: Left: General scheme of the profile determination via detection of the residual gas fluorescence. Right: Scheme of an image intensifier consisting a photo-cathode, an MCP and a phosphor screen.

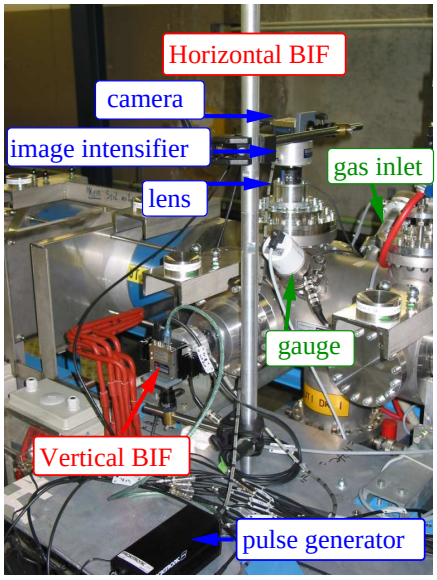

Figure 3.21: The installation of the BIF monitors at the GSI-LINAC consisting of two intensified cameras for the horizontal and vertical profile measurement, respectively. Right:

to the spatial resolution of the MCP) if a magnetic field of $B \simeq 0.1$ T is applied. The movement along the field is a linear acceleration with a typical time of flight of ~ 2 ns. The necessary magnetic field of about 0.1 T is generated in most cases with a dipole magnet of the same type as used for the beam bending, see e.g. [53].

3.6 Beam induced fluorescence monitor

By the collision of the beam particles with the residual gas, the molecules are not only ionized but also excitation of internal energy levels can occur. The excitations decay electro-magnetically by light emission leading to fluorescence [57]. In particular, the excitation of N_2 results in transition bands in the optical region. The band is originated by the decay of molecular ions N_2^+ excited by the collision with the beam ions in the wavelength range 390 nm $< \lambda <$ 470 nm, i.e., in the near UV to blue color. The lifetime is in the range of 60 ns (depending on the involved upper and lower molecular state). About 1 % of the energy loss in N_2 gas is converted to the optical wavelength interval [58]. The general scheme of a **B**eam **I**nduced **F**luorescence monitor **BIF** is shown in Fig. 3.20 and reviewed in [48].

In LINACs, the most prominent vacuum constituent is N_2; if the signal strength is insufficient, a

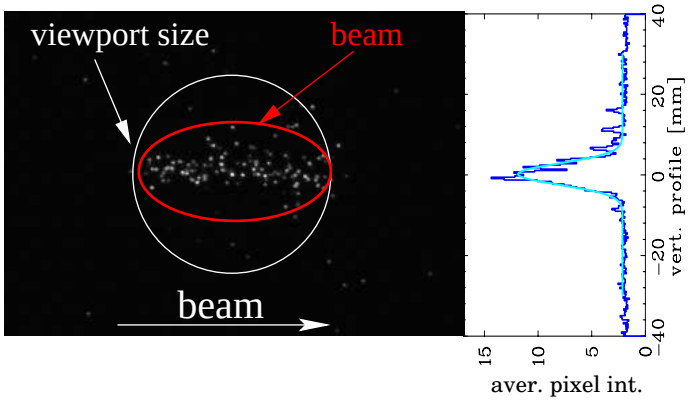

Figure 3.22: Image of an Ar^{10+} beam of $I_{beam} = 2.5$ mA and 250 μs duration with a vacuum pressure of 10^{-5} mbar recorded at the GSI LINAC. The original image (recorded with a double MCP intensifier) is shown and the projection for the vertical profile [59].

pressure bump of N_2 gas can be injected in the vacuum pipe with the help of a regulated gas valve. The fluorescence can be monitored by an image amplified CCD camera [59]. The advantage of this non-intercepting method is that nothing has to be installed in the vacuum pipe and the commercially available CCD data acquisition can be used. The rate of photons N_{photon} for the detected light is given by

$$N_{photon} \propto \frac{dE}{ds}\Delta s \cdot p \cdot \frac{f}{h\nu} \cdot \frac{\Omega}{4\pi} \cdot \frac{I_{beam}}{qe} \tag{3.6}$$

where $\frac{dE}{ds}\Delta s$ is the energy loss of ions with charge state q in N_2 for an observation length s and the pressure p, $f \sim 1$ % the fraction of the light conversion to $h\nu$ and Ω the solid angle converted by the CCD. In the image intensifier (see Fig. 3.20) the photons hit a photo-cathode and with a probability of about 20 %, electrons are created. The electrons are accelerated toward an MCP and amplified by a factor of maximally 10^6, as described above. A phosphor screen converts the electrons back to photons, which are then imaged by the CCD camera via relay optics or fibers. The total conversion efficiency can be up to 15%, i.e. 15% of the arriving photons are visible as a light-spots in the image. An example is shown in Fig. 3.22 recorded at the pulsed LINAC at GSI with a Ar-beam. Single photon spots are visible on the image, but the projection along the longitudinal direction shows a profile with sufficient statistics [59]. The method is also applied for higher energy at CERN SPS and LHC [60].

3.7 Optical transition radiation screens

At electron accelerators with relativistic particles the profile is determined from the electro-magnetic radiation at an intercepting thin metallic foil by the so-called **O**ptical **T**ransition **R**adiation **OTR**. The OTR is a pure classical electro-magnetic process including special relativity, as produced when a charged particle passes from one medium into another. While passing to the vacuum in front of the foil, the particle has a certain electro-magnetic field configuration, which is different from the field inside the medium, because the foil has a (complex) dielectric constant $\epsilon_r \neq 1$ i.e. different from vacuum. By approaching the foil, the particle's electro-magnetic field leads to a time-dependent polarization at the foil boundary. When the charged particle transverses the foil, the field configuration is changed suddenly. The change of this polarization at the foil surface generates the radiation with a characteristic intensity and angular distribution.

A typical setup of an OTR measurement is shown in Fig. 3.23. The foil is inserted under 45^o with respect to the beam path in most cases. The foil is made of Aluminum or Aluminum coated on Mylar with a thickness 1 μm or less. The light is emitted in the forward direction as well as at 90^o because the metallic surface acts as a mirror. Depending on the particle energy, the angular distribution is peaked at the angle $\theta = 1/\gamma$ with γ the relativistic Lorentz factor, see below. For typical values, 100 to 1000 beam particles yield 1 photon in the optical wavelength range. With appropriate optics, an

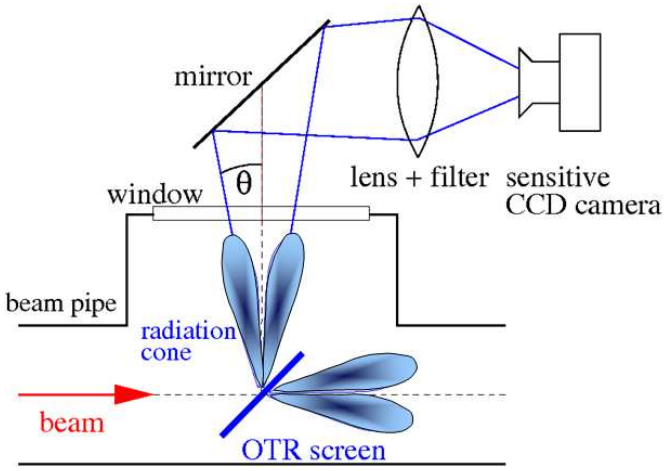

Figure 3.23: The scheme of an OTR screen measurement.

image of the foil is recorded with a CCD or CMOS camera. In some cases, an image amplified camera is used due to the relatively low number of photons.

The general process is treated in e.g. [12, 61, 62] leading to closed but extensive formula. For relativistic beam particles and some other valid assumptions, the radiated energy dW into a solid angle $d\Omega$ per frequency interval $d\omega$ can be approximated by

$$\frac{d^2W}{d\Omega d\omega} = \frac{2e^2\beta^2}{\pi c} \cdot \frac{\theta^2}{\left(\gamma^{-2} + \theta^2\right)^2} \tag{3.7}$$

with c, e, γ are the velocity of light, the elementary charge and the relativistic Lorentz-factor, respectively. The observation is oriented at an angle θ perpendicular to the beam path, the so called specular angle, see Fig. 3.23. There is no difference between the radiation for electrons or protons moving with the same Lorentz-factor, reflecting the fact that only the electro-magnetic fields of the beam particles are concerned. Note that the radiated energy does not depend on the frequency ω, i.e., the whole spectrum is covered. This is valid up to the plasma frequency of the metal, which is for most metals in the deep UV at about 10 eV. The radiated energy of Eq. 3.7 is converted to the number of photons by $W = N_{photon} \cdot \hbar\omega$ observed within a wavelength interval from λ_{begin} to λ_{end} in the optical region by the CCD camera and integration over the interval $\lambda_{begin}...\lambda_{end}$. This yields the number of photons per solid angle

$$\frac{dN_{photon}}{d\Omega} = N_{beam} \cdot \frac{2e^2\beta^2}{\pi\hbar c} \cdot \log\left(\frac{\lambda_{begin}}{\lambda_{end}}\right) \cdot \frac{\theta^2}{\left(\gamma^{-2} + \theta^2\right)^2} \tag{3.8}$$

with N_{beam} is the number of beam particles. This function is plotted in Fig. 3.24 for three different values of γ. It is clearly seen that the radiation is more tightly focused for higher energies (more precisely high value of the Lorentz-factor γ), having the advantage that a larger fraction of the photon reaches the CCD camera. At electron accelerators OTR is used even at moderate energies above $\simeq$ 100 MeV (corresponding to a Lorentz-factor $\gamma \simeq 200$). For proton acceleration a Lorentz-factor $\gamma \simeq 200$ or equivalently a beam energy above 200 GeV, and is only reached at some high energy proton facilities like at CERN SPS and LHC where OTR screens are installed [63].

The angular distribution in Eq. 3.8 is given for a single particle incidence. A real beam has an angle distribution for the beam particles, which have to be convoluted to yield a realistic photon distribution. Assuming a Gaussian beam angular distribution with a standard deviation σ_{beam}, the photon angular distribution is modified by the convolution as

$$\frac{dN_{photon}}{d\Omega} = N_{beam} \cdot \frac{2e^2\beta^2}{\pi\hbar c} \cdot \log\left(\frac{\lambda_{begin}}{\lambda_{end}}\right) \cdot \int_{-\infty}^{\infty} \frac{1}{2\pi\sigma_{beam}} \exp\left(\frac{-\theta'}{2\sigma_{beam}}\right)^2 \cdot \frac{(\theta - \theta')^2}{\left(\gamma^{-2} + (\theta - \theta')^2\right)^2} d\theta'. \tag{3.9}$$

This integral has to be evaluated numerically and can contribute significantly to the resolution for small beam sizes. In addition, the diffraction by the finite aperture of the optics can limit the resolution, as discussed e.g. in [64, 65].

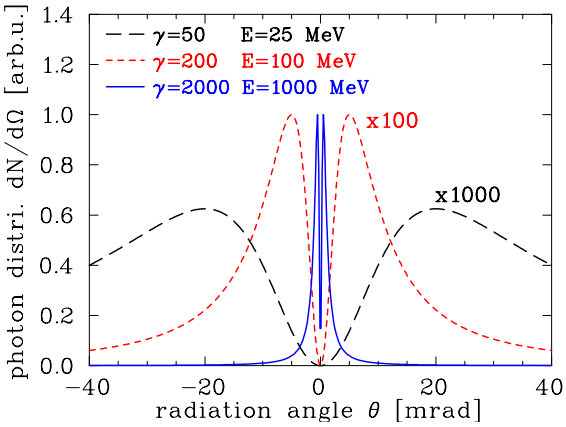

Figure 3.24: The intensity distribution of OTR as a function of the observation angle for three different value of the Lorentz-factor γ. The corresponding beam energies for electrons are also given. The photon intensity is enhanced by a factor of 1000 for $\gamma = 50$ and 100 for $\gamma = 200$ in the plot.

For the profile observation, the focus of the CCD optics coincides with the OTR screen. For the measurement of the photon angular distribution, the focus is set to infinity. Using the latter setting, the angular distribution of the beam can be evaluated. Doing both types of measurements (focus on foils yield the profile, focus on infinity yield the beam angular distribution), a transverse emittance measurement can be performed, see e.g. [64]. Fraunhofer diffraction has to be taken int account, limiting the resolution of the emittance measurement.

The OTR profile determination has some advantages and disadvantages compared to a scintillating screen measurement [34, 30]:

- It is based on a classical electromagnetic process, leading to a linearity between the number of photons and the beam intensity.
- The number of photons and their distribution is independent of the thickness of the foil. Therefore very thin foils of pure Al foil or Al coated on Mylar down to 0.25 μm can be used.
- It is still an intercepting method, but a thin foil minimizes the influence on the beam due to the low scattering probability. It can also be applied at high beam power, because of the low energy loss in the thin, low Z material.
- A measurement of profile and beam angular distribution yield the emittance of the beam.
- It is mainly used for electron beams with energies above 100 MeV. For proton beams, the needed γ is only reached at the very high energy accelerators.
- The disadvantage is the contribution of the photon angular distribution in Eq. 3.8, which might limit the resolution. This is different for a scintillation screen, where an isotropic emission occurs, and the diffraction starts to become important at much smaller beam sizes.
- The usable light of an OTR screen is orders of magnitude lower than for a scintillation screen. Therefore more advanced and expensive cameras have to be used.

3.8 Synchrotron radiation monitor

For electron accelerators, the effect of synchrotron radiation, emitted by accelerated electrons, can be used for a profile determination. As known from classical electrodynamics [12] the radiation power P_{synch} is given for a momentum change dp/dt of a particle with mass m_0 by

$$P_{synch} = \frac{e^2 c}{6\pi\varepsilon_0 (m_0 c^2)^2} \left[\frac{dp}{dt}\right]^2 . \tag{3.10}$$

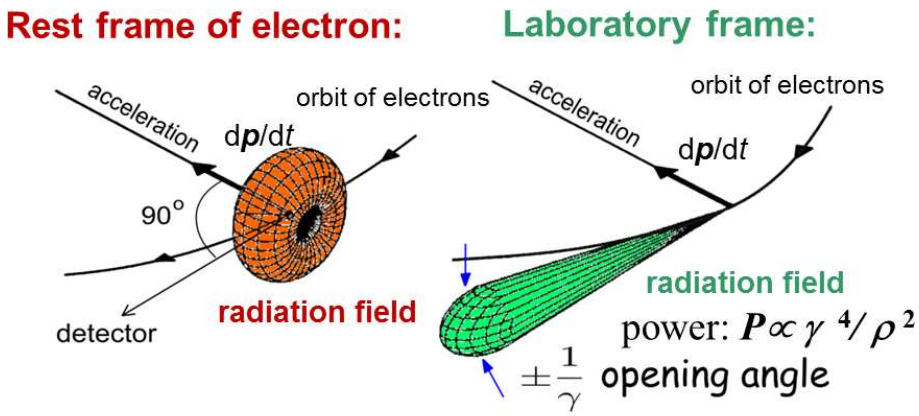

Figure 3.25: Forward peaked synchrotron radiation for relativistic particles from a bending magnet.

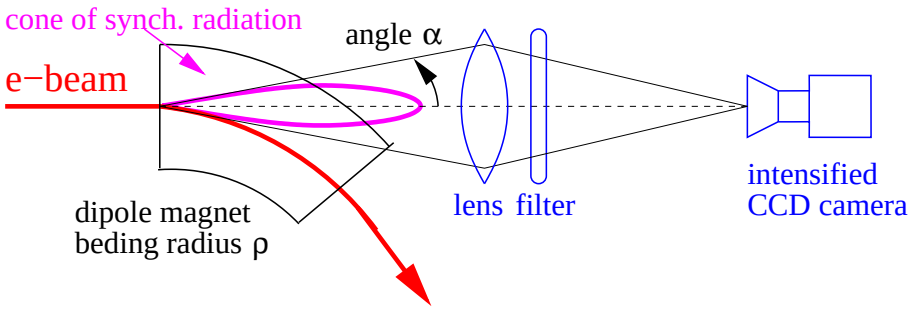

Figure 3.26: Scheme for a synchrotron radiation profile monitor observing the radiation from a dipole.

For linear acceleration we have $dp/dt \sim dW/dx$. Taking typical values of $dW/dx = 15$ MeV/m for the energy gradient of a LINAC, we find that the radiated power is negligible. This is entirely different in circular machines. Taking into account that $dp/dt = p \cdot v/R$ we obtain for the radiation power from a bending magnet

$$P_s = \frac{e^2 c}{6\pi\varepsilon_0 (m_0 c^2)^4} \frac{W^4}{R^2}. \tag{3.11}$$

For comparison of the radiation from electrons and protons for the same energy we have the ratio

$$\frac{P_{synch}^{electrons}}{P_{synch}^{protons}} = \left[\frac{932 \text{ MeV}}{511 \text{ keV}}\right]^4 \approx 10^{13}, \tag{3.12}$$

which means, that the power radiated by electrons is 10^{13} time higher than for protons of the same energy.

In the center-of-mass system, the radiation is emitted perpendicular to the momentum change. The Lorentz transformation to the laboratory frame gives a factor of γ, yielding a forward peak distribution with an opening cone of half-angle γ, as demonstrated in Fig. 3.25. The physical basis, the achievable resolution, and some applications are reviewed in [66].

The light emitted by the electron's bend in a dipole magnet can be used to monitor its horizontal and vertical beam profile, as schematically shown in Fig. 3.26. For diagnostic purposes, the visible part of the emitted spectrum is observed in most cases by using optical band-pass filters. For this wavelength, high-quality optics are available, and standard CCD cameras can be used. For most accelerator applications, the required wavelength is longer than the so-called critical wavelength, where the power spectrum falls off. Due to this, we can apply some approximation, see e.g. [67]. For the horizontally polarized synchrotron light of wavelength λ the radiation by the electrons is emitted into a cone with opening angle of

$$\alpha = 0.41\,(\lambda/\rho)^{1/3}, \tag{3.13}$$

with ρ being the radius of the bending magnet. For the optical system a 1:1 image from the beam spot to the CCD camera is obtained by a focusing lens of diameter D separated by a distance L from the

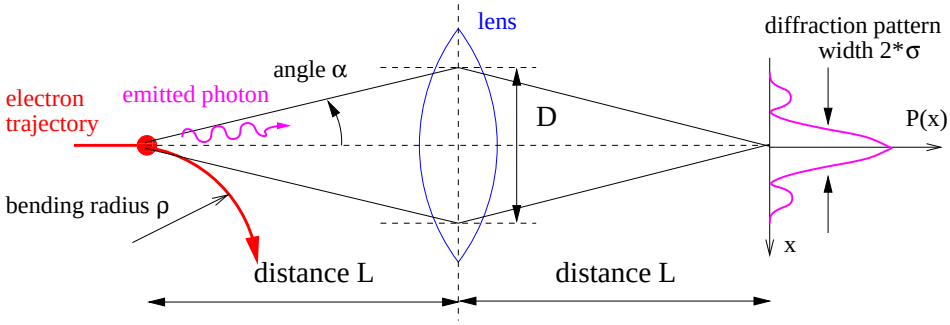

Figure 3.27: Scheme of the optical system for synchrotron radiation profile monitors and a 1:1 image explaining the diffraction limit.

beam and from the CCD, see Fig. 3.27. More precisely, the finite emission angle α results in an image of size D on the lens. From the theory of Fraunhofer diffraction on a round aperture, the pattern on the image plane has a half-width σ of

$$\sigma = \frac{\lambda}{2D/L} \quad . \tag{3.14}$$

Combining both equations with the geometrical dependency $D \simeq 2\alpha L$ yields the resolution due to diffraction

$$\sigma \simeq 0.6 \left(\lambda^2 \cdot \rho\right)^{1/3} \quad . \tag{3.15}$$

A small width of the diffraction pattern and therefore a good resolution is achieved for the given optical system by [68, 69]:

- using dipole magnets with small bending radius ρ; but this radius is fixed by the accelerator construction.
- a short wavelength; but due to technical reasons (optic components, CCD camera), it should not be shorter than near UV of $\lambda > 300$ nm.

Typical limits are in the order of ~ 100 μm, depending on the dipole bending radius. A higher resolution can be achieved by observing the light from wigglers or undulators, if they are installed in the synchrotron.

A realization of a synchrotron light profile monitor is shown in Fig. 3.28 at CERN LEP [70]. The bending radius is here 3.1 km and the diffraction gives the most substantial contribution to the resolution by about $\sigma \sim 300$ μm, which is comparable to the real electron beam size close to the final energy. The setup consists of a metallic mirror to deflect the light out of the plane of the beam. Due to the high power of the synchrotron radiation, the mirror has to be cooled, and possible deformations can spoil the optical quality. With the help of some curved mirrors, the light is focused, and an optical filter selects the wavelength range of blue or UV light; the detector is an image intensified CCD camera. Even though the resolution is not too high, this relatively straight forward system can be quite helpful due to its non-destructiveness, as demonstrated in Fig. 3.29 from the synchrotron light source APS [71].

An example of the application of a synchrotron radiation monitor is shown in Fig. 3.30 during the acceleration at the ALBA booster synchrotron [72]. For the two dimensional beam image the width in the horizontal and vertical direction can be calculated and compared to simulations. At first glance, the adiabatic damping is less pronounced as compared to the example of the hadron beam in Fig. 3.16: the reason is the contribution to the beam width by the relative momentum spread $\Delta p/p_0$ of the beam particles and the non-zero dispersion D at the measurement location as $x_{tot} = \sqrt{\varepsilon\beta + (D \cdot \Delta p/p_0)^2}$ and the contribution by the quantum fluctuations related to the emission of photons [72].

At dipoles in transfer lines such synchrotron light monitors can be installed as well, which is realized at some facilities e.g. [73]. However, there might be some technical problems as the amount of light emitted by the single pass of the electrons might be insufficient; instead OTR screens due to their simpler technical realization serve as a frequently used profile diagnostics in transfer lines at third-generation light sources or scintillation screens in case of low beam current applications at other electron accelerators.

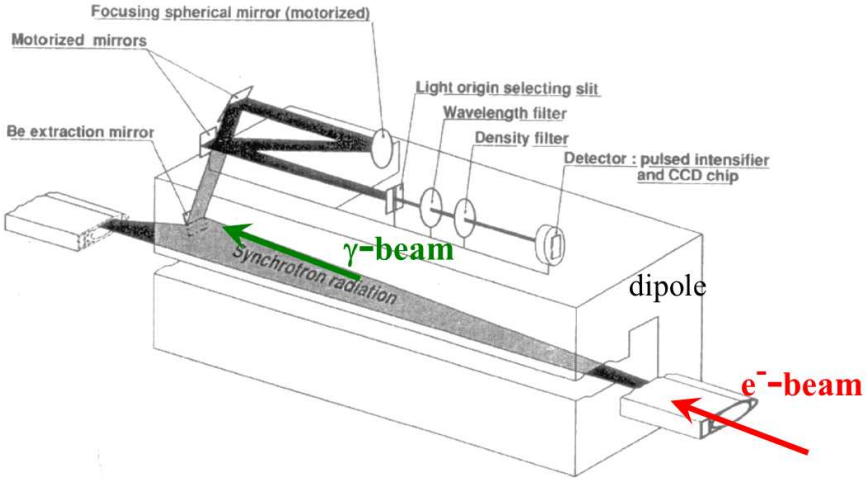

Figure 3.28: The synchrotron radiation profile monitor at LEP. The optical system is installed close to the 23 m long dipole magnet with bending radius of 3100 m, from [70].

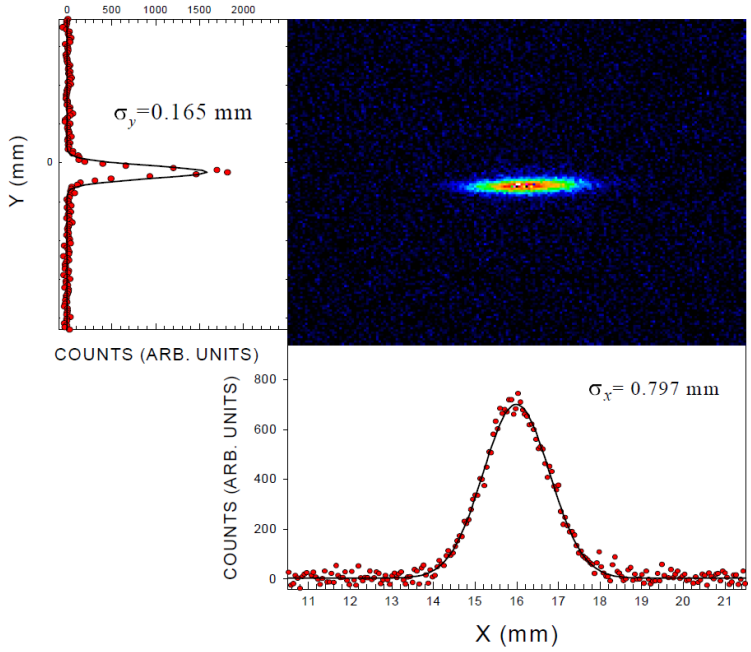

Figure 3.29: Image of the electron beam in the APS accumulator ring (Argonne National Laboratory) by a synchrotron radiation monitor [71].

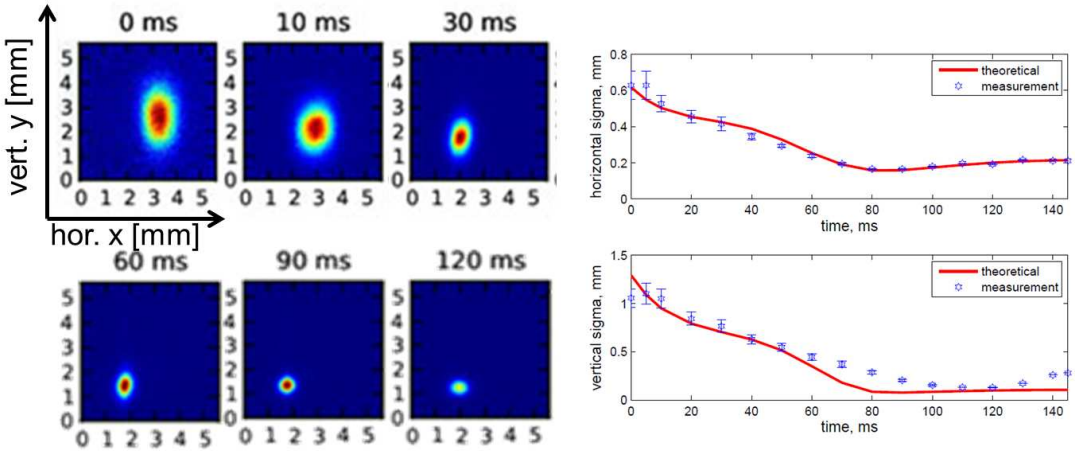

Figure 3.30: Left: Examples of two dimensional beam image by a synchrotron light monitor at ALBA booster synchrotron. Right: The fitted horizontal and vertical beam width during the acceleration 0.1 to 3 GeV within 130 ms and the comparison to simulations, from [72].

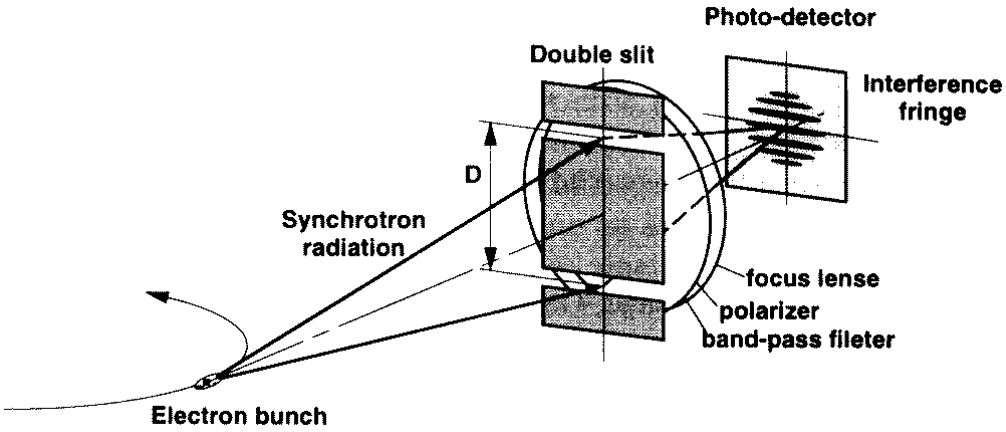

Figure 3.31: Schematics of a double slit synchrotron radiation interferometer.

The resolution limit given by the diffraction at the typically used optics can be compensated by using an interference technique by a double-slit as known from astronomy. From the distance of the minima of the interference pattern, the beam width can be calculated. A scheme of this is presented in Fig. 3.31. Due to the non-coherent emission by an ensemble of electrons, the fringes fade-out for large beam sizes. A resolution down to the 10 μm range has been realized with this method. For more details see e.g. [74].

A higher resolution can also be achieved by monitoring the profile at much shorter wavelengths. X-ray pin-hole cameras are used for this purpose. Only the emitted x-rays, scraped by a typically Ø1 mm aperture of high Z-material, are recorded with a detector.

Chapter 4

Measurement of transverse emittance

The emittance describes the quality of a beam. Its determination is based on profile measurements; it is unimportant what method of profile measurement is used, as long as it has an adequate resolution. In the following, we start with a slit-grid and pepper-pot device, where the spatial coordinate is fixed by an aperture and the angle distribution is measured. This is suited for particles having a range in matter below $\sim$ 1 cm i.e. proton or ions with $E_{kin} < 100$ MeV/u. The emittance can also be determined by fitting the beam envelope, measured at one location with different focusing conditions or different locations. This can be applied to transfer lines for all particle conditions. However, it is problematic to include emittance growth due to space charge forces, i.e., a blow-up of the transverse size due to the forces between the charged particles. A detailed review of the involved physics, technologies, and data acquisition is given in [75].

In a synchrotron, it is sufficient to measure the beam profile at one location only. For the stationary state of stable storage the orientation of the ellipse, which is equivalent to the knowledge of the lattice functions dispersion $D(s)$ and β-function $\beta(s)$, is fixed (or can be measured separately). The emittance is calculated from the beam width σ via

$$\epsilon = \frac{1}{\beta(s)} \left[\sigma^2 - \left(D(s) \frac{\Delta p}{p} \right)^2 \right] \tag{4.1}$$

which is valid for the horizontal and vertical plane, respectively. If only horizontal bends occur in a facility, the dispersion in vertical direction is in most cases $D_y = 0$ and equation simplifies to $\epsilon_y = \frac{\sigma_y^2}{\beta_y(s)}$.

4.1 Definition of the emittance

The motion of the beam particle can be described by a linear second-order differential equation. This assumes the absence of any non-linear coupling, like space charge forces or beam-beam effects as well as coupling between the two transverse and the longitudinal planes. The beam quality is given by the phase space volume, which is in this case a constant of the motion. The emittance for one plane is defined by

$$\epsilon_x = \frac{1}{\pi} \int_A dx dx', \tag{4.2}$$

where $A = \pi\epsilon$ is the area of the phase space occupied by the beam, see Fig. 4.1. A determination of the emittance is equivalent to the determination of the distribution of the spatial coordinate x (i.e., the beam profile), the distribution in angle x', and the correlation between x and x'.

The interpretation of an area assumes a hard-edge, homogeneous distribution. A more realistic case is the Gaussian density distribution $\rho(x, x')$ defined at the position of the vector $\vec{x} = (x, x')$ for each location s along the beam path. The 2-dim density is then (the meaning of the mathematical

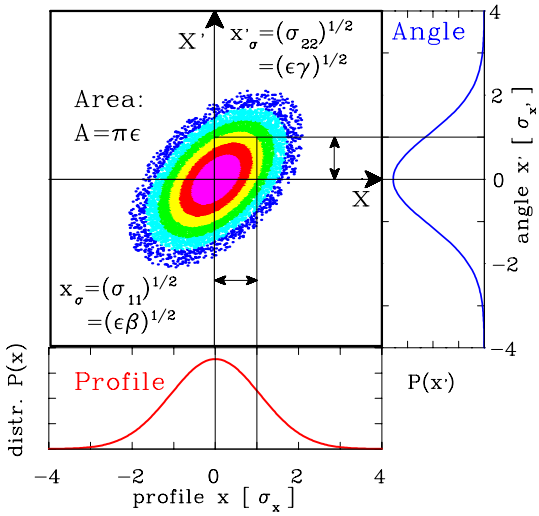

Figure 4.1: The emittance ellipse and the projection to space- and angle coordinates for a Gaussian density distribution. The values of the independent variables are given in units of the standard deviation.

abbreviations are described below)

$$\rho(x,x') = \frac{1}{2\pi\epsilon_x}\exp\left[\frac{-1}{2}\vec{x}^T\boldsymbol{\sigma}^{-1}\vec{x}\right] \equiv \frac{1}{2\pi\epsilon_x}\exp\left[\frac{-1}{2\det\sigma}\left(\sigma_{22}x^2 - 2\sigma_{12}xx' + \sigma_{11}x'^2\right)\right]. \tag{4.3}$$

The profile distribution $P(x)$ is obtained by integrating the density ρ over x' as $P(x) = \int \rho(x,x')dx'$ and the parameter $\sqrt{\sigma_{11}}$ is the standard deviation of this distribution. $\sqrt{\sigma_{22}}$ is the corresponding value for the angular distribution $P(x')$ obtained by integrating $\rho(x,x')$ over x as $P(x') = \int \rho(x,x')dx$. σ_{12} is called covariance as it describes the correlation between x and x' and is related to the orientation of the ellipse in the phase space. With the help of the three parameters σ_{ij} the so-called beam matrix $\boldsymbol{\sigma}$ can be defined in the following way:

$$\boldsymbol{\sigma}(s) = \begin{pmatrix} \sigma_{11}(s) & \sigma_{12}(s) \\ \sigma_{12}(s) & \sigma_{22}(s) \end{pmatrix} \tag{4.4}$$

at one location s in the beam line. The beam matrix $\boldsymbol{\sigma}$ is a representation of the beam ellipse at this location s and varies along the beam path. It is used in connection with the transfer matrix $\mathbf{R}$, which describes the action of the optical elements along the beam path in a linear approximation with optical elements like drifts, dipoles, quadrupole magnets or solenoids by

$$\boldsymbol{\sigma}(s_1) = \mathbf{R}\cdot\boldsymbol{\sigma}(s_0)\cdot\mathbf{R}^{\mathbf{T}} \tag{4.5}$$

from a location s_0 to s_1, see Chapter 4.4 for a more detailed discussion.

The absolute value of the emittance at each location can be defined using this notation as

$$\epsilon_x = \sqrt{\det\boldsymbol{\sigma}} = \sqrt{\sigma_{11}\sigma_{22} - \sigma_{12}^2} \tag{4.6}$$

and corresponds to an occupation of 15 % of the full phase space area. The unit of this value is m·rad or more frequently mm·mrad. To be consistent with the geometrical interpretation of an area surrounded by an ellipse, the number is multiplied by π; in this case 39 % of the beam is inside the area of $\pi\cdot\sqrt{\sigma_{11}\sigma_{22} - \sigma_{12}^2}$. In other words, the Gaussian beam quality at a given location s is fully described by the beam matrix $\boldsymbol{\sigma}(s)$.

Frequently the Twiss parameters are used, which are the beam matrix elements normalized by the emittance as

$$\alpha = -\sigma_{12}/\epsilon \qquad \beta = \sigma_{11}/\epsilon \qquad \gamma = \sigma_{22}/\epsilon. \tag{4.7}$$

The beam matrix is then

$$\boldsymbol{\sigma} = \epsilon\cdot\begin{pmatrix} \beta & -\alpha \\ -\alpha & \gamma \end{pmatrix} \tag{4.8}$$

and the equation of the beam ellipse can be written as

$$\gamma x^2 + 2\alpha x x' + \beta x'^2 = \epsilon \qquad \text{with the normalization} \qquad \beta\gamma - \alpha^2 = 1. \tag{4.9}$$

The width of profile- and angular distribution is given by

$$x_\sigma = \sqrt{\sigma_{11}} = \sqrt{\epsilon\beta} \qquad \text{and} \qquad x'_\sigma = \sqrt{\sigma_{22}} = \sqrt{\epsilon\gamma}. \tag{4.10}$$

Their geometric meaning is one standard deviation of the transverse profile and angular distribution of the beam. The geometrical size of the phase space ellipse is changed along the beam pass s; therefore the parameters $\alpha(s)$, $\beta(s)$ and $\gamma(s)$ are functions on the position s. In particular, for a synchrotron $\beta(s)$ is called the beta-function, describing the beam size via $x_\sigma(s) = \sqrt{\epsilon \cdot \beta(s)}$.

For theoretical calculations, one prefers analytical descriptions of the density distribution. One example is the Gaussian distribution of Eq. 4.3, other functions are discussed e.g. in [76]. However, the beam does not always have a Gaussian shape. For any arbitrary phase-space distribution, the beam emittance can be calculated via the statistical moments of a 2-dimensional distribution $\rho(x, x')$. In Appendix B the definitions for the statistical moments are compiled.

To describe the beam quality via the emittance the rms value (*r*oot *m*ean *s*quare) can be calculated as

$$\epsilon_{rms} = \sqrt{\det \begin{pmatrix} \langle x^2 \rangle & \langle xx' \rangle \\ \langle xx' \rangle & \langle x'^2 \rangle \end{pmatrix}} = \sqrt{\langle x^2 \rangle \langle x'^2 \rangle - \langle xx' \rangle^2} \tag{4.11}$$

and follows the same general mathematical role as Eq. 4.6.

For a Gaussian distribution the fraction f of the beam inside the certain value of the emittance can be expressed via the rms value as

$$\epsilon(f) = -2\pi\epsilon_{rms} \cdot \ln(1 - f) \tag{4.12}$$

leading to the following table:

factor to ϵ_{rms}	$1 \cdot \epsilon_{rms}$	$\pi \cdot \epsilon_{rms}$	$2\pi \cdot \epsilon_{rms}$	$4\pi \cdot \epsilon_{rms}$	$6\pi \cdot \epsilon_{rms}$	$8\pi \cdot \epsilon_{rms}$
faction of beam f [%]	15	39	63	86	95	98

When a certain value of emittance is given for a beam one has to check carefully its meaning, because there is no common definition for the emittance around the different accelerator facilities to what level of beam fraction for a given emittance value is referring to.

The emittance is a quantity defined in the laboratory frame due to the definition of the divergence. When a beam is accelerated, the divergence shrinks ('adiabatic damping') due to the changing ratio of longitudinal velocity v_s to transverse velocity v_x: $x' = v_x/v_s$. To compare emittance for different longitudinal momenta $p_s = m_0 \cdot \gamma_{rel} \cdot v_s$, the normalized emittance ϵ_{norm}

$$\epsilon_{norm} = \frac{v_s}{c}\gamma_{rel} \cdot \epsilon \tag{4.13}$$

is referred to a value $v_s/c \cdot \gamma_{rel} = 1$ (corresponding to $v_s = \sqrt{1/2} \cdot c = 0.71 \cdot c$). c is the velocity of light and $\gamma_{rel} = 1/\sqrt{1 - (v_s/c)^2}$ is the relativistic Lorentz factor. The normalized emittance is constant under ideal accelerating conditions.

A measurement of emittance means a determination of the numerical value of ϵ as well as the orientation and shape of the phase- space distribution.

4.2 Slit-grid method

A popular method at proton or ion LINACs is the slit-grid device, where the beam particles have a penetration depth below 1 cm as schematically depicted in Fig 4.2. Here the position x is fixed for one direction with a thin slit having an opening of typically 0.1 to 0.5 mm to filter out only a small fraction of the beam at a known location. In the perpendicular direction the full beam is transmitted to get a large signal. The angle x' is determined with an SEM-grid having a distance from the slit of 10 cm to 1 m depending on the ion velocity. In the field-free drift space, the trajectories of the particles, combined in a 'beamlet', are straight lines [77, 78]. The contribution to the emittance plot in the

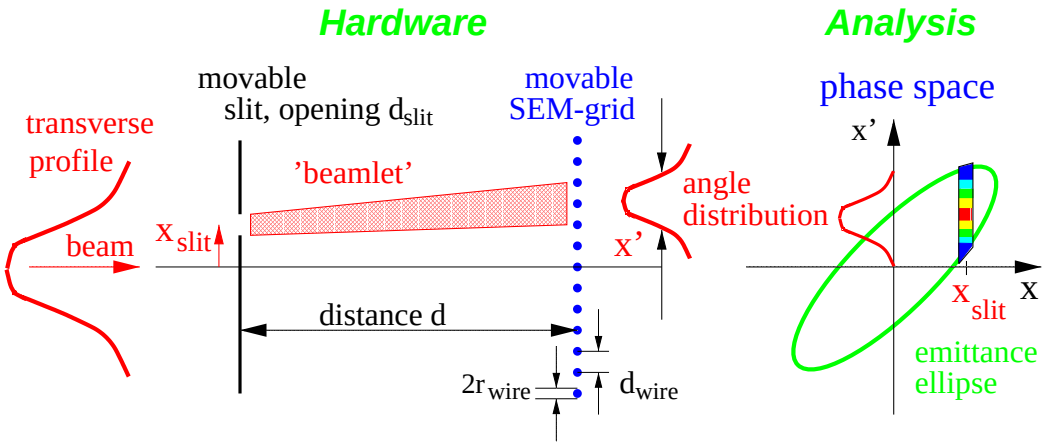

Figure 4.2: Scheme of a slit-grid emittance measurement device.

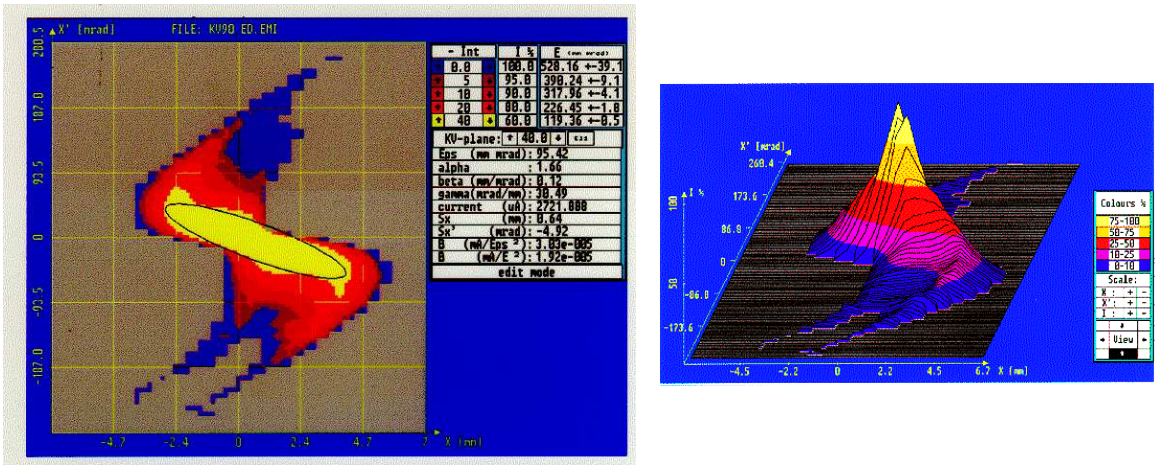

Figure 4.3: Emittance measurement using a slit-grid device with a low energy ion beam after the source at GSI display as a contour plot (left) and a mountain plot (right).

phase space is given by the angle distribution at the slit location. The slit is then scanned through the beam to get all positions. The data have to be normalized to a constant beam current as measured e.g., by the beam charges hitting the slit. After finishing the full scan, the emittance is plotted, and the *rms*-value of the emittance ϵ_{rms} is calculated using the statistical moments as given in Eq. 4.11 from the measured data. A fit with an elliptical shape is drawn to the data, and the Twiss parameters can be calculated. An example is shown in Fig. 4.3 for a low energy ion beam as a contour or three dimensional plot. Moreover, this method can determine more pathological phase-space distributions, not only Gaussian distributions. Close to an ion source, this happens quite often due to the large space charge forces or the large profile width, where aberrations of the magnets could be significant.

The resolution concerning the space coordinate Δx is limited by the slit width $\Delta x = d_{slit}$. The angle resolution $\Delta x'$, measured at the distance d, is given by the radius of the wire r_{wire} and the width of the slit resulting in $\Delta x' = (d_{wire} + 2r_{wire})/d$. The size of discrete elements in the phase space is given by $\Delta x \cdot \Delta x'$. This leads to a discretization error, in particular in the case of small beam sizes (focused beam) or small angle distributions (parallel beam). The resolution is improved by scanning the SEM-grid in steps lower than the distance of the wires d_{wire}, increasing the density of the discrete elements in the phase space analysis. This can lead to overlapping elements because of their size $\Delta x \cdot \Delta x'$ stays constant. The same holds for a movement of the slit with a step size lower than the slit width.

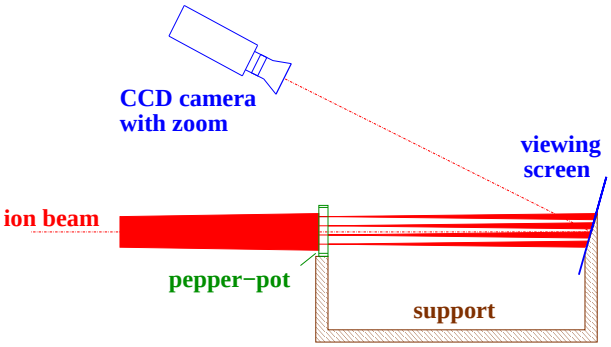

Figure 4.4: Scheme of a pepper-pot emittance measurement device.

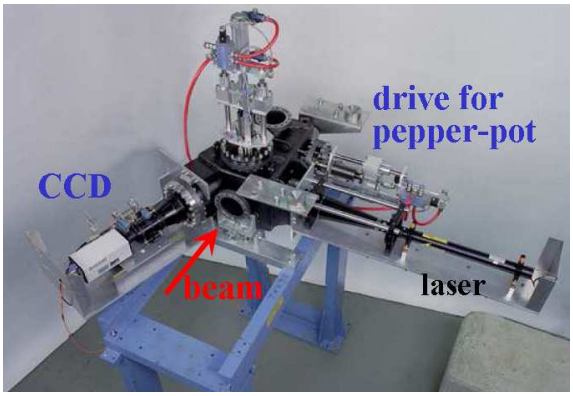

Figure 4.5: Photo of the hardware of a pepper-pot emittance device including the laser for calibration (right side), the CCD-camera (left), the pneumatic drive for the pepper-pot-screen support (right back) and the drive for the movable mirror for the laser light.

4.3 Pepper-pot device

Using a slit-grid device, the slit and the SEM-grid have to be scanned through the beam, which takes some time: up to several minutes per plane. In particular, for pulsed LINACs, only one step for the slit and the SEM-grid can be performed during a single pulse. Using a slit, the determinations for the two transverse planes have to be done separately. Having a matrix of holes in a plate, such a measurement can be performed within one shot. Moreover, if the ion sources may have fluctuations from pulse to pulse, the emittance is measured for a single beam setting. This is performed with a pepper-pot device [79, 80], shown in Fig. 4.4 schematically and a realization in Fig. 4.5. As an example, the pepper-pot plate of the GSI device has holes with 0.1 mm diameter and 3 mm spacing. To display a calibration grid on the screen, a HeNe laser beam illuminates the pepper-pot, and the image is recorded with a CCD camera, as shown in Fig. 4.6 (top). This calibration has to be performed before each beam measurement to prevent errors from probable misalignment. Relative to this, the position and size of the beamlets' spots created by the holes are determined, see Fig. 4.6 (bottom). For the device used at GSI [79], the size of the pepper-pot is 50×50 mm^2 having 15×15 holes with 0.1 mm diameter. The distance between the pepper-pot and the viewing screen is 25 cm. The screen is made of pure Al_2O_3 due to the high beam intensities. Other materials can be used for the screen, e.g., the phosphor screens discussed in Chapter 3.1.

The analysis for the emittance plot can be done by the evaluation of the individual spot's angular distributions; in this case, a possible coupling of the two transverse planes would be detectable. Alternatively, the data are projected to both transverse planes, as shown in the insert of Fig. 4.6 (bottom). The analysis for the phase space plot is similar to the slit-grid method. For an estimation of the the resolution, the arguments are comparable to the one for the slit-grid device:

- A good spatial resolution is generated by the illumination of many holes having small distances. But one has to avoid overlapping of the beamlets at the screen to distinguish the contributions

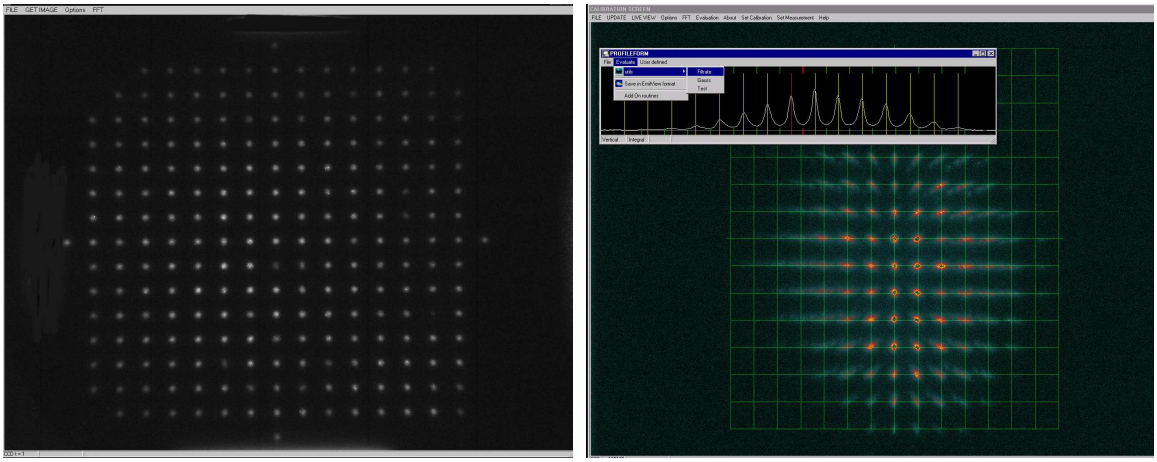

Figure 4.6: Screen shots of the pepper-pot device with a laser beam for calibration (top) and a single shot ion beam including the projection of the horizontal plane with a high current Ar^{1+} ion beam at 1.4 MeV/u (bottom), from [81].

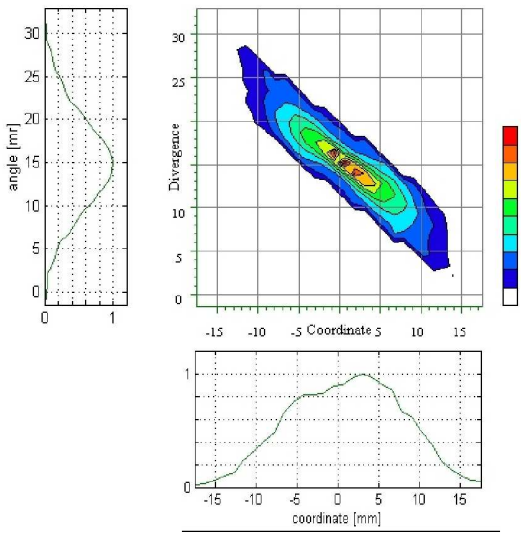

Figure 4.7: The horizontal emittance of the data above, including the projection to the axis.

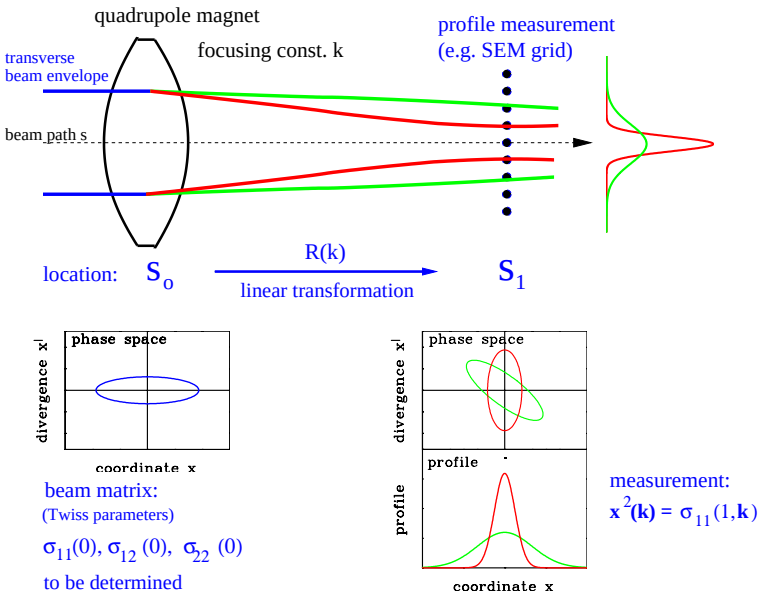

Figure 4.8: Variation of a quadrupole strength for the determination of the emittance at the location s_0.

of the individual holes.

- The diameter of the holes should be small, but in this case, the signal strength goes down.

In general, the resolution is inferior to the slit-grid, where the movable slit can have much smaller increments than the distance between the holes. Like for every destructive measurement, one has to evaluate the total beam power to prevent the melting of the uncooled pepper-pot aperture.

4.4 Quadrupole variation

The emittance can be determined from a series of profile measurements, either by changing the focusing strength of a quadrupole, or by measuring at three or more positions along a transfer line, as schematically shown in Fig. 4.8 and Fig. 4.10. To derive the emittance from such a measurement, linear transformations are used. The described measurement is just the reverse of standard transport calculations with codes like MADX or WinAgile: Starting for a given emittance (size and orientation) at the input of a transport line, the beam envelope is calculated along the line. If the profile is measured, one calculates the emittance at the input of the line by using the same transformations in reverse (see below).

For LINACs with a straight, non-dispersive transfer line, the transformation from a location s_0 to s_1 is given by the 2×2 transfer matrix $\mathbf{R}$. Important examples for these matrices are:
Drift with length L:

$$\mathbf{R_{drift}} = \begin{pmatrix} 1 & L \\ 0 & 1 \end{pmatrix} \tag{4.14}$$

Horizontal focusing quadrupole with quadrupole constant k and effective length l:

$$\mathbf{R_{focus}} = \begin{pmatrix} \cos\sqrt{k}l & \frac{1}{\sqrt{k}}\sin\sqrt{k}l \\ -\sqrt{k}\sin\sqrt{k}l & \cos\sqrt{k}l \end{pmatrix} \tag{4.15}$$

Horizontal de-focusing quadrupole with quadrupole constant k and effective length l:

$$\mathbf{R_{defocus}} = \begin{pmatrix} \cosh\sqrt{k}l & \frac{1}{\sqrt{k}}\sinh\sqrt{k}l \\ \sqrt{k}\sinh\sqrt{k}l & \cosh\sqrt{k}l \end{pmatrix}. \tag{4.16}$$

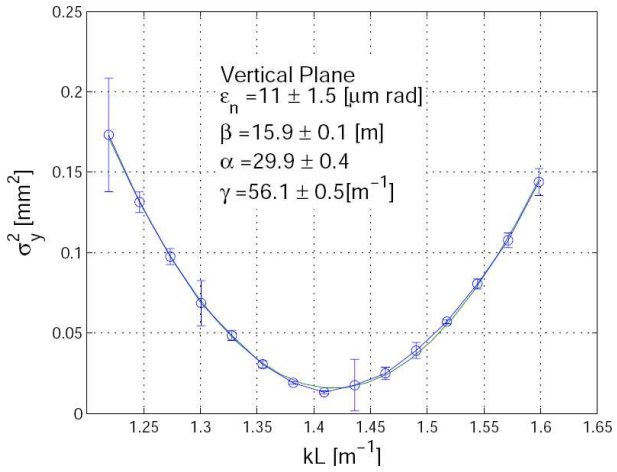

Figure 4.9: Profile width determined with a YAG:Ce screen at Elettra electron LINAC for a quadrupole variation and the parabolic fit, from [82].

The quadrupole constant $k = |g|/(B\rho)_0$ is given by the ratio of the field gradient $g = B_{pole}/a$, with B_{pole} is the field at the pole and a the aperture, and the magnetic rigidity $(B\rho)_0$ within the dipoles of bending radius ρ.

A determination of the emittance at the position s_0 is equivalent to the evaluation of the beam matrix $\boldsymbol{\sigma}$ at this position. The beam matrix is transformed to a second location s_1 with the help of the product of transfer matrices for the individual elements $\mathbf{R} = \prod \mathbf{R_{elements}}$ from the quadrupole to the profile measurement location via

$$\boldsymbol{\sigma}(1) = \mathbf{R} \cdot \boldsymbol{\sigma}(0) \cdot \mathbf{R^T} \tag{4.17}$$

The beam width $x_{rms}(1)$ is measured at s_1 and the equation for the element $\sigma_{11}(1)$ is given by

$$x^2_{rms}(1) \equiv \sigma_{11}(1) = R^2_{11}\sigma_{11}(0) + 2R_{11}R_{12}\sigma_{12}(0) + R^2_{12}\sigma_{22}(0). \tag{4.18}$$

This is a linear equation for the unknown three beam matrix elements $\sigma_{ij}(0)$ at location s_0, in Fig. 4.8 in front of the focusing quadrupole magnet.

To get a solution, we need at least three different settings of the quadrupole strength k_i, and therefore different transfer matrices $\mathbf{R}(k_i)$ leading to three different readings of the profile width, as depicted in Fig. 4.8. Assuming $i = 1, 2...n$ different settings of the quadrupole strength $k_1, k_2...k_n$ and n measurements of the beam width $x^2_{rms}(1, k_i) \equiv \sigma_{11}(1, k_i)$ a redundant system of linear equations is obtained in the form

$$\begin{aligned}
\sigma_{11}(1,k_1) &= R^2_{11}(k_1)\cdot\sigma_{11}(0) + 2R_{11}(k_1)R_{12}(k_1)\cdot\sigma_{12}(0) + R^2_{12}(k_1)\cdot\sigma_{22}(0) \quad \text{focusing } k_1 \\
\sigma_{11}(1,k_2) &= R^2_{11}(k_2)\cdot\sigma_{11}(0) + 2R_{11}(k_2)R_{12}(k_2)\cdot\sigma_{12}(0) + R^2_{12}(k_2)\cdot\sigma_{22}(0) \quad \text{focusing } k_2 \\
&\vdots \\
\sigma_{11}(1,k_n) &= R^2_{11}(k_n)\cdot\sigma_{11}(0) + 2R_{11}(k_n)R_{12}(k_n)\cdot\sigma_{12}(0) + R^2_{12}(k_n)\cdot\sigma_{22}(0) \quad \text{focusing } k_n
\end{aligned} \tag{4.19}$$

The solution of this system are the values of the beam matrix $\sigma_{ij}(0)$ (or equivalently the Twiss parameters) at the location s_0, the entrance of the quadrupole magnet. With theses values, the size and orientation of the phase space ellipse is fixed. For three measurements (k_1, k_2, k_3) we can have a unique solution, but nothing is learned about the errors. Therefore, more than three measurements have to be performed, leading to a redundant system of linear equations. The solution is reached by a least-square fit to the best parameters of $\sigma_{ij}(0)$ or by solving the linear regression problem via so-called normal equations. Both algorithms are described in textbooks of Linear Algebra or Numerical Mathematics.

An example is shown in Fig. 4.9 performed at the electron LINAC at ELETTRA for a beam with 107 MeV using a YAG:Ce scintillation screen for profile determination. To get a small error for the emittance determination, it is recommended to pass a beam waist by the quadrupole variation. Only in this case, a parabola can be fitted through the profile data with sufficient accuracy.

Instead of solving the redundant system of linear equations, one can start from the parabola fit of the beam size squared as a function of the quadrupole strength as shown in Fig. 4.9. Most frequently the transfer line comprises of a quadrupole followed by a drift toward the profile measurement location. A quadratic dependence is observed for the following reason: Assuming a thin lens approximation with a focal length f of the quadrupole action one can write the transfer matrix as:

$$\mathbf{R_{focus}} = \begin{pmatrix} 1 & 0 \\ -1/f & 1 \end{pmatrix} \equiv \begin{pmatrix} 1 & 0 \\ K & 1 \end{pmatrix}. \tag{4.20}$$

After a drift of length L one gets the transfer matrix of the transfer line

$$\mathbf{R} = \mathbf{R_{drift}} \cdot \mathbf{R_{focus}} = \begin{pmatrix} 1+LK & L \\ K & 1 \end{pmatrix}. \tag{4.21}$$

Inserting this matrix into Eq. 4.17 for the transformation of the beam matrix $\boldsymbol{\sigma}(1) = \mathbf{R} \cdot \boldsymbol{\sigma}(0) \cdot \mathbf{R}^T$ one gets for the measured beam matrix element $\sigma_{11}(1) = x_{rms}^2(1)$:

$$\sigma_{11}(1) = L^2\sigma_{11}(0) \cdot K^2 + 2\left(L\sigma_{11}(0) + L^2\sigma_{12}(0)\right) \cdot K + \sigma_{11}(0) + 2L\sigma_{12}(0) + L^2\sigma_{22}(0) \quad . \tag{4.22}$$

This is the expected quadratic function in the quadrupole gradient K. From the beam width measurement for various quadrupole setting a parabola fit is performed as performed for Fig. 4.9 with the fit-parameters a, b and c (this parametrization is chosen to yield a simple expression for the absolute value of the emittance as shown for Eq. 4.26 below)

$$\sigma_{11}(K) = a\,(K-b)^2 + c = aK^2 - 2abK + ab^2 + c. \tag{4.23}$$

A comparison of the coefficients of the last two Eqn. 4.22 and 4.23 yields

$$\begin{aligned} a &= L^2\sigma_{11}(0) \\ -ab &= L\sigma_{11}(0) + L^2\sigma_{12}(0) \\ ab^2 + c &= \sigma_{11}(0) + 2L\sigma_{12}(0) + L^2\sigma_{22}(0) \quad . \end{aligned} \tag{4.24}$$

These linear equations can finally be solved and the result are the requested matrix elements at the entrance of the optical system:

$$\begin{aligned} \sigma_{11}(0) &= \frac{a}{L^2} \\ \sigma_{12}(0) &= -\frac{a}{L^2}\left(\frac{1}{L} + b\right) \\ \sigma_{22}(0) &= \frac{1}{L^2}\left(ab^2 + c + \frac{2ab}{L} + \frac{a}{L^2}\right). \end{aligned} \tag{4.25}$$

The absolute value of the emittance is calculated from these fit parameters via

$$\epsilon = \sqrt{\det \boldsymbol{\sigma}(0)} = \sqrt{\sigma_{11}(0)\sigma_{22}(0) - \sigma_{12}^2(0)} = \frac{\sqrt{ac}}{L^2} \quad . \tag{4.26}$$

Be aware, that the fit-parameters have some units as given in Eq. 4.23.

In the above discussion, it is assumed that the method is performed at sections where no dispersion is present. The 'lattice function' dispersion D gives rise to an additional contribution to the beam width Δx by the momentum deviation Δp of the particles with respect to the mean momentum p as $\Delta x = D \cdot \Delta p/p$. The dispersion effect is added in a quadratic manner to the measured beam width as $x_{rms}^2 = \sigma_{11}(0) + (D \cdot \Delta p/p)^2$. To avoid the measurement of the 'lattice function' D and a longitudinal momentum spread determination, the location within the transfer line for the transverse emittance measurement should be dispersion free.

The described method is based on linear transformations and conservation of the emittance during the manipulation by the quadrupole. Moreover, an elliptical shape of the emittance is assumed. Depending on the general beam properties, this is a reasonable assumption as long as non-linear effects, like an aberration of magnets by higher order field contributions or space charge forces are low. If the investigations are done with intense beams, an emittance blow-up may occur, depending on the particle density, i.e., on the beam size. However, the size is to be changed, and even a waist has to be created. For high intensity beams, self-consistent, iterative algorithms have to be applied to get an estimation of the emittance at the quadrupole entrance, see e.g. [83, 84].

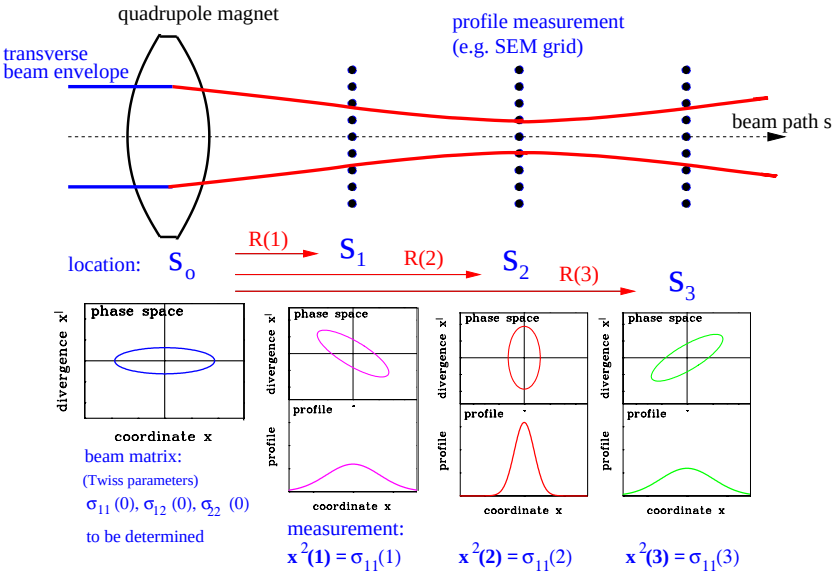

Figure 4.10: Scheme for the emittance determination at a transfer line using a profile measurement at three locations.

4.5 'Three grid' method

Instead of varying a quadrupole, the beam profiles at different locations along a transfer line can be measured with fixed magnet settings. This is easier to perform at long transfer lines, where the profile monitors are installed anyhow. There is no general restriction to the involved optics as long as they can be described by linear optics, e.g., dipoles can be included with their known transfer matrix $\mathbf{R_{dipole}}$.

The profile has to be measured at three or more locations, see Fig. 4.10. To get good accuracy, one profile monitor should be close to a beam waist. For the determination of the beam matrix elements $\sigma_{ij}(0)$ at the entrance of the line s_0, the profile widths and therefore the beam matrix elements $\sigma_{11}(n)$ are determined at n different locations s_n. A system of redundant linear equations for the entrance emittance $\sigma_{ij}(0)$ is given by

$$\begin{aligned}
\sigma_{11}(1) &= R_{11}^2(1)\cdot\sigma_{11}(0) + 2R_{11}(1)R_{12}(1)\cdot\sigma_{12}(0) + R_{12}^2(1)\cdot\sigma_{22}(0) \qquad \mathbf{R}(1): s_0 \rightarrow s_1 \\
\sigma_{11}(2) &= R_{11}^2(2)\cdot\sigma_{11}(0) + 2R_{11}(2)R_{12}(2)\cdot\sigma_{12}(0) + R_{12}^2(2)\cdot\sigma_{22}(0) \qquad \mathbf{R}(2): s_0 \rightarrow s_2 \\
&\vdots \\
\sigma_{11}(n) &= R_{11}^2(n)\cdot\sigma_{11}(0) + 2R_{11}(n)R_{12}(n)\cdot\sigma_{12}(0) + R_{12}^2(n)\cdot\sigma_{22}(0) \qquad \mathbf{R}(n): s_0 \rightarrow s_n. \quad (4.27)
\end{aligned}$$

This is a comparable formula as for the quadrupole variation (Eq. 4.19), but the transfer matrix $\mathbf{R}(i)$ describes now the beam transport from the starting point of the transfer line s_0 to the location of the individual measurements s_i. The algorithm of the emittance calculation (least square fit or normal equations) is the same as for the quadrupole scan. Such a measurement is shown in Fig. 4.11, compared to the fitted beam envelope, to visualize also the possible errors. In practice, the parameters of the entrance ellipse are fitted to match the measured profiles using a linear optics code (e.g. MADX, WinAgile) for this transfer line.

To get a reliable measurement, the transfer matrix $\mathbf{R}(n)$ should be an adequate description of the action of the optical elements on the beam. In particular, one has to make sure that the beam center passes the quadrupoles on their magnetic axes, i.e. no 'steering' of the quadrupoles is present. This might be a source of errors in practical situations. As discussed before, no emittance growth, e.g., due to space charge forces, is assumed here.

The algorithm is not limited to straight transport lines. If a dipole magnet is present in addition, one has to take its action on the beam also into account. This results in a dispersion D, i.e., a coupling between the momentum spread $\delta = \Delta p/p$ and the transverse beam size with $\Delta x = D \cdot \Delta p/p$. For the transport matrix we get an additional matrix element R_{13}. Also, a dipole has an influence of the angular distribution called angular dispersion, resulting in a additional matrix element R_{23}. The

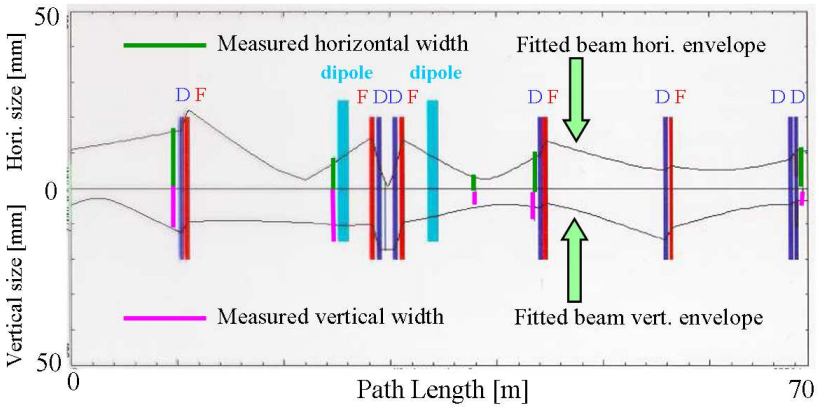

Figure 4.11: Determination of the beam envelope by linear transformations in horizontal (top curve) and vertical (bottom curve) direction using different profile measurements. The width of the profile is shown as green lines, performed at a transfer line at GSI.

single particle trajectory is now made of a 3-dim vector $\vec{x} = (x, x', \Delta p/p)$ and the transfer matrix $\mathbf{R}$ is now a 3×3 matrix. The effect of dispersion has to be included into the symmetric beam matrix σ with three new elements σ_{13}, σ_{23} and σ_{33}. To determine the values of these beam matrix elements, at least 6 profile measurements have to be done, resulting in at least 6 equations in the (redundant) system of linear equations for $\sigma_{ij}(0)$ in Eq. 4.19 and Eq. 4.27.

Chapter 5

Pick-ups for bunched beams

The longitudinal bunch shape, as well as the position of a beam, is very frequently determined with pick-up plates. The idea is to measure on an insulated metal plate the image current induced by the electro-magnetic field of the beam particles, see Fig. 5.1. Because the electric field of a bunched beam is time-dependent, an ac signal is seen on the plate, and the coupling is done using rf technologies. Only time-varying signals can be detected by this principle as generated by a bunched beam. The principle signal shape, as well as the most often used types of pick-ups are described. The application is the determination of the beam position, i.e., the transverse center-of-mass of the bunches. To this end, four pick-up plates are installed, and the difference of the signals yields the center-of-mass in both transverse axes. The device of the plates is called **P**ick-**U**p **PU** the corresponding installation for the center-of-mass determination is referred as **B**eam **P**osition **M**onitor **BPM**. A review on general BPM properties and BPM types is given in [85]–[88]. In a synchrotron, the closed orbit is determined by the BPMs. Measurements based on this position information are discussed at the end of this chapter, namely the determination of the tune and the lattice functions of a synchrotron.

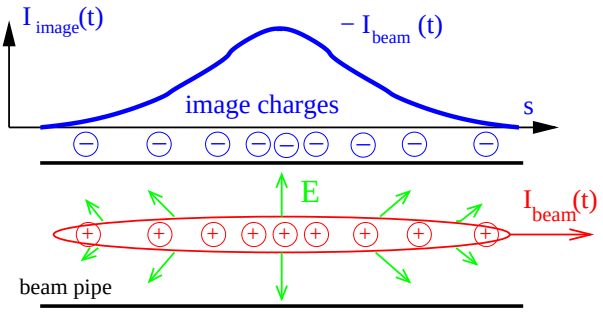

Figure 5.1: The beam current induces a wall current of the same magnitude and time structure but reversed polarity.

5.1 Signal treatment of capacitive pick-ups

As shown in Fig. 5.2, a capacitive pick-up consists of a plate or a ring inserted in the beam pipe. Here the induced image charge of the beam is coupled via an amplifier for further processing. The plate at a distance a from the beam center has an area of A and a length in longitudinal direction of l. The current I_{im} driven by the image charge Q_{im} as a function of time t is

$$I_{im}(t) \equiv \frac{dQ_{im}}{dt} = -\frac{A}{2\pi a l} \cdot \frac{dQ_{beam}(t)}{dt}. \tag{5.1}$$

Having a beam with velocity β we can write for the derivative of the beam charge $dQ_{beam}(t)/dt$

$$\frac{dQ_{beam}(t)}{dt} = \frac{l}{\beta c}\frac{dI_{beam}}{dt} = -\frac{l}{\beta c} \cdot i\omega I_{beam}(\omega) \tag{5.2}$$

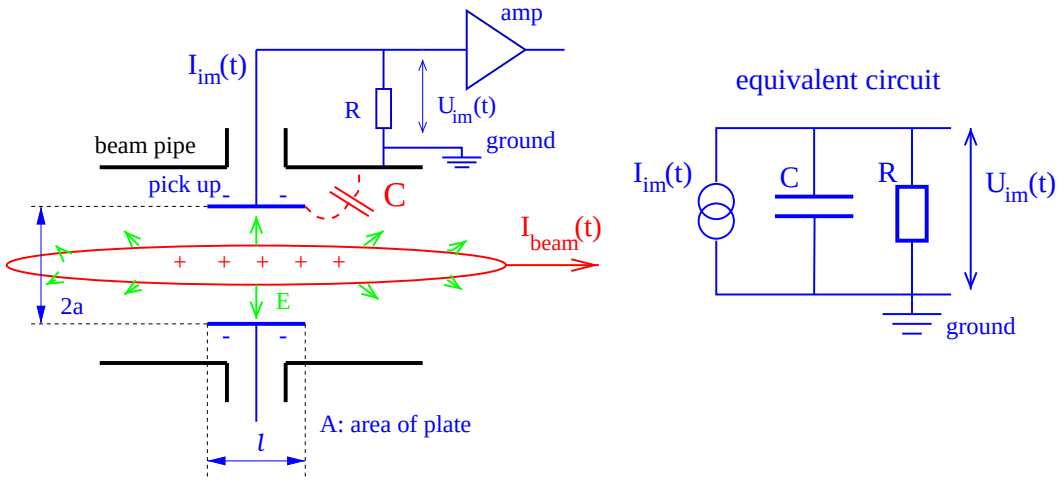

Figure 5.2: Scheme of a pick-up electrode and its equivalent circuit.

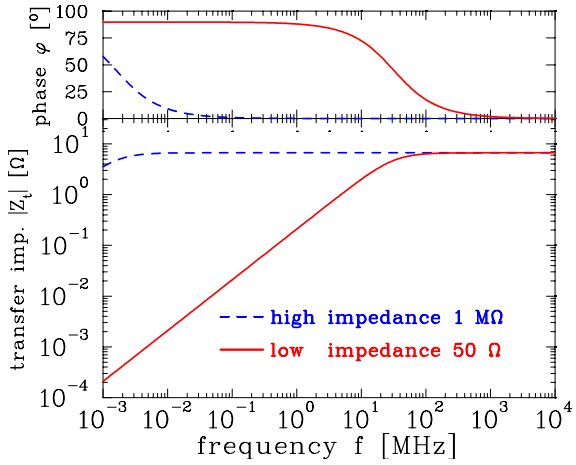

Figure 5.3: Absolute value and phase of the transfer impedance for a $l = 10$ cm long cylindrical pick-up with a capacitance of $C = 100$ pF and an ion velocity of $\beta = 50\%$ for high (1 MΩ) and low (50 Ω) input impedance of the amplifier.

where the beam current is expressed in frequency domain using the angular frequency ω as $I_{beam} = I_0 e^{-i\omega t}$ [1]. Combining Eq. 5.1 and Eq. 5.2 the image current can be written as

$$I_{im}(t) = \frac{1}{\beta c} \cdot \frac{A}{2\pi a} \cdot i\omega I_{beam} \quad . \tag{5.3}$$

As the signal we use the voltage drop at a resistor R

$$U_{im}(\omega) = R \cdot I_{im}(\omega) = Z_t(\omega, \beta) \cdot I_{beam}(\omega) \quad . \tag{5.4}$$

For all types of pick-up plates, the general quantity of longitudinal transfer impedance $Z_t(\omega, \beta)$ is defined by Eq. 5.4 in the frequency domain according to Ohm's law; for more detailed discussion see [85]–[88]. The transfer impedance describes the effect of the beam on the pick-up voltage, and it is dependent on frequency, on the velocity of the beam particles β, and on geometrical factors. It is beneficial to make the description in the frequency domain, where the independent variable is the angular frequency ω, related to the time domain by Fourier transformation. The relevant theorems for the Fourier transformation are complied in Appendix C.

The pick-up of Fig. 5.2 has a certain capacitance C, which is determined by the distance of the plate with respect to the beam pipe and a capacitance contributed by the cable between the plate

[1] More precisely: The derivative of a function df/dt can be expressed as a multiplication of its Fourier transformation $\tilde{f}(\omega)$ with $-i\omega$, see Appendix C with Eq. C.7 for the mathematical basis and Chapter 5.3 for more stringent derivation.

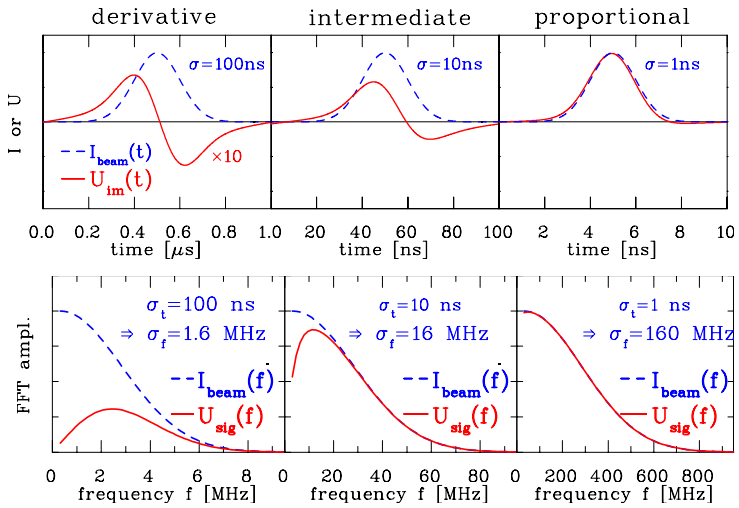

Figure 5.4: Simulation of the image voltage $U_{im}(t)$ for the values of the pick-up used in Fig. 5.3 terminated with $R = 50\ \Omega$ for three different bunch lengths of Gaussian distribution with σ of 100 ns, 10 ns and 1 ns, respectively. The cut-off frequency f_{cut} is 32 MHz. Note the different time scales. (The bunch length in the last case is artificially short for a proton synchrotron.) The shape of U_{im} is generated by the following steps: Given $I_{beam}(t) \rightarrow$ FFT yields $\tilde{I}_{beam}(\omega) \rightarrow$ multiplying by $Z_t(\omega)$ yields $\tilde{U}_{im}(\omega) = Z_t(\omega) \cdot \tilde{I}_{beam}(\omega) \rightarrow$ inverse FFT yields $U_{im}(t)$. The Fourier transformations are shown in the lower plots. A Gaussian function in time domain of width of σ_t has a Fourier transformation described by a Gaussian function of width $\sigma_f = 1/(2\pi\sigma_t)$ centered at $f = 0$.

and the amplifier input. This amplifier has an input resistor R. Using a current source to model the beam and the parallel connection of the equivalent circuit we can write its impedance Z as

$$\frac{1}{Z} = \frac{1}{R} + i\omega C \quad \Longleftrightarrow \quad Z = \frac{R}{1 + i\omega RC} \tag{5.5}$$

Inserting this impedance in the Ohm's law as given in Eq. 5.4 and using the expression for the image current of Eq. 5.3 the measurable voltage of the pick-up is

$$U_{im} = \frac{R}{1 + i\omega RC} \cdot I_{im} = \frac{1}{\beta c} \cdot \frac{1}{C} \cdot \frac{A}{2\pi a} \cdot \frac{i\omega RC}{1 + i\omega RC} \cdot I_{beam} \equiv Z_t(\omega, \beta) \cdot I_{beam} \tag{5.6}$$

which results in general transfer impedance

$$Z_t(\omega, \beta) = \frac{1}{\beta c} \cdot \frac{1}{C} \cdot \frac{A}{2\pi a} \cdot \frac{i\omega RC}{1 + i\omega RC} \quad . \tag{5.7}$$

This is a description of a first-order high-pass filter for the transfer impedance $Z_t(\omega, \beta)$ with a cut-off frequency $f_{cut} = \omega_{cut}/2\pi = (2\pi RC)^{-1}$. For the case of the so called linear cut pick-ups used at proton synchrotrons (see below), a typical value of the capacitance is $C = 100$ pF with a length of $l = 10$ cm. The high-pass characteristic is shown in Fig. 5.3 for a 50 Ω and a high impedance 1 MΩ amplifier input resistor. In the figure the absolute value

$$|Z_t| = \frac{1}{\beta c} \cdot \frac{1}{C} \cdot \frac{A}{2\pi a} \cdot \frac{\omega/\omega_{cut}}{\sqrt{1 + \omega^2/\omega_{cut}^2}} \quad \text{and the phase relation} \quad \varphi = \arctan\left(\omega_{cut}/\omega\right) \tag{5.8}$$

is shown. A pick-up has to match the interesting frequency range, which is given by the accelerating frequency and the bunch length. In a proton synchrotron typical values of the accelerating frequency are in the range from 1-10 MHz, while for LINACs and electron synchrotrons typically 100 MHz to 3 GHz are applied.

We can distinguish two extreme cases for the transfer impedance of Eq. 5.7:

- **High frequency range $\omega \gg \omega_{cut}$:** Here the transfer impedance converges to

$$Z_t \propto \frac{i\omega/\omega_{cut}}{1 + i\omega/\omega_{cut}} \longrightarrow 1. \tag{5.9}$$

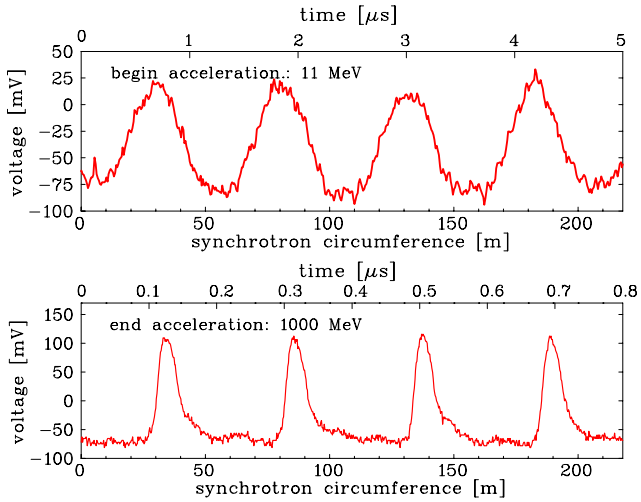

Figure 5.5: Bunch signals from a 'shoe-box' pick-ups for 1 MΩ termination as installed at the GSI ion synchrotron. The upper curve shows the bunches of the proton beam along the synchrotron circumference at the begin of the acceleration, the lower curve after reaching the final energy. Note the different time scales on top of the plots.

The resulting voltage drop at R is for this case

$$U_{im}(t) = \frac{1}{\beta c C} \cdot \frac{A}{2\pi a} \cdot I_{beam}(t). \tag{5.10}$$

Therefore, the pick-up signal is a direct image of the bunch time structure with no phase shift, i.e. $\varphi = 0$. To get a low cut-off frequency $\omega_{cut} = 1/RC$, high impedance input resistors are used to monitor long bunches, e.g. in a proton synchrotron. The calculated signal shape is shown in Fig. 5.4 (right). Note that in the figure a 50 Ω termination is considered, leading to a large value of the cut-off frequency $f_{cut} = 32$ MHz. In the application of a proton synchrotron, high impedance (~ 1 MΩ) termination yielding a much lower value of the cut-off frequency of $f_{cut} = 10$ kHz in this case as shown in Fig. 5.3 where the condition corresponds to the enlarged flat part of the depicted transfer impedance. A typical signal from this circuit is given in Fig. 5.5.

- **Low frequency range $\omega \ll \omega_{cut}$:** The transfer impedance is here

$$Z_t \propto \frac{i\omega/\omega_{cut}}{1 + i\omega/\omega_{cut}} \longrightarrow i\frac{\omega}{\omega_{cut}}. \tag{5.11}$$

Therefore, the voltage across R is in this case

$$U_{im}(t) = \frac{R}{\beta c} \cdot \frac{A}{2\pi a} \cdot i\omega I_{beam} = -\frac{R}{\beta c} \cdot \frac{A}{2\pi a} \cdot \frac{dI_{beam}}{dt} \tag{5.12}$$

using again the frequency domain relation $I_{beam} = I_0 e^{-i\omega t}$. We see that the measured voltage is proportional to the derivative of the beam current. This can also be seen from the phase relation of the high-pass filter in Fig. 5.3, where a phase shift of 90^o corresponds to a derivative. The signal is bipolar, as shown in Fig. 5.4 (left). A measurement from the GSI-LINAC is shown in Fig. 5.6 which fulfills the condition above.

The signal at the amplifier output depends on the frequency range as compared to the cut-off frequency. Of cause, the bunches are not pure sine waves, and therefore it might be that a mixture of proportional and derivative components are present, see Fig. 5.4 (middle).

With respect to the different limits of the transfer impedance, two important applications are discussed:

- **Range $\omega \gg \omega_{cut}$ realized by a *low* ω_{cut} due to high impedance:**
  In a proton or ion synchrotron a low frequency is applied for the acceleration in the range of

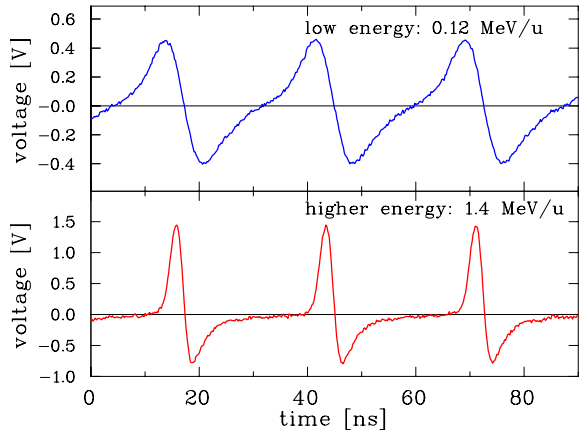

Figure 5.6: Bunch signal from a capacitive pick-up with 0.12 MeV/u (top) and 1.4 MeV/u (bottom) energy at the GSI ion LINAC. The derivative behavior is caused by 50 Ω termination to achieve a large bandwidth of the amplifier. The accelerating frequency is 36 MHz.

f_{acc} = 1...10 MHz, resulting in bunches of several meters in length. In these machines, large apertures are necessary of typically $a = 10$ cm lowering the transfer impedance due to $Z_t \propto 1/a$. To achieve a larger sensitivity, the length of the pick-up in beam direction is increased, typically $l \sim 10$ cm due to $Z_t \propto l$. Note that the pick-up length is still much shorter than the bunch length. To have a flat curve of the sensitivity, i.e., a large bandwidth, a low $\omega_{cut} = 1/RC$ is used by feeding the signal into a high impedance FET transistor as the first step of the amplifier. A bandwidth of the amplifier circuit of 100 MHz can be reached, but it is difficult to build them with a larger bandwidth. To prevent signal degeneration due to the limited amplifier bandwidth, the application of high impedance amplifiers is restricted to proton or ion synchrotrons with less than $\sim$ 10 MHz acceleration frequency. The observation of the contribution in the bunch spectrum from the tenth harmonic of the acceleration frequency is sufficient for most applications. As stated above and shown in Fig. 5.5, a direct image of the bunch is seen in this case.

- **Range $\omega \ll \omega_{cut}$ realized by a high ω_{cut} due to 50 Ω impedance:**
  At proton LINACs and all electron accelerators, the bunches are short, up to mm range, due to the higher accelerating frequencies of f_{acc} = 100 MHz to 3 GHz. Firstly, one does not gain signal strength by making the length l larger. Secondly, a 50 Ω termination is used to prevent reflections and to get smooth signal processing with a large bandwidth up to several GHz. The short l, and therefore a lower capacitance C, and the $R = 50$ Ω leads to a high ω_{cut} and the derivative of the bunches is seen as displayed in Fig. 5.6.

The preceding discussion does not take into account the effect of the frequency response of the associated cables; see [86, 90] for a more detailed discussion.

5.2 Signal treatment for a train of bunches

In the previous section, the transfer impedance Z_t was discussed for a single bunch passage only, which might be realized at transfer-lines between synchrotrons. But most other accelerators deliver a train of bunches separated by the time $t_{acc} = 1/f_{acc}$ as given by the acceleration frequency f_{acc}. In Appendix C and Eq. C.15 the mathematical basis for such a case is briefly discussed. There it is shown that the frequency spectrum for periodic signals is composed of lines at the all harmonics h of the acceleration frequency $h \cdot f_{acc}$ with an envelope function given by the single bunch frequency spectrum.

As an example of transfer impedance properties and the resulting image voltage $U_{im}(t)$, the application for a typical linear-cut BPM used at proton synchrotrons is discussed here with the same parameter as in the previous section and the transfer impedance Z_t shown in Fig. 5.3, i.e. the following values are used: The length in beam direction is $l = 10$ cm; the distance of the plates from the beam center is $a = 5$ cm covering the full circumference; the capacitance is $C = 100$ pF. For this example, we assume a synchrotron, where the acceleration is performed by $f_{acc} = 1$ MHz acceleration

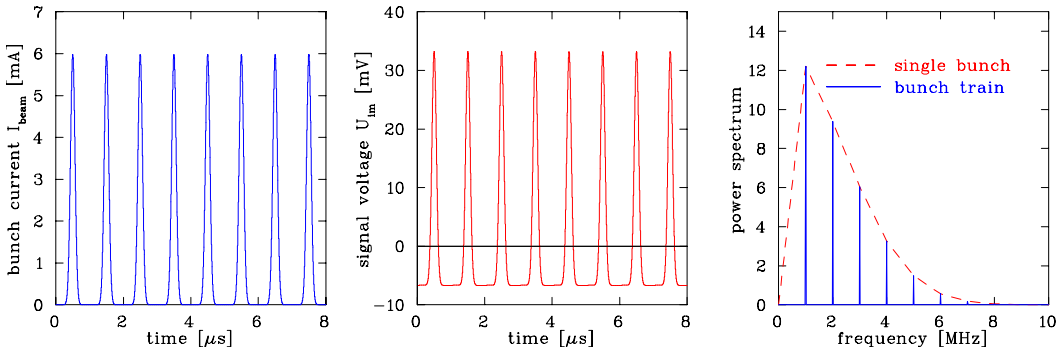

Figure 5.7: Signal simulation for 1 MΩ termination of a BPM, see text for further parameters. Left: beam current, middle: signal voltage , right: frequency spectrum of the signal voltage $\tilde{U}_{im}(f)$.

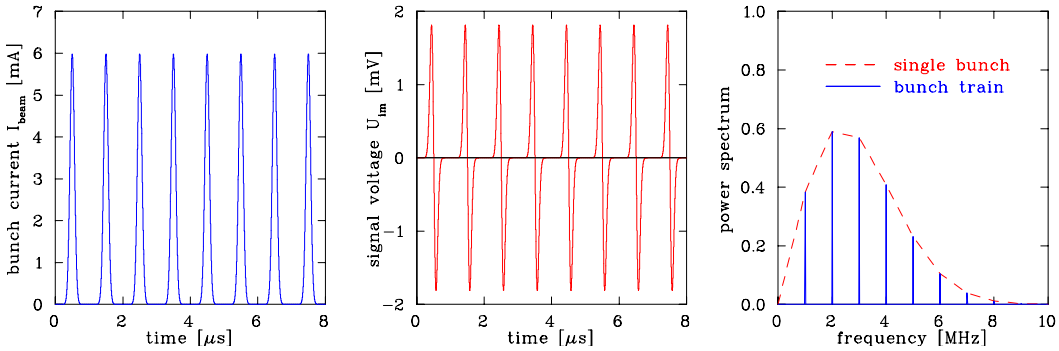

Figure 5.8: Signal simulation for 50 Ω termination of a BPM, see text for further parameters. Left: beam current, middle: signal voltage , right: frequency spectrum of the signal voltage $\tilde{U}_{im}(f)$.

frequency, a revolution time of 8 μs and an average current of 1 mA. The beam has a velocity of $\beta = 50$ % and a bunch duration of $\sigma_t = 66$ ns for a Gaussian distribution, corresponding to a bunch length of $\sigma_l = 10$ m, i.e. much longer than the BPM length of typically 10 cm. The following calculations use the concept of frequency-dependent transfer impedance $Z_t(\omega)$ and the calculation as depicted in Fig. 5.4.

High impedance termination: In Fig. 5.7 a high impedance termination of $R = 1$ MΩ is chosen for the BPM signals leading to the high-pass cut-off frequency $f_{cut} = (2\pi RC)^{-1} = 1.6$ kHz. The signal shape for $U_{im}(t)$ is proportional to the beam current $I_{beam}(t)$ with the proportional constant $Z_t \simeq 5$ Ω. However, the signal voltage shows some negative values, the so-called baseline shift. Due to the BPM's high-pass characteristic any dc-signal part is disregarded by the BPM. The uni-polar beam current is therefore transformed into an ac-signal with the condition that the integral over one turn is zero, i.e. the baseline is lowered to a value in a way to counteract the positive signal strength; note that the value of the baseline depends on the bunch width. The frequency spectrum of this periodic signal is composed of lines at the acceleration frequency and its harmonics. In other words, the signal power is concentrated in narrow frequency bands separated by the acceleration frequency. It is quite common for the position evaluation to use only one of these frequency bands with high power density e.g. by filtering or narrow-band processing to suppress broadband noise contributions, see Chapter 5.9. The envelope of these lines is given by the Fourier transformation of the single bunch current multiplied by the frequency-dependent transfer impedance. For the bunch duration σ_t of this example, the maximum frequency is at about 10 times the acceleration frequency. For the layout of a broadband electronics it is reasonable to enlarge the bandwidth up to at least the tenth harmonics to record the full signal shape and its full power spectrum, correspondingly. Using a Gaussian bunch shape, the relation of the Fourier transformation $\sigma_f = (2\pi\sigma_t)^{-1}$ can be used for the bandwidth estimation. Note that for non-Gaussian bunch shapes of the same σ_t, the frequency spectrum continues to higher values.

50 Ω termination: It is quite common in rf-technologies to use 50 Ω terminations for signal transmission, therefore a related impedance for the BPM amplifier input seems to be adequate, the

resulting signal shape is depicted in Fig. 5.8. However, for the parameters of this example a termination with a 50 Ω resistor leads to a signal of differentiating shape with a voltage amplitude decrease by a factor $\simeq 20$ compared to the high impedance termination. This is caused by the $f_{cut} = 32$ MHz BPM's high pass characteristic, which is larger than the relevant frequencies as given by the single bunch envelope, see Fig. 5.8, right. This low signal amplitude is the reason why at proton synchrotrons a higher impedance termination is preferred. As for the high impedance case, the frequency spectrum contains significant lines up to the tenth harmonics for typical beam parameters and therefore the electronics bandwidth should be chosen accordingly for a broadband recording.

5.3 Formal derivation of transfer impedance formula

In this chapter a formal derivation of the frequency domain transfer impedance as of Eq. 5.7 is discussed using some formulas given in Appendix C; the related arguments are based on [89].

The time dependent image current $I_{im}(t)$ can be written according to Eq. 5.1 as

$$I_{im}(t) \equiv \frac{dQ_{im}}{dt} = -\frac{A}{2\pi a l} \cdot \frac{dQ_{beam}(t)}{dt}. \tag{5.13}$$

for the image charges Q_{im} and beam charge Q_{beam} at an electrode at a distance a from the beam center, an area of A and a length in longitudinal direction of l, see Fig. 5.2. The Fourier transformation $\tilde{I}_{im}(\omega)$ of the frequency dependent image current can be expressed using the differential law of Eq. C.7 as

$$\tilde{I}_{im}(\omega) = -\frac{A}{2\pi a l} \cdot i\omega \tilde{Q}_{im}(\omega) \quad . \tag{5.14}$$

The related beam charge $Q_{beam}(t)$ is given by the beam current $I_{beam}(t)$ in time domain as a convolution with window function $W(t)$ as

$$Q_{beam}(t) = \int_{-\infty}^{\infty} I_{beam}(\tau) \cdot W(t-\tau)\ d\tau \quad . \tag{5.15}$$

This window function can be defined by the time t_0 the particles of velocity βc need to pass half of the electrode length $t_0 = \frac{1}{2} \cdot \frac{l}{\beta c}$ as

$$W(t) = \begin{cases} 1 \text{ if } & -t_0 \le t \le t_0 \\ 0 \text{ if } & |t| > t_0 \end{cases} \tag{5.16}$$

The Fourier transformation is given by the law of convolution Eq. C.10 and the Fourier transformation of a rectangular window as

$$\begin{aligned} \tilde{Q}_{beam}(\omega) &= \tilde{I}_{beam}(\omega) \cdot \tilde{W}(\omega) \\ &= \tilde{I}_{beam}(\omega) \cdot 2\frac{\sin \omega t_0}{\omega} \\ &= \tilde{I}_{beam}(\omega) \cdot \frac{l}{\beta c} \cdot \frac{\sin \omega \frac{l}{2\beta c}}{\omega \frac{l}{2\beta c}} \end{aligned} \tag{5.17}$$

with the insertion of the passage time t_0.

For bunches much longer than the pick-up electrode the so called sinc-function (see Appendix C) can be approximated by $\mathrm{sinc}(x) \equiv \frac{\sin x}{x} \approx 1$ for small $|x| \ll 1$. This yield for the frequency dependent beam charge

$$\tilde{Q}_{beam}(\omega) = \frac{l}{\beta c} \cdot \tilde{I}_{beam}(\omega) \quad . \tag{5.18}$$

Inserting this relation in Eq. 5.14 results in

$$\tilde{I}_{im}(\omega) = -\frac{A}{2\pi a} \cdot \frac{1}{\beta c} \cdot i\omega \tilde{I}_{beam}(\omega) \quad . \tag{5.19}$$

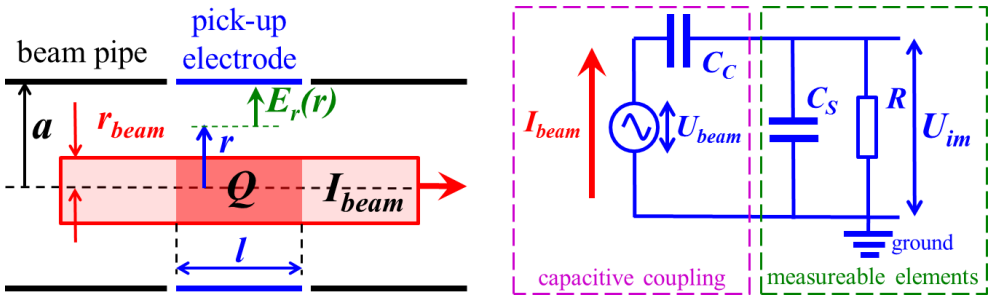

Figure 5.9: Left: The cylindrical geometry used for the calculation of the coupling capacitance for the beam to the pick-up electodes, see text for the meaning of the symbols. Right: The equivalent circuit for a capacitive pick-up.

As we want to measure a voltage across a resistor for the equivalent circuit depicted in Fig. 5.2 the impedance of the parallel RC-shunt given by Eq. 5.5 has to be used, which yields with the previous equation the relation for the frequency dependent signal voltage

$$\begin{aligned} \tilde{U}_{im}(\omega) &= \frac{R}{1+i\omega RC} \cdot \tilde{I}_{im}(\omega) \\ &= \frac{i\omega RC}{1+i\omega RC} \cdot \frac{1}{\beta c} \cdot \frac{1}{C} \cdot \frac{A}{2\pi a} \cdot \tilde{I}_{beam}(\omega) \\ &\equiv Z_t(\omega,\beta) \cdot \tilde{I}_{beam}(\omega) \quad . \end{aligned} \tag{5.20}$$

This exactly the same formula as Eq. 5.7 but now derived with a mathematically more stringent argumentation. Only the assumption was made that the bunches are much longer the pick-up electrode which is related to a 'quasi-statical' approach. This is valid at least for most proton synchtrotrons and LINACs.

5.4 Alternative derivation of the transfer impedance

This chapter concerns an alternative approach of the transfer impedance which points more clearly to the capacitive coupling between the beam and the pick-up electrode as the transfer impedance Z_t for a pick-up as of Eq. 5.7 can be derived directly for the Gaussian Law and the property of the equivalent circuit for long bunches. This description acts as a physical basis of the previously depicted current source used for the description related to the equivalent circuit of Fig. 5.2. There are only minor changes of the resulting equation, and therefore this section acts only as an alternative approach.

Assuming a cylindrical pick-up electrode of length l and radius a much shorter than the bunch length and a round beam of radius r_{beam}, then the electric field of the bunch has only a radial component $E_r(r)$ as depicted in Fig. 5.9 left. Form the Gaussian Law $\oint \mathbf{E} \cdot d\mathbf{A} = \frac{1}{\epsilon_0} \int \rho \; dV$ for the electric field vector $\mathbf{E}$ generated by the charge density ρ within a volume V the radial electric field $E_r(r)$ can be calculated between the beam edge r_{beam} and the pick-up electrode by integration over the surface vector $d\mathbf{A}$. For the geometry of Fig. 5.9 the electric field at a radius r between the beam edge and the electrode for a cylinder of length l with a barrel surface of $A_b = 2\pi r l$ is

$$\oint \mathbf{E}_r(r) \cdot d\mathbf{A} = \frac{1}{\epsilon_0} \int \rho \; dV \tag{5.21}$$

$$\Longrightarrow \quad E_r(r) \cdot A_b = \frac{Q}{\epsilon_0} \tag{5.22}$$

$$\Longrightarrow \quad E_r(r) = \frac{1}{2\pi\epsilon_0} \cdot \frac{Q}{l} \cdot \frac{1}{r} \tag{5.23}$$

with Q is the total charge within the integration volume. Due to the assumption of a bunch much longer than the pick-up electrode, the eclectic field $\mathbf{E}_r$ is perpendicular to the surface vector $d\mathbf{A}$ at the end caps and does not contribute to the surface integral and only the barrel surface remains. The induced voltage U_{beam} on the circulating pick-up electrode of radius a by the beam of radius r_{beam} is

calculated using the electric field as

$$U_{beam} = \int_{r_{beam}}^{a} E_r(r)\ dr = \frac{1}{2\pi\epsilon_0}\cdot\frac{Q}{l}\cdot\int_{r_{beam}}^{a}\frac{1}{r}\ dr \tag{5.24}$$

$$= \frac{1}{2\pi\epsilon_0}\cdot\frac{Q}{l}\cdot\ln\frac{a}{r_{beam}} \quad . \tag{5.25}$$

Substituting the line charge density Q/l by the beam current for particles moving with velocity β as $I_{beam} = Q/l\cdot\beta c$, the induced voltage is written as

$$U_{beam} = \frac{1}{2\pi\epsilon_0}\cdot\frac{1}{\beta c}\cdot\ln\frac{a}{r_{beam}}\cdot I_{beam} \quad . \tag{5.26}$$

The coupling between the the beam and the electrode is modeled electronically as a capacitance C_C as

$$C_C = \frac{Q}{U_{beam}} = 2\pi\epsilon_0\cdot l\cdot\frac{1}{\ln\frac{a}{r_{beam}}} \quad . \tag{5.27}$$

As depicted in the equivalent circuit of Fig. 5.9 right the image voltage U_{im} across a resistor R is measured, where R is part of a parallel shunt to the unavoidable stray capacitance C_S. The impedance of the RC_S parallel shunt is

$$\frac{1}{Z_S} = \frac{1}{R} + i\omega C_S \iff Z_S = \frac{R}{1+i\omega RC_S} \quad . \tag{5.28}$$

In general the whole circuit represents a voltage divider with the input voltage U_{beam} and the measured voltage U_{im}. Together with the serial capacitance C_C of impedance

$$Z_C = \frac{1}{i\omega C_C} \tag{5.29}$$

and using the relation

$$Z_C + Z_S = \frac{1}{i\omega C_C} + \frac{R}{1+i\omega RC_S} = \frac{1+i\omega R\,(C_C+C_S)}{i\omega C_C(1+i\omega RC_S)} \tag{5.30}$$

the image voltage is written as

$$U_{im} = \frac{Z_S}{Z_C+Z_S}\cdot U_{beam} = \frac{C_C}{C_C+C_S}\cdot\frac{i\omega R\,(C_C+C_S)}{1+i\omega R\,(C_C+C_S)}\cdot U_{beam} \tag{5.31}$$

$$= \frac{l}{\beta c}\cdot\frac{1}{C_C+C_S}\cdot\frac{i\omega R\,(C_C+C_S)}{1+i\omega R\,(C_C+C_S)}\cdot I_{beam} \quad . \tag{5.32}$$

for the last step Eq. 5.26 and 5.27 is used. Finally, the transfer impedance Z_t of the pick-up can be written as

$$Z_t(\omega) \equiv \frac{U_{im}(\omega)}{I_{beam}(\omega)} = \frac{l}{\beta c}\cdot\frac{1}{C_C+C_S}\cdot\frac{i\omega R\,(C_C+C_S)}{1+i\omega R\,(C_C+C_S)} \quad . \tag{5.33}$$

This is a comparable relation to Eq. 5.7 but it distinguishes between the stray capacitance C_S and the capacitive coupling between the beam and the pick-up electrodes C_C and judges the name capacitive pick-up for such an arrangement.

Using as an illustration the values of the previously discussed pick-up example with an electrode length $l = 10$ cm, a radius of $a = 10$ cm for a beam of velocity $\beta = 50$ % and radius $r_{beam} = 1$ cm the value of the coupling capacitance is $C_C = 12.7$ pF as given by Eq. 5.27. This shows that C_C is significantly lower than the unavoidable stray capacitance $C_S \simeq 100$ pF for a typical technical realization. Hence, the transfer impedance Z_t of Eq. 5.33 is dominated by C_S and can be approximated by the previously given Eq. 5.7 for many practical cases.

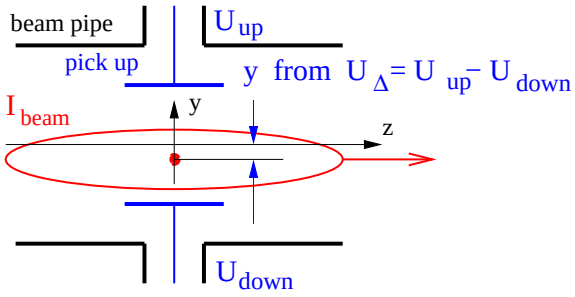

Figure 5.10: Schematics of a BPM for the vertical position reading based on the proximity effect.

5.5 Characteristics for position measurement by BPMs

5.5.1 Definition and properties of position sensitivity

The deviation of the beam center with respect to the center of the vacuum chamber is frequently monitored using four isolated plates or buttons by determining the voltage difference $\Delta U_x = U_{right} - U_{left}$ or $\Delta U_y = U_{up} - U_{down}$ of opposite plates. The closer distance to one of the plates leads to a higher induced voltage. This is called the 'proximity effect' and schematically shown in Fig. 5.10. Normalizing to the total signal $\Sigma U_x = U_{right} + U_{left}$, the horizontal displacement x can be obtained via

$$x = \frac{1}{S_x} \cdot \frac{U_{right} - U_{left}}{U_{right} + U_{left}} = \frac{1}{S_x} \cdot \frac{\Delta U_x}{\Sigma U_x} \quad \text{(horizontal)} \tag{5.34}$$

which is independent of the beam intensity. For the vertical plane the position y is given by

$$y = \frac{1}{S_y} \cdot \frac{U_{up} - U_{down}}{U_{up} + U_{down}} = \frac{1}{S_y} \cdot \frac{\Delta U_y}{\Sigma U_y} \quad \text{(vertical).} \tag{5.35}$$

This position measurement is the most frequent application of pick-ups, hence they are called **B**eam **P**osition **M**onitor **BPM**. The proportional constant S_x respectively S_y between the measured normalized voltage difference and the beam displacement is called position sensitivity and its unit is $S = [\%/\text{mm}]$. Sometimes the inverse is used $k = 1/S$ given in units of $k = [\text{mm}]$ and is called BPM position constant or position sensitivity as well. It is possible that the position sensitivity depends on the beam position itself, corresponding to a non-linear voltage response for a large beam displacement and, additionally on the evaluation frequency, hence it is a function $S = S(x, y, \omega)$.

For typical beam displacements less than 1/10 of the beam pipe aperture, the difference ΔU is lower by about this factor compared to the sum voltage ΣU i.e.

$$\text{typically} \qquad \Delta U < \frac{\Sigma U}{10} \quad . \tag{5.36}$$

Sensitive signal processing is required for the difference voltage to achieve a sufficient signal-to-noise ratio. This concerns the usage of low noise amplifiers, which have to be matched to the signal level. Sometimes difference and sum voltage are generated by analog means using a so-called $\Delta - \Sigma$ hybrids. For these cases, the difference voltage can be more amplified than the sum signal (typically by 10 dB equals to a factor of 3 for the voltage amplification) to match the optimal signal level for the successive electronics or analog-digital conversion. The most effective noise reduction is achieved by a limitation of the signal processing bandwidth, because the thermal noise voltage U_{eff} at a resistor R scales with the square root of the bandwidth Δf as $U_{eff} = \sqrt{4 k_B T R \Delta f}$ with k_B being the Boltzmann constant and T the temperature. The bandwidth limitation is performed by band-pass filtering at a harmonics of this frequency or mixing with the accelerating frequency in the narrow-band processing as discussed in Chapter 5.9. A review on general BPM properties and BPM types is given in [85]–[88].

An example of a capacitive pick-up used at the GSI-LINAC is shown in Fig. 5.11. The plates consist of (nearly) a quarter cylinder segment with radius a. For typical displacements up to $x < 1/2 \cdot a$ the function $S(x) = a$ is sufficiently constant. For larger displacements, the response is non-linear, and a correction algorithm has to be applied to the digitized signals. For the device shown, the aperture is 50 mm and a relatively large length of $l = 20$ mm in the beam direction is used to attain a large signal strength.

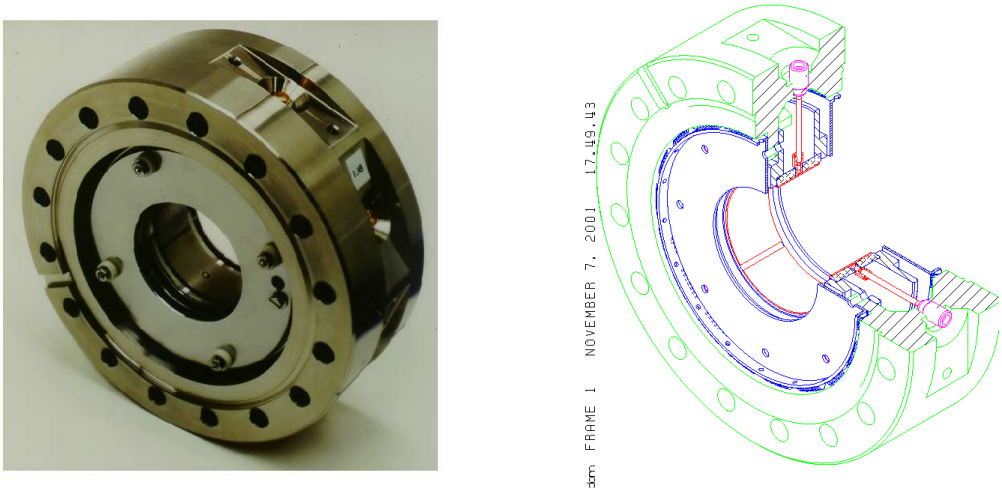

Figure 5.11: Photo and schematic drawing of a BPM at the GSI-LINAC. The aperture is 50 mm and the electrode length 20 mm.

Alternatively to the usage of the position sensitivity S, we can define the transverse transfer impedance $Z_\perp$ in analogy to the longitudinal case as

$$\Delta U_x = Z_\perp \cdot x I_{beam} \tag{5.37}$$

for an off-center position x and a beam current I_{beam}; the product xI_{beam} is sometimes called the dipole moment of the beam. $Z_\perp$ can be written as a product of the longitudinal transfer impedance Z_t as of Eq. 5.7 and a geometric non-linear function $g(x)$ as

$$Z_\perp = \frac{Z_t}{g(x)}. \tag{5.38}$$

5.5.2 Characteristic quantities for position measurements

For the characterization of a position measurement system several phrases are frequently used, which are compiled for completeness [85]:
Position sensitivity: It is the proportional constant between the beam displacement and the signal strength. It is defined by the derivative

$$S_x(x) = \frac{d}{dx}\left(\frac{\Delta U_x}{\Sigma U_x}\right) = [\%/\text{mm}] \quad \text{(linear)} \qquad S_x(x) = \frac{d}{dx}\left(\log\frac{U_{right}}{U_{left}}\right) = [\text{dB/mm}] \quad \text{(logarithmic)} \tag{5.39}$$

for the horizontal direction and for the vertical direction, correspondingly. The unit is $S = [\%/\text{mm}]$ in case of linear processing or $S = [\text{dB/mm}]$ in case of logarithmic processing [85]. For small displacements a constant value is expected. For larger displacements the horizontal sensitivity S_x might depend on beam position in the horizontal direction, called non-linearity, and additionally dependence in the vertical direction, called horizontal-vertical coupling. Moreover, it might depend on the evaluation frequency, hence in the most general case the position sensitivity $S(x, y, \omega)$ is a function of horizontal x and vertical y displacement as well as frequency ω. Sometimes the inverse of S is used having the abbreviation $k = 1/S$ and is given in the unit of $k = [\text{mm}]$.
Accuracy: It refers to the ability of position reading relative to a mechanical fix-point or any other absolutely known axis e.g. the symmetry axis of a quadrupole magnet. The accuracy is mainly influenced by the BPM's mechanical tolerances as well as the long-term stability of the mechanical alignment. For cryogenic installations, the mechanical position reproducibility after cool-down cycles influences the accuracy. Besides these mechanical properties, it is influenced by electronics properties

like amplifier drifts, noise and pickup of electro-magnetic interference. By calibrating the electronics in regular time intervals long-term drifts can be compensated. The digitalization leads to a granularity of values, which might limit the reachable accuracy; for modern installations this limitation is compensated by enhanced ADCs with a high number of bits.
Resolution: It refers to the ability to measure small displacement variations; in contrast to the accuracy relative values are compared here. In most cases, the resolution is better by a factor 2 to 5 as compared to the accuracy. It depends strongly on the measurement time because averaging procedures can exceed the accuracy by a factor of 100. Typical values for the resolution for a broadband, single bunch reading is 10^{-3} of the beam pipe radius or roughly $\simeq 100$ μm. For averaged readings on a typical time scale of 10 to 1000 ms, a resolution of 10^{-5} of the beam pipe radius or roughly $\simeq 1$ μm can be reached. As for the accuracy, it depends on the electronics noise contribution as well as short-term and long-term drifts.
Analog bandwidth: The lower and upper cut-off frequency of the analog electronics has to be matched to the frequency spectrum delivered by the bunched beam. For noise reduction, the bandwidth can be limited by analog filters.
Acquisition bandwidth: It refers to the frequency range over which the beam position is recorded and should be matched to the analog bandwidth. For monitoring fast changes of beam parameters, a much larger bandwidth is required, resulting in a lower position resolution. The same is valid for short beam deliveries, e.g. in transport lines, preventing from averaging. The bandwidth can be restricted to achieve a high resolution in case of slow varying beam parameters, as it is the case for the analog narrow-band processing described in Chapter 5.9.
Real-time bandwidth: The data rate of producing an analog or digital position signal with predictable latency to be used, e.g. by an orbit feedback system is characterized by this quantity.
Dynamic range: It refers to the range of beam current for which the system has to respond to. In most cases, the signal adoption is done by a variable gain amplifier at the input stage of the electronics processing chain. Within the dynamic range, the position reading should have a negligible dependence with respect to the input level.
Signal-to-noise ratio: It refers to the ratio of the wanted signal to unwanted noise. An unavoidable contribution is given by thermal noise. Cooling of the first stage amplifier reduces this thermal noise. Other sources, like electro-magnetic interference or ground-loops can contribute significantly to an unwanted signal disturbance and are incorporated in this phrase even though they are not caused by noise. Careful shielding and grounding is required to suppress these disturbances.
Detection threshold: It refers to the minimal beam current for which the system delivers usable information. It is limited by noise contributions. Sometimes this quantity is called signal sensitivity.

5.6 Position measurement using button pick-ups

For a round arrangement of buttons, a simple 2-dimensional electro-static model can be used to calculate the voltage difference as a function of beam displacement. According to Fig. 5.12 we assume a thin, 'pencil' beam having a transverse extension much lower the beam pipe radius of current I_{beam} which is located off-center by the amount r at an angle θ. The wall current density j_{im} at the beam pipe of radius a is given as a function of the azimuthal angle ϕ as

$$j_{im}(\phi) = \frac{I_{beam}}{2\pi a} \cdot \left(\frac{a^2 - r^2}{a^2 + r^2 - 2ar \cdot \cos(\phi - \theta)} \right) \tag{5.40}$$

and is depicted in Fig. 5.12. A mathematical derivation of this electro-static formula is given in [93], where a point-like charge located at the coordinates r and θ is assumed.

As discussed above, this represents the proximity effect, where the current density depends on the distance with respect to the beam center. The button-type BPM electrodes covering an angle α and the image current I_{im} is recorded as given by:

$$I_{im} = a \int_{-\alpha/2}^{+\alpha/2} j_{im}(\phi)\ d\phi \quad . \tag{5.41}$$

The resulting signal difference for opposite plates as a function of horizontal beam displacement, corresponding to $\theta = 0^o$, shows a significant non-linear behavior as displayed in Fig. 5.13. The signal

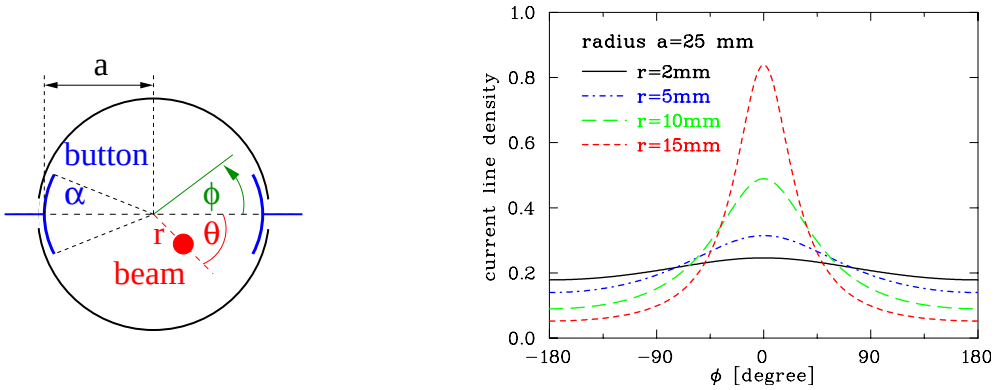

Figure 5.12: Schematics for a button BPM and the image current density generated by a 'pencil' beam at different displacements r for an azimuth $\theta = 0$.

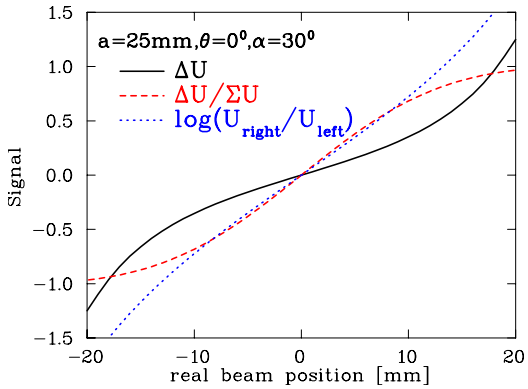

Figure 5.13: Difference voltage, normalized difference and logarithmic ratio for a button BPM arrangement of angular coverage $\alpha = 30^o$ as a function of horizontal beam displacement i.e. $\theta = 0$ for a beam pipe radius $a = 25$ mm.

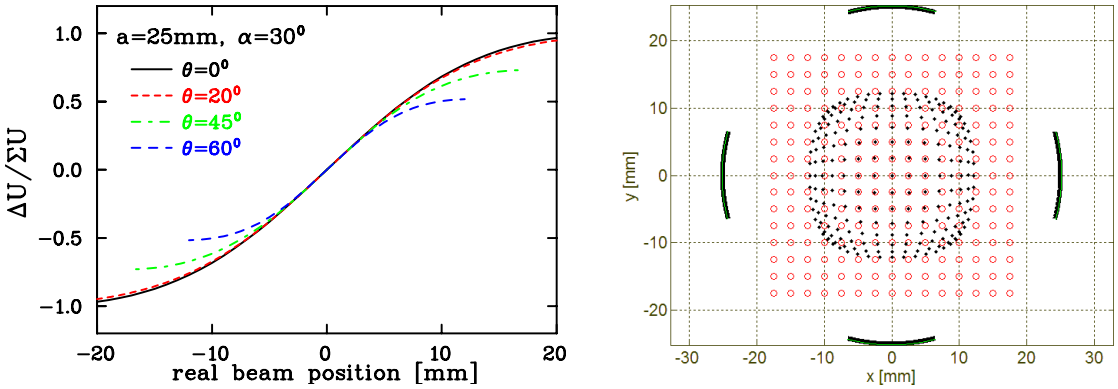

Figure 5.14: Left: Horizontal position calculation for different azimuthal beam orientation θ for the parameters of Fig. 5.13. Right: In the position map the open circles represent the real beam position and the dots are the results of the $1/S \cdot \Delta U/\Sigma U$ algorithm with $S = 7.4$ %/mm for the central part.

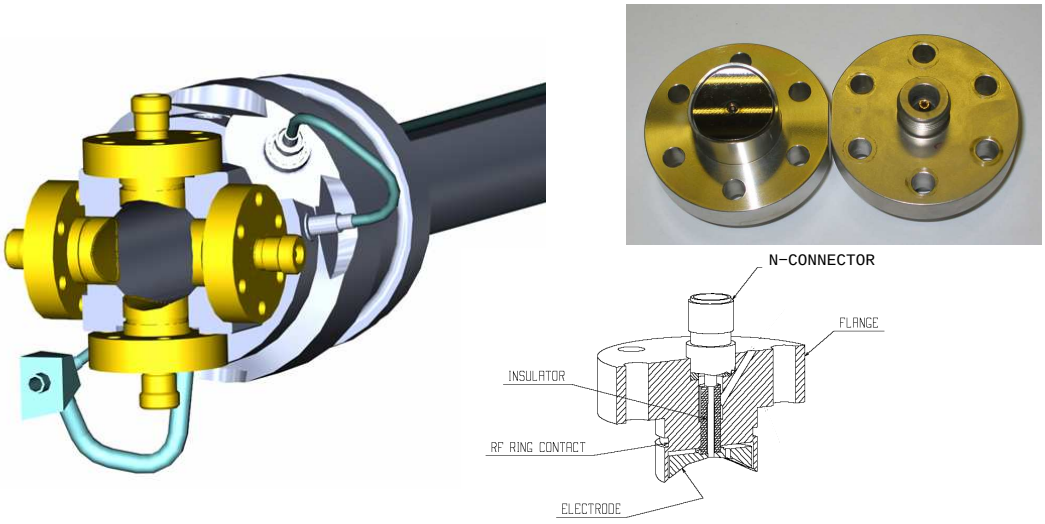

Figure 5.15: Left: The installation of the curved Ø 24 mm button BPMs at the LHC beam pipe of Ø 50 mm, from [96]. Right: Photo of a BPM used at LHC, the airside is equipped with an N-connector as well as a technical drawing for this type.

voltage is calculated according to Eq. 5.4 as $U = R \cdot I_{im}$. It can be seen that for the normalized difference $\Delta U/\Sigma U$ the linear range continues to larger beam offsets. The non-linearity increases if the beam center moves outside the horizontal axis, which is depicted in Fig. 5.14 for different values of the azimuthal orientation θ as a function of horizontal displacement $x = r \cdot \cos\theta$ according to Eqs. 5.40 and 5.41. For an orientation along the diagonal line $\theta = 45^0$, a significant deviation from linearity starts for this case even at about 1/4 of the beam pipe radius. This non-linearity can be influenced by the button size as represented in this approach by the angle α. However, in the central part the reading is nearly independent of the orientation leading to a universal position sensitivity S. The dependence between the horizontal and vertical plane is better depicted in the position map of Fig. 5.14, right: Here the real beam positions with equidistant steps are plotted as well as the results using $1/S \cdot \Delta U/\Sigma U$ calculations with S fitted at the central part. The preceding 2-dimensional electrostatic model delivers satisfying results for typical electron beams of relativistic beam velocities i.e. TEM-like field pattern; only minor corrections are necessary in case of a circular pick-up.

If the beam is accelerated to a non-relativistic velocity $\beta \ll 1$ only, as for proton LINACs and cyclotrons, the electric field cannot be described by a TEM wave anymore. Instead, the field pattern, as originated by the charged particles, has a significantly longitudinal extension because the electric field propagation is faster than the beam velocity, see the discussion in Chapter 6.1. Moreover, this field pattern and, therefore, the wall current depends strongly on the beam displacement for opposite BPM plates resulting in velocity β dependence of the position sensitivity $S(\beta)$. This is discussed analytically in [94] and a numerical example is given in [95].

A BPM arrangement obeying the circular beam pipe geometry is installed at CERN LHC and depicted in Fig. 5.15. Due to the size and the round electrodes, this arrangement is commonly called button BPM. The reason for such installation is to ensure a smooth transition from the regular beam pipe to the BPM region and to prevent for excitation of electro-magnetic fields by the beam, the so called wake-field. In most other cases, planar buttons are used due to their more straightforward mechanical realization.

Button pick-ups are the most popular devices for electron accelerators. They consist of a circular plate of typically 10 mm diameter mounted flush with the vacuum chamber, as shown in Fig. 5.16. The cross-section of the chamber is not changed by this insertion to avoid excitation of wake-fields by the beam. The button itself should have a short vacuum feed-through with a smooth transition to the 50 Ω cable, to avoid excitation of standing waves and to reach a bandwidth up to 10 GHz.

Fig. 5.16 shows a typical setup used at the storage ring of a synchrotron light source within a planar arrangement, where the buttons are not mounted in the horizontal plane only to avoid synchrotron

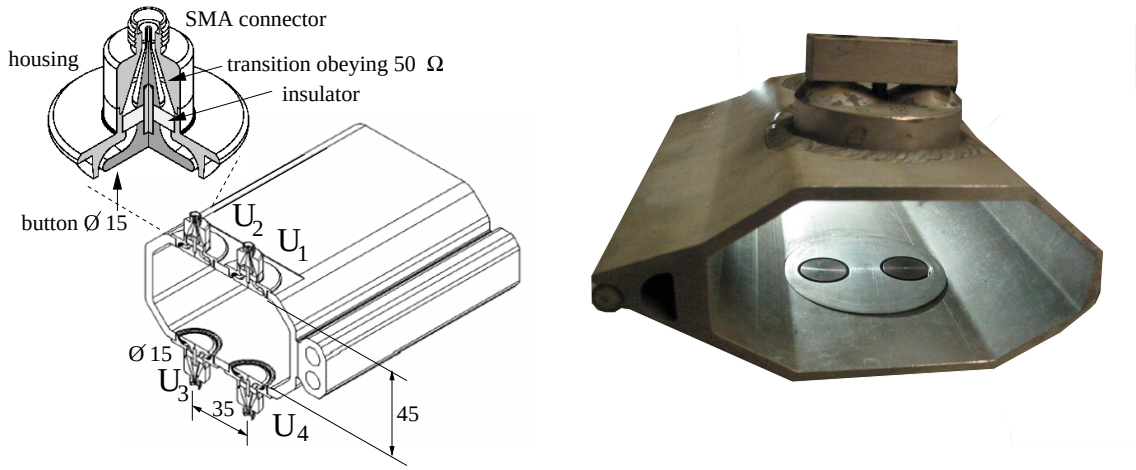

Figure 5.16: Left: Typical button BPM arrangement within a vacuum chamber at a synchrotron light source, from [97]. Right: Photo of the realization at HERA, DESY.

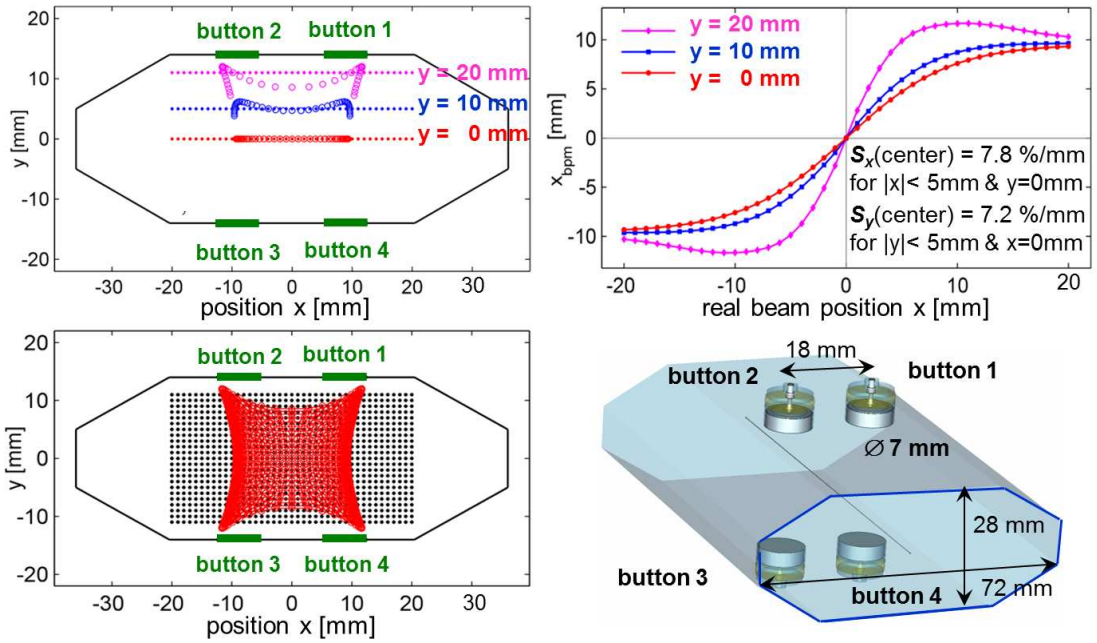

Figure 5.17: Numerical calculation of the position map for the arrangement at the synchrotron light source ALBA. Top left: Results of position calculation for a horizontal scan from -20 mm $< x <$ 20 mm for three vertical offsets using constant horizontal $S_x(center)$ and vertical $S_y(center)$ position sensitivities. Top right: The calculated position for the horizontal scan for these three vertical offsets; the horizontal position sensitivity $S_x(center)$ at the central part is determined from the slope of the curve with zero vertical offset. Bottom left: Position map for the entire horizontal and vertical range. Bottom right: The geometry of the Ø 7 mm button pick-ups of 18 mm horizontal distance within the chamber; from [100].

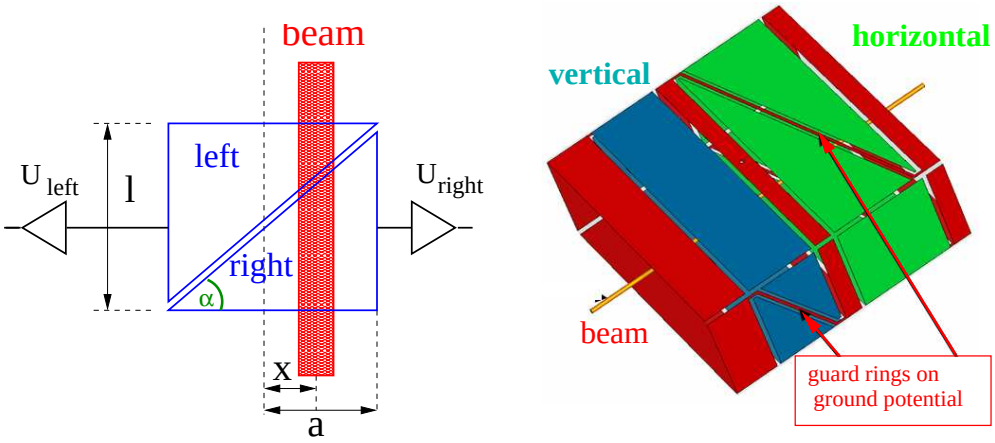

Figure 5.18: Left: Scheme of the position measurement using the so-called linear cut and an example of an electrode arrangement for the horizontal plane. Right: Schematic drawing for a linear cut BPM for both planes.

light hitting the feed-through. According to Fig. 5.16 (left) the position is evaluated via

$$\text{horizontal: } x = \frac{1}{S_x} \cdot \frac{(U_1+U_4)-(U_2+U_3)}{U_1+U_2+U_3+U_4} \qquad \text{vertical: } y = \frac{1}{S_y} \cdot \frac{(U_1+U_2)-(U_3+U_4)}{U_1+U_2+U_3+U_4} \tag{5.42}$$

using all four pick-up voltages for the position determination. An appropriate size and location of the buttons for a linear sensitivity within a maximal range at the central part and comparable values of the related horizontal and vertical position sensitivity has to be calculated numerically, see e.g. [98, 99, 100]. The optimized location depends on the size and distances of the pick-ups plates, as well as the chamber cross-section. A result for such an optimized setting is shown in Fig. 5.17 for the typical geometry of the storage ring at a synchrotron light source. The inherent geometry of the vacuum chamber leads to a non-linear position sensitivity and a strong coupling between horizontal and vertical displacements (i.e. non-linear position sensitivity $S(x, y)$ in Eq. 5.39). in case only one value for position sensitivity is given it concerns the central part of the BPM arrangement, as e.g. shown in Fig. 5.17 (top right) for the curve $y = 0$ mm; the vertical position sensitivity $S_y(center)$ is calculated form a corresponding (but not shown) diagram. After optimization the values of the position sensitivity at the central part, in this example $S_x(center) = 7.8$ %mm for $y = 0$ and $S_y(center) = 7.2$ %/mm for $x = 0$ are nearly equal and comparable to the values one would obtain for the circular beam pipe. But in contrast to the circular arrangement, even at the central part the horizontal position sensitivity $S_x(x, y)$ depends significantly on the vertical displacement y as well and a corresponding dependence for the vertical direction $S_y(x, y)$; the related non-linearity and horizontal-vertical coupling is visualized in Fig. 5.17 (bottom left) by a complete position map using constant values for the the sensitivity $S_x(center)$ and $S_y(center)$. However, in case the beam diameter is much smaller than the chamber size, numerical corrections can be applied to compensate for the non-linearity and coupling via polynomial interpolation incorporated in the analysis software, see e.g. [100].

5.7 'Shoe box' pick-ups using the so-called linear cut

Due to the long bunches at proton or ion synchrotrons and long plates of typically 20 cm are installed to enhance the signal strength. A box-like device is used frequently, to get a precise linear dependence with respect to the beam displacement, see Fig. 5.18. For the previously discussed button pick-up geometries, the signal of the plate closer to the beam's center-of-mass is larger than that of the more distant plate; this is called the proximity effect. In contrary to that, the shoe-box pick-ups have another principle: The influenced signal is proportional to the actual plate length at the beam center position. For a given beam displacement x the electrode's image voltage U_{im} is proportional to the length l_{left} and l_{right} of the beam projected on the electrode surface as shown for the horizontal

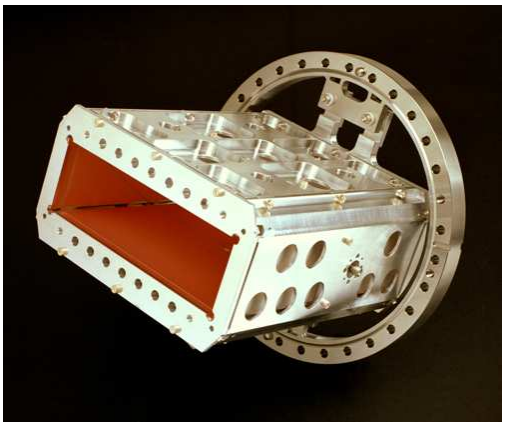

Figure 5.19: Linear cut position pick-up from the GSI synchrotron ring with an aperture limitation of 200×70 mm^2.

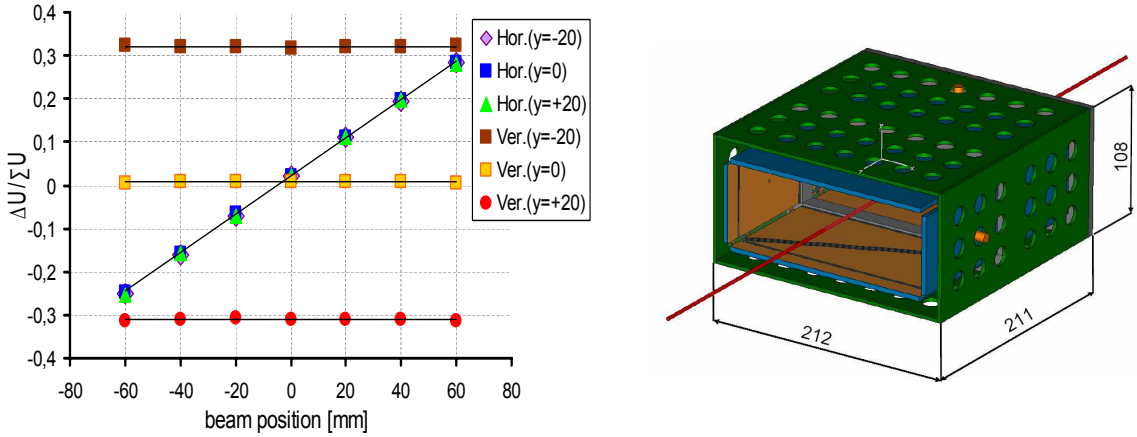

Figure 5.20: Left: Numerical calculation of the position reading $\Delta U/\Sigma U$ as a function of beam displacement for the horizontal plane. The simulated beam is swept in horizontal direction (curves with constant slope) and vertical direction (constant functions) and proves the decoupling of both planes [101]. Right The BPM geometry for these calculations is depicted right having a horizontal half-aperture of $a = 100$ mm and vertical half-aperture of $b = 35$ mm and a length of 211 mm comparable, to the one shown in Fig 5.19.

Table 5.1: Simplified comparison between linear-cut and button BPM.

	Linear-cut BPM	**Button BPM**
Precaution	bunches longer than BPM	bunches comparable to BPM
BPM length (typ.)	10 to 20 cm per plane	Ø 0.5 to 5 cm
Shape	rectangular or cut cylinder	orthogonal or planar orientation
Mechanical realization	complex	simple
Coupling	often 1 MΩ, sometimes 50 Ω	50 Ω
Capacitance (typ.)	30 - 100 pF	3 - 10 pF
Cut-off frequency (typ.)	1 kHz for $R = 1\text{M}\Omega$	0.3 to 3 GHz for $R = 50\ \Omega$
Usable bandwidth (typ.)	0.1 to 100 MHz	0.3 to 5 GHz
Linearity	very linear, no x-y coupling	non-linear, x-y coupling
Position sensitivity	good	good
Usage	at proton synchrotron, $f_{acc} < 10$ MHz	proton LINAC, all electron acc. $f_{acc} > 100$ MHz

direction in Fig. 5.18, left. For triangle electrodes with half-aperture a one can write:

$$l_{right} = (a + x) \cdot \tan\alpha \quad \text{and} \quad l_{left} = (a - x) \cdot \tan\alpha \quad \Longrightarrow \quad x = a \cdot \frac{l_{right} - l_{left}}{l_{right} + l_{left}} \quad . \tag{5.43}$$

The position reading is linear and can be expressed by the image voltages as

$$x = a \cdot \frac{U_{right} - U_{left}}{U_{right} + U_{left}} \equiv \frac{1}{S_x} \cdot \frac{\Delta U_x}{\Sigma U_x} \quad \Longrightarrow \quad S_x = \frac{1}{a} \tag{5.44}$$

which shows that the position sensitivity for this ideal case is simply given by the inverse of the half-aperture. Compared to other types of pick-ups, the position sensitivity is constant for nearly the full range of displacements, i.e. nearly no corrections due to non-linearity have to be applied [101]. This is demonstrated in Fig. 5.20 where the result of numerical simulations show a linear scaling of the difference voltage ΔU_x of opposite plates normalized to the sum voltage ΣU_x as a function of beam offset up to about 2/3 of the half aperture. Moreover, the position reading in the horizontal plane is independent on the beam position in the vertical plane. Due to the linearity, the position reading is independent of the beam size, which is of importance for the relatively large beam size compared to the chamber aperture for low energy proton or ion synchrotrons. This position linearity is the main advantage of the linear-cut type as compared to the button BPM type. An analog signal from such linear-cut BPM used at an ion synchrotron is shown in Fig. 5.5.

As a summary the basic parameters for linear-cut and button BPMs are compared in Table 5.1; this table contains significant simplifications and serves as an overview only.

5.8 Signal treatment of a stripline pick-up

In the discussion of capacitive BPMs above, basically an electrostatic approach was used disregarding effects based on the signal propagation. If the bunch length becomes comparable to the size of the BPM, the final propagation time leads to a signal deformation, or in other words: For short bunches, button BPMs have to be small and can therefore deliver only a low signal strength. Stripline BPMs are well suited for short bunch observation because the signal propagation is considered in the design like for transmission-lines in microwave engineering. The azimuthal coverage of the stripline BPM can be larger than of a button type yielding an increased signal strength. Moreover, stripline BPMs have the characteristic of a directional coupler which is of great importance for the installation in a collider of counter-propagating beams within the same beam pipe: With stripline BPMs one can distinguish between the directions of beam propagation and can record only the position from one beam by suppressing the signal from the counter-propagating beam, as explained below. The electrical properties of such a BPM are comparable to a directional coupler used for microwave devices [102].

A stripline pick-up consists of a transmission line of several cm length, having at both ends a feed-through with an impedance of R_1 and R_2 matched to 50 Ω, see Fig. 5.21. The stripline of length

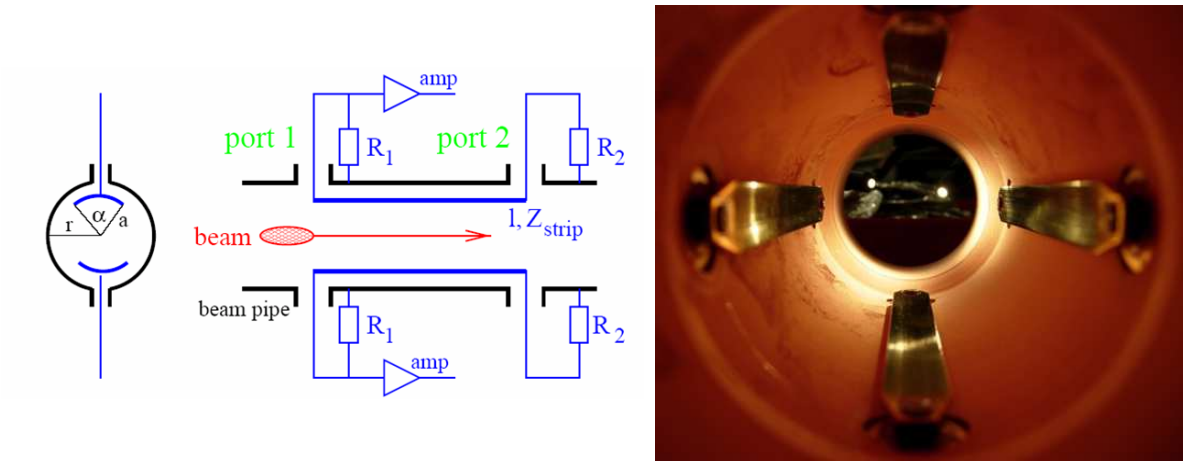

Figure 5.21: Left: Scheme of a stripline pick-up. Right: Photo of the LHC stripline BPM of 12 cm length, from [96].

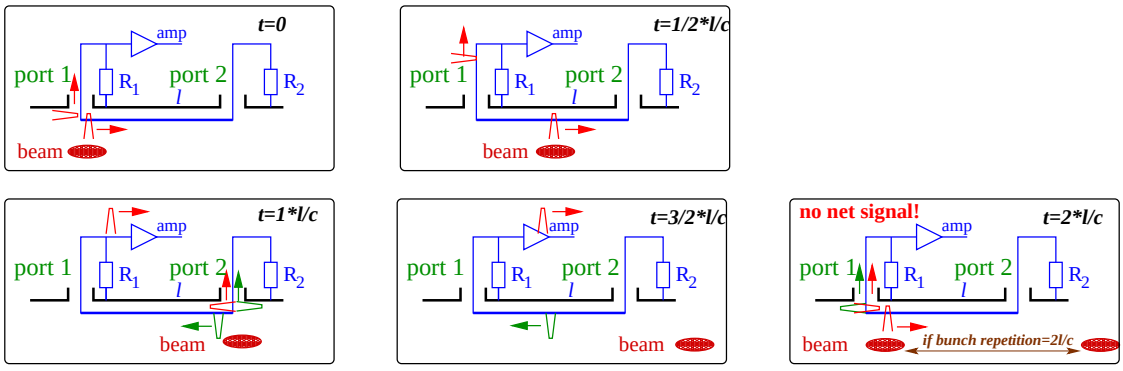

Figure 5.22: Four plots visualize the signal generation at a stripline BPM. The plot on the lower right shows the signal cancellation in case of a bunch repetition by $t = 2l/c$.

l is installed at a distance a from the beam center covering an angle of α within a cylindrical vacuum chamber of radius r. The characteristic impedance Z_{strip} of this strip depends on the parameters r, a and α, like for a micro-strip line on a printed-circuit board [102]. It is chosen to be $Z_{strip} = 50\ \Omega$ for matching the characteristic impedance at the two ports, i.e. the condition $Z_{strip} = R_1 = R_2 = 50\ \Omega$ is fulfilled. Further on, we assume that the beam is relativistic and can be approximated by a traveling TEM wave with velocity v_{beam}, which equals the signal propagation on the strip $c_{strip} = v_{beam} = c$. The bunch length should be shorter than the strip length to prevent signal overlapping. The signal generation at the upstream port 1 during the bunch passage is visualized in Fig. 5.22 and described in the following:

- At $t = 0$ the bunch passes the front edge of the strip. The wall current is divided in two parts due to the matching of the voltage divider $Z_{strip} = R_1 = 50\ \Omega$. Half of this signal travels towards port 1 and half travels downstream along the stripline.
- During $0 < t < l/c$ the beam and the signal travel in phase according to the condition $c_{strip} = v_{beam} = c$.
- At $t = l/c$ the bunch reaches the upstream port 2. Here the image charge leaves the stripline, generating an equal amplitude but opposite sign of current which is split in two halves according to $Z_{strip} = R_2 = 50\ \Omega$. However, the image current is leaving the detector and has the opposite sign to that generated at the upstream port. Therefore, half of the signal cancels the initially generated signal at port 1. The other half travels now back towards the upstream port 1.
- At time $t = 2 \cdot l/c$ the back traveling signal generated at port 2 reaches the upstream port 1.
- If the bunch repetition time of the bunches is $t_{acc} = 2 \cdot l/c$ the reflected, inverted signal from the first bunch cancels the signal from this second bunch.

This ideal behavior has two important consequences: Firstly, there is no signal at the upstream port 2 for a beam propagating in the described direction. For a second beam traveling in opposite direction, the roles of the ports are interchanged, which enables the separation of signal from counter-propagating beams like in colliders; this is not possible for other types of BPMs. However, due to imperfections of the mechanical and electrical realization, the suppression of the counter-propagating signals (i.e. signal strength at port 2 compared to strength at port 1) is typically 20 to 30 dB, i.e. the voltage at port 2 is lower by a factor 10 to 30. Secondly, the voltage signal for the ideal case at port 1 is given by

$$U_1(t) = \frac{1}{2} \cdot \frac{\alpha}{2\pi} \cdot R_1 \left(I_{beam}(t) - I_{beam}(t - 2l/c) \right) \quad . \tag{5.45}$$

Inserting a Gaussian bunch distribution as $I_{beam}(t) = I_0 \cdot \exp(-t^2/2\sigma_t^2)$ this equation can be written as

$$U_1(t) = \frac{Z_{strip}}{2} \cdot \frac{\alpha}{2\pi} \left(e^{-t^2/2\sigma_t^2} - e^{-(t-2l/c)^2/2\sigma_t^2)} \right) \cdot I_0 \quad . \tag{5.46}$$

This voltage signal at port 1 is shown in Fig. 5.23 for several bunch durations σ_t.

The related transfer impedance Z_t is obtained from the Fourier transformation of such a stripline BPM to be

$$Z_t(\omega) = Z_{strip} \cdot \frac{\alpha}{4\pi} \cdot e^{-\omega^2\sigma_t^2/2} \cdot \sin(\omega l/c) \cdot e^{i(\pi/2 - \omega l/c)} \tag{5.47}$$

and is shown in Fig. 5.23. For a short bunch it shows the following features:

- $|Z_t|$ is composed of a series of maxima for $f_{max} = \frac{c}{4l} \cdot (2n-1)$ for $n = 1, 2, ...$
- For a given acceleration frequency f_{acc}, the length l must be chosen to work close to such a maximum. The first maximum is located at $l = \frac{c}{4f_{acc}} = \lambda/4$, with λ being the 'wave length' of the bunch repetition. Due to this behavior such BPMs are also called quarter wave couplers.
- The sensitivity is zero for $l = n \cdot \lambda/2$. This means no signal is present when the spacing between bunches is equal to $2l$ due to the destructive interference between consecutive bunches.
- The phase φ as a function of frequency is built of straight lines with a zero phase shift at the maxima locations for $l = (2n-1) \cdot \lambda/4$. For those frequencies, the recorded signal is a direct image of the bunch. In contrast to capacitive pick-ups, short bunches can be monitored without significant signal deformation close to these frequency locations.

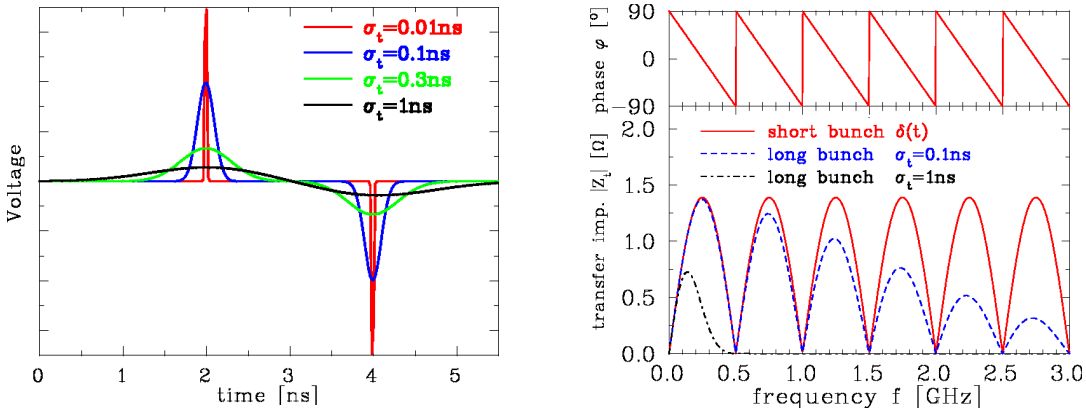

Figure 5.23: Left: Calculation of a voltage signal at the upstream port of a stripline BPM of $l = 30$ cm and a coverage of $\alpha = 10^o$ for different bunch durations σ_t. Right: The corresponding transfer impedance.

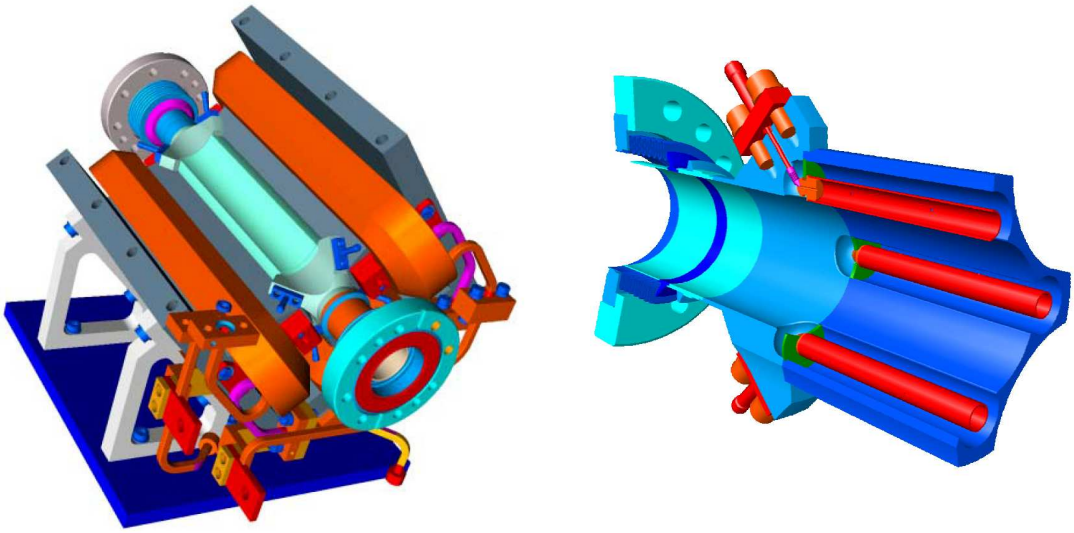

Figure 5.24: Technical drawing of the stripline BPM installed inside a quadrupole magnet at TTF2 (left) and the design of the transition for the strip to the feed-through (right). The beam pipe has Ø 34 mm, from [103, 104].

For a finite bunch duration σ_t, the transfer impedance decreases for increasing frequencies as given by the term $|Z_t| \propto e^{-\omega^2\sigma_t^2/2}$ in Eq. 5.47. This is related to the fact that the overlap of direct and reflected signals leads to destructive interference. For a bunch length comparable to the stripline length, even the first maximum of the transfer impedance can be effected. However, in most cases the length of the stripline can be chosen with the objective of avoiding signal damping.

The position sensitivity of the four strips of such BPM can be calculated in the same way as for button types, see Eq. 5.40 and 5.41. In the case of low beam current, the azimuthal coverage α can be enlarged to intercept more image current leading to an increased signal amplitude without too much signal distortion. However, the characteristic impedance of the strips has to be kept to $Z_{strip} = 50\ \Omega$, resulting in an increased mechanical size of the beam pipe. Moreover, the signal propagation towards the feed-through has to fulfill this matching condition. Even for smaller azimuthal coverage, the electrical transition for the strips to the coaxial vacuum feed-through has to be designed carefully obeying sensitive radio-frequency and mechanical requirements. The realization of a stripline BPM is more complex compared to the button type. An example of the technical design [103] for the electron LINAC at TTF2 is shown in Fig. 5.24. The striplines can be installed inside a quadrupole magnet reducing the insertion length for the BPM installation.

The basics of stripline BPMs are summarized in Table 5.2 and compared to the button type. Due

Table 5.2: Simplified comparison between stripline and button BPM

	Stripline BPM	**Button BPM**
Idea for design	traveling wave	electro-static
BPM size (typical)	length: 5 to 30 cm per plane transverse coverage up to $\alpha \simeq 70^0$	Ø 0.5 to 3 cm signal deformation for larger Ø
Signal quality	minor deformation	possible deformations due to finite size and capacitance
Signal strength	large depending on trans. coverage	small
Bandwidth	nearly broadband with well defined minima	high-pass with $f_{cut} \simeq 3$ GHz
Requirement	careful 50 Ω matching	50 Ω more easy achievable
Mechanical realization	complex	simple
Installation	inside quadrupole possible	compact due Ø $\leq$ 3 cm
Directivity	**yes**	no

to the precise matching condition required for the stripline type, the technical realization is complex. Besides the possibly larger signal strength and bandwidth, the main advantage of stripline BPMs is their directivity, which is necessary at any collider with counter-propagating beams in a common beam pipe.

For the position measurement other techniques are used in addition, including monitors measuring the magnetic field with so-called inductive pick-ups or the excitation of cavity modes within a so-called cavity BPM. Further descriptions and citations can be found in [85, 87, 88, 108].

5.9 Electronic treatment for position determination

To get the position of the beam, the signals from the electrodes have to be compared. For this comparison, the signal shape (differentiation or proportional behavior) is of minor importance. The electronics used for this purpose are described only briefly in this contribution; a detailed review is given in [105, 106]. For the position resolution, the signal-to-noise ratio is essential. Besides the stray fields from the rf cavities, the broadband amplifier noise, as well as the electronic noise of the following devices contribute. Therefore a minimum bunch current is needed for a reliable position measurement. Two different principles are commonly used based on analog electronics, the so-called broadband and narrow-band processing:

Broad-band processing: In the broadband case, as shown in Fig. 5.25, the signals from the individual plates are amplified (or even attenuated) to adapt the signal strength to the ADC input level. The sum and difference signal is then calculated from the digitized values. For noise reduction and alias-product suppression, a low-pass filter is used matched to the sample rate of the ADC. In older installations, fast sampling was not possible and an external trigger, as generated from the bunch passage in an analog manner forced the digitalization. In many applications, the sum and difference voltages are analogously generated by a 180^o hybrid or a differential transformer. Because they are purely passive devices, they can be mounted quite close to the BPM plates even in case of high radiation. The resulting sum and difference signals are then stored in the ADC. The difference signal, which is usually lower by at least a factor of 10, can be amplified by a higher amount than the sum signal to exploit the full ADC range. (An overview of standard rf components can be found in [107].) The analog electronics is required to match the signal shape to the properties of the ADCs, and an appropriate trigger is used for the digitalization. Modern installations do not use these types of analog electronics, instead the signal is directly digitized by a fast ADCs or digital receivers, which are even commercially available [109]. With the help of high-speed digital signal processing the bunch signal is then reduced to one value per bunch, and the beam position is calculated from the sum and difference value, see e.g. [110]. The precision of this method is lower as compared to the narrow-band processing described below. For electron machines, with small beam size, a resolution of 100 μm can be achieved by this broadband processing. The advantage is the possibility to perform a bunch-by-bunch analysis (i.e. measuring the position of always the same bunch rotating in a synchrotron) by

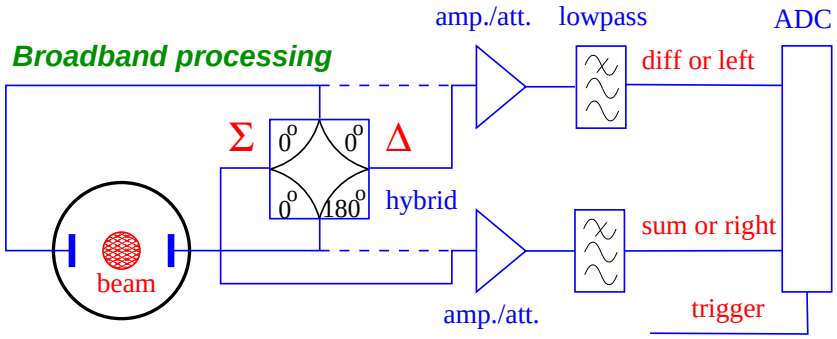

Figure 5.25: Scheme of a broadband signal processing. The plate signals are either fed directly to the amplifier (dashed line) or via a hybrid the sum and difference is generated in an analog manner (solid line).

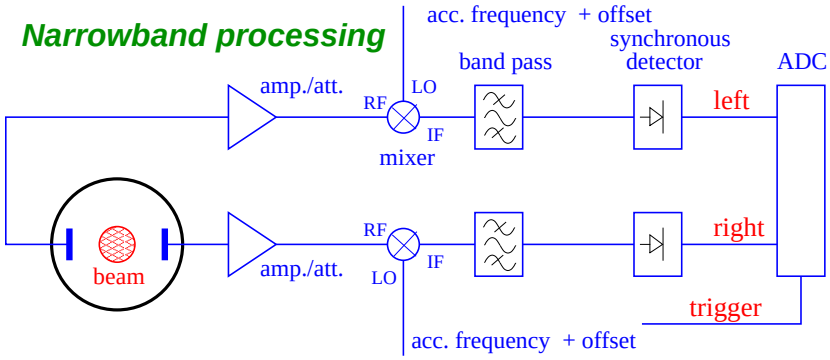

Figure 5.26: Schematic signal analysis for a narrow-band treatment.

using an appropriate trigger setting or precise digital signal processing. The broad-band scheme is installed at transfer lines between synchrotrons where only one or few bunches are transferred. A further modification often installed at transfer lines is the use of logarithmic amplifiers where an order of magnitude increase of input signal is converted to a linear increase of the output signal; they are commercially available e.g. [5]. The advantage is that a large dynamic range can be covered by a single amplifier stage without range switching. The disadvantage is the lower achievable accuracy, which is often accepted at transfer lines.

Narrow-band processing: The narrow-band processing is used to get a higher precision of the position reading, attaining 1 μm in electron machines by this electronics scheme. The better signal-to-noise ratio is achieved by reducing the bandwidth of the signal processing by several orders of magnitude. As an illustrative example the Fourier-Transformation of the signal from the GSI-LINAC pick-up is shown in Fig. 5.27. The spectral power of the signal is mainly available at the bunch repetition harmonics nf_0. The position evaluation uses only this large signal power within the band of frequency span Δf, while the thermal noise is reduced as $U_{eff} \propto \sqrt{\Delta f}$. Technically, the pick-up signal is mixed with the accelerating frequency. A mixer is a passive rf-device multiplying the two waves at the port RF (for radio frequency) and LO (for local oscillator). The product is available at port IF (for intermediate frequency). From a mathematical point of view, the mixer multiplies the two waves at LO and RF and we get from a trigonometric theorem [2]

$$A_{IF}(t) = A_{RF}{\cdot}A_{LO}\cos\omega_{RF}t{\cdot}\cos\omega_{LO}t = \frac{1}{2}A_{RF}{\cdot}A_{LO}\left[\cos(\omega_{RF}-\omega_{LO})t + \cos\left(\omega_{RF}+\omega_{LO}\right)t\right]. \quad (5.48)$$

Typically 10.7 MHz, or one of its harmonics (due to it's large use in telecommunication), is filtered out by a narrow band-pass filter. The signal is rectified by a so called synchronous detector, for which the schematics are shown in Fig. 5.28 having the following functionality: The rf signal is split and one branch is fed into a limiter amplifier driven into saturation, which transforms the signal to a bipolar rectangular pulse. This signal is mixed with the original signal to yield a unipolar waveform

[2] $\cos x \cdot \cos y = 1/2 \cdot [\cos(x-y) + \cos(x+y)]$

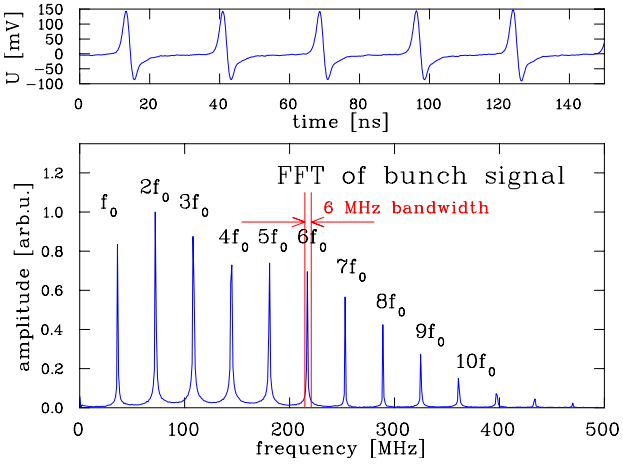

Figure 5.27: Bunch signal (top) and its Fourier transformation (bottom) at the GSI-LINAC of a 1.4 MeV/u beam. In the Fourier spectrum each line corresponds to the indicated harmonics of the 36 MHz accelerating frequency. The position evaluation is done at $6f_0 = 216.8$ MHz by a 6 MHz narrow-band processing as indicated by the red lines.

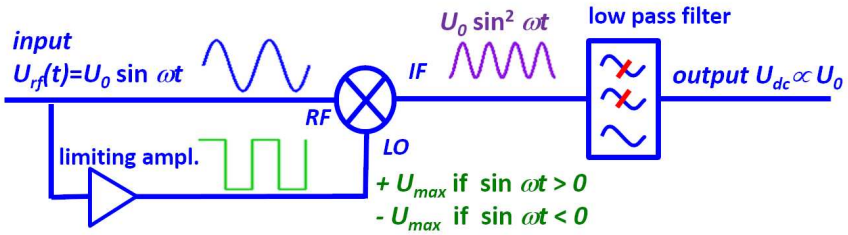

Figure 5.28: Scheme of a synchronous detector to rectify an rf signal.

(corresponding to the square). It is passed then through a low-pass filter. The resulting quasi-dc signal is then digitized by an ADC, and the position is calculated via software. In general, this technique is called heterodyne mixing, and the same principle is used in a spectrum analyzer. The mixing is equivalent to an average over many turns leading to much higher precision in the position reading. However, this method does not allow a turn-by-turn observation. For a synchrotron with varying acceleration frequency e.g. a proton synchrotron for non-relativistic velocities, this method can also be applied because the varying accelerating frequency is changed in phase with the bunch signal, resulting in a constant intermediate frequency. Such a system is commercially available [111].

The methods discussed above perform the BPM signal conditioning in an analog manner; for most cases, it leads to a low bandwidth output, which is then digitized with a slow sampling ADC. Motivated by the intensive use in telecommunication, the properties of ADCs in terms of sampling rate and voltage resolution were significantly improved during the last decade; an overview on ADC technology can be found in [112]. Additionally, the digital signal processing capabilities were enhanced. Modern technologies tend to digitize the signal on an early stage of the signal path and replace the analog conditioning by digital signal processing, e.g. performing the narrow-band treatment in the digital domain. In most cases, the required parallel processing is realized on an FPGA basis (Field Programmable Gate Array) to ensure fast, real-time response. On this digital basis, versatile treatments can be implemented without any hardware exchange [113] leading to higher flexibility for the application. An example is the filtering of one data set with different bandwidths to match the position and time resolution to the requirements; such digitalization and processing units are commercially available [109]. The related methods compared to the analog treatment are reviewed in [106].

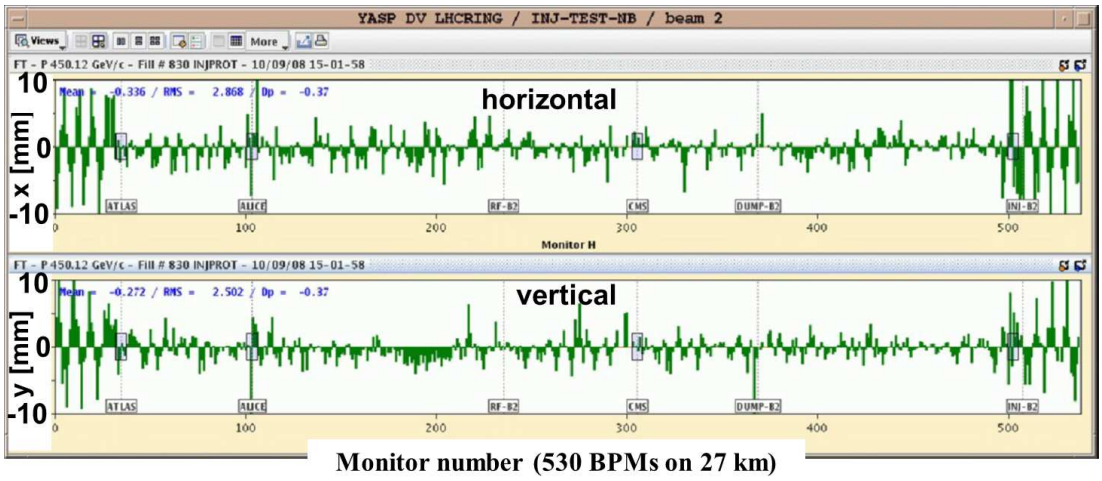

Figure 5.29: Measurement of the trajectory of a single bunch injected in the LHC with a position display at the 530 BPMs around the synchrotron, from [114].

5.10 Trajectory measurement

With the term trajectory, the position of a single bunch during its transport through the accelerator is meant, and it is the basic information of the initial alignment of the accelerator setting. Because the single bunch position is monitored, a broadband processing for the BPM electronics is used; the reduced position resolution is of minor concern for this measurement. As an example Fig. 5.29 depicts the measurement of the trajectory of a single bunch injected into the LHC at the first days of its commissioning [114]. The position reading at each of the 530 BPM on the 27 km long synchrotron is displayed showing some oscillations caused by mismatched injection parameters, which could be aligned later on with the help of this diagnostics. The same type of measurement can be done at LINACs and transport lines in case an appropriate electronics chain is installed. For the transfer between synchrotrons, only a few bunches are transferred in most cases, and a broadband processing chain is installed there.

5.11 Closed orbit measurement at a synchrotron

In a synchrotron, several BPMs for the determination of the closed orbit are installed. As a rule of thumb, an appropriate choice is to have four BPMs per tune value separated approximately by about $\mu \simeq 90^o$ betatron phase advance. The pick-ups should be located at position with a large value of the betatron function to have a reasonable spatial resolution even for smaller average beam excursions. The closed orbit is the central beam path along the machine, taking existing imperfections into account. The closed orbit might differ from the ideal path, defined by the center of the quadrupole magnets. Only for a good alignment, the real beam behaves as expected from beam optics calculations, e.g. no beam steering by the quadrupole magnets occurs. An example of the use of position measurement is displayed in Fig. 5.30 during the acceleration in the GSI synchrotron.

The position reading of the BPMs around the ring can be used as the input of a feedback loop to do an active beam correction, see e.g. [115]. Such a feedback system is installed in most synchrotrons, but a description is out of the scope of this lecture.

5.12 Tune measurement

One essential parameter of a synchrotron is its tune. For machines running at high current, the incoherent tune spread, related to the space charge of the beam, is of interest to find a large stable region in the working diagram. For these parameters, the tune as a function of stored current has to be evaluated. Pick-ups measure the center of the bunched beam. First we define the betatron frequency f_β as

$$f_\beta = Q \cdot f_0 \tag{5.49}$$

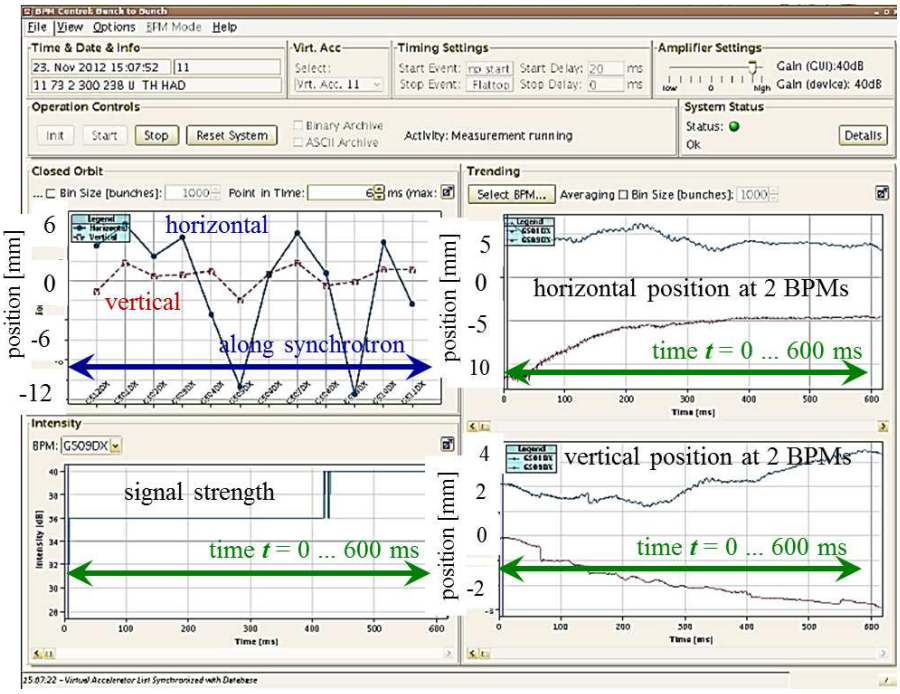

Figure 5.30: Example of a position measurement done at the GSI synchrotron for a partly misaligned beam during a 0.6 s long acceleration. The upper left top plot shows the position around the ring at 12 locations at the begin of the ramp; the upper right plot shows the horizontal position during the acceleration ramp for two BPM locations, the lower right plot the vertical position for these BPMs; the lower left plot is a signal power $\propto U_\Sigma^2$ during the ramp for a single BPM. The panel at the top is used for the control of pre-amplifiers and timing.

as the tune Q expressed in relation to the revolution frequency f_0. The tune itself is the number of betatron oscillations per turn. The principle of a tune measurement related to position determination by pick-ups is to excite a coherent transverse betatron oscillation, whose frequency gives the value of the tune.

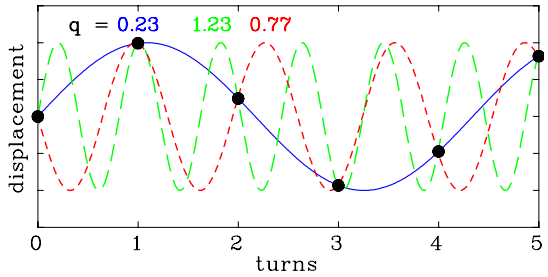

Figure 5.31: Schematic of the tune measurement for six subsequent turns determined with one pick-up, together with with the three lowest frequency fits.

The tune value can be split in two parts as $Q = Q_n + q$ with Q_n is the integer part and q fractional part; most measurement methods can only determine the fractional part q. The integer number of oscillations Q_n cannot be seen, but this is normally of no interest, as it is known from calculations. This behavior is schematically shown in Fig. 5.31 for the case of a turn-by-turn reading of one pick-up: Having the position reading, a sine function can be fitted through the data, but one cannot distinguish between the lowest frequency (here $q = 0.23$) and higher values, leading to the fact that the fractional part is only uniquely defined for $0 < q < 0.5$. To distinguish between a value below or above 0.5, the focusing by the quadruples (i.e. the tune) can be slightly changed and the direction of the shift of q can be observed. The calculation of q is done by a Fourier analysis of the time domain data.

Most methods used today are based on a frequency domain treatment [116]. Before discussing

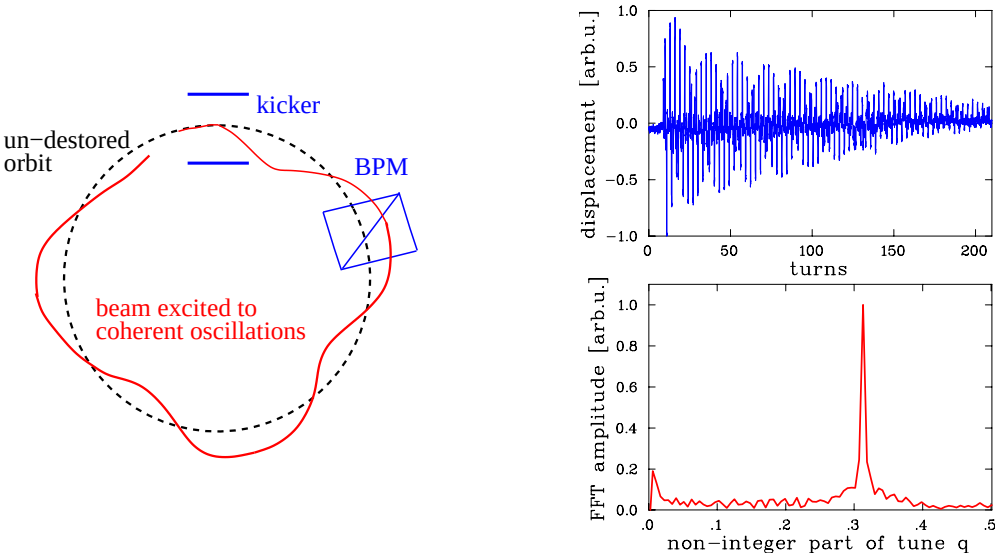

Figure 5.32: Left: Scheme of the beam excitation and detection of coherent bunch oscillations by a BPM. Right: Beam oscillations after a kick excitation recorded in the time domain for 200 turns (top) and its Fourier transformation for q determination (bottom) at the GSI synchrotron.

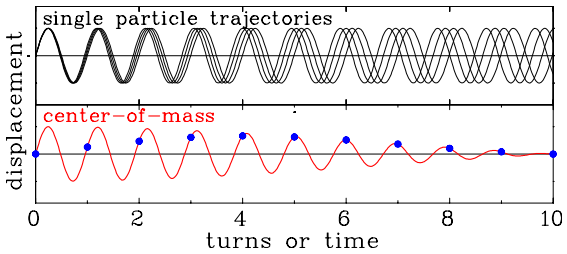

Figure 5.33: Plot of the individual trajectories of four particles after a kick (top) and the resulting coherent sum signal as measured by a pick-up (bottom). (The tune spread is much too large for a real machine.)

this, a more straightforward excitation method is described first, using a time-domain point of view.

5.12.1 The kick method, time-domain method

For this method, coherent betatron oscillations are excited by a fast kick. This kick has to be much shorter than the revolution time $1/f_0$ and is provided in most cases by the injection or extraction kicker installed in the machine anyhow. The strength of the kick has to be chosen with care, so the beam is not lost. To acheive a reasonable resolution, the pick-up should be located at a lattice point with a large value of the betatron function. The beam position is monitored turn-by-turn (broadband processing only), and it is stored as a function of time. The Fourier transformation of the displacements gives the fractional part q of the tune. An example from the GSI synchrotron is shown in Fig. 5.32.

To understand the limitation of this method, one has to look at the single particle behavior. At the time of the kick, the particles start a free betatron oscillation with the same phase, but each particle has a slightly different betatron frequency due to the tune spread. Even if the individual oscillations last for a long time, the coherent motion detected by a pick-up is damped as a consequence of the de-coherence of the individual motion given by the time of the inverse betatron frequency spread, see Fig. 5.33. A description is given in the frame of Landau damping. This damping as given by the de-tuning of the transverse oscillation limits the observation time and therefore the precision of the tune determination by this method. The tune is calculated from the position reading via Fourier transformation: A limited series of position measurements $x_1, x_2, ..., x_N$ of N consecutive turns with non-vanishing displacements are taken into account. The distribution function of the tune $P(q_i)$ is

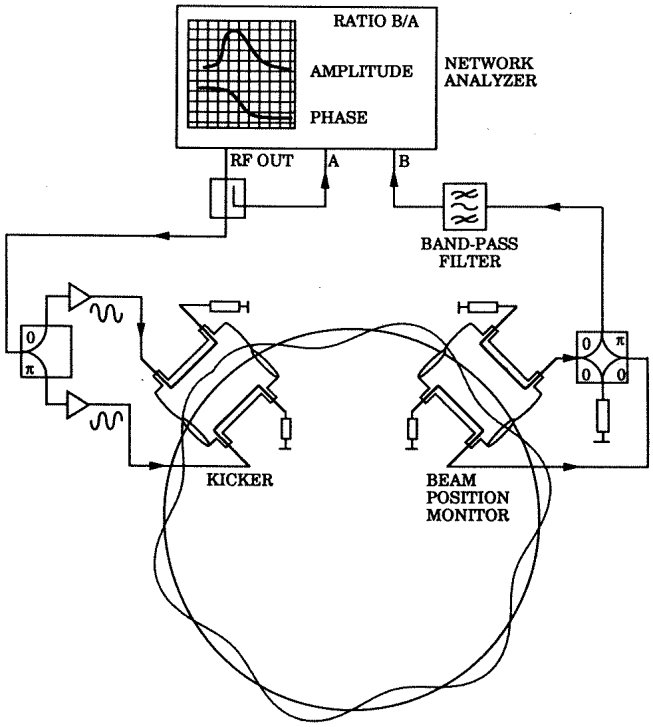

Figure 5.34: Scheme of a beam transfer function (BTF) measurement.

calculated via discrete Fourier expansion from the displacement reading via [117]

$$P(q_i) = \frac{1}{N} \sum_{n=1}^{N} x_n e^{-2\pi i n q_i} \quad . \tag{5.50}$$

As given by the properties of Fourier transformations, the discretization of the obtained peak is generally related to the number of position samples N by [116, 117]

$$\Delta q = \frac{1}{2N} \quad . \tag{5.51}$$

Therefore the peak in the distribution function $P(q_i)$ has at least this width. To achieve an adequate resolution of typically $\Delta q \simeq 10^{-3}$, at least $N = 500$ turns of non-vanishing displacements are needed. In a lot of practical cases, the de-coherence time is shorter than this border as demonstrated in Fig. 5.32. Therefore this straightforward method is not very precise. However, there exist some improved analysis methods using digital filters to achieve better precision, see e.g. [118].

An additional drawback of such a measurement is a blow-up of the transverse emittance of the stored beam, because the excitation of the individual particles are damped much slower than the coherent motion as depicted in Fig. 5.33. This method can thus be used for electron synchrotrons, where the particle's motions are damped relatively fast by synchrotron radiation (typical time scale of seconds), and the tune resolution requirement is not more than typically 10^{-3}.

5.12.2 Beam transfer function measurement by a frequency chirp

For this method, an rf method for tune determination uses a beam excitation driven by a continuous sine wave stimulus. This wave is swept slowly within seconds over a certain band, and the response of the beam is measured in coincidence. The device used in rf engineering for this purpose is a network analyzer, see [119]. It provides a frequency scan over a user-given range, which is amplified and applied to the beam via an rf exciter. The exciter is built like a pick-up. The normalized difference signal U_Δ/U_Σ from the pick-up is fed to the input of the network analyzer, as shown in Fig 5.34. Here the amplitude and phase relative to the excitation are measured precisely and displayed. The horizontal axis of the display corresponds to the frequency band for the beam excitation. The displayed spectrum

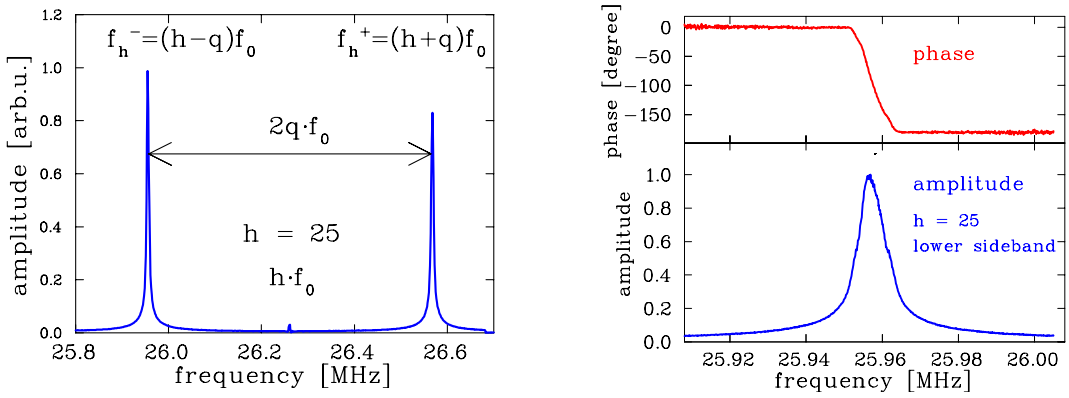

Figure 5.35: BTF measurement at the GSI synchrotron with a 500 MeV/u U^{73+} beam having a revolution frequency of $f_0 = 1.048$ MHz. The wide scan around the $h = 25^{th}$-harmonics is shown left and a scan around a lower sideband centered at f_{25}^- on the right for amplitude and phase. The fractional tune is $q = 0.306$ for these data.

represents the **B**eam **T**ransfer **F**unction **BTF**, which can be defined as the transverse velocity response to the given acceleration by the kicker. Besides the name BTF measurement, this method is sometimes called 'beam excitation by a frequency chirp'.

Due to practical reasons, a harmonics of the revolution frequency f_0 is used for the excitation, and the resulting resonance line is expressed in terms of these harmonics. An example of such a measurement with an excitation around the $h = 25^{th}$ revolution harmonics is shown in Fig. 5.35. The beam reacts as a driven oscillator with a resonance as given by the tune value. Because only the fractional part can be measured, this resonance is located at $f_h^{\pm} = (h \pm q)f_0$ on both sides of the revolution frequency and are called lower and upper sideband. From the distance of the sidebands, the fractional part of the tune q is determined. The resonance nature of the BTF measurement can also be seen from the phase shift of 180^o during resonance crossing, as shown in on the right side of Fig. 5.35. An analytic expression for the BTF can be found in [120] based on the theory of a driven oscillator including Landau damping. From the width of a sideband the tune spread can roughly be estimated as $\Delta q \simeq \frac{\Delta f}{h f_0}$. For a more detailed evaluation of the sideband-width for beams with low space charge contributions, i.e. for the validity of linear beam optics, one has to take the longitudinal momentum into account, resulting in a more complex description of the sideband width (see Eq. 7.24) as discussed in the frame of transverse Schottky analysis in Chapter 7; due to the driving force for BTF measurements, the signal strength is several orders of magnitude higher as compared to a Schottky scan.

With this method, a high precision of the tune value q up to 10^{-4} can be reached. Such a measurement might take some time (up to several minutes) because the frequency has to be swept, and the response to one single frequency is measured at a given time. The resolution is determined by the sweep velocity, i.e. a slow sweep yields a better resolution. In addition, the sweep velocity has to be slow enough to allow the transient beam response dying out and a steady-state response to be attained. Using a sensitive pick-up electronics, the measurement can also be done with an un-bunched beam.

5.12.3 Noise excitation of the beam

Instead of single frequency excitation, a wide-band rf signal can be applied. The beam is excited by the same frequency spectrum as delivered by a network analyzer. However, here the excitation takes place for all frequencies at the same time, using white noise of adequate bandwidth being larger than the tune variation. The position reading is done in the time domain using a fast ADC recording each bunch. The position data for each bunch are Fourier analyzed, and the spectrum is drawn corresponding to the tune value. An example is shown in Fig. 5.36 from the GSI synchrotron during acceleration [121]. The resolution for the tune is given by the inverse of the averaging time for one FFT calculation (for the data in Fig. 5.36 in the order of some ms, corresponding to 4096 turns), leading to about $\Delta Q \sim 3 \cdot 10^{-3}$ for one single scan. Due to the band excitation a time resolved observation of the tune is possible during the entire acceleration ramp.

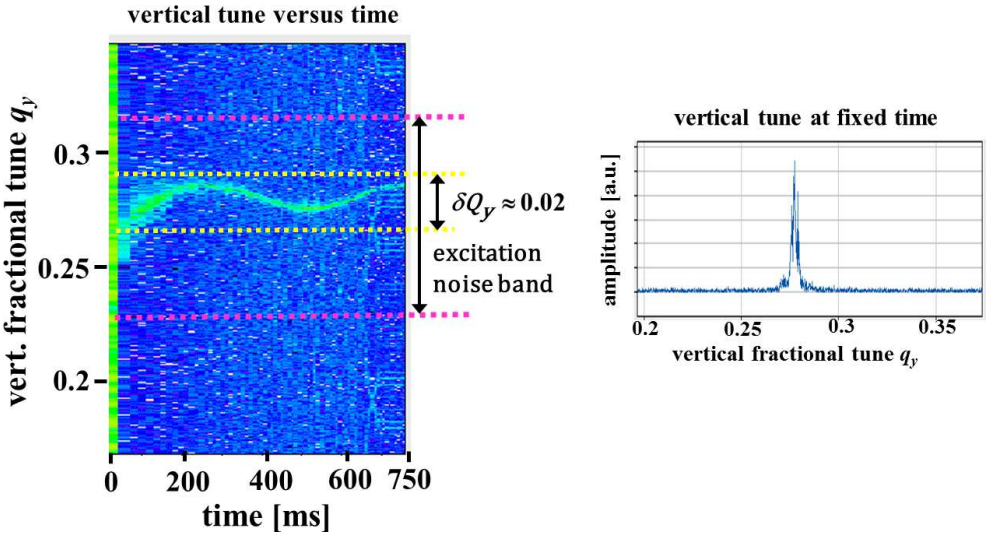

Figure 5.36: Left: Measurement of the tune at the GSI synchrotron for an Ar^{10+} beam accelerated from 11 to 300 MeV/u within 0.75 s [121]. Displayed is the Fourier transformation of displacements of successive individual bunches over 4096 turns excited by the depicted noise band during acceleration as a function of time. The maximum of the Fourier transformation is color-coded in a linear manner; δQ_y is the variation of the tune value. Right: Single tune spectrum 110 ms after the ramp start averaged over 4096 turns corresponding to $\sim$ 15 ms.

5.13 Measurement of lattice functions

The technique of beam excitation can also be used to determine parameters of the so-called lattice functions as calculated by the beam optics. In particular, local values of dispersion and beta-function as well as the global quantity chromaticity has been measured with this technique. A knowledge of these parameters is of importance during the commissioning of a new machine, the control of mechanical misalignment, as well as a check of critical settings, e.g. close to a low-beta insertion. If required, the values of the local lattice function can be corrected by applying correction magnets inside the synchrotron.

The dispersion function $D(s)$ at a position s in the synchrotron is defined as

$$x(s) = D(s)\frac{\Delta p}{p} \tag{5.52}$$

with $x(s)$ being the displacement for a given momentum deviation Δp from the nominal momentum p. The dispersion function $D(s)$ can be determined at the pick-up location s by a slight momentum change of the beam with the help of a frequency detuning of an accelerating cavity while keeping the setting of all magnets constant, which leads to small acceleration or deceleration of all particles. For several momentum settings Δp a position measurement x with the BPM is performed. The resulting position measurements x are then plotted as a function of the momentum deviation $\Delta p/p$ and D at the BPM location is given by the slope of this curve.

Having a turn-by-turn readout of several pick-ups, the coherent betatron oscillation of a single bunch can be monitored. The position reading at a pick-up i located at s_i for turn number k is given by

$$x_{ik} = \hat{x}_i \cdot \cos\left(2\pi Q k + \mu_i\right) = \hat{x}_0 \cdot \sqrt{\frac{\beta(s_i)}{\beta(s_0)}} \cos\left(2\pi Q k + \mu_i\right) \tag{5.53}$$

with $\hat{x}_i$ the amplitude at the pick-up i, $\hat{x}_0$ the amplitude at a reference pick-up at s_0, $\beta(s_i)$ and $\beta(s_0)$ the beta-functions at these pick-ups, Q the tune and μ_i the betatron phase at s_i with respect to the reference location.

The ratio of the beta-functions can be determined by a comparison of the amplitudes at these two

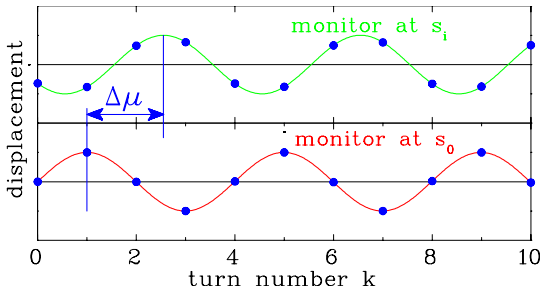

Figure 5.37: Scheme of the individual measurements at two pick-ups for a phase advance $\Delta\mu$ determination. A sine function can be fitted through the data points.

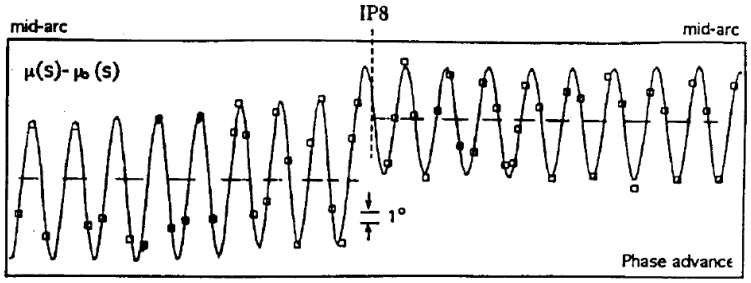

Figure 5.38: Result of a betatron phase measurement at LEP. The difference of the measured phase $\mu(s)$ and the calculated phase $\mu_0(s)$ for the linear optics model is shown for each BPM location around the interaction point IP, from [122].

locations

$$\frac{\beta(s_i)}{\beta(s_0)} = \left(\frac{\hat{x}_i}{\hat{x}_0}\right)^2 . \tag{5.54}$$

The accuracy of such a measurement might not be too good, because the absolute calibration of the pick-up enters the calculation.

The phase advance between two locations can be determined by this measurement as

$$\Delta\mu = \mu_i - \mu_0 \tag{5.55}$$

with a high accuracy by fitting a sine function to the measured data, as schematically plotted in Fig. 5.37. This leads to another way of beta-function measurement using the betatron phase difference $\Delta\mu$ between the two locations s_0 and s_i using the relation

$$\Delta\mu = \int_{s_0}^{s_i} \frac{ds}{\beta(s)} \quad , \tag{5.56}$$

where the measured value $\Delta\mu$ is compared to the result using the theoretical beta-function for the optical model of the synchrotron.

In Fig. 5.38 such a measurement is shown as recorded at the $e^+ - e^-$ collider LEP previously in operation at CERN [122]. The difference between the theoretical phase as calculated by the optical model using MAD code and the measured phase determined from 1024 turn for each BPM is plotted. The deviation is in the order of 10^o with an additional shift related to the strong focusing close to the interaction point, where a strong focusing is applied to achieve the luminosity at the collision point of the e^+ and e^- beams. Such deviations are caused by unavoidable mechanical and electrical mis-alignments of the magnets, for the depicted case it corresponds to less than 1 % of the nominal quadrupole settings. With the help of the correction dipoles and separate controllable quadrupoles, the betatron phase advance can be adjusted, and hence the β-function and the related beam size is controlled. Such measurements are of great importance to control the corrector setting and to achieve the nominal beam parameters in particular at circular colliders and synchrotron light sources. Advanced measurement techniques and analysis methods for the determination of beta-functions and further optics parameters are summarized in [123].

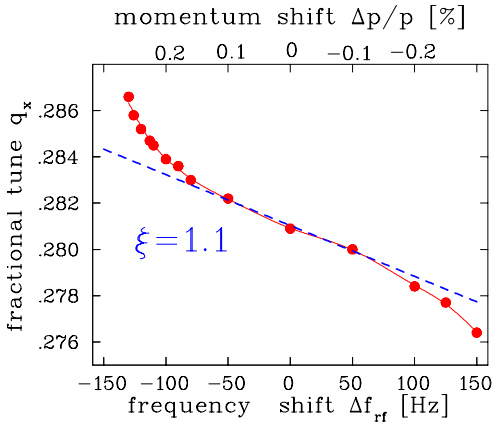

Figure 5.39: Measurement of the chromaticity at LEP. The horizontal tune is determined for different settings of the acceleration frequency and, therefore, of the momentum of the circulating beam. The chromaticity is fitted through the linear part of the data [125].

The focusing of a quadrupole is dependent on the particle momentum, resulting in a change of the tune for different momenta. It is described by the chromaticity ξ defined as

$$\frac{\Delta Q}{Q} = \xi \frac{\Delta p}{p} \quad . \tag{5.57}$$

This value can be determined directly by a slight momentum change using a detuned rf-frequency, i.e. the same procedure as described above for the dispersion function measurement. The tune is then measured as discussed above and plotted as a function of the momentum deviation; the value of ξ is given by the slope, as shown in Fig. 5.39. A linear behavior between $\Delta p/p$ and $\Delta Q/Q$ is only valid in a small momentum interval (here $\Delta p/p = \pm 0.1\%$). For larger deviations, non-linear forces from the synchrotron magnets contribute significantly. Instead of changing the rf-frequency, one can also change the magnetic field of the main dipole magnets, because this type of measurement is based on the detuning between ideal closed orbit and revolution frequency. The chromaticity can also be determined locally by comparing the measured betatron phase advance using Eq. 5.53 with the tune Q as a fit parameter (the beta-function has to be known of course). These measurements have to be repeated for different Δp. Examples of measurements and further references are given in [124].

Chapter 6

Measurement of longitudinal parameters

Longitudinal parameters are as important as the transverse ones. The longitudinal phase space is spanned by:

- The longitudinal spread of the bunch l is given in units of length (mm), time (ns) or phase (^{o} degrees with respect to the accelerating frequency), see Fig. 6.1. The mean value is the center of the bunch relative to the rf or relative to the ideal reference particle. The corresponding transverse value is the transverse beam profile. For an un-bunched dc beam, e.g. in a proton storage ring, the quantity is of no meaning.
- The momentum spread $\delta = \Delta p/p$ is the deviation relative to the momentum p of the ideal reference particle. Instead of the momentum it is sometimes common for proton or ion LINACs and cyclotrons to relate the quantity beam energy $\Delta E_{kin}/E_{kin}$ or even only ΔE_{kin} is given. The corresponding transverse value is the beam divergence.

The value of emittance ϵ_{long} is given by the the product of the two quantities

$$\epsilon_{long} = \frac{1}{\pi}\int_A dl d\delta. \tag{6.1}$$

where A is the area of the phase space occupied by the beam particles, see Fig. 6.1. Linear transformations can be applied in the same way as for the transverse case, see Chapter 4.1. The normalized longitudinal emittance

$$\epsilon_{long}^{norm} = \frac{v_s}{c}\gamma_{rel} \cdot \epsilon_{long} \tag{6.2}$$

is preserved under ideal conditions with v_s is the longitudinal velocity and γ_{rel} is the relativistic Lorentz factor.

Using a pick-up, the projection of the phase space on the time axis is determined, resulting in the bunch position and width. A determination of the emittance by linear transformation is possible. Some conditions have to be fulfilled for a capacitive pick-up to guarantee an adequate interpretation: First, the bunch has to be much longer in the longitudinal direction than the pick-up. For bunches with a length comparable to the pick-up, a second condition is that the beam must be sufficiently relativistic, to ensure that the beam's electric field is essentially transverse. For the transverse electric field component $\vec{E}_\perp$, relativity gives an enhancement in the lab-frame compared to the rest-frame of moving charge by

$$E_{\perp,lab}(t_{lab}) \simeq \gamma \cdot E_{\perp,rest}(t_{rest}) \quad , \tag{6.3}$$

see the more detailed discussion in Chapter 6.1, in particular concerning the transformation of the time t_{rest} to t_{lab} which is important for low energetic, non-relativistic particles, e.g. at proton LINACs. In the case of a slow beam from a proton/heavy ion LINAC, the last condition is not fulfilled, and other methods have to be applied. For bunches shorter than the capacitive pick-up, the signal does not reflect the longitudinal bunch shape. Stripline pick-ups can still be used. For electron beams, the bunch length is so short that the bunch structure is smeared out by integration on the pick-up

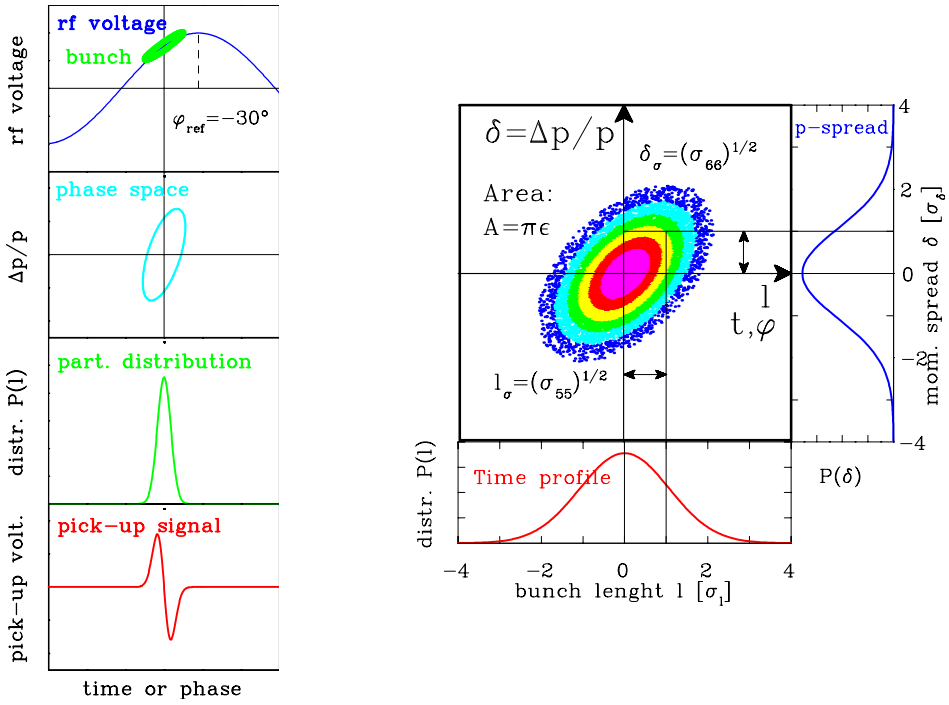

Figure 6.1: Left: The relation between the accelerating voltage and the longitudinal emittance as well as the time distribution of the bunches as measured with the differentiated pick-up signal. Right: The longitudinal phase space plot of a Gaussian distribution.

capacitance, i.e. expressed in terms of electrical parameters by the limited bandwidth. Here the monitoring of synchrotron radiation is used in connection with the fast optical method using streak cameras.

A measurement of the energy- or momentum spread $\delta = \Delta p/p$ is not discussed in detail here. A magnetic spectrometer can be used for this purpose, having a point-to-point focus in connection with small slits located at appropriate locations. This is discussed in textbooks on beam optics, e.g. in [126].

6.1 Electric fields of a relativistic charge

Due to the finite velocity of light, the electric field of a moving charge is modified as given by the Lorentz transformation. This effect for different velocities β of the moving charge is shown in Fig. 6.2, where the longitudinal electrical field $E_\parallel(t)$ in the lab-frame has been calculated for a single particle with a charge of $1e$ traveling in empty space measured according to the time in the lab-frame, i.e. $t_{lab} \equiv t$. It is calculated by the relativistic Lorentz-boost including the transformation of the time coordinate [12] to be

$$E_{\parallel,lab}(t) = -\frac{e}{4\pi\varepsilon_0} \cdot \frac{\gamma\beta ct}{\left[R^2 + (\gamma\beta ct)^2\right]^{3/2}} \tag{6.4}$$

R is the distance of closest approach and $\gamma = \left(1-\beta^2\right)^{-1/2}$ the relativistic Lorentz factor. The transverse field component $E_\perp$ in the lab-frame is given by

$$E_{\perp,lab}(t) = \frac{e}{4\pi\varepsilon_0} \cdot \frac{\gamma R}{\left[R^2 + (\gamma\beta ct)^2\right]^{3/2}} \quad . \tag{6.5}$$

The formula is a bit different from the simple one of Eq. 6.3 as $E_{\perp,lab}(t_{lab}) = \gamma \cdot E_{\perp,rest}(t_{rest})$ due to the additionally required transformation of the time coordinate $t_{rest} \rightarrow t_{lab}$. The above formulas are valid for a free particle and are modified by the boundary condition of the metallic surface e.g. of the beam pipe or the pick-up plates. A beam bunch consist of many particles distributed within a certain

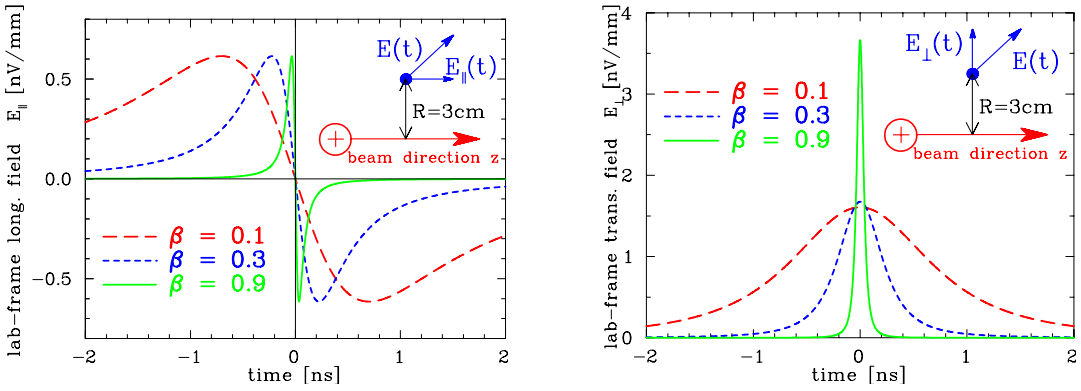

Figure 6.2: Effect of the advanced longitudinal (left) and transverse (right) electric field at an observation location $R = 30$ mm from the beam axis for different velocities of a point-like charge. For $t_{rest} = t_{lab} = 0$ the closes approach is reached.

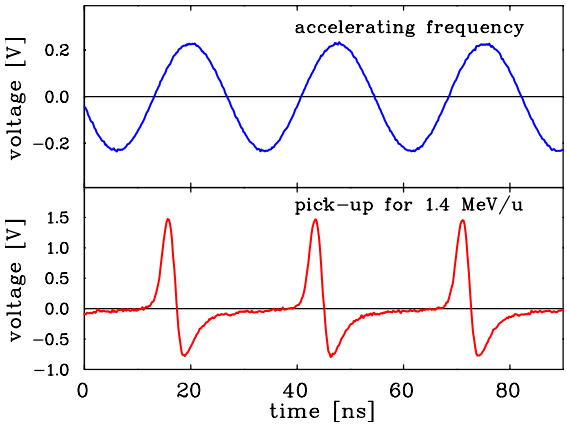

Figure 6.3: The LINAC module accelerating frequency (top) and the corresponding pick-up signal recorded by a capacitive pick-up (bottom) for the determination of the bunch zero crossing from a 1.4 MeV/u ion beam.

volume; to calculate the accompanying electric field, one has to integrate over the bunch volume. For low velocities the electric field arrives earlier at the pick-up and does not reflect the charge distribution of the bunch, see Chapter 6.7 for more details.

6.2 Determination of phase position

For the matching of successive LINAC modules, the right phase relation between the accelerating frequency and the bunch arrival has to be determined with a beam-based measurement. A typical plot is shown in Fig. 6.3 for a slow 1.4 MeV/u ion beam recorded by a capacitive pick-up as shown in Fig. 5.11. Due to the differentiated beam signal, the center of the bunch is well determined. There is an arbitrary, but fixed phase shift between the signal for the pick-up and the accelerating frequency f_{rf} due to the different cable lengths. The corresponding quantity concerning the transverse beam position is the center-of-mass of a bunch relative to the accelerating rf sine-wave.

6.3 Determination of non-relativistic mean energy

The final energy of a LINAC module is sensitive to the actual setting of the rf amplitude and the phase relative to the preceding modules. Therefore, energy determination is important. A measurement can be performed for non-relativistic energies using two pick-ups separated by the distance L and a **T**ime-**o**f-**F**light **ToF** measurement, see e.g. [50, 127]. As displayed in Fig. 6.4, two pick-ups are installed in a straight section with a typical distance of several meters. This distance L has to be known precisely, to

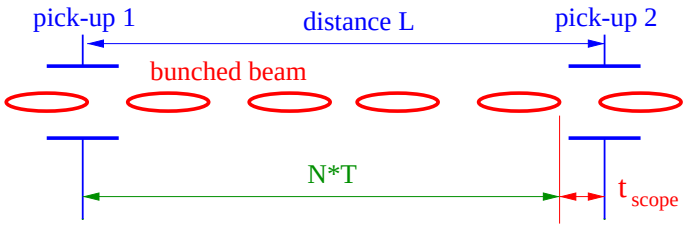

Figure 6.4: Principle of a ToF measurement using two pick-ups.

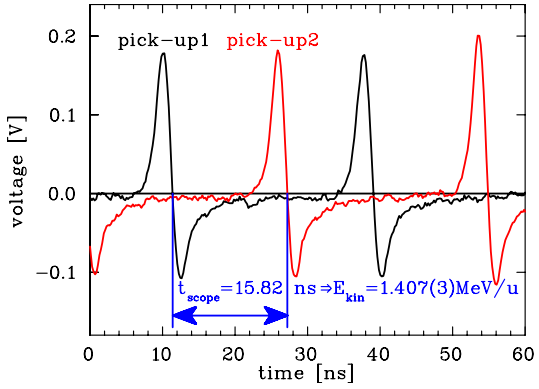

Figure 6.5: Time-of-flight signal from two pick-ups with $E_{kin} \simeq 1.4$ MeV/u at the GSI-LINAC. The frequency is $f_{rf} = 36.136$ MHz $\Leftrightarrow T = 1/f_{rf} = 27.673$ ns. For the distance of $L = 1.629$ m between the pick-ups $N = 3$ bunches are between the pick-ups. Inserting the time difference of $t_{scope} = 15.82$ ns in Eq. 6.6, the velocity $\beta = 0.05497(7)$ and the corresponding beam energy $E_{kin} = 1.407(3)$ MeV/u is calculated. The error is given by Eq. 6.7 inserting the uncertainties of $\Delta t = 0.1$ ns and $\Delta L = 1$ mm.

within 1 mm. The bunch center-of-mass can be read from the oscilloscope, or the correlation function between the two signals can be calculated. A typical measurement is displayed in Fig. 6.5. As shown in the schematic, several bunches are between the pick-ups, and an estimate of the velocity is needed. This is normally known, but in case of trouble, a third pick-up has to be installed much closer to one of the others. The velocity is calculated for the measured time t_{scope} via

$$\beta c = \frac{L}{NT + t_{scope}} \tag{6.6}$$

with N bunches between the pick-ups and the bunch repetition time of $T = 1/f_{rf}$.

The accuracy of such a velocity measurement $\Delta\beta/\beta$ is given by the uncertainty of the distance ΔL and the scope reading Δt to be

$$\frac{\Delta\beta}{\beta} = \sqrt{\left(\frac{\Delta L}{L}\right)^2 + \left(\frac{\Delta t}{NT + t_{scope}}\right)^2} \tag{6.7}$$

An accuracy better than 0.1 % for the energy spread $\Delta E_{kin}/E_{kin} = 2\Delta\beta/\beta$ can be reached, assuming a accuracy for the distance of $\Delta L = 1$ mm and $\Delta t = 100$ ps for the time measurement; the parameters used at the GSI-LINAC are summarized in Table 6.1.

The final energy of a LINAC module depends on the applied amplitude and phase of the accelerating rf. This is depicted in Fig. 6.6 for an ion beam of 1.400 MeV/u nominal energy. This nominal energy is reached only in a small interval; for the displayed case the allowed amplitude range is below ±2 %, and the phase should be aligned within $\pm 10^o$. This corresponds to a relatively small range, and it calls for a precise beam alignment and a substantial accuracy in the ToF measurement, as demonstrated by the small error bars in Fig. 6.6. Matching the nominal beam energy of a LINAC module is an important task, because the energy acceptance of the following module is typically restricted within several percent and a sufficient beam transmission through a chain of LINAC modules

Table 6.1: The energy resolution for a ToF measurement with a pick-up distance of 3.25 m for some GSI LINAC modules (GSI-internal LINAC module names are given). The rf-frequency is $f_{rf} = 36.14$ MHz and the assumed time accuracy is 100 ps.

Physical parameter	Units	RFQ	IH1	IH2	AL4
energy W	[MeV/u]	0.12	0.75	1.4	11.4
velocity β	%	1.6	4.0	5.5	15.5
total ToF	[ns]	677	271	197	70
bunch spacing $\beta c/f_{rf}$	[cm]	13	33	45	129
resolution $\Delta W/W$	%	0.07	0.10	0.12	0.22

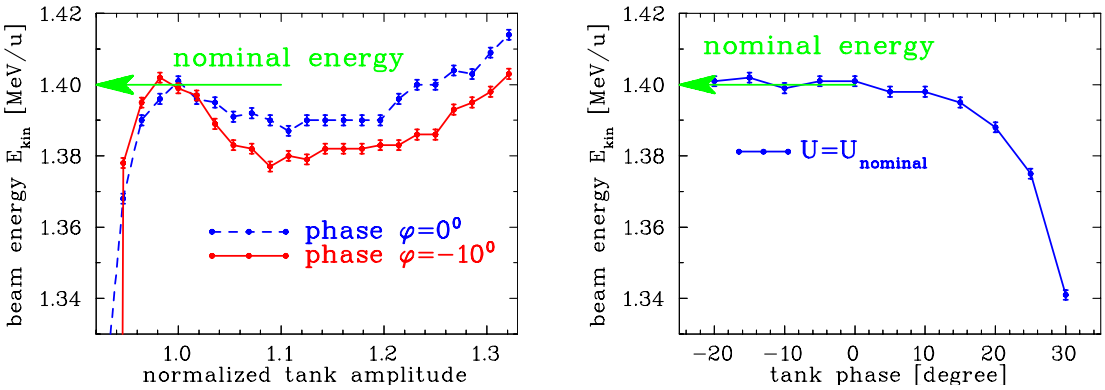

Figure 6.6: Left: The output energy of the GSI-LINAC is depicted as a function of the applied rf-amplitude inside the tank as recorded like displayed in Fig. 6.5. Right: The phase for the nominal amplitude is shown. The required energy of this module is 1.400 MeV/u. The distance between the pick-ups is in this case $L = 1.97$ m with $N = 4$ bunches between.

is only achieved if all modules produce the right energy increase. Moreover, the longitudinal emittance depends strongly on the right rf amplitude and phase setting, as shown in Chapter 6.7.2.

Even though the ToF method is commonly called energy measurements, it is basically a velocity determination. For electron beams, this method can not be applied, because electrons are relativistic after the first LINAC modules. Acceleration of electrons is more related to an increase of their momentum, and therefore the energy determination by the bending of a dipole magnet is more appropriate in this case. Because of the dependence of the bending radius on the particle momentum Δp with respect to the reference particle of momentum p_0, the momentum distribution is transferred to a distribution in the horizontal plane. This is described by the optical parameter dispersion $D(s)$ as the additional beam offset is $\Delta x(s) = D(s) \cdot \Delta p/p_0$. However, the resulting profile is a mixture of the transverse and longitudinal parameters, and transverse collimation is required at the entrance of the optical system; see the discussion in textbooks on beam optics, e.g. [126].

6.4 Longitudinal emittance from linear transformation

There are some cases where the length of the bunches fits the length of the capacitive or stripline pick-ups to get reliable information of the bunch structure. The longitudinal emittance can then be determined from linear transformations, like in the transverse case, as described in Chapter 4.4 and 4.5. The quadrupole variation corresponds to the change of the longitudinal focusing performed by a buncher, see Fig. 6.7. The phase of a buncher is adjusted to 0^o, so no acceleration is present. By varying the amplitude, the bunch can be longitudinally focused, i.e. compressed at the measurement location. The action s described in the longitudinal sub-space $(l, \delta = \Delta p/p)$, which is a part of the full 6-dim phase space describing both transverse and the longitudinal planes[1]. The general transfer matrices

[1]e 6-dim phase space is spanned by the vector $\vec{x}^{\,t} = (x, x', y, y', l, \delta)$ and with the help of the 6×6 transport matrices $\mathbf{R}$ the linear behavior of the accelerator can be described including the coupling between the horizontal, vertical and longitudinal degree of freedom. For the formula used here the bunch length l is given unit of spatial length in [m] to have the same units for all three degrees of freedom.

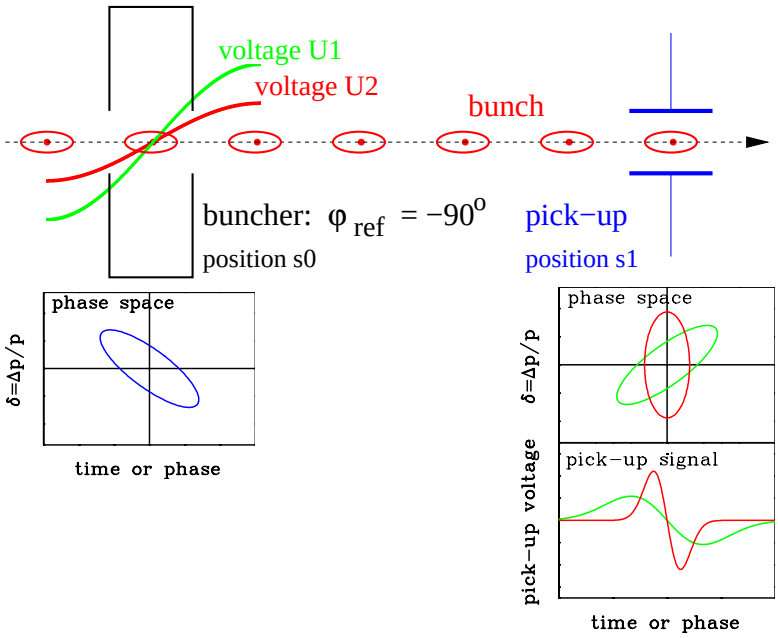

Figure 6.7: Scheme for a longitudinal emittance measurement using a buncher and one bunch shape monitor.

R for the transverse and longitudinal phase space have 6×6 elements, as does the beam matrix $\boldsymbol{\sigma}$. Disregarding any transverse-longitudinal coupling (e.g. by a dipole magnet), the longitudinal phase space corresponds to the 'lower right' part of the full 6×6 matrices, having the indices 5 and 6. The reduced 2×2 transfer matrix of a buncher $\mathbf{R}_{buncher}$ is given in thin lens approximation by

$$\mathbf{R}_{buncher} = \begin{pmatrix} 1 & 0 \\ -1/f & 1 \end{pmatrix}. \tag{6.8}$$

by the focal length f

$$\frac{1}{f} = \frac{2\pi q U_0 f_{rf}}{A p v^2} \tag{6.9}$$

with the voltage amplitude U_0 of the accelerating frequency f_{rf} for a particle of charge q and mass number A with velocity v and momentum p. The transfer matrix for a drift space of length L is given by

$$\mathbf{R}_{drift} = \begin{pmatrix} 1 & L/\gamma_{rel}^2 \\ 0 & 1 \end{pmatrix}. \tag{6.10}$$

γ_{rel} is the relativistic Lorentz factor. As for the transverse case, the emittance can be determined by an amplitude variation U_0 of the buncher leading to different longitudinal focusing. A measurement of the bunch length at the pick-up location s_1 has to be performed for at least three settings of the buncher. The beam matrix $\boldsymbol{\sigma}(0)$ at the buncher location s_0 has to be determined. For the bunch width $l_{max}(1, f_k) = \sqrt{\sigma_{55}(1, f_k)}$ at the pick-up location s_1, a system of linear equations for $\sigma_{ij}(0)$ in the form

$$\begin{aligned}
\sigma_{55}(1, f_1) &= R_{55}^2(f_1) \cdot \sigma_{55}(0) + 2R_{55}(f_1)R_{56}(f_1) \cdot \sigma_{56}(0) + R_{56}^2(f_1) \cdot \sigma_{66}(0) \quad \text{focusing } f_1 \\
\sigma_{55}(1, f_2) &= R_{55}^2(f_2) \cdot \sigma_{55}(0) + 2R_{55}(f_2)R_{56}(f_2) \cdot \sigma_{56}(0) + R_{56}^2(f_2) \cdot \sigma_{66}(0) \quad \text{focusing } f_2 \\
&\vdots \\
\sigma_{55}(1, f_n) &= R_{55}^2(f_n) \cdot \sigma_{55}(0) + 2R_{55}(f_n)R_{56}(f_n) \cdot \sigma_{56}(0) + R_{56}^2(f_n) \cdot \sigma_{66}(0) \quad \text{focusing } f_n
\end{aligned} \tag{6.11}$$

is obtained for $k = 1, 2...n$ measurements with $f_k = f_1, f_2...f_n$ different settings of the buncher. This redundant system of linear equations has to be solved as discussed in Chapter 4.4. A measurement is shown in Fig. 6.8. For the method it is of no importance which device is used for determination, as long as it reflects the actual bunch shape of the beam.

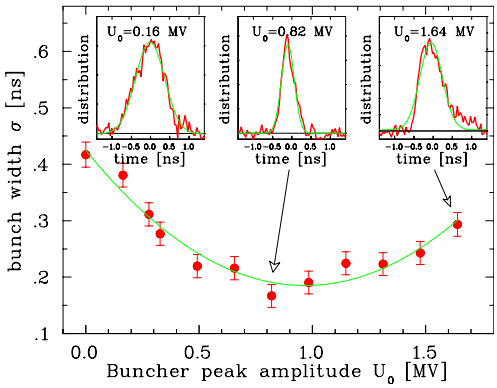

Figure 6.8: Measurement of the bunch width (one standard deviation) as a function of the buncher voltage 31 m upstream. The bunch shape is not measured by a pick-up, but a specially designed monitor for low energetic beams [128].

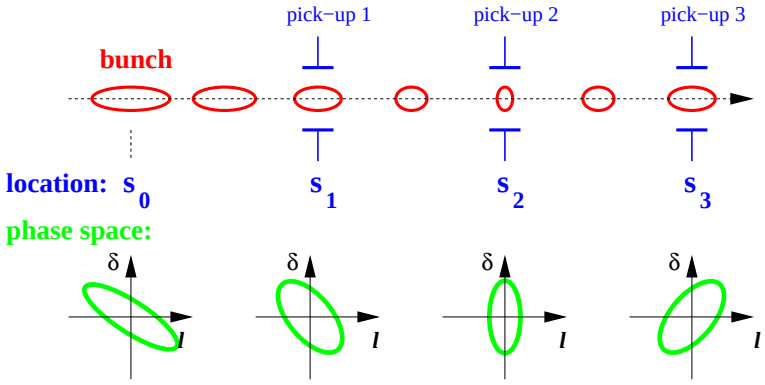

Figure 6.9: Scheme for a longitudinal emittance measurement using pick-ups in a transfer line.

Corresponding to the 'three grid method', the bunch width can also be determined from a series of measurement along a transfer line, see Fig. 6.9. As in the transverse case Chapter 4.5 we get a redundant system of linear equations for the transformation $\mathbf{R}(k)$ from the buncher to the pick-up at s_k of the form

$$\begin{aligned}
\sigma_{55}(1) &= R_{55}^2(1)\cdot\sigma_{55}(0) + 2R_{55}(1)R_{56}(1)\cdot\sigma_{56}(0) + R_{56}^2(1)\cdot\sigma_{66}(0) \qquad \mathbf{R}(1): s_0 \rightarrow s_1 \\
\sigma_{55}(2) &= R_{55}^2(2)\cdot\sigma_{55}(0) + 2R_{55}(2)R_{56}(2)\cdot\sigma_{56}(0) + R_{56}^2(2)\cdot\sigma_{66}(0) \qquad \mathbf{R}(2): s_0 \rightarrow s_2 \\
&\vdots \\
\sigma_{55}(n) &= R_{55}^2(n)\cdot\sigma_{55}(0) + 2R_{55}(n)R_{56}(n)\cdot\sigma_{56}(0) + R_{56}^2(n)\cdot\sigma_{66}(0) \qquad \mathbf{R}(n): s_0 \rightarrow s_n \qquad (6.12)
\end{aligned}$$

For a precise determination, a longitudinal focus has to be placed close to one pick-up.

As discussed for the transverse case, the restrictions are the presence of simple e.g. Gaussian phase-space distributions, linear beam manipulations and the lack of non-linear space-charge forces. Moreover, one has to underline, that the above methods are only used at LINACs; in most cases the resolution of pick-up is insufficient, and special detectors are used as discussed in Chapter 6.7 for proton beam and Chapter 6.8 for electron beams.

For beam extracted from a synchrotron, the variation of the bunch length within the beam transfer line is negligible in most cases, due to the low momentum spread $\Delta p/p$ of the circulating beam and the short flight time t_{drift} to the target of a further synchrotron as the increase of the bunch length is $\Delta t = \Delta p/p \cdot t_{drift}$. As an example, the following number can be inserted: For a relativistic beam of velocity $\beta \simeq 1$ and a distance of $L = 100$ m from the synchrotron to the target, the drift time $t_{drift} = L/\beta c = 333$ ns; assuming a momentum spread of $\Delta p/p = 10^{-3}$ the resulting lengthening of the bunch is $\Delta t = \Delta p/p \cdot t_{drift} = 0.3$ ns, which is shorter than the typical bunch length of $\sigma_{bunch} > 10$ ns in a proton synchrotron. Therefore, the measurement inside the synchrotron is sufficient and the current transformer mounted in the synchrotron can be used for monitoring.

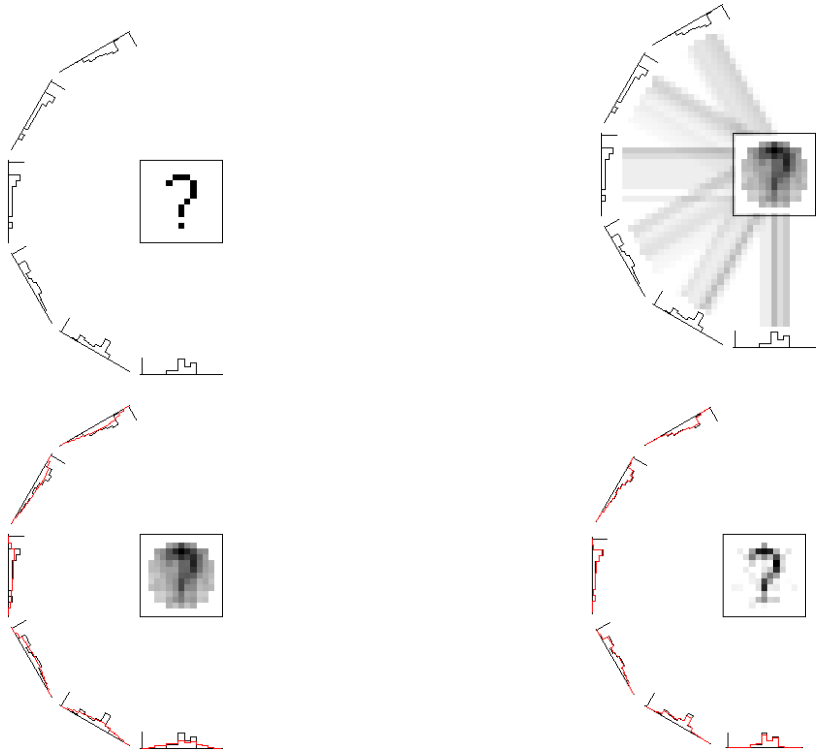

Figure 6.10: Schematic plots for the tomographic reconstruction technique [129]. The original 2-dimensional image and the 1 dimensional projections are shown to the left. A first back projection is shown top right. The first iteration step for the generation of the differences in the projected data is plotted bottom left. After ~ 50 iterations, the original image can be reconstructed.

6.5 Longitudinal emittance using tomographic reconstruction

In a proton synchrotron the bunch length is much longer than the typical pick-up size or the gap of a resistive wall current monitor, see Chapter 6.6. This allows the recording of a true image of the bunch shape. Observation and control of the longitudinal behavior at injection, acceleration and possible bunch manipulations, like combining or splitting of bunches, can be performed.

An innovative analysis method has been developed at CERN [129] to determine the longitudinal phase space distribution and hence the emittance from a measurement of the bunch shape on a turn-by-turn basis. The idea is based on the well known tomographic reconstruction used as an imaging technique in medicine for x-ray tomography and nuclear magnetic resonance NMR tomography and described in textbooks on medical physics.

The underlying principle of tomography is to combine the information from a sufficiently large number of projections to unambiguously reconstruct the more complete picture with the extra dimension reinstated. The application of tomography to longitudinal phase space in an accelerator becomes obvious once it is realized that a bunch of particles performing synchrotron motion is analogous to a patient rotating in a stationary body scanner. On each turn around the machine, a longitudinal pick-up provides a "snapshot" of the bunch projected at a slightly different 'angle', i.e. the oscillation of the bunch shape as given by the inverse of the synchrotron frequency f_{synch} is in nearly all cases much lower than the revolution frequency $f_{rev} \gg f_{synch}$. It suffices to combine such profiles tomographically to obtain a two-dimensional picture of phase space density. Moreover, non-linear emittance growth can be included [129]. A general, well-fulfilled condition is that the synchrotron frequency is much lower than the revolution frequency. At least half a synchrotron period has to be recorded, corresponding to a 180^o degree image of the patient body in the medical application.

The general idea for tomography is based on algebraic reconstruction techniques (described in textbooks on medical physics) as depicted in Fig. 6.10 from [129]. The contents of the bins of a one-dimensional histogram are redistributed over the two-dimensional array of cells which comprise the reconstructed image. Assuming no a-priori knowledge of the original two-dimensional distribution,

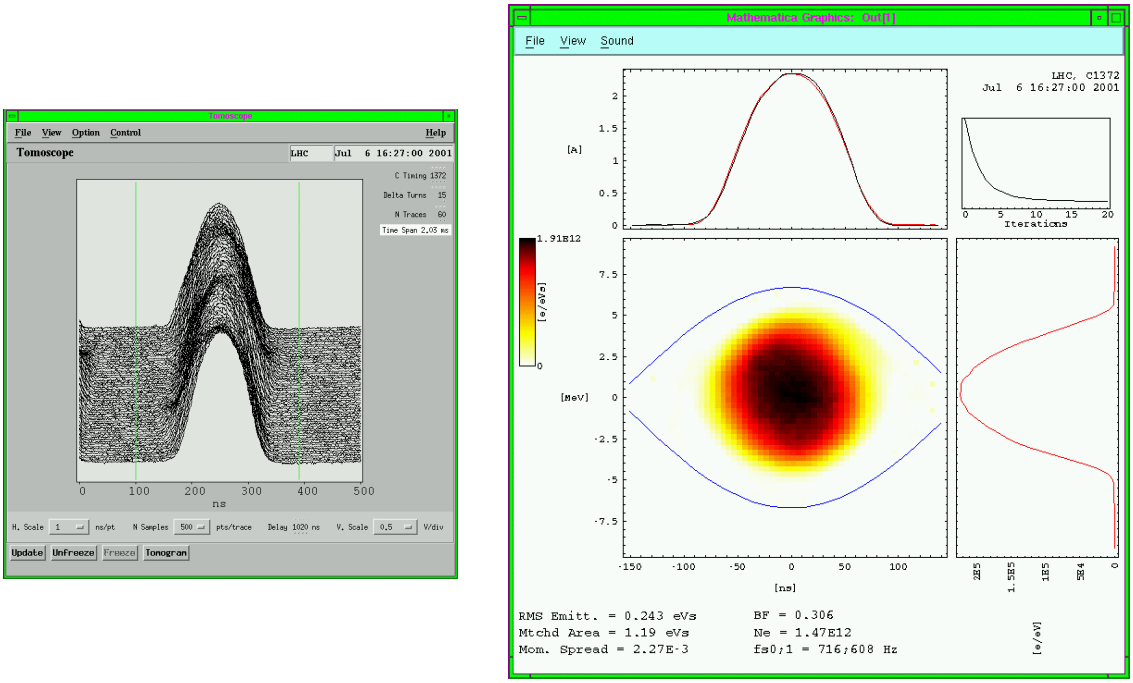

Figure 6.11: The recorded bunch shape at CERN PS using a resistive wall current monitor for 500 turns (left) and the reconstructed longitudinal phase space. The bucket size is shown in the phase space and the projections to the time axis (top) and energy (right) are displayed, from [130].

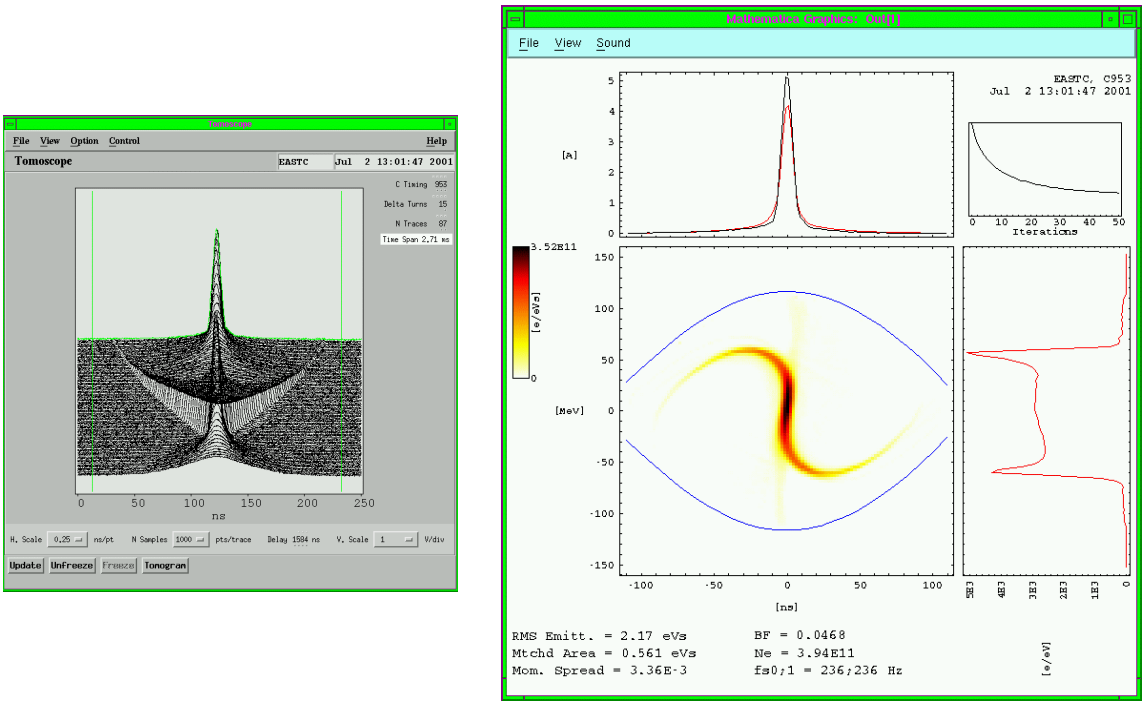

Figure 6.12: Same as Fig. 6.11 but for a mismatched bunch. The complex rotation of the bunch width is seen left and the reconstructed phase space density (right) for one specific time slice. The filamented distribution rotates to yield varying bunch shapes, form [130].

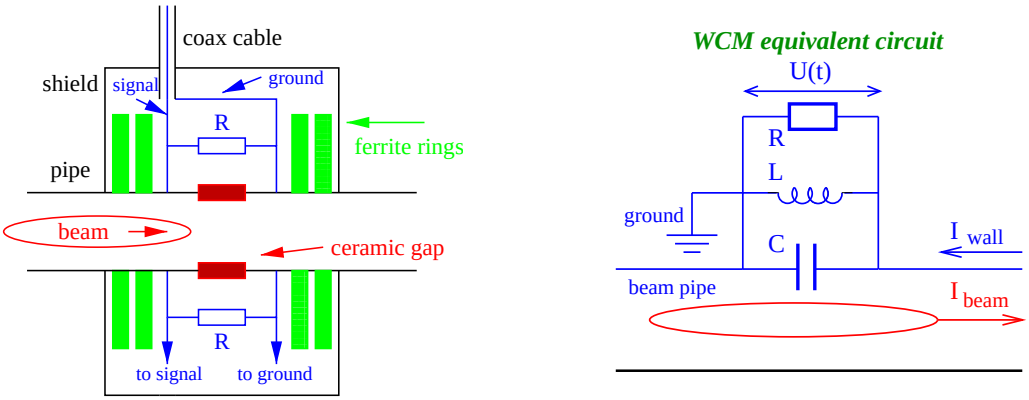

Figure 6.13: Schematics of a wall current monitor used for fast bunch observations and its equivalent circuit.

the contents of one bin are spread over all the cells that could have contributed to that bin. The back-projection of all bins of all profiles yields a first approximation to the original distribution. Back projection of the bin-by-bin difference between the original set of profiles and this new one yields an improved approximation. Further iterations converge more rapidly if any cell whose contents have become negative is reset to zero. A more detailed description is found in [129].

Two examples [130] demonstrate the high analyzing power of tomography. The first example, displayed in Fig. 6.11, is a standard, constant bunch shape recorded with a digital scope. The reconstruction of the first time slice shows a good filling of the bucket. The second example in Fig. 6.12 is related to a particular bunch manipulation. In phase space (as shown for a small bunch width), the distribution rotates at the synchrotron frequency, resulting in varying bunch shapes as a function of time. This type of compact bunches are created to fulfill the demands of the user, who wants to use a short bunch for the dedicated experiments. The observation inside the synchrotron has the advantage of observing the entire creation process of the so-called bunch rotation and enable the right trigger timing for the extraction of this bunch.

6.6 Resistive wall current monitor

For the observation of the bunches and their structure, a large bandwidth for the device itself and the associated electronics is required. With a resistive **W**all **C**urrent **M**onitor **WCM**, a bandwidth up to several GHz can be reached [131]. The beam always induces an image current flowing along the vacuum pipe, having the same magnitude and the same time structure. To measure this image current, the vacuum pipe is interrupted by a ceramic gap, as displayed schematically in Fig. 6.13. The gap is bridged by typically n =10 to 100 resistors with a low resistivity on the order of R =10 to 100 Ω leading to a total value of $R_{tot} = R/n \sim 1\ \Omega$. The resistors are azimuthally distributed on a printed circuit board so that the signal amplitude is independent of the actual beam position. At several locations, the signal is connected to a coaxial cable, feeding an amplifier. The voltage across the resistors U_{tot} is given by

$$U_{tot} = \frac{R}{n} \cdot I_{beam}. \tag{6.13}$$

The resistors have to be shielded carefully against noise from the surroundings as caused, e.g. by ground currents from the rf-system. The shield also acts as a short circuit for low frequencies. In addition, ferrite rings are mounted across the vacuum pipe to force the image current through the resistors by damping the high frequencies penetrating the rings. Using ferrites with a high permeability μ resulting in a large value of inductance $L \propto \mu$, the lower cut-off frequency $f_{low} = (2\pi)^{-1} \cdot R_{tot}/L$ can be decreased. Values of about $f_{low} \sim 10$ kHz are typical and allow un-differentiated bunch structure observation. The upper cut-off frequency is given by the capacitance C of the gap to be $f_{high} = (2\pi)^{-1} \cdot (R_{tot}C)^{-1}$. Several GHz are realizable with a careful design of all rf-components. The equivalent circuit is the same as for a passive transformer and hence its properties, as discussed in Chapter 2.1.1. The only exception is that the capacitance for the WCM is given by the ceramic gap,

Figure 6.14: Photo of the wall current monitor used at FERMI-Lab for protons, from [131]. The ceramic gap is shown separately. The ferrite rings and the printed circuit with the resistors are visible.

which is larger than any stray capacitance. The wall current monitor is well suited for broadband bunch shape observations at proton synchrotrons with bunch lengths down to the ns region.

6.7 Bunch structure for non-relativistic energies

For a beam of non-relativistic velocity, the electric field of a bunch has a significant longitudinal component, as calculated for Fig. 6.2. This longitudinal field is seen by the pick-up, leading to a smearing of the signal. The structure of a bunch can not be monitored with a pick-up, as demonstrated in Fig. 6.15 for a 1.4 MeV/u ion beam corresponding to $\beta = 5.5$ %. Moreover, the required resolution of 1^o in phase, or less than 50 ps in time, corresponds to a bandwidth of more than 10 GHz, which is hardly achieved by rf technologies. Other methods have to be applied for such a measurement. The result is important for the adjustment of the LINAC modules, including bunchers for the injection to following accelerators, and the comparison of measurements and beam dynamics calculations, as e.g. required during a commissioning phase of a new accelerator. The bunch width and structure enter the numerical codes in the same manner as the transverse parameters, e.g. for the estimation of emittance growth by space charge forces. Moreover, as is shown below, a Gaussian distribution is not a good approximation for the bunch structure at these low energies. Three different devices are discussed below.

6.7.1 Coaxial Faraday cups for bunch shape observation

Faraday cups, as described in Chapter 2.5, are used to monitor the structure of bunches for non-relativistic protons or ions at LINACs up to an energy of about 100 MeV/u and a bunch length of down some 100 ps. This should be a direct measurement of the beam charges arriving at the metallic surface of the cup. The electric signal is then guided via a 50 Ω matched transition line to a broadband amplifier. All components of this electrical chain must have a bandwidth of several GHz for an undistorted image of the bunch shape, which is not easily achievable. In Fig. 6.16 the schematics of a coaxial Faraday cup is shown: The beam hits a collector, which is mounted in a rotational symmetric configuration inside an outer conductor leading to a 50 Ω transmission line. To ensure the large bandwidth of several GHz and prevent signal reflection, it is necessary to keep a constant ratio of the collector radius r_{coll} and the outer radius of the shield r_{shield}. The impedance Z of a coaxial transmission line should be 50 Ω everywhere and is determined via

$$Z = \frac{Z_0}{2\pi} \cdot \ln \frac{r_{shield}}{r_{coll}} \quad . \tag{6.14}$$

The constant Z_0 is the 'impedance of the vacuum' and is given by $Z_0 = \sqrt{\mu_0/\epsilon_0} = 377\ \Omega$. If the impedance is not constant, part of the signal is reflected, leading to a deformation of the beam image

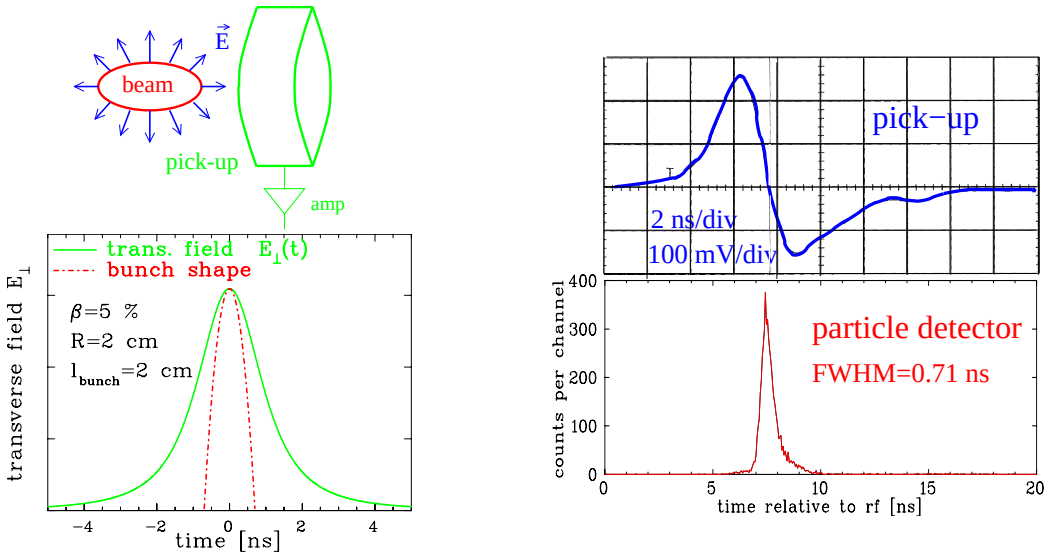

Figure 6.15: Left: Time evolution of transverse electric field as seen by the pick-up is simulated for the for a bunch with $\cos^2$-distribution.Right: The comparison of a pick-up signal to the bunch structure measured with a particle detector at the GSI LINAC with 1.4 MeV/u. The broadening of the pick-up signal due to the longitudinal field component is visible.

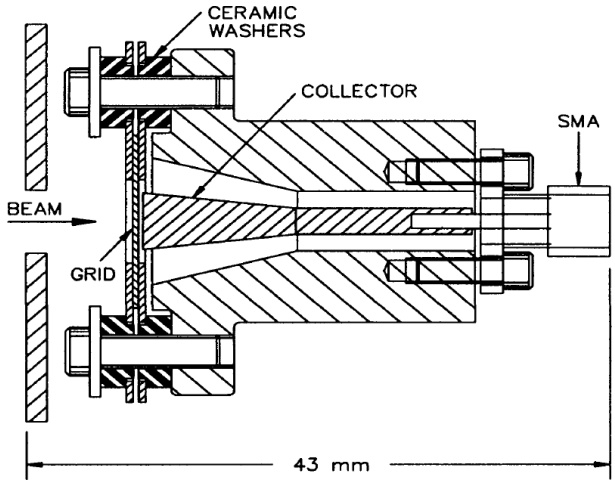

Figure 6.16: Scheme of a 50 Ω cup. A smooth transition to the SMA connector, maintaining 50 Ω impedance, is used. The grid for minimizing the advanced electrical field component is mounted close to the collector [132].

Figure 6.17: Head of a coaxial Faraday cup. The grid for shielding of the advanced field and suppression of secondary electrons is shown in the middle. The collector including the ceramic cooling water feed-through is seen on the right-hand side.

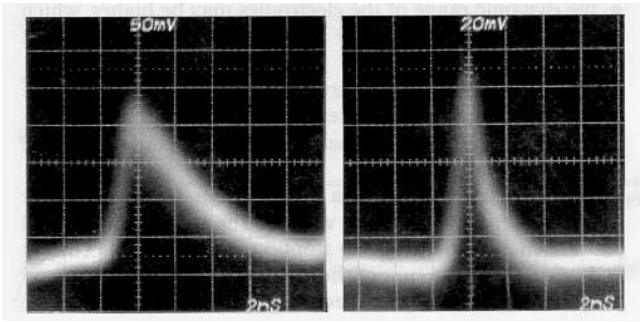

Figure 6.18: Observed bunch signal with 2 ns/div from a coaxial Faraday cup. Left: without suppressor voltage on the grid, right: -500 Volts on the grid.

[2].

Most coaxial Faraday cups have a relatively small collector area, comparable with the size of the transmitting coaxial cable; in Fig. 6.16 it is only a few mm [132, 138]. In this case, only the central part of the beam hits the collector. This does not influence the bunch shape measurement, because usually no correlation between the transverse and longitudinal planes exists.

Due to the creation of secondary particles, Faraday cups can only be used for protons or ions with

[2] A general measure of the matching quality is the voltage reflection coefficient ρ_V of a transmission line, defined by

$$U_{back} = \rho_V \cdot U_{forward} \tag{6.15}$$

with $U_{forward}$ the input voltage and U_{back} the reflected voltage. Expressed in terms of the transmission line impedance Z_1 and the impedance of the load Z_2 the voltage reflection coefficient ρ_V is

$$\rho_V = \frac{Z_2 - Z_1}{Z_2 + Z_1}. \tag{6.16}$$

There are three extreme cases:

- $Z_2 = Z_1 \Rightarrow \rho_V = 0$ the matching is perfect, no signal is reflected.
- $Z_2 = 0 \Rightarrow \rho_V = -1$ corresponding to a short circuit, the reflected signal has the same amplitude but opposite sign.
- $Z_2 = \infty \Rightarrow \rho_V = 1$, corresponding to an open circuit, the reflected signal comes back with the same amplitude and sign.

Another description of the matching is the so-called 'Voltage Standing Wave Ratio' which is defined as

$$\text{VSWR} = \frac{Z_2}{Z_1} = \frac{1 + \rho_V}{1 - \rho_V} \quad . \tag{6.17}$$

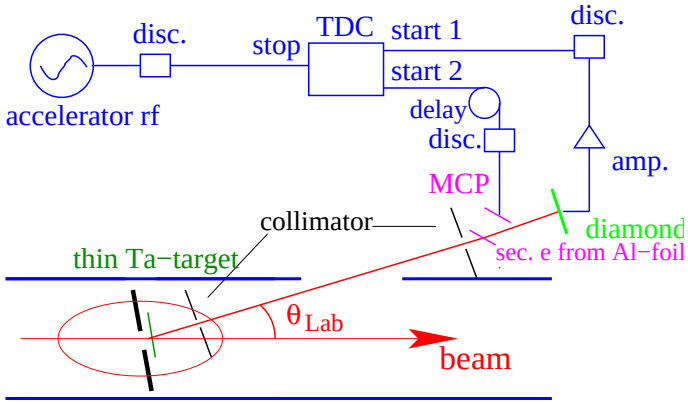

Figure 6.19: Principle of a particle detector using the ToF-technique for bunch structure and longitudinal emittance measurement.

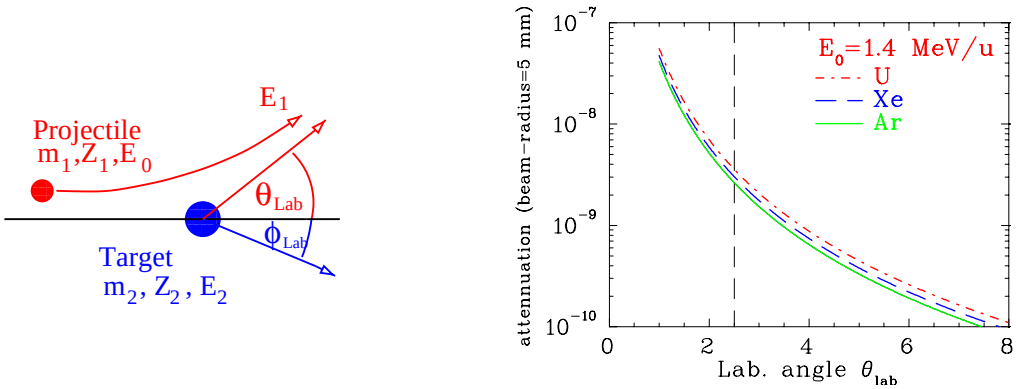

Figure 6.20: Calculated attenuation of a 1.4 MeV/u ion beam by Rutherford scattering in a 130 nm Ta foil for 1.4 MeV/u ions as a function of the angle in the lab-frame.

energies below about 100 MeV/u. For this non-relativistic velocities of about $\beta \leq 50\%$ the advanced electric field, as calculated in Chapter 6.1, leads to an induced voltage on the collector prior to the arriving particles. Therefore a grid is mounted very close to the collector plate, which acts as an equi-potential surface shielding the collector. In addition, one has to prevent the escape of secondary electrons. By supplying a negative voltage to the grid, the secondary electrons are repelled back to the collector in connection to the shielding of the advanced electrical field. Figure 6.17 shows all important parts of the cup, including the grid. Fig. 6.18 gives an example of measured bunch signals with and without voltage on the grid. The signal from the coaxial cup is recorded with an oscilloscope in most cases. These devices have a bandwidth limitation of less than $\sim$ 10 GHz. Therefore the time resolution of this method is limited and sometimes insufficient for the application at modern LINACs driven by an accelerating frequency $f_{rf} \geq 500$ MHz.

6.7.2 Time-of-flight using particle detectors

Particle detectors can have a fast response to a hit by a single beam particle. The signal width from such a single particle detector output can be less than 1 ns with a rise time of less than 100 ps and therefore a precise timing corresponding to bandwidth of larger than 10 GHz can be reached easily. Examples for adequate detectors are synthetic diamond counters [133], which work like solid-state detectors, or Multi-Channel-Plates equipped with an anode in 50 Ω-geometry [134], where the anode shape is similar to that discussed for 50 Ω Faraday cups (Chapter 6.7.1). The arrival of a beam particle with respect to the accelerating frequency reflects the bunch structure with a time resolution of several tens of picoseconds.

The principle of such a setup [81, 135] is shown in Fig. 6.19. It can work with less than one ion hit per rf-period due to the use of a single hit particle detector. In the setup used at the GSI-LINAC, this reduction is performed by Rutherford scattering in a 210 μg/cm^2 tantalum foil ($\sim$ 130 nm thickness)

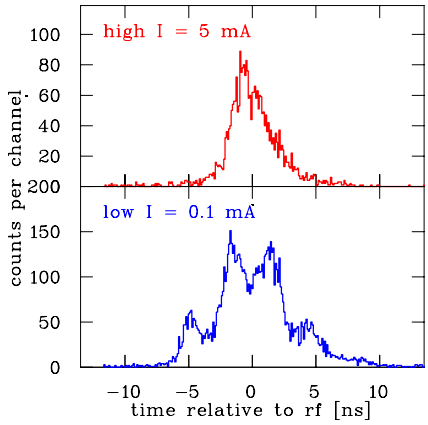

Figure 6.21: The bunch structure measured at the GSI LINAC with a 120 keV/u Ar^{1+} beam for different currents inside the RFQ [81]; one rf-period is shown.

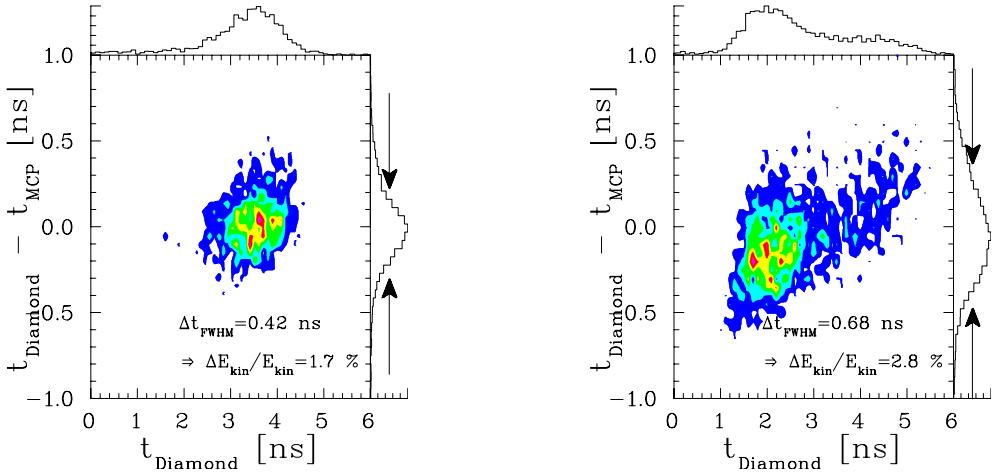

Figure 6.22: Phase space plot for a 1.4 MeV/u ion beam recorded with two detectors in coincidence at the GSI LINAC [81]. The time relative to the rf is plotted along the horizontal axis, the time difference of the individual particles on the vertical axis corresponding to the energy distribution. Left: The low current ($I_{beam} = 0.1$ mA) results are plotted. Right: The high current beam ($I_{beam} = 5$ mA) results is depicted.

at a scattering angle of 2.5^o defined by a collimator with 16 cm distance and Ø0.5 mm apertures to give a solid angle of $\Delta\Omega_{lab} = 2.5 \cdot 10^{-4}$. The parameters are chosen to get an attenuation of $\sim 10^{-8}$ of the beam current, see Fig. 6.20. The calculated value is nearly independent of the ion species due the transformation from the center-of-mass frame (where the scattering cross-section has the Rutherford-scaling $\sigma_{ruther} \propto Z^2 W_{beam}^{-2} \sin^{-4}\theta/2$) to the lab frame (where the ratio of the projectile and target mass enters). A high target mass is preferred, so the additional energy spread by the scattering is lower than the required resolution. A contribution to the energy spread might arise from the electronic stopping power in the foil. After a drift space of ~ 1 m the scattered particles hit the detector. Its output pulse is converted to a logic pulse with a special discriminator, and the time relative to the accelerating rf is determined. A resolution of 25 ps, corresponding to 0.3^o rf-phase is attained here [81, 135].

A typical measurement behind a low energy LINAC module is shown in Fig. 6.21, which also acts as an example for the probable non-Gaussian shape typically created in high current proton or ion LINACs. The two measurements for high (top) and low (bottom) current show an entirely different bunch shapes. A larger width corresponding to a filamented phase space distribution for the low current case is observed. Particle tracking calculations for this case confirm the strong ion current dependence for the longitudinal emittance. The applied rf-power in the cavity counteracts the space

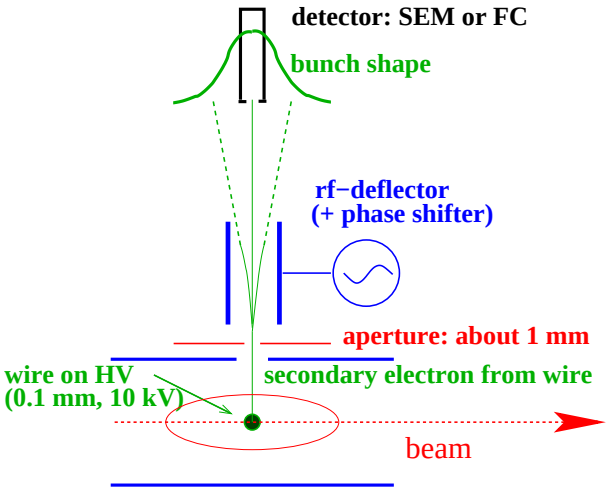

Figure 6.23: Principle of a deflector technique for bunch structure observation by a Bunch Shape Monitor. SEM means secondary electron multiplier.

charge force for a high current beam. For a low current, filamentation occurs due to the missing damping by the space charge, which has to be corrected by a lower rf-power.

There are not many method to determine the longitudinal emittance at low energies because this requires correlated time and energy spread measurements. With particle detectors, it is possible to measure the longitudinal emittance using a coincidence technique. As shown in Fig. 6.19, a second detector can be moved into the path of the scattered ions. For the GSI setup, this consists of a 15 μg/cm^2 Aluminum foil ($\sim$ 50 nm) where several secondary electrons per ion passage are generated. These electrons are accelerated by an electric field of 1 kV/cm toward a micro channel plate equipped with a 50 Ω anode. The time relative to the accelerating rf, as well as the arrival time of the same particle at the diamond detector located 80 cm behind the MCP, are measured. From the difference in time of the individual particles (ToF method), the energy can be calculated and the phase space can be spanned.

An example of such a measurement is given in Fig. 6.22 for low and high current Ar beams. The arrival times at the diamond detector are used as the phase (or time) axis having a width of 1.4 ns, corresponding to 18^o phase, for the plotted case. The time difference between diamond and MCP is plotted on the vertical axis. The width for the low current operation is about 0.4 ns (FWHM), corresponding to an energy spread of $\Delta E_{kin}/E_{kin} = 1.7$ %. For a high current beam, a double structure is visible in the bunch profile and an energy broadening to $\Delta E_{kin}/E_{kin} = 2.8$ % with a clear correlation in the phase space. This demonstrates the emittance growth due to the very high space-charge forces.

6.7.3 Time structure using secondary electrons

In several low energy proton or ion LINACs, a device for the bunch structure observation, the so-called **B**unch **S**tructure **M**onitor **BSM** is installed, based on the observation of secondary electrons liberated from a single wire intersecting the beam, as shown in Fig. 6.23 and reviewed in [136, 137]. The beam hits a wire, which is held on a negative potential of typically -10 kV. By the related electric field, the liberated secondary electrons are accelerated toward a thin slit on the side of the vacuum chamber. Here they pass a pair of plates, where an rf-field is applied having the same frequency as the accelerating rf or a higher harmonics of it. This field deflects the electrons, and the different arrival times are transformed via varying deflection angles to a difference in space, i.e. this deflector acts as a 'time-to-space converter'. (The same principle is used in a non-resonant way in an analog oscilloscope.) After a drift of typically 0.5 m, the electrons are detected with a Faraday cup or a secondary electron multiplier with a small slit in front. (A secondary electron multiplier is just the same as a photo-multiplier but without a photo-cathode.) For a fixed slit position, the phase of the deflecting rf relative to the accelerating rf can be changed to transmit electrons representing different time slots of the beam bunches, to get a full image of the bunch structure.

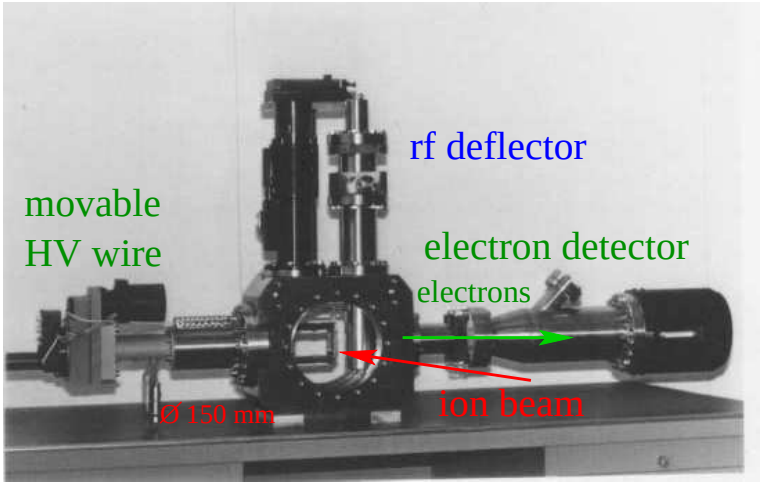

Figure 6.24: The BSM installed at CERN LINAC 2 [136]. The vacuum feed-through on the left side is the support for the high voltage wire. The rf-deflector is installed on the vertical flange and the detector is mounted on the right.

The resolution of this device is better than 1^o in phase, independent of the frequency of the rf, up to several hundred MHz. It is known that the emission of secondary electrons is a fast process with a time difference of less than 10 ps between the hit of the beam particle and the electron emission, i.e. much faster than the required resolution. The rf deflector is built as a resonator to get an electric field high enough for typically 100 mrad deflection to have an appropriate separation at the detector ~ 0.5 m apart. IA, the electrons have to be focused transversally. A constant dc-voltage applied to the deflector plates serves as an electrostatic lens. The HV-wire is movable so that the bunch shape can be measured for different horizontal locations, and it is possible to do a measurement with a high current beam by intercepting the beam edge with low power deposition.

6.8 Bunch structure for relativistic electron beams

In most cases, longitudinal diagnostics at electron accelerators is not performed by pick-ups, although, due to the relativistic velocities, it would be possible. However, the bunch length e.g. at a synchrotron light source is typically only of the order of several ten ps, so that even a pick-up bandwidth of several GHz is insufficient to reproduce the detailed bunch structure. Here we profit from the emission of synchrotron light at a dipole, or preferably from an insertion device. A review on this technique is given in [139].

The principle of such a measurement is shown in Fig. 6.25. It uses a streak camera as a commercially available device [134], which allows visible light observations with a time resolution down to typically 1 ps. The synchrotron light is focused and scraped by a pin hole onto the photo-cathode of a streak camera. The secondary electrons from the photo-cathode are accelerated and pass a fast deflector, driven by a frequency in the range of 50 to 300 MHz, which are locked to the accelerating frequency for synchronization. The general scheme is similar to the discussed 'time-to-space converter' in Chapter 6.7.3. After a certain drift space, the electrons are amplified by a MCP and converted to photons by a phosphor screen. With a standard CCD camera, the image from the phosphor is stored. The different arrival time of the synchrotron light, and therefore the bunch structure is converted to a difference in space with a full scale of typically several 100 ps and a resolution in the ps range. A second, perpendicular pair of plates is driven with a much lower frequency to separate the images from the individual bunches.

Fig. 6.26 depicted an example of a bunch length measurement, performed with synchrotron radiation from a dipole [141]. The slow scan for the separation of the individual bunches is displayed on the horizontal axis. The vertical axis has a full scale of 360 ps, and the bunch width is only $\sigma \simeq 40$ ps, demonstrating the high resolution of such a system. Synchrotron radiation users need short bunches for time-resolved spectroscopy. A large voltage is applied to the synchrotron rf cavities to produce and maintain these short bunches. In Fig. 6.27 the bunch width is plotted for different rf voltages.

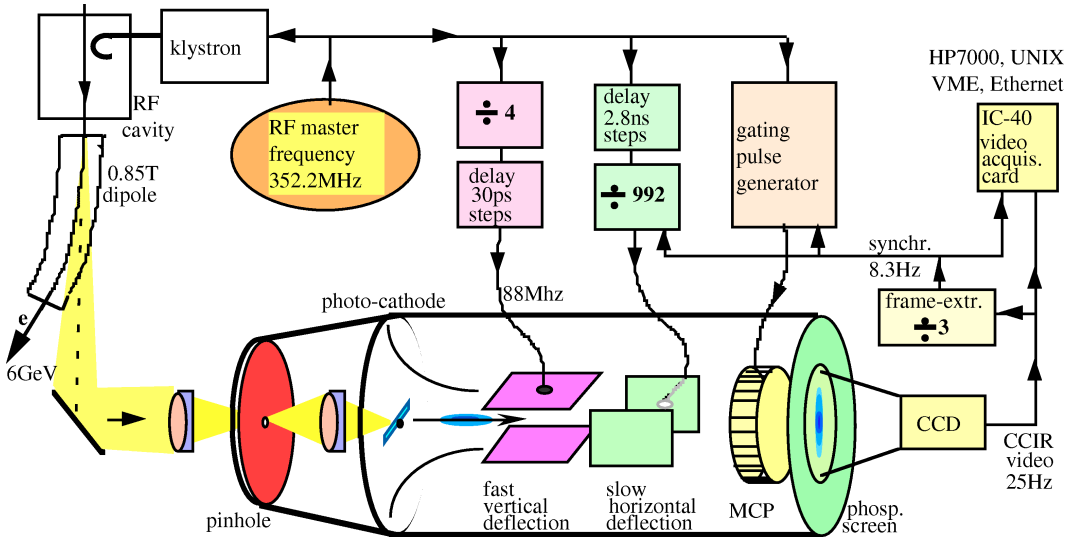

Figure 6.25: Principle of a streak camera measurement for bunch width determination at electron accelerators ESRF, from [140].

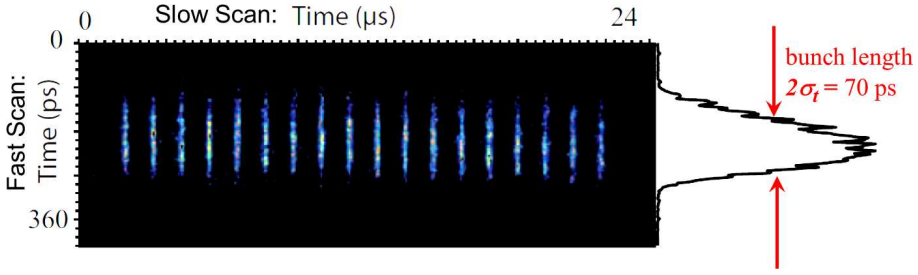

Figure 6.26: Bunch length measurement with a streak camera, using synchrotron light from individual bunches emitted by the passage through a dipole at SOLEIL [141]. The horizontal axis scaling is 24 μs full scale for the bunch repetition (slow scan direction) and the vertical axis is 360 ps full scale for the bunch structure (fast scan direction).

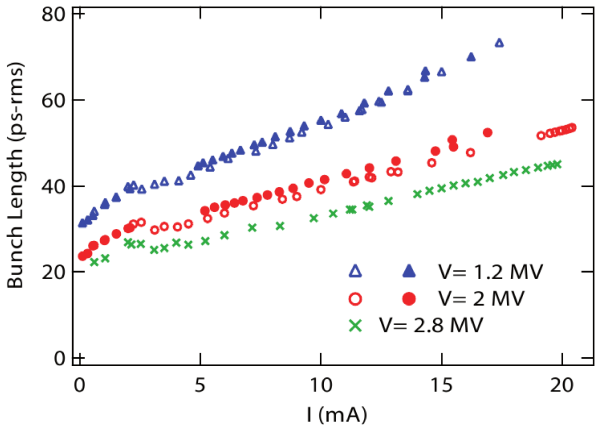

Figure 6.27: Example of the use of a streak camera at the synchrotron light facility SOLEIL achieved from measurements like depicted in Fig 6.26: For different accelerating voltages the bunch length is recorded as a function of the beam current stored in the synchrotron, from [141]

.

As displayed, the achievable bunch length depends on the stored electron current. Counteracting the rf bunching force, non-linear processes like wake-fields and instabilities increase for higher currents. Effects like head-tail oscillations or longitudinal bunch oscillation due to coupled bunch instabilities are visible with the help of the streak camera measurements as well, see e.g. [139].

Chapter 7

Schottky noise analysis

The beam in an accelerator consists of a finite number of particles. A current created by a finite number of charge carriers always has some statistical fluctuation. This was investigated first by W. Schottky in 1918 [142]. The detection of these fluctuations with a sensitive spectrum analyzer allows a non-destructive and precise measurement of several parameters, like momentum distribution, tune, transverse emittance, and chromaticity. The method is mainly used for coasting (de-bunched) beams in proton or ion synchrotrons and storage rings. At LINACs the method is not applicable. The strength of the detected incoherent signals is orders of magnitude lower than those produced by the coherent motion of bunched beams described in Chapter 5. Nevertheless, due to the high sensitivity, a Schottky scan with low currents can be performed, in particular with electron- or stochastically cooled beams.

For the following description we recall some basic formulas of accelerator optics in circular machines:

$$\frac{\Delta C}{C_0} = \alpha \frac{\Delta p}{p_0} \quad \text{Definition of momentum compaction factor} \tag{7.1}$$

$$\alpha = \frac{1}{\gamma_{tr}^2} \quad \text{Momentum compaction factor and } \gamma\text{-transition} \tag{7.2}$$

$$E_{tr} = \gamma_{tr} m_0 c^2 \quad \text{Definition of transition energy} \tag{7.3}$$

$$\frac{\Delta f}{f_0} = -\frac{\Delta T}{T_0} = -\eta \frac{\Delta p}{p_0} \quad \text{Definition of frequency dispersion or slip factor} \tag{7.4}$$

$$\eta = \frac{1}{\gamma_{tr}^2} - \frac{1}{\gamma_0^2} = \alpha - \frac{1}{\gamma_0^2} \quad \text{Frequency dispersion and } \gamma\text{-transition} \tag{7.5}$$

$$\frac{\Delta Q}{Q_0} = \xi \frac{\Delta p}{p_0} \quad \text{Definition of chromaticity} \tag{7.6}$$

$$f_s = \sqrt{\frac{1}{2\pi c^2} \cdot \frac{\zeta e}{A m_0} \cdot \frac{1}{\gamma_0 \beta_0^2} \cdot \frac{f_{rf}}{f_0} \cdot |\eta| \cdot U_{rf} \cdot \cos\varphi_0} \quad \text{Synchrotron frequency} \tag{7.7}$$

with C_0 circumference of the synchrotron and c the velocity of light. The parameter of the reference particle with mass Am_0 and charge ζ are: β_0 velocity, p_0 momentum, f_0 revolution frequency, T_0 revolution time, γ_0 relativistic factor and Q_0 the transverse tune. The particles are bunched by the accelerating frequency f_{rf} with amplitude U_{rf} and a phase φ_0 concerning the reference particle relative to the crest of f_{rf}. Δ... describes the width of the width of the distribution for the corresponding parameter.

7.1 Spectrum analyzer

A spectrum analyzer is used to determine the amplitude of a frequency component of a time-varying signal. It is basically equivalent to a Fourier transformation realized by analog electronics components. A tunable bandpass filter could be used, where the center frequency is swept; however, this is difficult to realize. Instead, a mixer in the input port of the spectrum analyzer is used. See Eq. 5.48 for a description of a mixer.

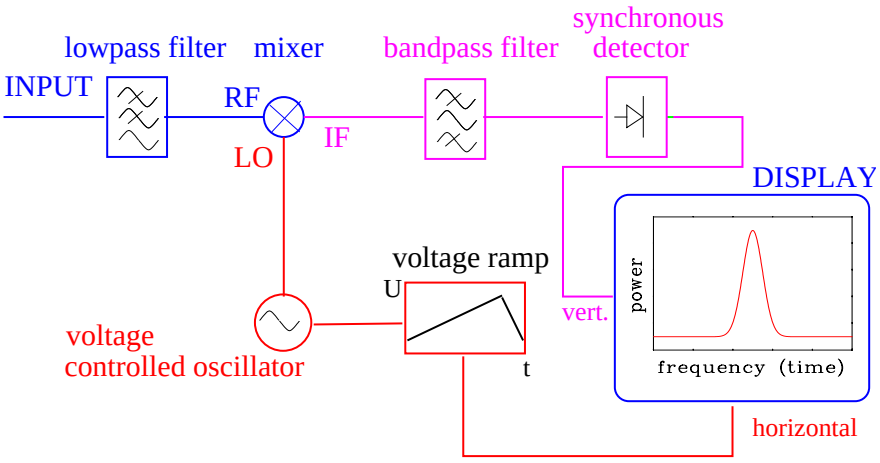

Figure 7.1: Principle of a spectrum analyzer.

The simplified principle of a spectrum analyzer is shown in Fig. 7.1. The input signal passes a lowpass filter, which limits the bandwidth of the device. Typical values for the bandwidth of high performance models are 100 Hz to 3 GHz. The filtered signal is then mixed with a tunable frequency of constant amplitude applied to the LO port of the mixer. This frequency can be ramped, and its maximum value is twice the maximum input frequency (in this case from 3 to 6 GHz). A narrow bandpass filter selects the wave with the difference frequency. A linear synchronous detector rectifies the signal to get the amplitude (or power) of the mixed signal. The amplitude or power is displayed as a function of the LO frequency. The described principle is that of a heterodyne receiver. In commercial devices several steps of mixers are used.

The operator can choose four main parameters:

- the frequency range for the LO sweep
- the sweep time i.e. the time needed for the frequency sweep
- the reference level i.e. the power of the LO wave
- the resolution bandwidth corresponding to the width of the bandpass filter.

Short, excellent descriptions of the functionality of spectrum- and network analyzers are given in [119]. For a fixed LO frequency this principle is discussed in Chapter 5.9 for the narrowband position pick-up processing.

For a Schottky scan, typical values of an LO frequency range is 10 to 100 kHz with a sweep time of 0.1 to 1 s. One should be aware that due to the relatively long sweep time, possible changes of the beam parameters during this time are displayed in a wrong manner. Instead of using a spectrum analyzer, one can also use an ADC recording the data in the time domain and apply an FFT, see e.g. [143]. In modern applications, this is a cheaper alternative if the frequencies of interest are not too high.

7.2 Longitudinal Schottky signals for a coasting beam

We first consider a single particle with charge [1] ζe in a storage ring with a revolution period T_0 and a revolution frequency $f_0 = 1/T_0$. The current at a fixed location is given by the passing of the particle at time $t = 0, 1 \cdot T_0, 2 \cdot T_0, ...$ is

$$I(t) = \zeta e f_0 \sum_{h=1}^{\infty} \delta(t - hT_0) = \zeta e \sum_{h=-\infty}^{\infty} e^{2\pi i h f_0 t}. \tag{7.8}$$

[1] Here ζ is used as the abbreviation for the charge to distinguish it from the non-integer part of the tune q.

A real detector can only measure positive frequencies. Or in other words, the phase information is lost, when detecting a real signal using an ADC or a spectrum analyzer. Therefore the current of a single charge is

$$I(t) = \zeta e f_0 + 2\zeta e f_0 \sum_{h=1}^{\infty} \cos\left(2\pi h f_0 t\right) \tag{7.9}$$

The first term is the dc part of the current $I_{dc} = \zeta e f_0$, while the sum gives the Schottky signal, as we will see. The Fourier transformation is given by

$$I(f) = \zeta e f_0 \cdot \delta(0) + 2\zeta e f_0 \sum_{k=1}^{\infty} \delta(f - k f_0) \tag{7.10}$$

which is a line spectrum with peaks at all harmonics of the revolution frequency f_0, with finite height for a real beam and a real equipment, see Fig. 7.2.

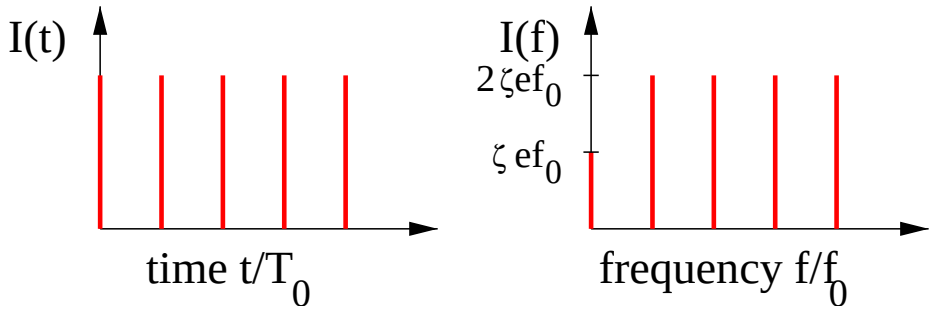

Figure 7.2: The time domain signal of a single particle in a storage ring and its frequency spectrum made of single lines.

Now consider a coasting (debunched) beam of N particles randomly distributed along the storage ring at an angle θ_n with slightly different revolution frequencies f_n. One can rewrite Eq. 7.9 for the N particles as

$$I(t) = \sum_{n=1}^{N} \zeta e f_0 \cos\theta_n + 2\zeta e f_0 \sum_{n=1}^{N} \sum_{h=1}^{\infty} \cos\left(2\pi h f_n t + h\theta_n\right) \tag{7.11}$$

A spectrum analyzer measures the power density spectrum, which is given for the frequency band of the harmonic h by the rms (root-mean-square) current $\langle I^2 \rangle$ as

$$\begin{aligned} \langle I^2 \rangle &= \left(2\zeta e f_0 \sum_{n=1}^{N} \cos h\theta_n\right)^2 = \left(2\zeta e f_0\right)^2 \cdot \left(\cos h\theta_1 + \cos h\theta_2 + ... + \cos h\theta_N\right)^2 \\ &= \left(2\zeta e f_0\right)^2 \cdot N/2 \end{aligned} \tag{7.12}$$

because all terms of the from $\cos^2 h\theta_i$ are positive. Or, in other words the term in brackets is

$$\left(\cos h\theta_1 + \cos h\theta_2 + ... + \cos h\theta_N\right)^2 = N\langle \cos^2 h\theta_i \rangle = N/2. \tag{7.13}$$

This means that only the dc part remains. All others cancel due to averaging. The rms signal is finally

$$I_{rms} = \sqrt{\langle I^2 \rangle} = \zeta e f_0 \sqrt{2N} \tag{7.14}$$

This total current per band is proportional to the square root of the number of particles due to its incoherent distribution. It is independent of the harmonic number h. This is different from the coherent beam signal recorded with a pickup for a bunched beam, having $I \propto N$. A more stringent treatment can be found in [120, 144, 145].

A pick-up, as described in Chapter 5, is used to monitor the signal. The measured current I_{rms} has to be transformed with the help of the transfer impedance Z_t to voltage $U = Z_t \cdot I_{rms}$.

A measurement using a spectrum analyzer shows the power spectrum density $P(f)$ within a frequency range Δf, which is given by

$$P(f) = Z_t \frac{I_{rms}^2}{\Delta f}. \tag{7.15}$$

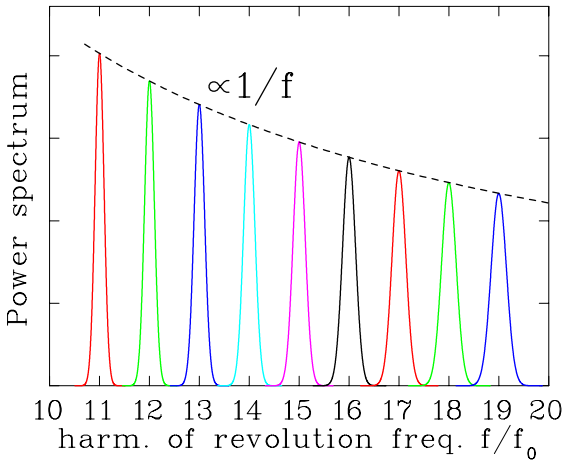

Figure 7.3: Hypothetical longitudinal Schottky lines for a Gaussian momentum distribution with $\Delta p/p = 1$ % and an artificial small value of $\eta = -0.005$. The different peaks correspond to the different harmonics.

Because the total power within a band is constant, the Schottky lines become broader for a increasing harmonic number h and their heights decrease. This is shown in Fig. 7.3. The width of all harmonics corresponds to the spread in the revolution frequency. Using the frequency dispersion η (Eq. 7.4), this can be transformed to the momentum distribution $\Delta p/p$. From the center frequency at each harmonic f_h and the width Δf_h, one can calculate the momentum width as

$$\frac{\Delta p}{p} = -\frac{1}{\eta} \cdot \frac{\Delta f_h}{f_h} = -\frac{1}{\eta} \cdot \frac{\Delta f_h}{h f_0}. \tag{7.16}$$

The plot in Fig. 7.3 uses a momentum width of 1%, but an artificially small value of $\eta = -0.005$ to get unusually broad lines. From the figure we can see, that the lines from ascending harmonics starts to overlap for

$$h > \frac{|\eta|}{2} \cdot \frac{p}{\Delta p} \tag{7.17}$$

which happens for real beams only at very high harmonics. Schottky lines at lower harmonics are well separated because $\Delta p/p < 10^{-3}$ and an absolute value of η close to unity are typical values for the injection to a synchrotron. The resolution is larger for higher harmonics due to a wider peak. On the other hand, the signal-to-noise ratio is better for a lower harmonic number due to the required lower bandwidth Δf and the scaling of the noise voltage $U_{noise} \propto \sqrt{\Delta f}$. At most proton or ion synchrotrons with a typical revolution time of 1 μs (corresponding to $f_0 = 1$ MHz), harmonic numbers between 10 and 30 are used. The typical frequency range for a scan of the distribution is less than 100 kHz.

In proton or ion synchrotrons or storage rings, cooling is very often used to achieve highly brilliant beams by transverse emittance and momentum distribution width reduction. This is important for high resolution experiments or the increase of the number of stored particles using stacking methods. This is performed by electron cooling (see e.g.[54]) or stochastic cooling (see e.g. [55]), in most cases with an un-bunched beam. Schottky diagnostics is an essential tool to control the cooling process. An example is given in Fig. 7.4, where the momentum width of an ion beam is reduced by two orders of magnitude within seconds by electron cooling.

The pick-up installed at the ESR at GSI is shown in Fig. 7.5. The device can also be used for transverse Schottky diagnostics (see below). For the horizontal and vertical direction, a pair of plates is installed, respectively. The edges are bent to get a constant position sensitivity, independent of the orbital offset perpendicular to the direction under investigation.

7.3 Longitudinal Schottky signals for a bunched beam

For a bunched beam, the Schottky spectrum splits into several lines for the following reason: In addition to the discussed fluctuations because of their finite number, the beam particles oscillate with

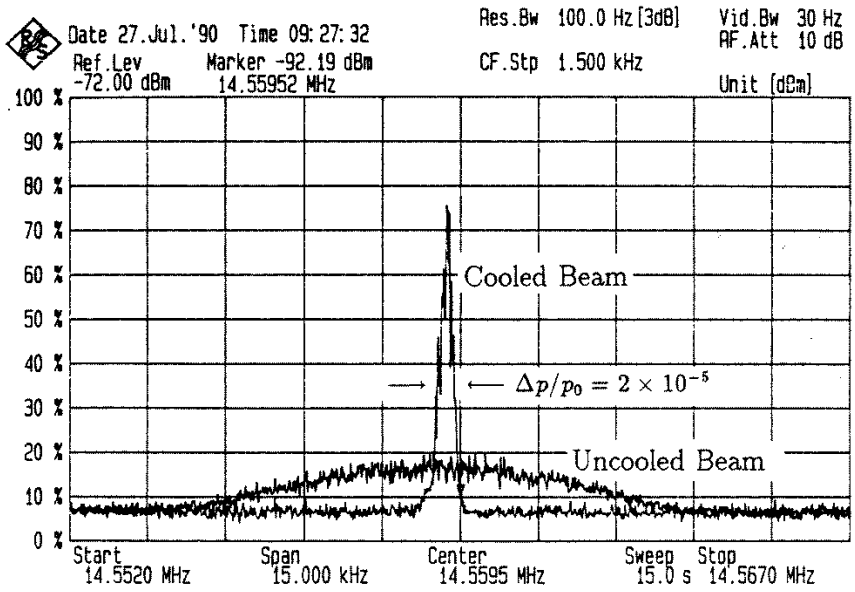

Figure 7.4: Longitudinal Schottky scan at the 10^{th} harmonic of Ar^{18+} at the GSI storage ring. The broad curve is the frequency spectrum at injection with $\Delta p/p = 1 \cdot 10^{-3}$ and the narrow curve is recorded after electron cooling down to a momentum width of $\Delta p/p = 2 \cdot 10^{-5}$.

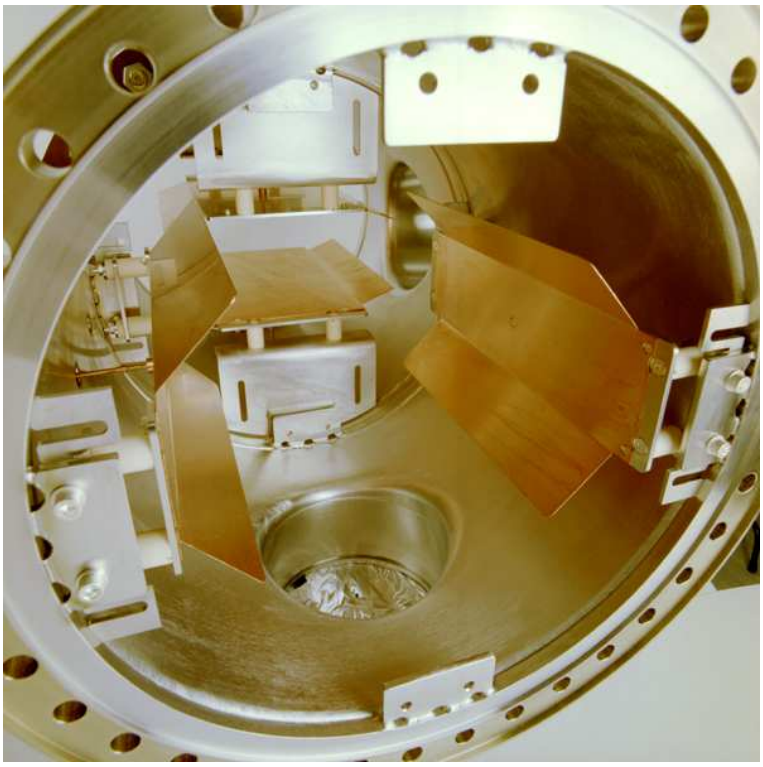

Figure 7.5: Photo of the Schottky pick-up installed at the storage ring at GSI. It can be used for longitudinal as well as for transversal diagnostics. In front we see the plates for the horizontal, at the back for the vertical direction. The flange diameter is Ø 350 mm.

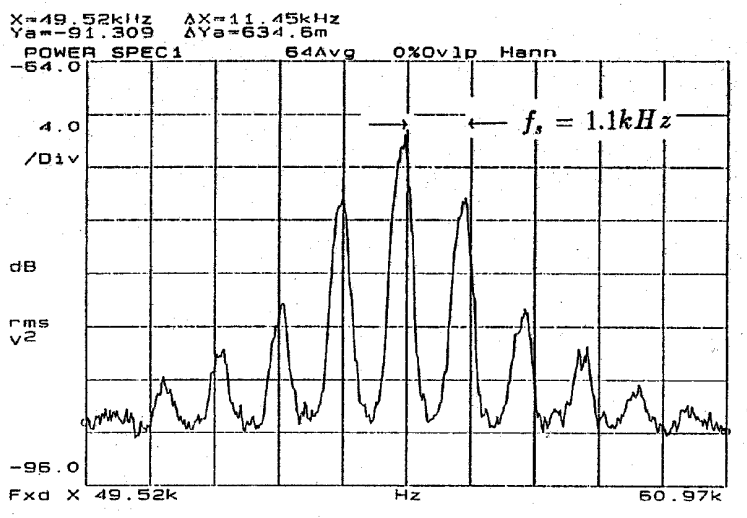

Figure 7.6: Schottky spectrum of a bunched ion beam at the GSI storage ring. f_s is the synchrotron frequency.

the synchrotron frequency. This corresponds to a modulation in time of the particles' passage through the pick-up. Therefore, the spectrum becomes more complicated since each of the harmonic lines $h \cdot f_0$ (center of the Schottky bands) split into sidebands from the synchrotron oscillation.

The passage of the particles at the pick-up is modulated by the synchrotron frequency f_s for particle n with $\tau_n = \hat{\tau}_n \sin(2\pi f_s t + \varphi_n)$. The synchrotron frequency is much lower than the revolution frequency. It can be shown [120], that this leads to a modulation of the un-bunched peak according to the Bessel functions J_p of order p. The second term of Eq. 7.11 has to be modified for each harmonic as

$$I_h(t) = 2\zeta e f_0 \cdot \mathrm{Re}\left[\sum_{n=1}^{N}\sum_{p=-\infty}^{\infty} J_p(h\omega_n\hat{\tau}_n)e^{i(h\omega_n t + h\theta_n + p\omega_s t + p\varphi_n)}\right] \qquad (7.18)$$

The distance between the maxima is given by the synchrotron frequency. The sidebands decrease symmetrically with respect to the center and get broader. The number of sidebands above the noise increases for increasing harmonics. A measurement is shown in Fig. 7.6. The synchrotron frequency can be determined with this method.

7.4 Transverse Schottky signals for a coasting beam

As in the case of a beam position pick-up, one can use the difference signal of opposite electrodes for the monitoring of transverse noise signals. The finite number of particles perform betatron oscillations around the beam center (and the electrical center of the pick-up) with

$$x_n(t) = A_n \cos(2\pi q f_0 t + \mu_n) = A_n \cos(2\pi f_\beta t + \mu_n) \qquad (7.19)$$

where A_n is the betatron amplitude of the particle n with an individual phase μ_n and q is the non-integer part of the tune and $f_\beta = q f_0$ the betatron frequency. The difference Schottky signal, which corresponds to the dipole moment d_n of the beam, is a composition of the longitudinal noise and a transverse modulation. For one particle and a harmonic h, the dipole moment $d_n(t)$ is

$$\begin{aligned} d_n(t) &= \zeta e f_0 \cdot A_n + 2\zeta e f_0 \cdot A_n \sum_{h=1}^{\infty} \cos(2\pi q f_0 t) \cdot \cos(2\pi h f_0 t) \\ &= \zeta e f_0 \cdot A_n + \zeta e f_0 \cdot A_n \sum_{h=1}^{\infty} \cos[2\pi(h-q) f_0 t] + \cos[2\pi(h+q) f_0 t] \end{aligned} \qquad (7.20)$$

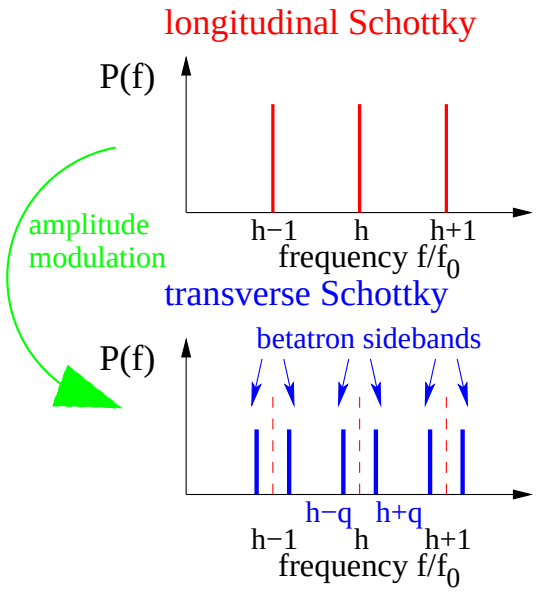

Figure 7.7: Schematic plot of the line splitting of a transverse Schottky scan as compared to the longitudinal case.

as given by a theorem of trigonometry [2]. In the frequency domain this corresponds to a splitting into two sidebands for each harmonic, distributed symmetrically at $h-q$ and $h+q$. In electrical-engineering this is called a frequency modulation. This is schematically shown in Fig. 7.7. The reason for the two bands arises from the fact that the Fourier transformation is defined for frequencies from $-\infty$ to $+\infty$, while a real device can only measure positive frequencies.

As in the longitudinal case, a coasting beam of N particles randomly distributed around the ring and with random betatron phase μ_n is considered. The rms-value per band is

$$\begin{aligned} d_{rms}^2 = \langle d^2 \rangle &= (\zeta e f_0)^2 \cdot A_{rms}^2 \cdot N/2 \\ &= (\zeta e f_0)^2 \cdot \epsilon \cdot \beta(s) \cdot N/2. \end{aligned} \tag{7.21}$$

The average of the individual betatron amplitudes A_n gives the beam width. The square of the width is related to the beam emittance ϵ times the value of the beta-function $\beta(s)$ at the location of the pick-up. A first result is that from the total power of the transverse band, one can deduce the emittance. In particular, one can monitor transverse cooling with the help of the transverse Schottky noise. This is demonstrated in Fig. 7.8, where the time evolution of the beam during stochastic cooling is shown. The curves are recorded every 80 ms. The decrease of the power within the sidebands is related to the shrinking of the emittance, and not due to particle losses.To get the absolute value of the emittance, a calibration is needed with respect to a residual gas monitor or a scraper, as too many inaccurately known device properties of the pick-up contribute to the spectrum. (A precise knowledge of the transverse transfer impedance $Z_\perp(\omega)$ Eq. 5.37 is needed, because the voltage $U = Z_\perp d$ is measured.) The middle peak of the figure is the longitudinal signal, which should vanish according to the theory above. However, here the beam was not perfectly centered in the pick-up. The increase of its height is due to longitudinal cooling.

Another widely used application of transverse Schottky is the tune measurement of coasting beams. The maxima of the two sidebands for the same harmonic are located at $f_h^- = (h-q)f_0$ and $f_h^+ = (h+q)f_0$. The non-integer part of the tune is calculated via

$$q = h \cdot \frac{f_h^+ - f_h^-}{f_h^+ + f_h^-}. \tag{7.22}$$

With this method, one can easily get the incoherent value of the tune without any beam influence. This is in contrast to a measurement via BTF discussed in Chapter 5.12, where the beam is excited

[2] $\cos x \cdot \cos y = 1/2[\cos(x-y) + \cos(x+y)]$

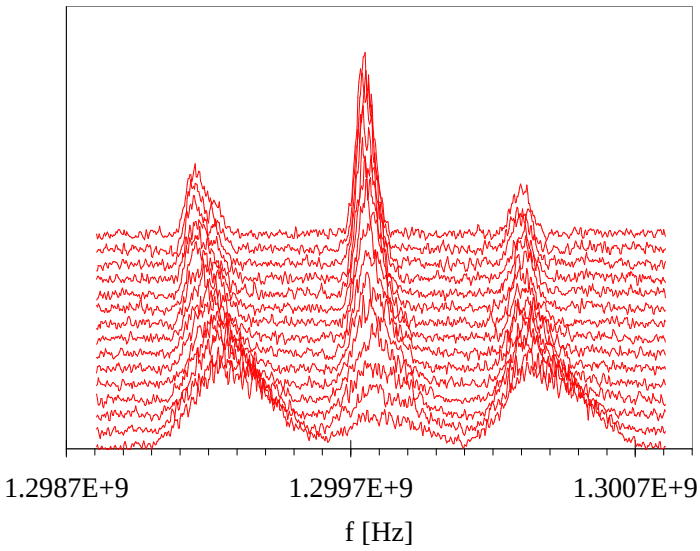

Figure 7.8: Transverse Schottky spectra recorded every 80 ms during stochastic cooling at the GSI storage ring at a high harmonic.

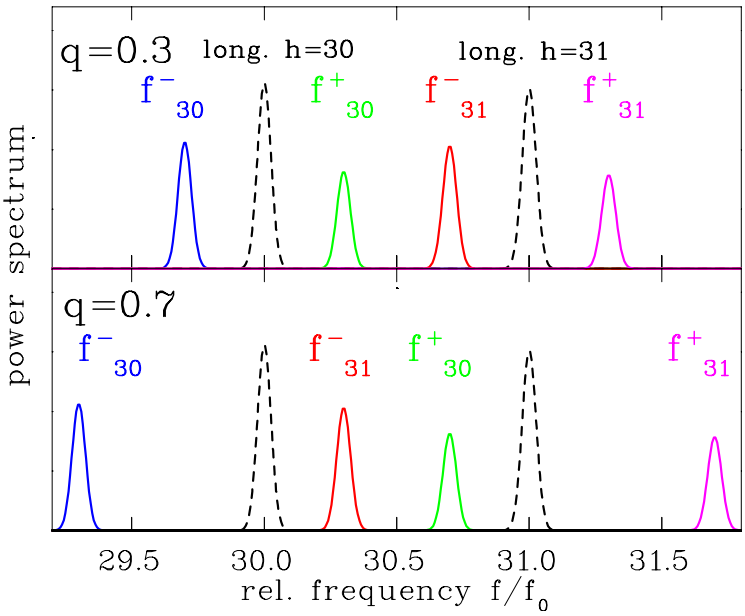

Figure 7.9: Transverse Schottky spectra for the harmonics 30 and 31. The plot on top shows the frequency position for $q = 0.3$. Here the sidebands are close to the longitudinal peak. The lower plot is for $q = 0.7$ and here the position are interchanged. The parameters for the calculation are: $f_0 = 1$ MHz, $\Delta p/p = 2 \cdot 10^{-3}$, $\eta = -1$, $\xi = -1$, $Q = 4.3$ or 4.7. The sideband for other harmonics are not shown.

gently. Moreover, for the BTF the coherent tune is determined, which might differ from the incoherent one, if space charge forces are significant.

Looking at a transverse Schottky scan, it is not directly evident where the two sidebands of one harmonic are located. The ordering of the lines can be interchanged. This is demonstrated in Fig. 7.9 for $q < 0.5$ (top) and $q > 0.5$ (bottom). As described for the BTF, this can be checked by a small variation of the tune while watching the direction of the line center shift.

From the width of the sidebands, the chromaticity can be deduced. From the position of the sidebands $f_h^{\pm} = (h \pm q) f_0$ and the product rule of the frequency derivative for the frequency distribution and the tune q one gets

$$\Delta f_h^{\pm} = \Delta f_0 (h \pm q) \pm \Delta q f_0. \tag{7.23}$$

Inserting the definition of frequency dispersion Eq. 7.4 and chromaticity Eq. 7.6 (the latter equation implies that the tune spread is mainly determined by chromaticity in connection with momentum spread and not by space charge effects) leads to

$$\begin{aligned} \Delta f_h^{-} &= \eta \frac{\Delta p}{p} \cdot f_0 \left(h - q + \frac{\xi}{\eta} Q \right) \quad \text{lower sideband} \\ \Delta f_h^{+} &= \eta \frac{\Delta p}{p} \cdot f_0 \left(h + q - \frac{\xi}{\eta} Q \right) \quad \text{upper sideband.} \end{aligned} \tag{7.24}$$

First, one can see that the widths of the sidebands are not equal. Which band is broader depends on the sign of the chromaticity ξ (in most case negative), on q and the harmonic number. In Fig. 7.9 this is not clearly seen due to the large scale, but the height is lower for the left sideband corresponding to a large width, because the integral power is equal for both sidebands. From the width of the sideband, we have a measurement of the chromaticity without any beam excitation. Of course the other parameters $\Delta p/p$, η (or γ_{tr}) and q have to be measured independently.

7.5 Some further remarks to Schottky analysis

- The transverse Schottky signals can also be observed for a bunched beam. Like in the longitudinal case, the sidebands are modulated due to synchrotron oscillations. This can make the spectrum quite complex.
- No space charge effects are considered in the discussion above. In particular, we assume that the tune is independent of the single particle betatron amplitude, and the tune spread is only given by the chromaticity. If this is not the case, the tune can be evaluated using a slightly more complex method, see e.g. [146].
- The longitudinal spectrum can be significantly deformed by observing cooled beams, perverting the interpretation of the width as the momentum spread. For cold and sufficiently dense beams, the signal shows a splitting related to plasma waves, see e.g. [145].
- We did not discuss the device noise level contribution to the spectra. In general, for the transverse case, the signal-to-noise is at least two orders of magnitude worse as compared to the longitudinal.
- If low currents have to be observed (like for anti-protons), the signal strength can be raised by an external resonator.

Chapter 8

Beam loss detection

In a real accelerator, the transmission from the source to the target is never 100 %. The fraction of beam particles lost has to be controlled carefully to achieve optimal transmission. The lost beam particles cause some activation of the accelerator components by nuclear reactions. Moreover, the surrounding material can be destroyed by the radiation, as well as by the heating due to the particles' energy loss. The important nuclear physics processes leading to secondary particles are reviewed briefly. To detect the shower of secondary particle a large variety of **B**eam **L**oss **M**onitors **BLM** exists. Most of them are particle counters, detecting secondary reaction products. At nearly every high current accelerator facility, these monitors are installed for the protection of the accelerator components. The relatively cheap BLM instruments are mounted outside of the vacuum pipe at crucial locations as schematically depicted in Fig. 8.1. Their signals serve as an essential information to prevent unwanted loss during the operation, e.g., caused by malfunctions of components. A careful analysis of the location and time structure of possible losses has to be performed before the choice of the suitable types of beam loss monitors can be made, see [147, 148, 149, 150] for a review. Beam loss monitors can be sensitive devices, which detect even a tiny fraction of losses; therefore they are also used for machine tuning. Two examples are presented in the last section.

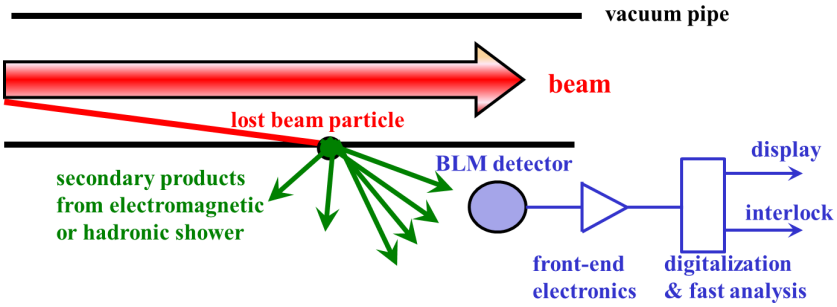

Figure 8.1: Scheme for the installation of Beam loss monitors outside of the vacuum pipe.

8.1 Secondary particle production

When a high energy particle hits the vacuum pipe or any other material, secondary particles are generated. The relevant processes are described e.g. in [157, 153]. Here only a brief overview is given:

- **Interaction of electrons**
  For electron energies above $\sim$ 100 MeV, Bremsstrahlung dominates the slow-down process in materials, as shown in Fig. 2.18. The created high energy γ photons give rise to further particles via $e^+ - e^-$ pair production. If the energy of the γ photons are high enough, other particles, like $\mu^\pm, \pi^\pm$... can also be produced, an electro-magnetic shower is generated. Moreover, the nucleus can be excited to so-called giant resonances: This is a collective nuclear excitation, where the neutrons oscillate against the protons. The dipole mode of these giant resonances has a threshold of about 6 MeV for typical materials. The de-excitation proceeds with high

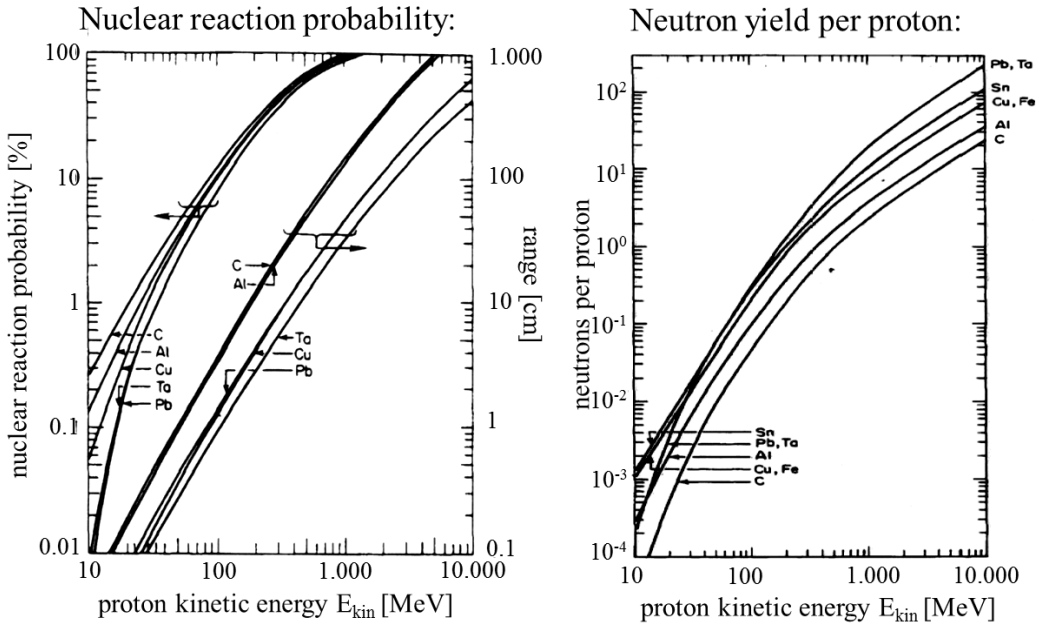

Figure 8.2: Left: The ranges of protons in various metals and the probability of an inelastic nuclear reaction within the range as a function of the proton energy, i.e. within a thick target. Right: The total number of neutrons per proton incident on a thick target of various metals as a function of the proton energy, from [153].

probability via neutron emission as a (γ, n) reaction. For higher energies also (γ, p) and (γ, np) channels are open.
When the electron is slowed down below $\sim$ 10 MeV, ionization loss by electronic stopping dominates, resulting in soft x-rays, which are absorbed within a short distance.

- **Interaction of protons**
  Beside electronic stopping, as shown in Fig. 2.17, nuclear interactions are possible. First, we define the term 'thick target' applicable if the interaction length is comparable to the range as given by the electronic stopping. In these thick targets, the probability of a nuclear reaction rises to nearly 100 % for energies above 1 GeV, see Fig. 8.2. Most of the final channels of these nuclear reactions include neutron emission. As an example, for the stopping of 1 GeV proton in copper or iron, $\sim$ 10 fast neutrons are liberated. The neutron yield scales approximately with E_{kin} for energies above 1 GeV. In addition, hadron showers (by the strong interaction at the quark level) are possible, resulting in various species of 'elementary' particles.

- **Interaction of ions**
  Besides the interactions also valid for the protons, an ionic projectile can be fragmented, or fission can be induced, leading to radioactive nuclei and fast proton and neutron emission. Simple scaling laws do not exist due to the complex nuclear physics involved.

Common to all interactions is the production of radioactive nuclei leading to activation of the accelerator components. The emitted charged particles are relatively quickly stopped by the surrounding material. However, the neutrons, produced by most primary interactions, can travel long distances. Some of the beam loss monitors are, therefore, sensitive to these neutrons. Except for the production of radioactive nuclei, all processes are fast, compared to the timescale of interest in accelerator physics, i.e. faster than $\sim$ 10 ns. In this sense, a beam loss monitor reacts promptly to the particle loss. Due to the kinematics of the primary interaction, the secondaries are emitted into a (more or less) forwardly peaked angular distribution. This leads to a spatial resolution of the loss detection by the monitor position close to the loss point.

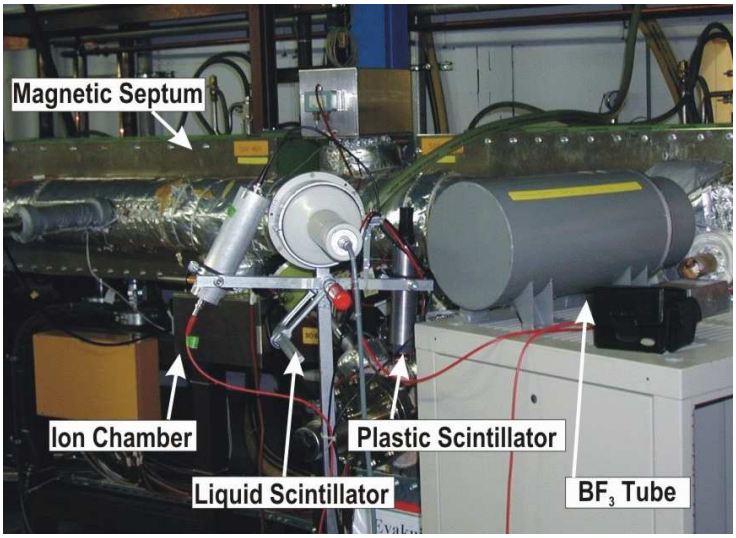

Figure 8.3: The tested beam loss detectors installed at the extraction from the GSI heavy ion synchrotron [154].

8.2 Types of beam loss monitors

The task for beam loss monitors is to localize the position and time of the loss. Their signals should be proportional to the amount of loss at this position. A high sensitivity is needed to measure low losses. A high dynamic range is required to deal with a sudden loss of a sizable fraction of the beam. Depending on the application, a bunch-to-bunch resolution on a ~ 10 ns time scale is needed, as well as up to 100 ms for a slow detection. All loss monitors are installed outside of the vacuum pipe, detecting mostly secondary particles. These can be neutrons, which are not much absorbed by the surrounding material, charged particles like protons, e^- and e^+ or γ-rays. Fig. 8.3 shows a photo of some frequently used types as tested at the GSI synchrotron. An overview of the different types is given in [150].

8.2.1 Plastic scintillators

Plastic scintillators detect charged particles due to their electronic stopping, as discussed in Chapter 2.8.1. γ-rays are detected additionally, as they liberate electron from the molecules via photo effect or Compton scattering; those electrons generate than the optical photons via their electronic stopping. Moreover, they are also sensitive to neutrons due to their elastic scattering on the hydrogen atoms of the polymers [11]. Due to the elastic scattering process generated by the relativistic neutrons, a large momentum transfer to the Hydrogen atoms of the macro-molecules is probable, which leads to a fast proton traveling through the scintillator material and finally generates the light emission by its electronic stopping. The light is guided to a photomultiplier, converted to electrons and amplified, see Fig. 8.4 for a typical realization. The readout of the resulting electronic signal can be effected by digitizing the analog voltage using a relatively small photomultiplier gain, or a particle counting mode can be used for higher sensitivity and larger dynamic range. A typical output for the counting mode is depicted in Fig. 8.4 showing analog pulses of ~ 10 ns duration. Due to the wide spectrum of incoming particle species and related energies, the pulse height distribution is quite broad. (This should be compared to the narrow pulse height distribution of single energetic particles in Fig 2.32.) In the counting mode, the plastic scintillators have an extensive dynamic range, from single particle counting up to a count rate of 10^7 s^{-1}. In most cases the scintillation monitors are located in the crucial areas, like the injection or extraction devices, or close to scrapers. The disadvantage is the low radiation hardness of the plastic materials due to the complex chemical composition of the polymers from the plastic matrix. A very rough number of the destruction threshold is given by the dose $D = 1$ Mrad $= 10^4$ Gy; around this value the light transmission is reduced by a factor $1/e = 0.37$. Typical sizes of plastic scintillators are cylindrical rods of 2 cm diameter and 10 cm length. Sometimes also long fibers of plastic or inorganic materials are used.

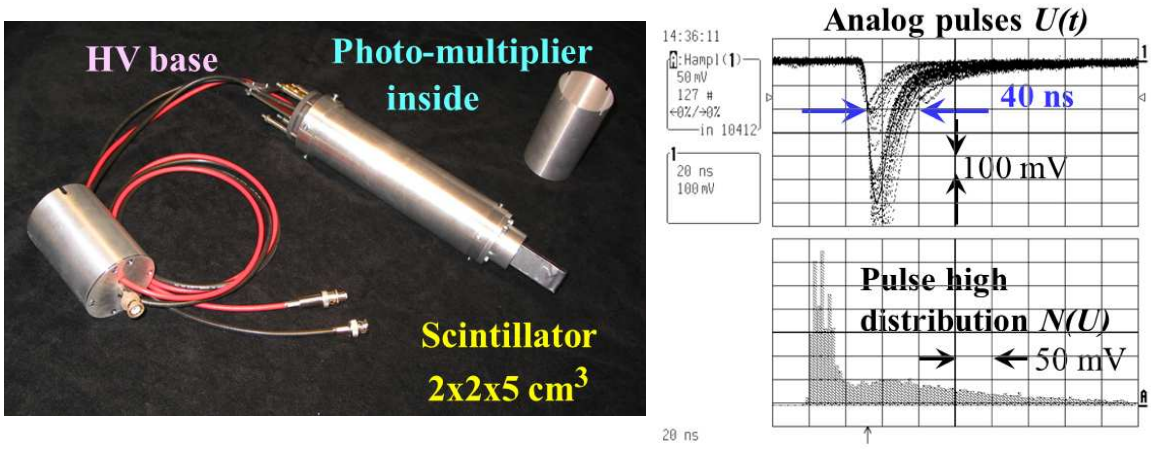

Figure 8.4: Left: Photo of a typical BLM based on a plastic scintillator connected to a photo-multiplier. Right: Typical pulses from a plastic scintillator (top, 100 mV/div and 20 ns/div) and their pulse height distribution (bottom, 50 mV/div) as measured at the GSI heavy ion synchrotron.

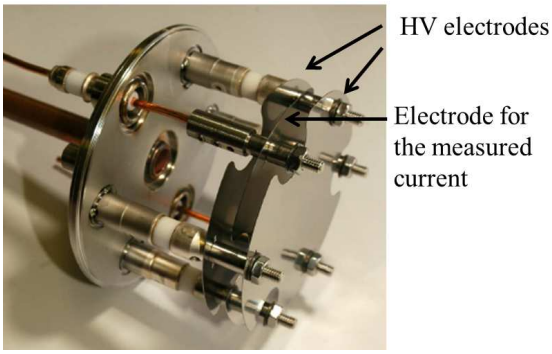

Figure 8.5: Photo of a three plate SEM beam loss monitor [151].

8.2.2 Liquid scintillator

A scintillator material within a liquid solvent of about 1 liter is used [11]. The device is also sensitive to charged particles, $e^{\pm}$, γ and neutrons by the same mechanisms as discussed for the plastic scintillators. A comparable pulse height distribution is observed. The pulse length of the scintillation process is about 1 order of magnitude longer and therefore the dynamic range is a factor of 10 lower for the counting mode. Due to the microscopic light creation, discrimination between γ-rays and neutron can be performed using selected electronics, the so-called pulse shape discrimination [11]. The liquid is about a factor of 10 more radiation hard than the plastics, due to the simpler chemical composition of the solvent.

8.2.3 Secondary Electron Multiplier and Secondary Electron Monitor

An Aluminum Coated Electron Multiplier (ACEM) is an electron multiplier, where the photo-cathode is replaced by an Aluminum surface. Secondary electrons are liberated by the interaction of the radiation and amplified by the dynodes. It offers a fast rise time and high dynamic range, but a sensitivity much lower as for scintillators.

In case the loss rate is very high, the current of secondary electrons from a surface is high enough to be measured directly. This can be realized by a secondary electron monitor by three plates installed in a small vacuum vessel [151]. The outer plates are biased by some +100 V and the secondary electron current emitted from the central plate is measured by a trans-impedance amplifier or a current-to-frequency converter. The inner part of such an monitor is shown in Fig. 8.5. Relevant simulations and tests of the response to different radiation are reported in [151].

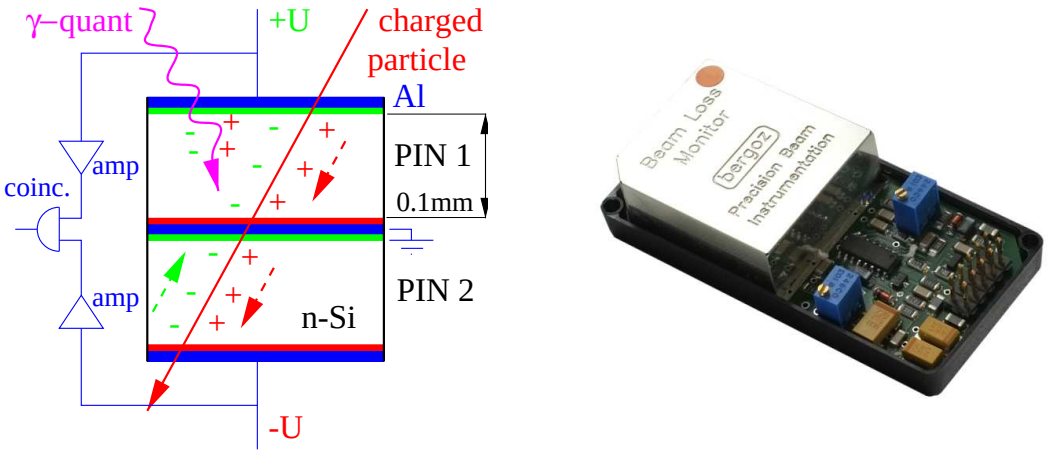

Figure 8.6: Scheme of a two PIN diodes driven in coincidence and a photo of the device [5].

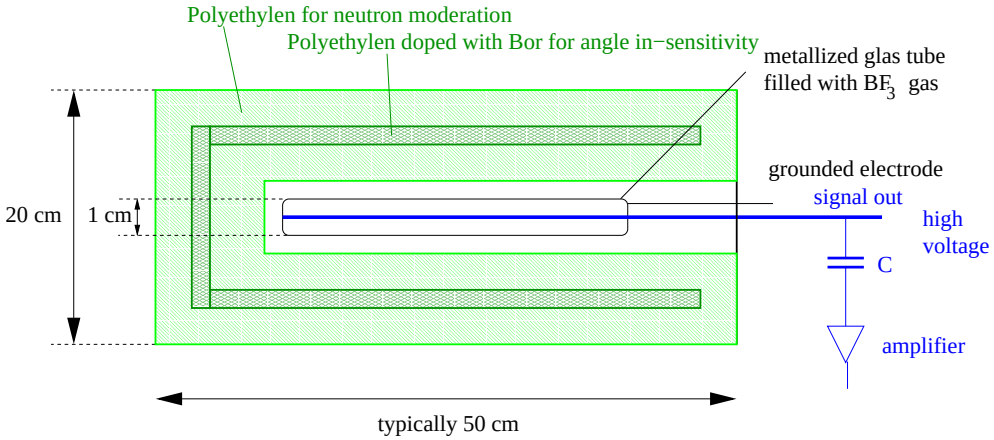

Figure 8.7: Scheme of a BF_3 proportional tube as used for beam loss detection. The proportional tube is filled with BF_3 gas surrounded by polyethylene for the moderation of the neutrons.

8.2.4 PIN diode

Solid-state detectors can be used as particle counters. In the typically 100 μm thick depletion layer of the doped Si-crystal, electron-hole pairs are generated. For a minimum ionizing particle (MIP), say, a charged proton at the minimum of its electronic stopping power, about 10^4 electron-hole pairs are generated. This signal has to be amplified by a charge sensitive pre-amplifier and can then be counted. As depicted in Fig. 8.6 two face-to-face mounted PIN diodes are used in coincidence to count only the charged particles and not the low energy photons, as emitted at electron accelerators by synchrotron radiation. These photons are absorbed in one PIN diode and do not arrive at the second. The detection efficiency is relatively low due to the small active area of typically 10×10 mm^2 and the 0.1 mm depletion depth. A device made of two PIN diodes including the amplifier and the counter is commercially available [5] and are often installed at synchrotron light sources.

8.2.5 BF_3 proportional tube

To have the possibility to measure only neutrons, a cylindrical proportional tube (typical diameter 10 mm and length 500 mm) filled with the gas BF_3 can be used [11]. For thermal neutrons, the reaction $^{10}B+n \rightarrow {}^7Li + \alpha$ has a high cross-section ($\sim$ 1 kbarn) and is exothermic by a Q-value (total kinetic energies of Li and α) of 2.3 MeV. The gas-filled tube is surrounded by concentric layers of polyethylene with an outer diameter of $\sim$ 200 mm. The neutrons from the primary beam interaction are slowed down by elastic collisions with the hydrogen nuclei of the polyethylene. Special precautions are taken to get a flat detection efficiency as a function of the angle. Frequently these detectors are used at nuclear power plants for neutrons with an energy up to 10 MeV, but the thermalization yield of the

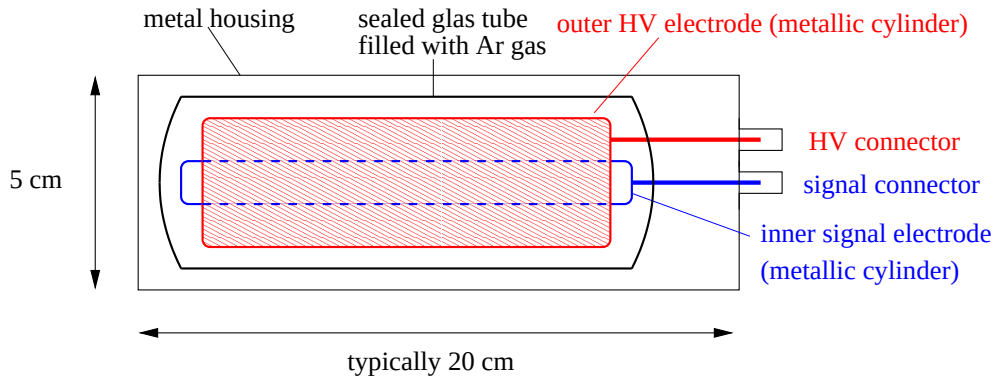

Figure 8.8: Scheme of an ionization chamber as used for beam loss detection.

Table 8.1: Basic parameters for the so called RHIC-type co-axial IC [152] and the planar LHC-type IC [156] for beam loss measurement.

Parameter	Co-axial IC	Planar IC
Outer length & diameter [cm]	20 & 6	50 & 9
Active gas volume [l]	0.11	1.5
Gas type & pressure [bar]	Ar at 1.1	N_2 at 1.1
Number of electrodes	2	61
Distance of electrodes [mm]	$\emptyset_{inner} = 6.3$, $\emptyset_{outer} = 38$	5.7
Voltage [kV]	1	1.5
Reaction time [μs]	$\simeq 3$	$\simeq 0.3$

neutrons can be extrapolated at least up to 100 MeV. In the traditional application, the glass tube is operated as a proportional tube; the count rate is limited to several 10^4 s^{-1} due to the time needed for recharging the inner wire of the proportional tube. Instead of the BF_3 working gas comparable types are used, but filled with ^{3}He, having a comparable cross section of thermal neutron absorption by the reaction $^3_2\mathrm{He} + \mathrm{n} \rightarrow {}^3_1\mathrm{H} + {}^1_1\mathrm{H}$ [11].

8.2.6 Ionization chamber

Ionization chambers measure the number of secondary charges created in a gas volume, see also Chapter 2.8.2. Fig. 8.8 shows such a round ionization chamber filled with Ar or N_2 gas. Typically, a sealed glass or metal tube contains $\sim$ 100...1000 cm^3 of gas between an outer high voltage electrode and an inner grounded and readout electrode [152]. The output current is measured with a sensitive current-to-voltage or current-to-frequency converter [155]. The IC is not sensitive to neutrons and has a low detection efficiency for γ-rays; mainly charged hadrons and $e^{\pm}$ are detectable. By definition, the signal strength gives directly the absorbed dose in Gy. Because an inert, rare gas like Ar or diatomic gases like N_2 or air are used in the detection volume, the device is very radiation hard. The signal strength is orders of magnitude lower than for detectors in a particle counting mode. In Fig. 8.8 the scheme of a co-axial IC is depicted. For this geometry, the IC does not react as fast as the scintillators, because the gas ions, created by the radiation, need $\sim$ 10 μs to reach the electrode. This time constant leads to a convolution of the primary signal, which for most applications is acceptable. The readout of the IC current by the digital electronics is therefore not faster than 1 ms in typical applications. The important parameters for such an IC are summarized in Table 8.2.6. A typical installation of a co-axial IC at an accelerator beam line or synchrotron is depicted in Fig 8.9.

The detection threshold of an IC is proportional to the gas volume. To achieve a fast reaction time, even for a large gas volume, the drift time of the gas ions and electrons should be shortened. This can be realized by a parallel electrode arrangement with alternating biased and read-out electrodes. Such an IC is shown in Fig. 8.10 as installed at CERN LHC and other facilities. About 4000 BLMs are installed along the 27 km long LHC corresponding to an average distance of about 6 m. They serve as the main detectors for beam protection and can trigger a fast abortion. The design of such IC for LHC and relevant simulations concerning the response to various radiation species are discussed e.g.

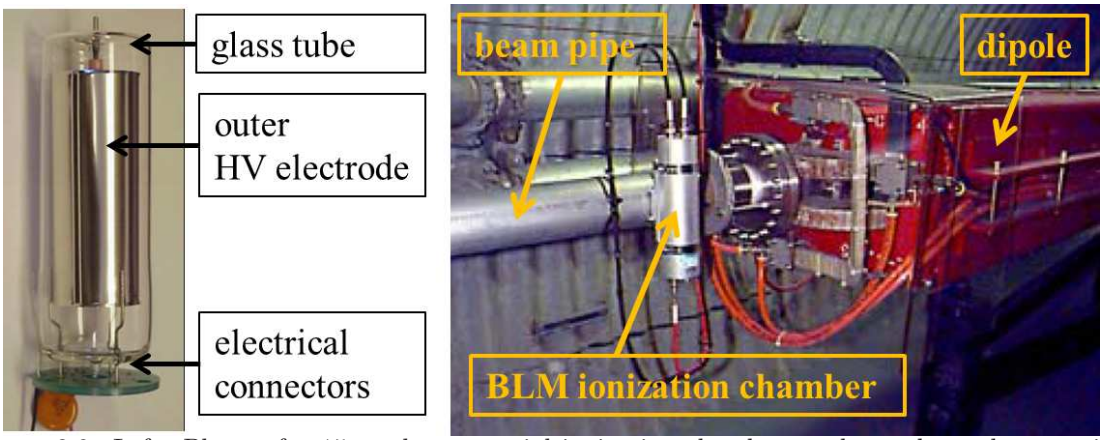

Figure 8.9: Left: Photo of a 15 cm long co-axial ionization chamber used as a beam loss monitor. Right: The installation of such a ionization chamber for beam loss detection in a transport line.

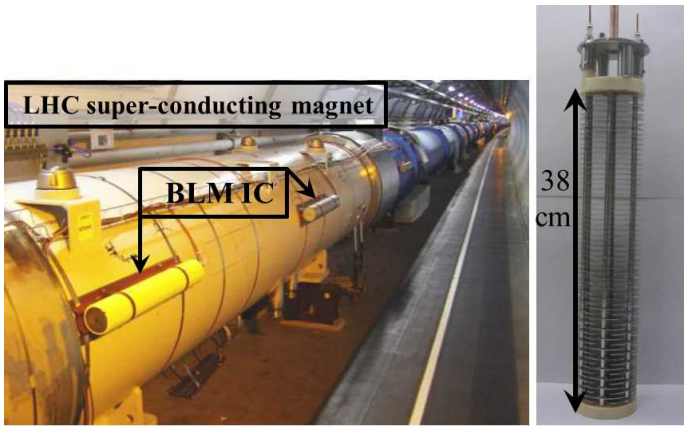

Figure 8.10: Photo of the installation of a 50 cm long ionization chamber comprising of 61 parallel plates at CERN LHC [156].

in [156].

A further type of IC is the so-called long, cable-based IC. It comprises of an air-filled long co-axial cable of some cm diameter as regularly used for medium power transmission of rf signals, see Fig. 8.11. Here the air itself acts as the ionization medium, and the cable can be 10 to 100 m long. The spatial resolution can be achieved by recording the arrival time of the signal at both ends using particle counting technologies; a typical time resolution of 10 ns corresponds to a spatial resolution of 1.5 m. This detector is e.g. suited for loss location at long transfer lines by using only one single detector with two readout channels.

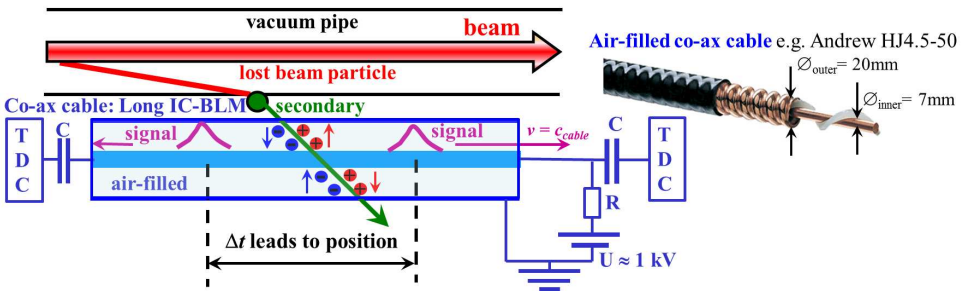

Figure 8.11: Scheme of a long, cable-based ionization chamber as installed along a beam line and a photo of a typically used rf-cable.

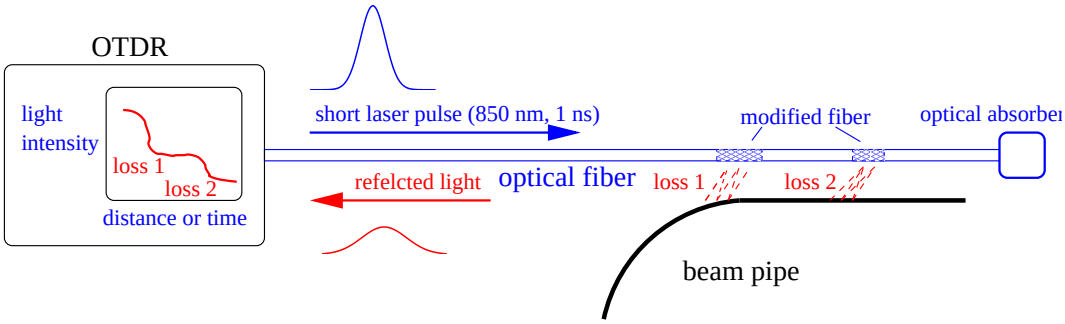

Figure 8.12: Principle of an OTDR beam loss detection with optical fibers.

8.2.7 Optical fiber

All discussed devices so far are particle counters. A different scheme uses material modifications by the absorbed dose, as reviewed in [158]. Optical fibers, like those used in telecommunication, can be fabricated in nearly arbitrary length at low cost. A fiber is installed close to the beam pipe with up to several km length [159]. Due to radiation destruction, secondary particles modify this fiber by creating color centers. This leads to a change in light transmission of the fiber and a noticeable amount of reflected light. As used in telecommunication, the quality of a fiber is tested by an optical time domain reflector (OTDR), see Fig. 8.12: A ~ 1 ns laser pulse is coupled to the fiber and travels along the fiber. If the optical properties of the fiber are modified due to the radiation, part of the light is reflected. Its intensity, as well as the arrival time with respect to the input pulse is measured. Due to the known velocity of light in the fiber of $\sim 0.66c$, this can be converted to a distance. With this arrangement, a reasonable spatial resolution can be achieved, and critical loss regions can be identified. An annealing process can partially repair the fiber, either by time or by heating the fiber to about 150 ^{o}C. Dedicated doping of the fibers makes them sensitive to different beam loss mechanisms. This monitor has a slow time response of more than 1 s due to the use of the OTDR.

Another method uses optical fibers as a scintillator, where the ionizing particles create light during their passage [158]. With a photomultiplier at each end of the fiber, the location of the interaction can be determined by comparing the arrival time of the light at both photomultiplier. No only scintillation but also Cherenkov light is detected as created by a charge traveling fast than the velocity of light inside the medium.

8.2.8 Comparison of different beam loss monitors

Several of the described types are tested at the extraction septum magnets at the GSI synchrotron [154]. A typical example is shown in Fig. 8.13 for a O^{8+} beam accelerated from 11.4 MeV/u to 800 MeV/u and then extracted slowly over 3 s; the maximum number of stored particles was 4×10^{10}. The signal as a function of time seen at the figure is displayed together with the signal for the synchrotron dc-transformer (top, arbitrary units) and a reference signal proportional to the extracted current measured at the experiment location (second plot, using a secondary electron monitor in arbitrary units, see Chapter 2.8.3). The general feature is that the signals for the different loss monitors are showing the same time behavior. This is not evident apriori due to the different detection mechanisms. This shows the predominant role of the 'prompt' radiation (prompt within a time scale of ms) whatever the type of secondary radiation is. The signals of all detectors are background-free, showing the minor role of permanent activation compared to the signals induced during the beam delivery. The choice of a BLM type is, therefore, mainly driven by the expected count rate.

The linearity of the different detectors is shown in Fig. 8.13 right, where the total counts for one spill are shown as a function of the current detected at the experiment. The count-rate is quite different: The plastic scintillator shows the maximum rate, about a factor of 30 more than the BF_3-tube, due to the detection of more categories of secondary particles. The liquid scintillator shows a lower rate; the saturation for the highest rate is due to the slow integrating pre-amplifier. The signal strength of the IC is lower by a factor of 200 as compared to the plastic scintillator. The dynamic range is highest for the plastic scintillator. The PIN diode is not shown here, but the count rate would have been about three orders of magnitude below that of the plastic scintillator.

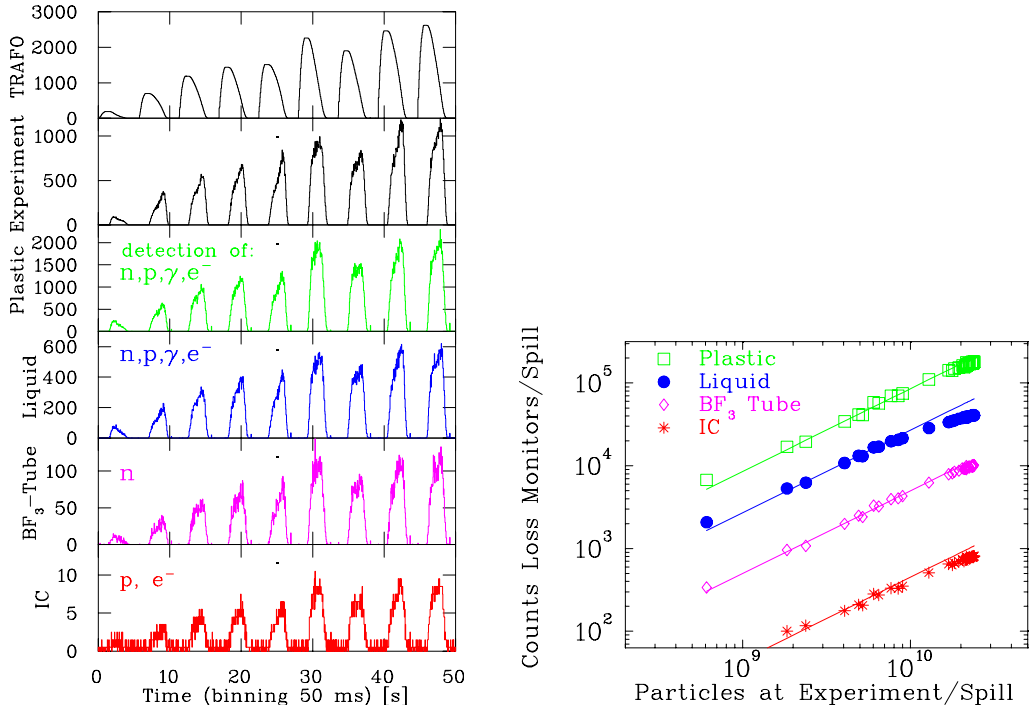

Figure 8.13: Left: Typical example from different beam loss monitors for a O^{8+} beam accelerated from 11 to 800 MeV/u for nine cycles with varying intensities up to 4×10^{10} particles per cycle [154]. Right: Linearity of the loss monitors as a function of the current for the same parameters. The lines are linear fits.

8.3 Machine protection using beam loss detectors

The most frequent application of beam loss monitors is the protection of the accelerator components. The high energy stored in the beam can lead to damage to the surroundings when the projectiles hit its materials. In particular, the vacuum pipe can be destroyed by the temperature rise due to the energy release of the particles, leading to a vacuum leakage. Moreover, other materials, like electrical feed-through, the isolation of the magnet coil, or any electronic devices can be destroyed due to the modification of the material by the radiation. As discussed in Chapter 8.1, the nuclear interaction leads to radioactive nuclei, which have lifetimes of hours or more. An activation of the accelerator components is the result, preventing the access of persons into the accelerator tunnel, and maintenance is strongly hampered. As a general rule, the power dissipation of the beam losses should be below 1 W/m to enable 'hands-on maintenance'.

Another important application of beam loss monitors is the quench protection of super-conducting magnets and cavities. Even a small amount of loss can heat the super-conducting material above the critical temperature causing a quench, i.e. a transition to normal conductivity. Loss monitors always control this dangerous situation. They create an interlock: as soon as a critical count rate or dose is reached, the beam is kicked out of the accelerator immediately. The design criteria of an interlock system are discussed in [155]. Last but not least the reason for low losses is the protection of the environment and an efficient transfer of particles to the experiment. In the control room of most high current accelerator facilities, the loss rate at sensitive locations is monitored online to visualize the full functionality of the machine.

We discuss briefly two categories of losses:

- **Irregular or fast losses** occur by a malfunction of an accelerator device, like magnets- or rf cavities power supplies, leading to a beam with wrong parameters and subsequently, the loss of part or all beam particles. Moreover, a misalignment of the device settings (e.g., the beam is not centered inside a quadrupole leading to steering, or wrong kinetic energy of the beam by a wrong rf cavity phase or amplitude) results in a mismatch of the beam at the following stages of the accelerator and part of the beam might be lost. The task of the beam loss monitors is to localize these losses, warning the operator or triggering an interlock to stop the beam delivery.

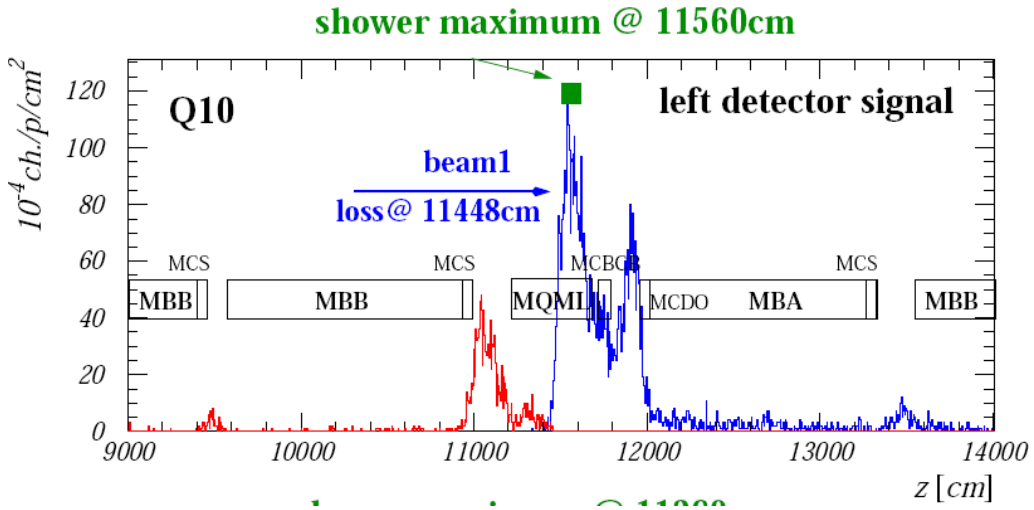

Figure 8.14: Simulation of a secondary particle distribution (hadron shower) due a proton loss inside a quadrupole for the LHC and 7 TeV protons [160]. The maximum of the shower is about 1 m from the loss point.

- **Regular or slow losses** are known losses, e.g. at aperture limits of a collimator system, or losses due to the finite lifetime of the beam in a synchrotron. Most of them are unavoidable, but an increase in the loss rate shows a malfunction. In addition, beam loss monitors can be used to find the appropriate parameters, e.g. for an emittance reducing collimator.

It is obvious, by looking in particular to the first item, that a beam loss monitor system should have a high sensitivity as well as an extensive dynamic range. The high sensitivity is needed to get a usable signal when only a tiny fraction of the beam is lost. Using scintillators or PIN diodes, single particle counting can be performed with a very low detection threshold. Detecting the lost particles directly gives a much higher sensitivity than looking at the lost fraction of the total signal by a current transformer. The high dynamic range is mainly needed for the detection of irregular losses because the losses at one location can easily vary by several orders of magnitude, e.g. due to a power failure of a magnet or cavity. The monitoring has to be operated over several orders of magnitude concerning the signal strength without changing the full-scale-range, to prevent the saturation of the signal for large losses. Here, a particle counting mode delivers this high dynamic for rates ranging from 10 s^{-1} up to 10^7 s^{-1}. Close to a collimator, scintillators offer the high dynamic range, which is needed for the sensitive detection of the tails in the transverse particle distribution. For other regular losses, the required dynamic range can be lower due to the slower time variation. For the detection of those applications, ionization chambers are often installed.

Beam loss monitors are relatively cheap instruments and are installed outside the vacuum pipe, see Fig 8.3. At most facilities, they are mounted at many locations along the accelerator to have good spatial coverage. The required time resolution depends very much on the application: For resolving the properties of individual bunches, fast responding detectors (reaction time less than 100 ns), like scintillators or PIN diodes, are needed. Ionization chambers are much slower having, in conjunction with the connected analog and digital electronics, only $\sim$ 100 μs time response. However, ICs offer the direct determination of dose and are therefore often installed for machine projection systems.

The position of the beam loss monitors should be well chosen. For highest sensitivity, the distribution of the secondary particles should have a maximum at this location. The secondary particle distribution has to be calculated using adequate software code. For high energies, the well-known code `GEANT` [161] is used in most cases, as shown in Fig. 8.14 for the case of the LHC beam. Of course, an assumption of the primary particle loss is needed. A loss of beam particles at a quadrupole is assumed in Fig. 8.14. This is the most probable location because the beam has the largest width there.

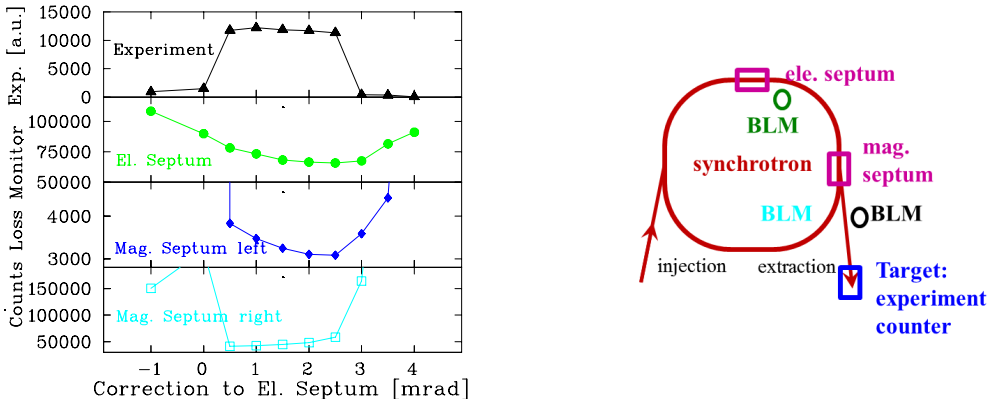

Figure 8.15: Left: Counts per spill from three loss monitor locations and the current at the experiment as a function of the angle electrostatic septum at the GSI synchrotron [154]. Right: The location of the BLMs and target diagnostics realted to the measurement.

8.4 Beam loss monitoring for alignment

Beam loss monitors have two main advantages, namely the large sensitivity and the fact that these monitors can be installed at many locations. For the alignment of the beam at critical positions having small beam pipes, beam loss monitors can be mounted densely. An example of the slow extraction at the GSI synchrotron is shown in Fig. 8.15. Here, the septum elements, used to kick the beam, have small pipe diameters, comparable to the actual beam size. If the angle at the input of the septum magnets is slightly wrong, part of the beam is lost there. Therefore, the angle kick at the first element (here the electro-static septum) has to be aligned carefully in small steps to find the minimal loss rate. Using beam loss monitors, the alignment procedure can be executed with higher sensitive input signals than by monitoring the transmitted current, as demonstrated by the top curve in Fig. 8.15.

To have a stable beam stored inside a synchrotron, the tune has to be chosen quite carefully to avoid tune-resonances resulting in a transverse beam blow-up. The mechanical alignment and the settings of the various magnets is never in perfect agreement with the theory; therefore the optimal setting for the beam has to be found experimentally. The beam blow-up can be measured precisely by putting a scraper close to the transverse beam tail inside the vacuum tube. The number of beam particles hitting this scraper can be determined by a beam loss monitor mounted close to the scraper. In Fig. 8.16, the loss rate normalized to the circulating current is determined as a function of the machine tune. The tune is varied by changing the main quadrupoles slightly. At certain settings, the loss rate increases. By a beam-optics theory aided alignment of all critical elements, the beam loss is minimized, and optimal storage is performed [162]. In Fig. 8.17 a the working diagram for a two-dimensional tune scan is show with the loss rate recorded by a BLM plastic scintillator in counting mode [163]. First, a scan was performed with a regular beam setting without closing an undulator. As expected, the highest loss rate is induced at a third order resonance along the line $Q_y = 6\frac{2}{3}$. Moreover, a high loss occurred in case the horizontal and vertical tune have the non-integer value of $q_{x,y} = \frac{3}{4}$. For the regular operation, the tune values $Q_x = 17.84$ and $Q_y = 6.72$ were chosen, as indicated in the figure. A second scan was done to show the additional effect of a closed undulator, and the modification of the loss rate was recorded. In particular, a high loss rate is visible on a line which couples the horizontal and vertical tune fulfilling the condition $Q_x + 3Q_y = 60$ as excited by the undulator's higher-order field components. Since there is a relationship between the resonant beam excitation and those higher field component as the driving term of the resonance, which allows to characterize the undulator's field components. For the displayed case, the working point was shifted in dependence of the undulator setting to avoid this beam loss.

More advanced experiments can be realized, for example, to get information about the beam lifetime limitations due to the interaction between the individual beam particles by Coulomb-scattering (i.e. intra-beam interaction by multiple Coulomb scattering leading to a transverse or longitudinal beam enlargement) or Touschek scattering (i.e. transfer of transverse particle momentum to the longitudinal plane by a single scattering process). A longitudinal increase of $\Delta p/p$ by Touschek scattering can be monitored by a scraper located at a dispersive region due to the coupling of $x = D \cdot \Delta p/p$, while at locations with $D = 0$ only the transverse effect is seen [163].

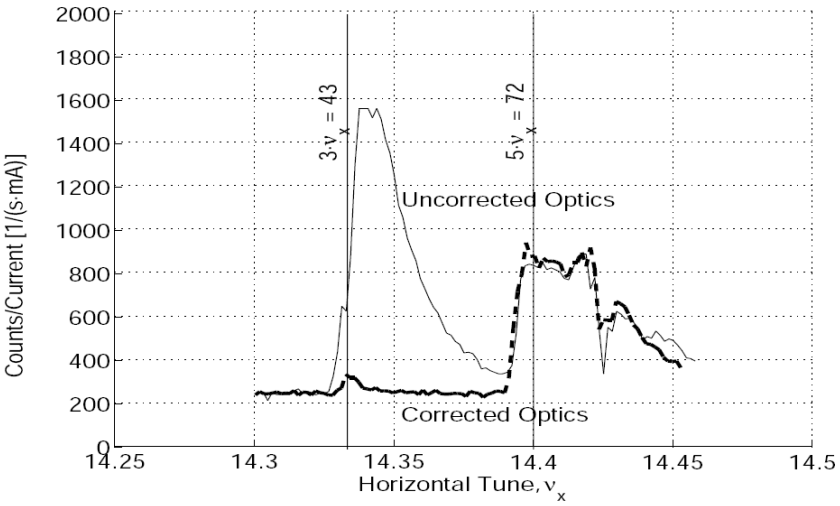

Figure 8.16: Tune scan at the ALS synchrotron light source [162]. For a fixed vertical tune, the horizontal tune is varied and the loss rate, as measured with a scintillator at a collimator is plotted. By changing the setting of some quadrupole, one resonance ($3 \cdot \nu_x$) can be avoided.

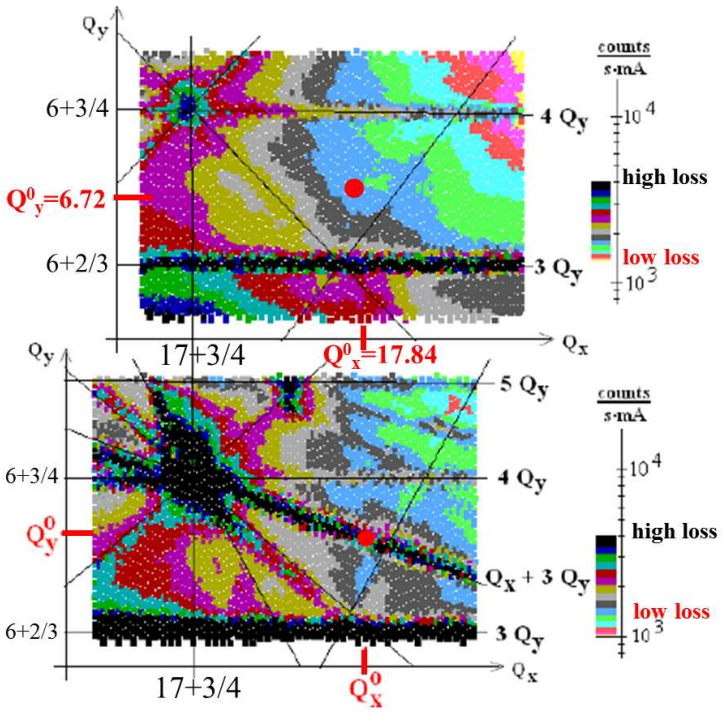

Figure 8.17: Loss rate at a plastic scintillator BLM for a two dimensional tune scan at BESSY synchrotron light source [163] without (top) and with (bottom) closed undulator. The horizontal Q_x and and vertical Q_y tune is changed; in case of the closed undulator (bottom) the coupling resonance fulfilling $Q_x + 3Q_y = 60$ is excited leading to strong losses.

Acknowledgment

The large and complex field of beam diagnostics can not be covered without participating in the open discussions held in the community of accelerator physicists, where one gets in contact with new and exciting physics and technologies. The valuable discussion with numerous colleagues is gratefully acknowledged.
A very clear description of diagnostics was presented Heribert Koiziol (previously CERN); I learned a lot from him. The content of this lecture was prepared during valuable discussions with Peter Strehl (previously GSI). I have to thank him for his ideas.
The members of the GSI beam diagnostic group were always open for discussion sharing their knowledge and were willing to prepare many good figures. In particular, I have to express my thanks to Mohammed Almalki, Frank Becker, Christoph Dorn, Tino Giacomini, Rainer Haseitl, Tobias Hoffmann, Wolfgang Kaufmann, Piotr Kowina, Andreas Reiter, Hannes Reeg, Thomas Sieber, Beata Walasek-Höhne and, in particular Rahul Singh. Also thanks many colleagues from GSI for the release of important and meaningful data.
The careful and critical reading of the script and the intense discussion on all subjects by Andreas Peters (HIT), Jeroen Belleman (CERN) and Jun He (CAS) is gratefully acknowledged and leads to important improvements.
Valuable comments by previous JUAS participants and further readers led to an improvements of the description; I acknowledge the related discussion warmly. Further criticisms and comments are always welcome.
Last but not least, thanks are given to my wife Elisabeth Forck and my children for their understanding and patient during a lot of long evenings, I was working for this lecture.

Appendix A

Frequently used abbreviations

ac	alternating current
ACCT	alternating current current transformer
ADC	analog-digital converter
amp	amplifier (electronic device)
BIF	beam induced fluorescence monitor
BLM	beam loss monitor
BPM	beam position monitor
BSM	bunch shape monitor
BTF	beam transfer function
BW	band-width for electrical devices
CCD	charged coupled device for a camera
dc	direct current
DCCT	direct current current transformer
CERN	centre européenne pour la recherche nucléaire
CMOS	complementary metal oxide semiconductor
DFT	discrete Fourier transformation
DTL	drift tube LINAC
DSO	digital signal oscilloscope
DSP	digital signal processor
EOM	electro-optical modulator
FCT	fast current transformer, identical to passive transformer
FFT	fast Fourier transformation
FWHM	full width half maximum
Grid	identical to SEM-grid for profiles
GSI	Gesellschaft für Schwerionenforschung
Harp	identical to SEM-grid for profiles
HV	high voltage above ~ 1 kV
IC	ionization chamber
IF	intermediate frequency for a rf-mixer
IPM	ionization profile monitor, identical to RGM
IR	infra red light
LHC	large hadron collider at CERN
LINAC	linear accelerator
LO	local oscillator for rf-mixer
MCP	micro channel plate
mw	micro waves with 1 GHz $< f <$ 100 GHz
MWPC	multi wire proportional chamber for profile measurement
NWA	network analyzer
op-amp	operational amplifier (electronic chip device)
OTR	optical transition radiation for profiles

PHD	pulse height distribution for particle detectors
PMT	photo-multiplier tube
pre-amp	first stage amplifier direct behind detector (fully equipped electronic device)
PU	pick-up used e.g. as the detecting device for beam position monitoring
rf	radio frequency with 100 kHz $< f <$ 1 GHz
RFQ	radio frequency quadrupole LINAC
RGM	residual gas (profile) monitor, identical to IPM
SEEM	secondary electron emission monitor, identical to SEM
SEM	secondary electron (emission) monitor, identical to SEEM
SEM-grid	secondary electron emission grid for profiles, identical to harp
SLM	synchrotron light monitor, identical to synchrotron radiation monitor
SPA	spectrum analyzer
SR	synchrotron radiation
SRM	synchrotron radiation monitor, identical to synchrotron light monitor
TOF	time-of-flight
UV	ultra violet light
WCM	wall current monitor

Appendix B

Definition of statistical moments

In this appendix the definition of the statistical moments of a two dimensional distribution are complied as used for the emittance calculation in Chapter 4.
Continuous case: A two dimensional density distribution $\rho(x, x') \in \mathbb{R}$ with independent, real variables $x \in \mathbb{R}$ and $x' \in \mathbb{R}$ is given. The first moments $\mu \equiv \langle x \rangle \in \mathbb{R}$ and $\mu' \equiv \langle x' \rangle \in \mathbb{R}$ are called expectation values and are defined as

$$\mu \equiv \langle x \rangle = \frac{\int_{-\infty}^{\infty}\int_{-\infty}^{\infty} x \cdot \rho(x,x')\ dx'dx}{\int_{-\infty}^{\infty}\int_{-\infty}^{\infty} \rho(x,x')\ dxdx'} \quad \text{and} \quad \mu' \equiv \langle x' \rangle = \frac{\int_{-\infty}^{\infty}\int_{-\infty}^{\infty} x' \cdot \rho(x,x')\ dxdx'}{\int_{-\infty}^{\infty}\int_{-\infty}^{\infty} \rho(x,x')\ dxdx'} \quad . \tag{B.1}$$

The n^{th} central moments of a density distribution $\rho(x, x')$ is calculated via

$$\langle x^n \rangle = \frac{\int_{-\infty}^{\infty}\int_{-\infty}^{\infty} (x-\mu)^n \cdot \rho(x,x')\ dx'dx}{\int_{-\infty}^{\infty}\int_{-\infty}^{\infty} \rho(x,x')\ dxdx'} \quad \text{and} \quad \langle x'^n \rangle = \frac{\int_{-\infty}^{\infty}\int_{-\infty}^{\infty} (x'-\mu')^n \cdot \rho(x,x')\ dxdx'}{\int_{-\infty}^{\infty}\int_{-\infty}^{\infty} \rho(x,x')\ dxdx'} \quad . \tag{B.2}$$

Using the abbreviation $P(x) = \int \rho(x, x')\ dx'$ and $P'(x') = \int \rho(x, x')\ dx$ as in Fig. 4.1 this is equivalent to

$$\langle x^n \rangle = \frac{\int_{-\infty}^{\infty} (x-\mu)^n \cdot P(x)\ dx}{\int_{-\infty}^{\infty} P(x)\ dx} \quad \text{and} \quad \langle x'^n \rangle = \frac{\int_{-\infty}^{\infty} (x'-\mu')^n \cdot P'(x')\ dx'}{\int_{-\infty}^{\infty} P'(x')\ dx'} \tag{B.3}$$

The second moments with $n = 2$ are called variances. If the variance is positive, its square root is the standard deviation $\sigma_x = \sqrt{\langle x^2 \rangle}$ and $\sigma_{x'} = \sqrt{\langle x'^2 \rangle}$.
The mixed quantity $\langle xx' \rangle$ is called covariance and is defined as

$$\langle xx' \rangle = \frac{\int_{-\infty}^{\infty}\int_{-\infty}^{\infty} (x-\mu) \cdot (x'-\mu') \cdot \rho(x,x')\ dxdx'}{\int_{-\infty}^{\infty}\int_{-\infty}^{\infty} \rho(x,x')\ dxdx'} \quad . \tag{B.4}$$

Discrete case: A real measurement leads to discrete values of the density distribution $\rho(x_i, x'_j)$ at discrete steps x_i and x'_j. The first moment is calculated for this case via

$$\mu \equiv \langle x \rangle = \frac{\sum_{i,j}\ x_i \cdot \rho(x_i, x'_j)}{\sum_{i,j}\ \rho(x_i, x'_j)} \quad \text{and} \quad \mu' \equiv \langle x' \rangle = \frac{\sum_{i,j}\ x'_j \cdot \rho(x_i, x'_j)}{\sum_{i,j}\ \rho(x_i, x'_j)} \quad . \tag{B.5}$$

The n^{th} central moment of the discrete distribution is

$$\langle x^n \rangle = \frac{\sum_{i,j}\ (x_i-\mu)^n \cdot \rho(x_i, x'_j)}{\sum_{i,j}\ \rho(x_i, x'_j)} \quad \text{and} \quad \langle x'^n \rangle = \frac{\sum_{i,j}\ \left(x'_j-\mu'\right)^n \cdot \rho(x_i, x'_j)}{\sum_{i,j}\ \rho(x_i, x'_j)} \quad . \tag{B.6}$$

The covariance is correspondingly

$$\langle xx' \rangle = \frac{\sum_{i,j}\ (x_i-\mu)\left(x'_j-\mu'\right) \cdot \rho(x_i, x'_j)}{\sum_{i,j}\ \rho(x_i, x'_j)} \quad . \tag{B.7}$$

Appendix C

Theorems of Fourier transformation

The Fourier transformation of a time-dependent function $f(t)$ is widely used to transform it into a frequency-dependent function $\tilde{f}(\omega)$. The technical application concerning the time-dependent function $f(t)$ is called time-domain processing, and its measurement uses typically an oscilloscope. The handling of the frequency-dependent function $\tilde{f}(\omega)$ is called frequency-domain processing, and the measurements uses typically a spectrum analyzer. (The physically used frequency f is related to the angular frequency ω via $\omega = 2\pi f$.) The transformation from time-domain to frequency-domain is often executed for the discussion of electronic circuits as the calculation methods might be more simple in one of the domains. The theorems below are extensively used for the discussion of BPMs in Chapter 5.
Firstly, the essential mathematical theorems in terms of continuous functions and infinite time observation are complied. Secondly, the crucial modifications for the realistic technical case of signal sampling with discrete time steps and finite observation time are given.

Theorems for continuous functions

Definition of Fourier transformation: Let $f(t) \in \mathbb{R}$ be a real, non-periodic and continuous function of the independent variable $t \in \mathbb{R}$ which is absolute integrable i.e. the integral $\int_{-\infty}^{\infty} |f(t)|dt < \infty$ exists and is convergent. Then the Fourier transformation $\tilde{f}(\omega)$ of $f(t)$ is defined as an integral transformation via

$$\tilde{f}(\omega) \equiv \int_{-\infty}^{\infty} f(t) \cdot e^{-i\omega t} dt \quad . \tag{C.1}$$

The Fourier transformation is a complex function $\tilde{f}(\omega) \in \mathbb{C}$ of a real variable $\omega \in \mathbb{R}$. In a technical application the absolute value $A(\omega) = |\tilde{f}(\omega)|$ called amplitude or magnitude or the square $A^2(\omega) = |\tilde{f}(\omega)|^2$ called power is often displayed as well as the phase $\tan\varphi(\omega) = \mathrm{Im}\left(\tilde{f}(\omega)\right)/\mathrm{Re}\left(\tilde{f}(\omega)\right)$ using the real and imaginary part of this complex function.
Definition of inverse Fourier transformation: For the frequency-domain function $\tilde{f}(\omega)$ the time-domain function $f(t)$ can be calculated via the inverse Fourier transformation

$$f(t) = \frac{1}{2\pi} \int_{-\infty}^{\infty} \tilde{f}(\omega) \cdot e^{i\omega t} d\omega \quad . \tag{C.2}$$

which results in the original time-domain function $f(t)$.
No loss of information: As a direct corollary of the definition it can be stated: Starting from a time-domain function $f(t)$ and performing the Fourier transformation yielding $\tilde{f}(\omega)$ and then executing the inverse Fourier transformation, the original time-domain function $f(t)$ is obtained. In other words: Each time-domain function $f(t)$ defines an unique transformation $\tilde{f}(\omega)$ and vice versa. For the technical application, this means that a description can either be performed in time- or frequency-domain yielding equivalent results.
Linearity: Let $a, b \in \mathbb{R}$ being some real numbers and $f_1, f_2 \in \mathbb{R}$ two Fourier transformable functions then it is

$$\int_{-\infty}^{\infty} [af_1(t) + bf_2(t)] \cdot e^{-i\omega t} dt = a\tilde{f}_1(\omega) + b\tilde{f}_2(\omega) \tag{C.3}$$

hence it is a linear transformation.
Time-shift theorem: Let $t_0 \in \mathbb{R}$ being a real number then it is

$$\int_{-\infty}^{\infty} f(t + t_0) \cdot e^{-i\omega t} dt = e^{-i\omega t_0} \cdot \tilde{f}(\omega) \tag{C.4}$$

i.e. the amplitude spectrum $A(\omega) = |\tilde{f}(\omega)|$ is equal to the un-shifted Fourier transformation while the phase is modified by the frequency dependent phase factor $\varphi(\omega) = \omega t_0$ with respect to the phase of the un-shifted function $\tilde{f}(\omega)$.

Frequency-shift theorem: Let $\omega_0 \in \mathbb{R}$ being a real number which is used as a harmonic modulation via $e^{i\omega_0 t}$ (technically called carrier frequency) of the original function $f(t)$ (technically called signal) then it is

$$\int_{-\infty}^{\infty} f(t)e^{i\omega_0 t} \cdot e^{-i\omega t} dt = \tilde{f}(\omega - \omega_0) \tag{C.5}$$

i.e. the original Fourier transformation is shifted by the modulation frequency ω_0. The effect of the modulation can be described as a replication of the signal transformation $\tilde{f}(\omega)$ (technically called base-band signal as centered around $\omega = 0$) to the modulation frequency as centered around $\omega = \omega_0$. This theorem is the basis for the technical application of frequency mixing, as e.g. used for narrow-band position determination by BPMs as described in Chapter 5.9.

Law of Similarity: Let $a \in \mathbb{R}$ being a real, non-zero ($a \neq 0$) number then it is

$$\int_{-\infty}^{\infty} f(t/a) \cdot e^{-i\omega t} dt = |a| \cdot \tilde{f}(a\omega) \tag{C.6}$$

i.e. a scaling law concerning the time or frequency range can be applied. Moreover, it can be stated that for a scalable time-domain function the Fourier transformation can easily be given. As an example consider a Gaussian function as it can be stated as wider the time-domain function is, as narrower is the frequency-domain function.

Differentiation law: Let $f(t) \in \mathbb{R}$ be a function and the n^{th} derivative $f^{(n)}(t)$ exists and is Fourier transformable then it is

$$\int_{-\infty}^{\infty} f^{(n)}(t) \cdot e^{-i\omega t} dt = (i\omega)^n \cdot \tilde{f}(\omega) \tag{C.7}$$

i.e. the Fourier transformation of the n^{th} derivative is given by the product of the of $(i\omega)^n$ with the Fourier transformation of the original function. This theorem is used in Eq. 5.3.

Parseval Formula: Let $f(t) \in \mathbb{R}$ be Fourier transformable and square integrable then

$$\int_{-\infty}^{\infty} |f(t)|^2 dt = \frac{1}{2\pi} \int_{-\infty}^{\infty} |\tilde{f}(\omega)|^2 d\omega \tag{C.8}$$

i.e. there is a simple relation between the integrated time-domain function and the integrated frequency spectrum.

Law of convolution: The convolution of two absolute integrable functions $f_1(t), f_2(t) \in \mathbb{R}$ is defined as

$$f_1(t) * f_2(t) \equiv \int_{-\infty}^{\infty} f_1(\tau) \cdot f_2(t-\tau)\ d\tau \quad . \tag{C.9}$$

The Fourier transformation of a time domain function $f(t) = f_1(t) * f_2(t)$ which is composed by the convolution of two functions $f_1(t)$ and $f_2(t)$ can be expressed as

$$\tilde{f}(\omega) \equiv \int_{-\infty}^{\infty} [\ f_1(t) * f_2(t)\ ] \cdot e^{-i\omega t}\ dt = \tilde{f}_1(\omega) \cdot \tilde{f}_2(\omega) \tag{C.10}$$

i.e. the action of a time-domain convolution of two functions can be calculated in frequency-domain by the multiplication of the individual Fourier transformed functions. This theorem is often used as the modification of the input signal $f_1(t)$ by a serial electronics chain of action $f_2(t)$ (comprises e.g. of low and high pass filters) is calculated by the product of the elements' Fourier transformations; the resulting product function in frequency domain is then inverse Fourier transformed to yield the final time-domain function $f_1(t) * f_2(t)$. This is widely used for the design of matched filters. Moreover, the theorem enables the choice to perform the filter calculation either in time-domain by convolution or in frequency domain as there is a one-to-one correspondence between the two methods.

Non-Fourier transformable functions: As the function $f(t)$ must be absolute integrable in terms of an indefinite integral, it must have the property $f(t) \to 0$ for $t \to \infty$ and $t \to -\infty$. Hence, polynomials (like $f(t) = \sum_{k=0}^{n} a_i \cdot t^k$), exponential functions (like $f(t) = e^t$) and periodic functions (like $f(t) = \sin t$) are not Fourier transformable in this mathematical sense. However, the Fourier transformation can artificially be

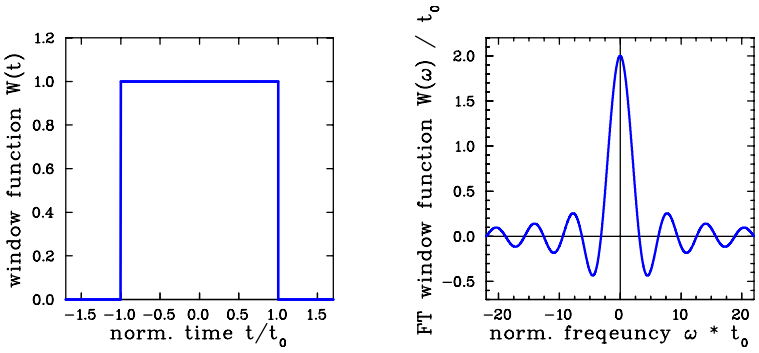

Figure C.1: The window function $W(t)$ (see text) and its Fourier transformation $\tilde{W}(\omega) = 2t_0 \cdot \frac{\sin \omega t_0}{\omega t_0}$.

restored if those functions have non-zero values only within a finite interval $[t_{min}, t_{max}]$ and are zero outside of this interval by the so called windowing, see Eq. C.11. This is a realistic assumption as a physical quantity is always measured within a limited time duration starting at t_{min} and ending at t_{max}. In this case, the frequency spectrum is modified, and the width depends on the choice of the duration $t_{max} - t_{min}$.
Windowing by integral kernel: The application of Fourier transformation can be extended by the insertion of a kernel or weight function $W(t)$ in the integral transformation as

$$\tilde{f}_W(\omega) \equiv \int_{-\infty}^{\infty} W(t) \cdot f(t) \cdot e^{-i\omega t} dt \tag{C.11}$$

which is called windowing. An example is the action of a rectangular window symmetric around $t = 0$ with $W(t) = 1$ for $t \in [-t_0, t_0]$ and $W(t) = 0$ for $t \notin [-t_0, t_0]$ as e.g. the case for a measurement within a limited time duration, see Fig. C.1. This procedure yields a convolution function in frequency-domain as $\tilde{W}(\omega) = 2 \cdot \frac{\sin \omega t_0}{\omega} = 2t_0 \cdot \mathrm{sinc}\,(\omega t_0)$, the so called sinc-function $\mathrm{sinc}\,(x) \equiv \frac{\sin x}{x}$. The central lope of this function has a base width of $2\pi/t_0$. For a Fourier transformable function $f(t)$ the multiplication in time-domain by a transformable weight function $W(t)$ corresponds to a convolution in frequency domain

$$\tilde{f}_W(\omega) = \tilde{W}(\omega) * \tilde{f}(\omega) \tag{C.12}$$

as given by the reversal of Eq. C.10.
Application for periodic signals: In the following the frequency spectrum for a train of bunches as e.g. stored in a synchrotron and depicted in Chapter 5.2 is discussed. The train of bunches is represented by a Fourier transformable time-domain function $f(t)$. This function can be de-composed by two functions: Firstly, the single bunch function $f_{sb}(t)$ defined within one acceleration-period of length t_{acc} i.e. for $t \in [0, t_{acc}]$ and being identically zero outside of the acceleration-period $f_{sb}(t) = 0$ for $t \notin [0, t_{acc}]$. Secondly, a periodic function $f_\delta(t)$ with the periodicity of the acceleration-period as composed of a train of δ-functions as $f_\delta(t) = \sum_{n=-\infty}^{\infty} \delta(t - n \cdot t_{acc})$. The train of bunches $f(t)$ can be written as a convolution of both functions as

$$f(t) = f_{sb}(t) * f_\delta(t) \equiv \int_{-\infty}^{\infty} f_{sb}(\tau) \cdot f_\delta(t - \tau)\, d\tau = \sum_{n=-\infty}^{\infty} \int_{-\infty}^{\infty} f_{sb}(\tau) \cdot \delta(t - \tau - n \cdot t_{acc})\, d\tau \quad . \tag{C.13}$$

The periodic expression $f_\delta(t)$ is called a Dirac Comb and it can be shown that the Fourier transformation is a Dirac Comb in frequency domain, i.e.

$$f_\delta(t) = \sum_{n=-\infty}^{\infty} \delta(t - n \cdot t_{acc}) \quad \Longrightarrow \quad \tilde{f}_\delta(\omega) = \sum_{n=-\infty}^{\infty} \delta(\omega - n \cdot \omega_{acc}) \quad . \tag{C.14}$$

This is true even though periodic functions can't be Fourier transformed and the mathematical argumentation uses the concept of Fourier series to approximate periodic functions. Using the law of convolution Eq. C.10 the frequency spectrum of the entire train of bunches can written as

$$\tilde{f}(\omega) = \sum_{n=-\infty}^{\infty} \tilde{f}_{sb}(\omega) \cdot \delta(\omega - n \cdot \omega_{acc}) \quad . \tag{C.15}$$

This shows that the spectrum is composed of lines at all harmonics of the acceleration frequency with an envelop related to the Fourier transformation of the single bunch as depicted in Fig. 5.7 and 5.8. In case of a finite observation time the formulas can be extended by a window function $W(t)$ and $\tilde{W}(\omega)$ according to Eqn. C.11 and C.12 leading to a finite width of the frequency lines, as e.g. depicted in Fig. 5.27.

Theorems for discrete sampling

In many technical applications a continuous time domain function $f(t)$ defined in an finite time interval is digitized at equidistant time steps Δt. This is an approximation of $f(t)$ by a finite number of $N \in \mathbb{N}$ samples $x(0), x(1)...x(N-1)$. An example is the digitalization of the voltage from a BPM electrode by an **A**analog **D**igital **C**onverter **ADC** to enable the subsequent numerical treatment by digital signal processing.

Discrete sampling and discrete Fourier transformation: Let us assume that a signal sequence of N elements $x(0), x(1)...x(N-1)$ is sampled equidistantly at with a frequency $f_{sample} = 1/\Delta t$. The **D**iscrete **F**ourier **T**ransformation **DFT** is defined in analogy to Eq. C.1 as

$$X(m) \equiv \sum_{n=0}^{N-1} x(n) \cdot e^{-i2\pi m \cdot n/N} \quad . \tag{C.16}$$

It is common to express time-domain quantities by lower case letters (here $x(n)$) and the corresponding frequency-domain quantities by capital letters (here $X(m)$). As all samples have finite values $x(n) < \infty$ and the sampling of the N values is performed during finite duration of $N \cdot \Delta t$, the restriction of absolute integrability by the indefinite integral in the mathematical description above is now obsolete. (As an example the DTF of a sine-wave recorded during a finite time can now be calculated.) The above mathematical theorems can be applied correspondingly, more details are described in textbooks on signal processing e.g. [117].

Inverse discrete Fourier transformation: The inverse DFT is called **IDFT** and is defined as

$$x(n) = \frac{1}{N} \sum_{m=0}^{N-1} X(m) \cdot e^{i2\pi m \cdot n/N} \quad . \tag{C.17}$$

DFT leakage and Nyquist-Shannon theorem: As there are only a finite number of samples N recorded with the frequency f_{sample}, the DFT is only given with steps of $f_{ana}(m) = \frac{m}{N} \cdot f_{sample}$ i.e. N equidistantly spaced frequency samples of $\Delta f_{ana} = \frac{1}{N} \cdot f_{sample}$ from zero up to half of the sample frequency $f_{ana}^{max} = \frac{f_{sample}}{2}$. Even for the case of a sine-wave recorded with finite time steps and finite duration the central lope of the frequency spectrum has a finite width, i.e. some of the power from the maximum 'leaks' to the sides of the frequency spectrum. The minimum width (defined by as the full width half maximum or technically expressed as 3 dB point) of the lope is given by the distance of two samples $\Delta f_{ana}^{res} = \frac{2}{N} f_{sample}$, i.e. the frequency resolution scales inversely proportional to the amount of non-zero samples; this is a consequence of the Nyquist-Shannon sampling theorem. The related resolution limit was discussed in the frame of tune measurement in Chapter 5.12.1. The finite frequency resolution can also be understood in terms of a continuous function $f(t)$ and a weight function $W(t)$ as discussed in Eq. C.11 and the convolution in frequency domain given by Eq. C.12.

DFT windowing: The properties of the spectrum can be influenced by weights $w(n)$ to be inserted in the definition of the DFT in terms of a kernel or window in analogy to Eq. C.11 as

$$X_W(m) \equiv \sum_{n=0}^{N-1} w(n) \cdot x(n) \cdot e^{-i2\pi m \cdot n/N} \quad . \tag{C.18}$$

Various types of windows are used as optimized to the required spectral information, see e.g. [117].

DFT and FFT, zero-padding: The DFT can be calculated for any amount of samples N. The abbreviation **F**ast **F**ourier **T**ransformation **FFT** refers to special type of algorithm for the calculation which requires that the amount of samples is given by $N = 2^k$ with $k \in \mathbb{N}$. In this case, the calculation can be executed much faster than for the general case, see e.g. [117]. If a real signal is sampled with $N \neq 2^k$ samples, additional zero-valued data can be appended to the data stream until the condition for the new amount of samples $N' = 2^k > N$ is reached; this is called zero-padding.

Bibliography

[1] **General readings on Beam Diagnostics**

1. V. Smaluk, *Particle Beam Diagnostics for Accelerators: Instruments and Methods,* VDM Verlag Dr. Müller, Saarbrücken 2009.
2. D. Brandt (Ed.), *Beam Diagnostics for Accelerators, Proc. CERN Accelerator School CAS,* Dourdan, **CERN-2009-005** (2009).
3. P. Strehl, *Beam Instrumentation and Diagnostics*, Springer-Verlag, Berlin 2006.
4. M.G. Minty and F. Zimmermann, *Measurement and Control of Charged Particle Beams,* Springer-Verlag, Berlin 2003.
5. S-I. Kurokawa, S.Y. Lee, E. Perevedentev, S. Turner (Eds.), *Proceeding of the School on Beam Measurement,* Proceeding Montreux, World Scientific Singapore (1999).
6. H. Koziol, *Beam Diagnostic for Acclerators, Proc. CERN Accelerator School CAS,* Uni. Jyväskylä, Finland, p. 565 **CERN 94-01**, http://schools.web.cern.ch/Schools/CAS/CAS_Proceedings.html (1993).
7. J.M. Month, S. Turner (Eds.), *Frontiers in Particle Beams; Observation, Diagnosis and Correction,* Proceeding Anacapri, Lecture Notes in Physics 343, Springer-Verlag, (1988).
8. These JUAS lecture notes are available at the JUAS INDICO web-site and www.gsi.de/work/fairgsi/linac_operations/ beam_instrumentation/ research_and_development_lobird/ veroeffentlichungen.htm.

[2] **Conferences**

1. *Dedicated beam diagnostics conferences:*
   - *International:* International Beam Instrumentation Conference (IBIC) Shanghai 2018, Grand Rapid 2017, Barcelona 2016, Melbourne 2015, Monterey 2014, Oxford 2013, Tsukuba 2012.
   - *Europe:* Diagnostics and Instrumentation at Particle Accelerators (DIPAC) Hamburg 2011, Basel 2009, Venice 2007, Lyon 2005, Mainz 2003, Genoble 2001, Chester 1999, Franscati 1997, Travemünde 1995, Montreux 1993.
   - *America:* Beam Instrumentation Workshop (BIW) Newport News 2012, Santa Fe 2010, Lake Tahoe 2008, Batavia 2006, Knoxville 2004, Brookhaven 2002, Cambridge (MA) 2000, Standford 1998 and earlier.

   Proceedings are available for IBIC, DIPAC (since 1999) and BIW (since 2008) on http://www.jacow.org.
2. *General accelerator conferences:*
   - *International:* International Particle Accelerator Conference (IPAC) Vancouver 2018, Copenhagen 2017, Busan 2016, Richmond 2015, Dresden 2014, Shanghai 2013, New Orleans 2012, San Sebastian 2011, Kyoto 2010.
   - *Europe:* European Particle Accelerator Conference (EPAC) Genoa 2008, Edinburgh 2006, Lucerne 2004, Paris 2002, Vienna 2000, Stockholm 1998, Sitges 1996, London 1994, Berlin 1992, Nice 1990, Rome 1988.
   - *America:* Particle Accelerator Conference (PAC) Pasadena 2013, New York 2011, Vancouver 2009, Albuquerque 2007, Knoxville 2005, Portland 2003, Chicago 2001, New York 1999, Vancouver 1997 and earlier.

   Proceedings are available on http://www.jacow.org.

[3] M. Bai et al., Nucl. Instrum. Meth. **A 499**, 372 (2003).
[4] M. Arinaga et al., Nucl. Instrum. Meth. **A 499**, 100 (2003).
[5] Company Bergoz, www.bergoz.com
[6] D. Belohrad, *Proc. Diag. Instrum. Part. Acc. Conf. DIPAC 11,* Hamburg, p. 564 (2011).
[7] R.C. Webber, *Proc. Beam Instr. Workshop BIW 94,* Vancouver, p. 3 (1994).
[8] H. Reeg, *Proc. Diag. Instrum. Part. Acc. Conf. DIPAC 01,* Grenoble, p. 120 (2001).
[9] K. Unser, IEEE Trans. Nucl. Sci., NS-28, p. 2344 (1981).
[10] W.R. Leo, *Techniques for Nuclear and Particle Physics Experiment,* Springer-Verlag Berlin (1994).
[11] G. F. Knoll, *Radiation Detection and Measurement*, John Wiley, New York (1999).
[12] J.D. Jackson, *Classical Electrodynamics*, John Wiley & Sons (1998).
[13] M. Tanabashi et al., Phys. Rev. D **98**, 030001 (2018), Chapter 33, see also pdg.lbl.gov.
[14] F. Ziegler, J.P. Biersack *SRIM*, see *The stopping and Ranges of Ions in Solids*, Pergamon Press (1985) and www.SRIM.org.
[15] O. Tarasov, D. Bazin et al., *LISE++* and subroutine *GOBAL*, lise.nscl.msu.edu/lise.html.
[16] M.J. Berger et al. Code ESTAR, National Institute of Standards and Technology NIST, see http://physics.nist.gov/PhysRefData/Star/Text/ESTAR.html.
[17] E.J. Sternglass, *Phys. Rev.* **108**, 1 (1957).
[18] C. G. Drexler, R.D. DuBois, Phys. Rev **A 53**, 1630 (1996).
[19] R.W. Müller, P. Strehl, *Nucl. Instrum. Meth.* **A 415**, 305 (1998).
[20] A. F. D. Morgan, *Proc. DIPAC 05,* Lyon, p. 51 (2005).
[21] P. Finocchiaro et al., *Proc. Diag. Instrum. Part. Acc. Conf. DIPAC 97,* Frascati, p.53 (1997).
[22] P. Forck et al., *Proc. Diag. Instrum. Part. Acc. Conf. DIPAC 97,* Frascati, p. 165 (1997).
[23] P. Forck et al., *Proc. of Beam Instrum. Workshop BIW 96,* Argonne, p. 422 (1996).
[24] e.g. P. Lecoq et al., *Inorganic Scintillators for Detector Systems,* Springer Verlag (2006).
[25] F. Sauli, *Prinziple of operation of multiwire and drift chambers,* CERN77-09 (1977).
[26] H. Reeg, *Proc. Diag. Instrum. Part. Acc. Conf. DIPAC 99,* Chester, p. 141 (1999).
[27] M. Sapinski, *Proc. of Beam Instrum. Workshop BIW 12,* Newport News, p. 245 (2012), corresponding code available at http://sapinski.web.cern.ch/sapinski/soft/pyTT.
[28] G. Ferioli, R. Jung, *Proc. Diag. Instrum. Part. Acc. Conf. DIPAC 97,* Frascati, p. 168 (1997).
[29] A. Peters et al., *Proc. of Beam Instrum. Workshop BIW 98,* Stanford, p. 163 (1998) and W. Vodel et al., *Proc. Int. Part. Acc. Conf. IPAC 13,* Shanghai, p. 497 (2013).
[30] R. Jung, G. Ferioli, S. Hutchins *Proc. Diag. Instrum. Part. Acc. Conf. DIPAC 03,* Mainz, p. 28 (2003) and R. Jung, *Proc. Diag. Instrum. Part. Acc. Conf. DIPAC 93,* Montreux, p. 4 (1993).
[31] B. Walasek-Höhne et al., *Proc. Diag. Instrum. Part. Acc. Conf. DIPAC 11,* Hamburg (2011) and workshop web-site http://www-bd.gsi.de/ssabd/index.html (2011).
[32] E. Gütlich et al., *Proc. of Beam Instrum. Workshop BIW 08,* Lake Tahoe (2008) and E. Gütlich et al.,*Proc. Diag. Instrum. Part. Acc. Conf. DIPAC 11,* Hamburg, p. 179 (2011).
[33] G. Kube et al., *Proc. Part. Acc. Conf. PAC 12,* New Orleans, p. 2119 (2012).
[34] U. Iriso et al., *Diag. Instrum. Part. Acc. Conf. DIPAC 09,* Basel, p. 200 (2009).
[35] R. Ischebeck et al., *Proc. Intern. Beam Instrum. Conf. IBIC 14,* Monterey, p. 259 (2014) and R. Ischebeck et al., *Phys. Rev. Special Topic Accel. Beams* **18**, 082802 (2015).
[36] T.J. Shea et al., *Proc. Part. Acc. Conf. PAC 97,* Vancouver, p. 2215 (1997).
[37] P. Forck et al., *Proc. Intern. Part. Acc. Conf. IPAC 14,* Dresden, p. 3482 (2014) and A. Lieberwirth et al., *Nucl. Instrum. Meth.* **B 365**, 533 (2015), P. Forck et al., *Proc. Diag. Instrum. Part. Acc. Conf. DIPAC 11,* Hamburg, p. 170 (2011) and reference their in.
[38] R.Haseitl et al., *Proc. PCs at Part. Acc. Conf. PCaPAC 2008*, Ljubljana, p. 180 (2008).
[39] M. Plum, *Beam Instrum. Workshop, Knoxville, AIP Conf. Proc. 732*, p. 23 (2004).
[40] S. Burger et al., *Proc. Diagn. Instrum Part Acc. Conf. DIPAC 03*, Mainz, p. 122 (2003).
[41] C. Fischer et al., *Proc. Euro. Part. Acc. Conf. EPAC 88,* Rome, p. 1081 (1988).
[42] U. Raich, *Proc. Diag. Instrum. Part. Acc. Conf. DIPAC 05,* Lyon, p. 1 (2005).
[43] R.J. Colchester, R. Jung, *Proc. Part. Acc. Conf. PAC 97, Vancouver IEEE Trans. Nucl. Sci.,* Vol NS-32 p. 1917 (1985).
[44] C. Field, *Nucl. Instrum. Meth.,* A360, p. 467 (1995).
[45] M. Matoba et al.,m *IEEE Trans. Nucl. Sci.,* Vol NS-32 p. 541 (1985).
[46] M. Benedikt et al., *Proc. Diag. Instrum. Part. Acc. Conf. DIPAC 01,* Grenoble, p. 189 (2001).
[47] C. Bovet et al., *Proc. Euro. Part. Acc. Conf. EPAC 98,* Stockholm, p. 1488 (1998).
[48] P. Forck, *Proc. Int. Part. Acc. Conf. IPAC 10,* Kyoto, p.1261 (2010) and P. Forck et al., *Proc. Diag. Instrum. Part. Acc. Conf. DIPAC 05,* Lyon, p. 221 (2005).
[49] T. Giacomini et al., *Beam Instrum. Workshop, Knoxville, AIP Conf. Proc. 732*, p. 286 (2004) and T. Giacomini et al. *Proc. Diag. Instrum. Part. Acc. Conf. DIPAC 05,* Lyon, p. 150 (2005).
[50] P. Forck, P. Strehl, *Proc. Diag. Instrum. Part. Acc. Conf. DIPAC 99,* Chester, p. 42 (1999) and P. Forck, A. Peters, P. Strehl, *Proc. Beam Instr. Workshop BIW 00,* Cambridge AIP 546, p. 606 (2000).
[51] R. Connolly et al., *Proc. Beam Instr. Workshop BIW 00,* Cambridge AIP 546, p. 330 (2000).

[52] K. Smith, Position-sensitive particle detection with microchannel-plate electron multiplier, *Experimental Methods in phys. science, Academic Press* Vol. 29A, p. 253 (1995).
[53] G. Ferioli et al., *Proc. Diag. Instrum. Part. Acc. Conf. DIPAC 01,* Grenoble, p. 201 (2001).
[54] D. Möhl, Stochastic cooling, in *CERN Acc. School,* CERN 95-06, p. 587 (1995) http://cas.web.cern.ch/cas/CAS_Proceedings.html.
[55] J. Bosser, Electron cooling, in *CERN Acc. School,* CERN 95-06, p. 673 (1995).
[56] A. Allisy (Ed.), *Secondary Electron Spectra from charged Particle Interaction*, International Commission on Radiation Units and Measurement Report No. 55 (1996).
[57] D. P. Sandoval et al., *Proc. Beam Instr. Workshop BIW 93,* Santa Fe, p. 273 (1993) and references their in.
[58] M.A. Plum et al., *Nucl. Instrum. Meth.* **A 492,** 74 (2002).
[59] P. Forck, A. Bank, *Proc. Euro. Part. Acc. Conf. EPAC 2002, Paris*, p. 1885 (2002) and A. Bank, P. Forck, *Proc. Diagn. Instrum Part Acc. Conf. DIPAC 03*, Mainz, p. 137 (2003).
[60] A. Variola, R. Jung, G. Ferioli, *Phys. Rev. Special Topic Accel. Beams* **10**, 122801 (2007), G. Burtin et al., *Proc. Euro. Part. Acc. Conf. EPAC 00, Vienna*, p. 256 (2000).
[61] Wartski et al., J. Appl. Phys. **46**, 3644 (1975).
[62] J. Bosser et al., Nucl. Instrum. Meth. **A 238**, 45 (1985).
[63] C. Bovet et al. *Proc. Diag. Instrum. Part. Acc. Conf. DIPAC 99,* Chester, p. 90 (1999) and V.E. Scarpine et al., *Proc. Part. Acc. Conf. PAC 2007 Albuquerque,* , p.2639 (2007).
[64] M.A. Tordeux and J. Papadacci, *Proc. Euro. Part. Acc. Conf. EPAC 00, Vienna*, p. 1818 (2000).
[65] P. Catravas et al., *Proc. Part. Acc. Conf. PAC 99, New York*, p. 2111 (1999).
[66] G. Kube, *Proc. Diagn. Instrum Part Acc. Conf. DIPAC 07*, Venice, p. 6 (2007).
[67] M. Wilke, *Proc. Beam Instr. Workshop BIW 94,* Vancouver, p. 128 (1994).
[68] A. Hoffmann, F. Meot, *Nuncl. Instrum. Meth.* **203**. p. 483 (1982).
[69] G. Kube et al., *Proc. Diagn. Instrum Part Acc. Conf. DIPAC 05*, Lyon, p. 202 (2005).
[70] C. Bovet et al., *Proc. Part. Acc. Conf. PAC 91,* San Francisco, p. 1160 (1991).
[71] B.X. Yang et al., *Proc. Part. Acc. Conf. PAC 97,* Vancouver, p. 2215 (1997).
[72] M. Pont et al., *Proc. IPAC 11,* San Sebastian, p. 3023 (2011) and G. Benedetti et al., *Proc. IPAC 11,* San Sebastian, p. 2059 (2011).
[73] B.K. Scheidt, *Proc. DIPAC 05,* Lyon, p. 24 (2005).
[74] T. Mitsuhashi, Beam size measurement by use of SR interferometers, in *Proceeding of the School on Beam measurement,* Montreux, p. 399 World Scientific Singapore (1999) and T. Mitsuhashi, *Proc. Beam Instr. Workshop BIW 2004,* Knoxville, AIP Conf. Proc. 732, p. 3 (2004).
[75] J.M. Stockli, *Proc. Beam Instr. Workshop BIW 06,* Batavia (Illinois), AIP Conf. Proc. 868, p. 25 (2006).

[76] M. Reiser, *Theory and Design of charged Particle Beams*, J. Wiley Publishing New York (1994).
[77] K.T. McDonald , D.P. Russell, *Methods of Emittance Measurement,* Proc. Anacapri, Lecture Notes in Physics 343, Springer-Verlag, p. 122 (1988).
[78] G. Riehl et al., *Proc. Diag. Instrum. Part. Acc. Conf. DIPAC 95,* Travemünde, DESY M9507, p. 6 (1995).
[79] M. Dolinska et al., *Proc. Diag. Instrum. Part. Acc. Conf. DIPAC 99,* Chester, p. 161 (1999) and T. Hoffmann et al., *Proc. Beam Instr. Workshop BIW 00,* Cambridge AIP 546, p. 432 (2000).
[80] M. Crecenti, U. Raich, *Proc. Diag. Instrum. Part. Acc. Conf. DIPAC 95,* Travemünde, DESY M9507, p. 66 (1995).
[81] P. Forck et al., *Proc. Linear Accel. Conf. LINAC 00,* Monterey, p. 166 (2000).
[82] G. Penco et al., *Proc. Euro. Part. Acc. Conf. EPAC 08,* Genoa, p. 1236 (2008).
[83] M.E. Schulze et al., *Proc. Linear Accel. Conf. LINAC 00,* Monterey, p. 575 (2000).
[84] V.A. Dimov et al., *Proc. High Brightness Hadron Beam Conf. HB 16,* Malmö, p. 433 (2016) and references therein.
[85] R.E. Shafer, *Proc. Beam Instr. Workshop BIW 89,* Upton, p. 26 (1989)
available e.g. at www.bergoz.com/en/mx-bpmf (1989).
[86] S.R. Smith, *Proc. Beam Instr. Workshop BIW 96,* Argonne AIP 390, p. 50 (1996).
[87] P. Forck in D. Brandt (Ed.), *Beam Diagnostics for Accelerators, Proc. CERN Accelerator School CAS,* Dourdan, **CERN-2009-005**, p. 187 (2009).
[88] M. Wendt, *Proc. Diag. Instrum. Part. Acc. Conf. DIPAC 11,* Hamburg, p. 18 (2011).
[89] F. Stulle (Company Bergoz), private communication.
[90] G. Kube, M. Werner, *Proc. Diag. Instrum. Part. Acc. Conf. DIPAC 07,* Venice, p. 105 (2007).
[91] J.M. Byrd, Bunched Beam Signals in the time and frequency domain, in *Proceeding of the School on Beam Measurement,* Montreux, p. 233 World Scientific Singapore (1999).
[92] J.F. Power et al., *Proc. Beam Instr. Workshop BIW 00,* Cambridge AIP 546, p. 535 (2000).
[93] B.G. Pine, *CARE-ABI Workshop Lüneburg 2006,*
see adweb.desy.de/mdi/CARE/Lueneburg/ABI-Lueneburg.htm (2006).
[94] R.E. Shafer, *Proc. Beam Instr. Workshop BIW 93,* Santa Fe, p. 303 (1993).

[95] C. Simon et al., *Proc. Int. Beam Instrum. Conf. IBIC 14,* Monterey, p. 303 (2014) and M. Almaki etal., *Proc. Int. Beam Instrum. Conf. IBIC 14,* Barelona, p. 319 (2016).
[96] C. Boccard, *CARE-ABI Workshop Lüneburg 2006,* see adweb.desy.de/mdi/CARE/Lueneburg/ABI-Lueneburg.htm (2006) and E. Calvo-Giraldo et al., *Proc. Diag. Instrum. Part. Acc. Conf. DIPAC 03*, Mainz, p. 187 (2003).
[97] N. Kurita et al., *Proc. Part. Acc. Conf. PAC 95,* Dallas, p. 2512 (1995).
[98] C.K. Ng et al, *Proc. Part. Acc. Conf. PAC 95,* Dallas, p. 2485 (1995).
[99] S. Varnasseri et al., *Proc. Diag. Instrum. Part. Acc. Conf. DIPAC 05,* Lyon, p. 90 (2005).
[100] A. A. Nosych et al., *Proc. Int. Beam Instr. Conf. IBIC 14,* Monterey, p. 298 (2014).
[101] P. Kowina et al., *Proc. Diag. Instrum. Part. Acc. Conf. DIPAC 05,*, Lyon, p. 114 (2005).
[102] Textbooks on micro-wave engineering, e.g., D.M. Pozar, *Microwave Engineering*, J. Wiley, New York (1998).
[103] D. Nölle, M. Wendt, *Proc. LINAC 04,* Lübeck, p. 435 (2004).
[104] D. Nölle et al., *Proc. LINAC 04,* Lübeck, p. 426 (2004).
[105] G. Vismara, *Proc. Beam Instr. Workshop BIW 00,* Cambridge AIP 546, p. 36 (2000) and G. Vismara, *Proc. Diag. Instrum. Part. Acc. Conf. DIPAC 99,* Chester, p. 11 (1999).
[106] M. Wendt, *Proc. Intern. Beam Instrum. Conf. IBIC 14,* Monterey, p. 468 (2014).
[107] R. Garoby, Low Level R.F. Building Blocks, in *CERN Acc. School,* CERN 93-03, p. 428 (1992), http://cas.web.cern.ch/cas/CAS_Proceedings.html.
[108] R. Lorenz, *Proc. Beam Instr. Workshop BIW 98,* Stanford AIP 451, p. 53 (1998).
[109] Company I-Tech, www.i-tech.si.
[110] J.M. Belleman, *Proc. Diag. Instrum. Part. Acc. Conf. DIPAC 05,* Lyon, p. 137 (2005).
[111] K. Unser, *Proc. Beam Instr. Workshop BIW 96,* Argonne AIP 390, p. 527 (1996) and www.bergoz.com.
[112] J. Belleman in D. Brandt (Ed.), *Beam Diagnostics for Accelerators, Proc. CERN Accelerator School CAS,* Dourdan, **CERN-2009-005**, p. 281 (2009).
[113] V. Schlott et al., *Proc. Euro. Part. Acc. Conf. EPAC 00,* Vienna p. 1809 (2000) and www.i-tech.si.
[114] R. Jones, *Proc. Beam Instr. Workshop BIW 10,* Santa Fe, p. 22 (2010), image: private communication.
[115] see e.g. J.D. Fox, E. Kikuzani, Bunch feedback system and signal processing, in *Proceeding of the School on Beam Measurement,* Montreux, p. 579 World Scientific Singapore (1999).
[116] R. Steinhagen in D. Brandt (Ed.), *Beam Diagnostics for Accelerators, Proc. CERN Accelerator School CAS,* Dourdan, **CERN-2009-005**, p. 317 (2009).
[117] See textbooks on Digital Signal Processing, e.g. R.G. Lyons, *Understanding Digital Signal Processing*, Prentice Hall Pearson Education, Boston (2011).
[118] R. Bartolini et al., *Proc. Euro. Part. Acc. Conf. EPAC 96,* Sitges, p. 1329 (1996) and R. Bartolini et al., CERN Sl/95-84 (1995).
[119] J.M. Byrd, Spectrum and network analyzser, in *Proceeding of the School on Beam measurement,* Montreux, p. 703, World Scientific Singapore (1999).
[120] D. Boussard, Schottky noise and Beam Transfer Function Diagnostics, in *CERN Acc. School,* CERN 95-06, p. 749 (1995), http://cas.web.cern.ch/cas/CAS_Proceedings.html.
[121] U. Rauch et al., *Proc. Diag. Instrum. Part. Acc. Conf. DIPAC 09,* Basel p. 324 (2009) and R. Singh et al., *Proc. High Brightness Hadron Beam Conf. HB 10*, Morschach, p. 226 (2010).
[122] J. Borer et al., *Proc. Euro. Part. Acc. Conf. EPAC 92,* Berlin, p. 1082 (1992) and P. Castro et al., *Proc. Part. Acc. Conf. PAC 93,* Washington, p. 2103 (1993).
[123] R. Tomas et al., *Phys. Rev. Accel. Beams,* **20**, 054801 (2017) and reference therein.
[124] J. Wenninger in D. Brandt (Ed.), *Beam Diagnostics for Accelerators, Proc. CERN Accelerator School CAS,* Dourdan, **CERN-2009-005**, p. 361 (2009).
[125] H. Burkhardt (CERN), private communication.
[126] H. Wollnik, *Optics of charged particles,* Academic Press (1987).
[127] J.C. Dooling et al., *Proc. Linear Accel. Conf. LINAC 00,* Monterey, p. 193 (2000).
[128] P. Forck et al., *Proc. Diag. Instrum. Part. Acc. Conf. DIPAC 05,* Lyon, p. 48 (2005).
[129] S. Hancock, M. Lindroos, S. Koscielniak, *Phys. Rev. Special Topic Accel. Beams,* **3**, 124202 (2000) and CERN-PS-2000-068-OP (2000) and http://cern.ch/tomography.
[130] S. Hancock, J.L. Sanchez Alvarez,
CERN PS/RF Note 2001-010, http://cern.ch/tomography.
[131] B. Fellenz, J. Crisp, *Proc. of Beam Instrum. Workshop BIW 98,* Stanford, p. 446 (1998).
[132] W.R. Rawnsley et al., *Proc. Beam Instr. Workshop BIW 00,* Cambridge AIP 546, p. 547 (2000).
[133] RD 42 Collaboration at CERN, E. Berdermann et al., *Proc. XXXVI Int. Winter Meeting of Nucl. Phys., Bormio* (1998).
[134] e.g. Campany Hamamatsu, www.hamamatsu.com
[135] P. Forck et al., *Proc. Diag. Instrum. Part. Acc. Conf. DIPAC 99,* Chester, p. 176 (1999).
[136] A.Feschenko, *Proc. Part. Acc. Conf. PAC 01,* Chicago, p. 517 (2001) and A. Feschenko, *Proc. Russian Part. Acc. Conf. RuPAC 12,* Saint Petersburg, p. 181 (2012).
[137] N. E. Vinogradov et al., *Nucl. Instrum. Meth.* **A 526**, p. 206 (2004).

[138] M. Ferianis et al., *Proc. Diag. Instrum. Part. Acc. Conf. DIPAC 03,* Mainz,p.113 (2003).
[139] K. Scheidt, *Proc. Euro. Part. Acc. Conf. EPAC 00,* Vienna, p. 182 (2000).
[140] K. Scheidt, *Proc. Euro. Part. Acc. Conf. EPAC 96,* Sitges, p. 1624 (1996).
[141] M. Labat et al., *Proc. Diagn. Instrum Part Acc. Conf. DIPAC 07*, Venice, p. 241 (2007).
[142] W. Schottky, *Annalen der Physik,* p. 57 (1918).
[143] L. Parker, *Proc. Beam Instr. Workshop BIW 04,* Knoxville, p. 393 (2004).
[144] S. Cattopadhyay, Some fundamental aspects of fluctuation and coherence in charged particle beams in storage ring, CERN 84-11 (1984).
[145] F. Nolden, *Proc. Diag. Instrum. Part. Acc. Conf. DIPAC 01,* Grenoble, p. 6 (2001).
[146] S. van der Meer, *Diagnostics with Schottky Noise* , Proc. Anacapri, Lecture Notes in Physics 343, Springer-Verlag, p. 423 (1988).
[147] K. Wittenburg, *Proc. Euro. Part. Acc. Conf. EPAC 02,* Paris, p. 109 (2002).
[148] K. Wittenburg in D. Brandt (Ed.), *Beam Diagnostics for Accelerators, Proc. CERN Accelerator School CAS,* Dourdan, **CERN-2009-005**, p. 249 (2009).
[149] A. Zhukov, *Proc. Beam Instrumtation Workhsop BIW 10,* Santa Fe, p. 553 (2010).
[150] R.E. Shafer, *Proc. Beam Instr. Workshop BIW 02,* Brookhaven AIP 648, p. 44 (2002).
[151] D. Kramer et al., *Proc. Diag. Instrum. Part. Acc. Conf. DIPAC 07,* Venice, p. 313 (2007) and D. Kramer *Design and Implementation of a Detector for High Flux mixed Radiation Fiels,* PhD Thesis Technical University of Liberec (2008).
[152] R.E. Shafer et al., *Proc. intern. Conf. High Energy Acc.*, Batavia, p. 609 (1983) and D. Gassner et al., *Beam Instrum. Workshop BIW 00*, Cambridge, p. 392 (2000).
[153] S. Roesler, M. Silari, R.H. Thomas, *Radiation effects and protection,* in *A.W. Chao, K.H. Mess, M. Tigner F. Zimmermann (Eds.), Handbook of Acceleration Physics and Engeneering,* World Scientific p. 767 (2013).
[154] P. Forck and T. Hoffmann, *Proc. Diag. Instrum. Part. Acc. Conf. DIPAC 01,* Grenoble, p. 129 (2001).
[155] B. Dehning, *Proc. Diag. Instrum. Part. Acc. Conf. DIPAC 05,*, Lyon, p. 117 (2005).
[156] E.B. Holzer et al., *Proc. Euro. Part. Acc. Conf. EPAC 08,* Genoa, p. 1134 (2008) and M. Stockner et al., *Proc. Diag. Instrum. Part. Acc. Conf. DIPAC 07,* Venice, p. 328 (2007).
[157] A.H. Sullivan, *A Guide to Radiation and Radioactivity Level near high Energy Particle Accelerators*, Nuclear Technology Publishing, Ashford (1992).
[158] F. Wulf, M. Körfer, *Proc. Diag. Instrum. Part. Acc. Conf. DIPAC 09,* Basel, p.411 (2009).
[159] H. Henschel et al., *Proc. Diag. Instrum. Part. Acc. Conf. DIPAC 01,* Grenoble, p. 73 (2001), H. Henschel et al., *Proc. Beam Instr. Workshop BIW 00,* Cambridge (MA), p. 647 (2000).
[160] E. Gschwendtner et al., *Proc. Euro. Part. Acc. Conf. EPAC 02,* Paris, p. 1894 (2002).
[161] http://wwwinfo.cern.ch/asd/geant4/
[162] D. Robin et al., *Proc. Euro. Part. Acc. Conf. EPAC 00,* Vienna, p. 136 (2000).
[163] P. Kuske, *Proc. Diag. Instrum. Part. Acc. Conf. DIPAC 01,* Grenoble, p. 31 (2001) and P. Kuske et al., *Proc. Part. Acc. Conf. PAC 001,* Chicago, p. 1656 (2001).